Mechanisms of Soil Erosion due to Defective Sewer Pipes

by

Yao Tang

A thesis submitted in partial fulfillment of the requirements for the degree of
Doctor of Philosophy
in
Geotechnical Engineering

Department of Civil and Environmental Engineering
University of Alberta

Abstract

Sinkholes are frequently reported around the world, and soil erosion around defective sewer pipe is found to be one of the possible cause of sinkholes. As water infiltrates through the defect in a pipe, soil can be washed into the pipe leading to a cavity or even sinkhole formation. Besides, water exfiltration through pipe defect can fluidize the adjacent soil leading to erosion. This thesis is focused on the mechanisms of soil erosion due to the defective sewer pipes.

Experiments were conducted to simulate soil erosion through a slot on a pipe for the two-dimensional condition, and the erosion through an orifice under three-dimensional condition was also studied. In the erosion process, it shows a steady relationship between the sand and water flow rate before the erosion void reaches the defect, and the relationship is dependent upon the sand particle size and defect size. The position of the defect on the pipe will affect the formation of erosion void while it has little effect on the sand flow rate in the erosion process.

A coupled three-dimensional discrete element model has been developed to simulate water/sand flow through an orifice. The water flow is simulated based on Darcy's model, which indicates this numerical model is valid if Reynolds number is less than 10, and the interaction between the fluid and solid phase is taken into account. The 'supply layer' is incorporated to study the continuous erosion process, which can simulate laboratory experiments on sand flow using this coupled model considering the current computing capacity.

If the sand is assumed to be the uniform sized circular particle, an analytical model is developed to predict the free-fall arch formation as the granular particles flow through a two-dimensional opening. Based on numerical simulations using discrete element method, the assumption of free-fall arch is shown to be reasonable. Based on this free-fall arch theory, an

analytical method is proposed to account for the effect of water flow on the granular discharge, which is developed using Stokes' law.

A numerical model based on computational fluid dynamics and kinetic theory of granular material is used to investigate the sand-bed erosion by an upward water jet. The numerical simulation shows that the inlet water velocity causing the sand-bed erosion increases as sand particle size increases. The increase in sand-bed height also increases the critical water velocity, whereas the critical velocity decreases as the decrease of sand friction angle. An analytical model based on the force equilibrium was developed to predict the critical water velocity. In this analytical model, the water flow was assumed as a uniform distribution over the mobilized zone in one-dimensional condition. The particle size in the sand bed was assumed to be uniformly distributed, whereas the shape and angularity of particle were taken into account using the sphericity coefficient.

From this thesis study, the sand particle size and defect size are the key factors on the soil erosion due to defective sewer pipes. In the soil erosion by water infiltration, the particle size can significantly affect the water flow due to the change of soil permeability. The steady relationship between sand and water in the erosion process can be explained by the free-fall arch theory and Stokes' law. The sand particle velocity reaches a small value as it moves to a specific boundary close to the defect, and the particle velocity will be significantly increased due to the gravity and drag force by water flow. From the theoretical derivation, it has been found the size of this boundary is dependent on the particle size and defect size, which is independent of the stress state above this boundary. In the study of sand-bed erosion by an upward water flow, the particle size can affect the seepage force on the mobilized sand bed, while the defect size controls the spread of water jet. Therefore, the particle size and defect size are also essential in the analysis of sand-

bed erosion by an upward water jet. The numerical and analytical models in thesis provide effective approaches to predict the soil erosion due to the defective sewer pipe, which also provides methods to carefully determine the particle size around the sewer pipe to reduce the soil erosion.

Acknowledgement

I would like to express my sincere gratitude to my supervisors, Dr. Dave Chan and Dr. David Zhu for their support, inspiration, invaluable supervision encouragement. Dr. Chan spent a lot of time helping me solve the problems in the research, and the way of thinking I learned from Dr. Chan will be my life-long fortune. Dr. Zhu helped me formulate this study. His patience and encouragement guided me to complete this thesis, and provided invaluable guidance for my future career. It is my honor and a great pleasure for me to study with Dr. Chan and Dr. Zhu.

I am grateful for the contributions of the committee members in my Ph.D. candidacy and final exams: Dr. Buddhima Indraratna, Dr. Lijun Deng, Dr. Alireza Nouri, Dr. Vivek Bindiganavile, Dr. Nallamuthu Rajaratnam and Dr. Alireza Bayat.

I would like to acknowledge the China Scholarship Council (CSC), Alberta Innovates Technology Futures (AITF) and Mitacs to support my Ph.D. study. I also appreciate the funding from the Department of Civil and Environmental Engineering and Dr. David Zhu.

I wish to thank my friends: Chao Kang, Yifei Cui, Shantanu Patel, Shuai Guo, Yuan Li, Yang Li, Chuan Lu and Xin Xu, for the stimulating discussions, and for all the fun we had in the past years. I also would like to thank my friends in different departments in U of A, Ligang Zhou, Lei Lu, Pengfei Wang, Jing Cao and Chenxin Ouyang. We met on the first day arriving Edmonton, and their support helped me get through the highs and lows of my life in Canada.

I would like to express my deep appreciation to my parents, my sibling, Ping and Yongchao. Their love helps me pass through these years away from home, and their support makes me progress further. This accomplishment would not have been possible without them.

Table of Contents

List of Figures

List of Tables

Abbreviations

2D	Two Dimensional
3D	Three Dimensional
CFD	Computational Fluid Dynamics
CT	Computed Tomography
DEM	Discrete Element Method
FDM	Finite Difference Method
FEM	Finite Element Method
LBM	Lattice Boltzmann Method
N-S	Navier-Stokes
PFC	Particle Flow Code
PIV	Particle Image Velocimetry
SPH	Smoothed Particle Hydrodynamics

Chapter 1 Introduction

1.1 Background

Sinkhole and ground surface collapse frequently occur in urban areas such as highway, roads or around buildings. Usually, the failure process is rather sudden without much evidence or obvious signs, which results in accidents, injuries or even death in some cases. The sinkhole in Guatemala led to 3 people killed in 2007 and 152 in 2010 (Hermosilla, 2012). A massive sinkhole occurred in Ottawa downtown in 2016 summer as shown in Figure 1.1, which caused power failure and gas leakage. It has been reported that 19 sinkhole accidents took place in Shenzhen city, China in 2013. Besides the threat to human life, almost every sinkhole brings a significant amount of capital loses. Normally the remediation of the incident cost millions of dollars depending on the particular condition, which may lead to consequential damages, e.g., interception of traffic, damage to adjacent buildings and other underground utilities.

Figure 1.1 Representative photos of sinkhole in Ottawa, Canada in 2016

(http://www.bbc.com/news/av/world-us-canada-36482438/footage-shows-moment-ottawa-sinkhole-swallows-car)

Unlike the geological definition of sinkhole, which is formed in limestone or karstic formations, sinkholes formed in urban areas during the past decade are accompanied with the deterioration of underground pipelines. One possible mechanism of sinkhole formation is soil loss into defective sewer pipe (Guo, 2013a; Indiketiya et al., 2017). It has been acknowledged that the most likely reason for the sinkhole in Ottawa is due to soil loss into the defective sewer lines.

Various researchers have conducted studies on defective sewer pipe. Based on the water head difference between the inside and outside of defective sewer pipe, water can either flow into pipe (infiltration) or flow out of pipe (exfiltration) through the defect. Several studies were conducted to estimate the rate of water infiltration/exfiltration (Lambert, 2001; Cassa et al., 2010; Guo et al., 2013b; Ssozi et al., 2015; Yang et al., 2016). Other studies were focused on the effect of soil loss on the mechanical behavior of defective pipes using numerical and experimental modeling (Tan and Moore, 2007; Spasojevic et al., 2007; Leung and Meguid, 2011, Kamel and Meguid, 2013). From current studies, the process of soil loss was neglected, whereas it has been found that the soil particles are gradually lost before the final urban sinkhole formation. Therefore, the assumptions in current studies are not reasonable.

Current studies on soil erosion due to defective sewer pipe are very limited. Fenner (1991) carried out laboratory tests to qualitatively assess the risk of soil migration process. Guo et al. (2013a) conducted a series of physical tests to study the soil erosion process caused by defective sewer pipe, and a simplified calculation model was proposed to predict the evolution of soil erosion based on experimental results. Mukunoki et al. (2009) and Mukunoki et al. (2012) studied the cavity formation around the pipe defect by water infiltration using X-ray Computed Tomography. An analytical method was proposed to predict the sand and water flow rate during erosion, which is developed based on the empirical equation accounting for the water pressure difference adjacent

to the defect by Guo and Zhu (2017). Indiketiya et al. (2017) conducted laboratory model tests to study soil mobilization around defective sewer pipe. Cui et al. (2012, 2014) attributed the sinkhole formation to the outflow of deteriorated underground pipeline with pressurized water, and numerical simulations were conducted using a coupled discrete element method (DEM). Alsaydalani and Clayton (2014) studied the soil fluidization mechanism around leaking pipe by experiments. Although sinkhole formation due to defective sewer pipe has attracted much attention recently, studies directly towards an understanding of the mechanism are rarely found.

1.2　Problem Statement

Current studies on defective sewer pipe mainly focus on the infiltration/exfiltration rate estimation through the defect or the mechanical behavior of defective sewer pipes, while the study on soil erosion due to defective sewer pipe is still preliminary. It has been found that soil erosion is an essential stage before ground collapse (Davies et al., 2001). Considering the increase of sinkhole incidents with serious consequences, there is a significant gap between sinkhole hazards and mechanism studies, which has motivated this work.

From the reported cases of sinkhole incidents, soil will be eroded due to water infiltration through defects in sewer pipe, and water exfiltration will fluidize the surrounding soil leading to soil erosion. In this study, model experiments were conducted to examine the effects on soil erosion due to water infiltration, and the effects of soil properties, size of the defect, defect position on pipe and water level. A coupled discrete element (DEM) model is developed in this study to simulate soil erosion adjacent to defective sewer pipe. Soil erosion caused by water infiltration can be simplified as granular flow through an opening assisting by flowing water. A free-fall arch model is developed and introduced to predict the soil erosion. Another scenario of soil erosion due

to defective sewer pipe is erosion due to upward water jet through a defect. Numerical simulation using the computational fluid dynamics (CFD) was conducted to explore the mechanism of soil erosion by water jet, and an analytical model was developed to evaluate the jet erosion. The research route of this thesis is shown in Figure 1.2.

```
                    ┌──────────────────────┐
                    │  Soil Erosion due to │
                    │  Defective Sewer Pipes│
                    └──────────────────────┘
           ┌──────────────────┴───────────────────┐
           ▼                                        ▼
┌────────────────────────┐              ┌──────────────────────────────┐
│ Eroded by water infiltration│          │ Eroded by water exfiltration │
│    through the defect   │              │ through the defect (water jet)│
└────────────────────────┘              └──────────────────────────────┘
      │    ┌──────────────────────┐          │   ┌──────────────────────┐
      ├───▶│ Experimental study   │          ├──▶│ Numerical simulation │
      │    │ - Laboratory modelling│         │   │ - CFD                │
      │    └──────────────────────┘          │   └──────────────────────┘
      │    ┌──────────────────────┐          │   ┌──────────────────────┐
      ├───▶│ Numerical simulation │          └──▶│ Analytical Model     │
      │    │ - A coupled DEM      │              │ -  Force equilibrium │
      │    └──────────────────────┘              └──────────────────────┘
      │    ┌──────────────────────┐
      └───▶│ Analytical model     │
           │ - Free-fall arch theory│
           └──────────────────────┘
```
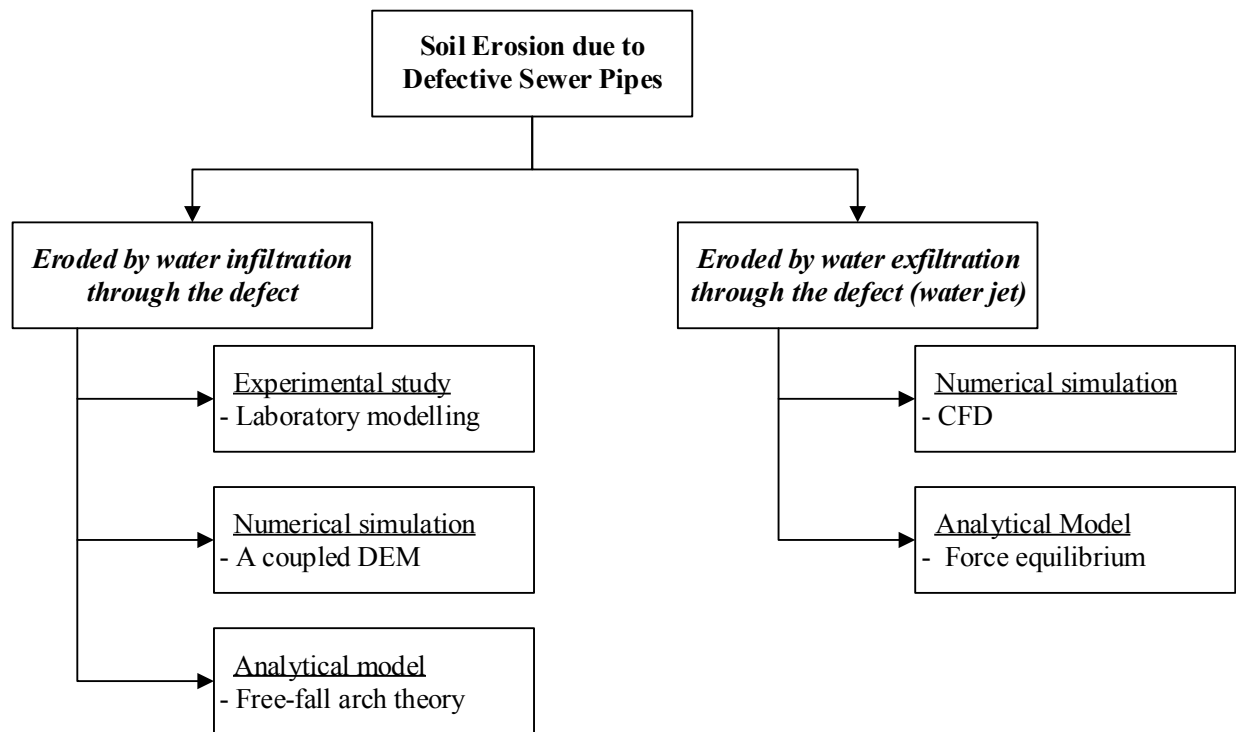
Figure 1.2 Flow chart of research route

Following the research route in Figure 1.2, the purpose of this study is focused on the following aspects:

1- To conduct comprehensive review on soil erosion due to the defective sewer pipes;

2- To conduct model experiments to investigate the mechanism of soil erosion by water infiltration through pipe defect;

3- To develop a coupling discrete element model to account for the interaction between fluid and solid phases, and calibrate this numerical model;

4

4- Propose an analytical model to predict the soil erosion due to the water infiltration into defective sewer pipe;

5- To conduct the numerical simulation of soil erosion by the exfiltration through pipe defect (upward water jet) using CFD, and propose an analytical model to evaluate the erosion.

1.3   Research Scope

This thesis will improve the understanding of soil erosion due to the defective sewer pipes. From recent studies (WRc, 2001), sandy soil has shown to be at a higher risk of soil loss than cohesive soils, and soil loss cannot be neglected if defect size is larger than 2 mm. Guo (2013b) stated that soil would not be eroded with only water infiltration if the defect size is small. In this study, the modeling experiment was firstly designed and conducted using sandy soil to investigate the effect of defect size on the soil loss, and the effect of various factors on the erosion, e.g., water head, defect position, were examined. From the experimental studies, the sand and water flow rate show a steady relationship in the erosion process, which is dependent on the sand particle size and the pipe defect size. Therefore, the sand flow rate in the erosion can be determined if the water flow rate is known.

Although the modeling experimental studies can effectively investigate the mechanism of soil erosion due to the defective sewer pipes, a coupled DEM has been developed to study the erosion process on a micro scale, and this numerical model can be verified and calibrated using the experimental results. This coupled numerical model is developed using Darcy's model, which is valid for the Reynolds number is less than 10 (Bear, 1972), and the soil permeability should be carefully determined. The sand erosion by the water infiltration through pipe defect can be

simplified as the granular flow through an opening assisted by water flow. An analytical model based on free-fall arch theory was developed to predict the dry sand flow through an opening, and the effect of water flow was taken into account by introducing the Stokes' law. These two analytical models can effectively predict the sand/water flow rates in the erosion process, which were verified by the experimental results. These analytical models were developed based on the two-dimensional conditions with the assumption of uniform-distributed particle size.

Besides soil erosion by water infiltration through a pipe defect, soil adjacent to the pipe defect can be eroded by the water exfiltration through the defect. A numerical method based on the CFD and the granular kinetic theory was used to investigate the erosion process and effect of various factors. This numerical method is efficient in comparison with the discrete element method, whereas the discontinuous behavior of the granular material cannot be simulated. An analytical model based on the force equilibrium was developed to predict the critical water velocity resulting in the sand-bed erosion. In this analytical model, the water flow was assumed as a uniform distribution over the mobilized zone in one-dimensional condition. The particle size in sand bed was assumed to be uniform sized, whereas the shape and angularity of particle were taken into account using the sphericity coefficient.

From this thesis study, sand particle size and defect size are key factors on soil erosion due to defective sewer pipes. In the soil erosion by water infiltration, particle size can significantly affect water flow due to changes of soil permeability, whereas sand and water flow rate show a steady relationship in the erosion process. This can be explained by the free-fall arch theory and Stokes' law. After sand particle velocity reaches a small value as it moves at a boundary close to the defect, the particle velocity will be significantly increased due to gravity and drag forces caused by water flow. Based on the theoretical derivation, it has been found that the size of this boundary

is dependent upon the particle size and defect size, which is independent of the stress state above this boundary. If the particle size is very big or the defect size is quite small, sand flow will cease without water flow due to jamming. Sand and water will discharge the defect as a mixture if the particle size is very small or the defect size is large. In the study of sand-bed erosion by an upward water flow, the particle size can affect the seepage force applied on the mobilized sand bed, while the defect size controls the spread of water jet. Therefore, the particle size and defect size are also essential in the analysis of sand-bed erosion by an upward water jet.

1.4 Thesis Outline

This thesis is written in paper format and composed of six contributions on soil erosion due to the defective sewer pipes. Each contribution is presented in a separate chapter, and following is a brief introduction.

Chapter Two starts with a comprehensive review of soil erosion due to defective sewer pipes. Studies on the granular or multiphase granular flow through an opening are reviewed, and the coupling discrete element models are reviewed as well. Representative sinkhole accidents are analyzed to generalize a simplified model for the following modeling studies. This chapter provides a foundation for the understanding of soil erosion by water infiltration/exfiltration through the pipe defect.

Chapter Three and Chapter Four are devoted to experimental study of soil erosion by water infiltration through an opening on defective pipe. In Chapter Three, the opening is a two-dimensional slot, while a three-dimensional orifice is simulated by the physical modeling in Chapter Four. The soil particle size, defect size, defect position and water level are controlled in the tests. The sand flow rate and water flow rate in the erosion process are measured, and particle

image velocimetry (PIV) technique is introduced for visualization analysis. A simple analytical model is proposed based on the experimental results to predict sand and water flow rate in the erosion process.

Chapter Five presents a coupling discrete element model to simulate sand erosion by water infiltration. The discrete element model is used to simulate large deformation behavior of sand particles, and Darcy fluid model is coupled with this approach to simulate the fluid flow through porous sand media. The coupled model is verified by comparing with the experimental results, and the erosion process is analyzed based on the numerical simulations.

Chapter Six develops an analytical model of the free-fall arch in the granular flow through a two-dimensional opening, which is developed based on the force equilibrium of granular particles. The granular flow rate can be estimated using this free-fall arch model, which provides an analytical approach to predict the free-fall arch size, position above the opening. This analytical model is verified by the numerical simulation and experimental results.

Chapter Seven provides an analytical method to estimate the sand and water flow rate based on the proposed free-fall arch model and Stokes' law, which is verified by the experimental results. Numerical simulation is conducted using the proposed coupling discrete element model, and the erosion process is analyzed in comparison with the experimental results.

Chapter Eight presents the numerical simulation of sand erosion by an upward water jet, which is based on CFD and kinetic theory of granular material. The numerical simulation is verified comparing with experimental results, and the effect of particle size, orifice size and sand bed height on the erosion is analyzed. An analytical model is proposed based on the force equilibrium and Ergun's equation.

Chapter Nine provides some general conclusions and recommendations for the future research.

Chapter 2 Literature Review

2.1   Study on Soil Erosion due to Defective Pipes

To the author's knowledge, limited studies are found on soil erosion due to defective pipes, which is also recognized by other researchers (Cui et al., 2012; Alsaydalani and Clayton, 2014). Studies were conducted on soil erosion by water infiltration through pipe defect (Mukunoki et al., 2009, 2012; Guo et al., 2013a; Sato and Kuwano, 2013, 2015; Indiketiya et al., 2017), while other studies were carried out to explore the mechanism of soil erosion by water exfiltration through pipe defect (Alsaydalani and Clayton, 2014; Cui et al., 2012, 2013, 2014; He et al., 2017). Soil erosion by water infiltration through pipe defect can directly lead to soil loss, while soil erosion by water exfiltration can either occur on water supply pipe or sewer pipe. There are differences in the mechanisms between these two studies which will be reviewed separately.

2.1.1   Soil erosion by water infiltration

Mukunoki et al. (2009) investigated the mechanism of road subsidence through laboratory model experiments. They found most of the accidents occurred during the rainy season based on statistical data in Japan, while ground subsidence was assumed to be formed by the water inflow and soil drainage through defective sewer pipe. A modeled defective pipe was buried in sandy soil under various water conditions, and X-ray Computed Tomography (CT) was used to capture cavity formation inside the model. Since there is a relationship between CT measurements and density, soil cavity can be detected. Based on experimental findings, they stated that neither the monotonic water inflow nor the soil drainage would not lead to the soil cavity formation, and only flow path or loose area was found in the model. The cycle of water inflow and soil drainage can cause fatal failure. The interlocking behavior of granular material around the defect was observed in the tests.

It was stated that the loss of capillary force could be another factor resulting in the soil cavity formation. Mukunoki et al. (2012) used the same experimental setup as Mukunoki et al. (2009) to investigate the effects of various controlling factors on cavity formation. From visualization analysis, soil cavity will not form if the relative density is larger than 0.8 since sand particles will be easily trapped. Based on their quantitative analysis, the ground surface can collapse if the ratio (D/d_{max}) of the crack width (D) on the defective pipe to the maximum grain size (d_{max}) is greater than 5.9.

Guo et al. (2013a) studied soil erosion caused by water inflow through pipe defects by model tests. The model tanks with bottom and lateral orifices are shown in Figure 2.1, which were used to simulate the erosion with various defective positions. Particle size, defect size, water level, and sand height were controlled in the tests. Sand flow rate, water flow rate, and the shape of eroded void were directly obtained from the experiments. From the visualization analysis, the erosion process can be divided into three stages. The first stage is the beginning of soil erosion until the occurrence of surface collapse. After that, the collapse is expanded until the water surface drops below soil surface. At the final stage, water seepages through the sand layer without significant erosion. From parameters analysis, the authors stated that water height and sand height mostly influence the geometric shape of erosion cavity, while the sand flow rate in erosion is affected by the particle size and defect size. Base on the free-fall model by Hilton and Cleary (2011), an analytical model was proposed to predict the water and sand flow rate. Guo and Zhu (2017) developed an analytical model to estimate the soil and water flow rate through the pipe defect, which was derived based on the Beverloo's equation (1961) considering the water pressure difference in the erosion process. This proposed analytical model was verified by comparing with experimental results (Guo et al., 2013a).

11

(a) Lateral orifice   (b) Bottom orifice
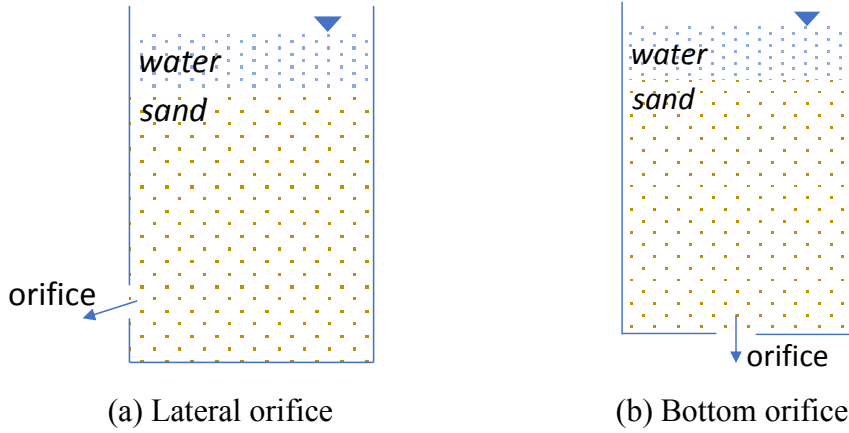
Figure 2.1 Schematic of experimental setups (Guo et al., 2013a)

Guo et al. (2013b) proposed an approximate solution using the equivalent circle assumption, which simplified the pipe defect as a small fully drained pipe with the perimeter of the pipe equal to the defect size. Therefore, the water flow rate when the opening is at the top of the pipe can be calculated from:

$$q_w^T = \frac{2\pi k}{\ln\left[\dfrac{h_s-r}{r'}+\sqrt{\dfrac{\left(h_s-r\right)^2}{r'^2}-1}\right]}\left[\left(h_s-r\right)\frac{r'^2-\left(h_s-r-\sqrt{\left(h_s-r\right)^2-r'^2}\right)^2}{r'^2+\left(h_s-r-\sqrt{\left(h_s-r\right)^2-r'^2}\right)^2}+\left(h_w-h_s\right)\right] \qquad (2.1)$$

where k is the permeability of sand; r is the radius of the pipe; and r' is the radius of the equivalent circle, which and can be determined using $r' = D/(2\pi)$, where D is the defect size.

Recently some modeling tests were conducted to examine soil erosion due to water flow through pipe defect. A sinkhole was assumed to form due to soil discharge into cracks accompanying internal erosion with seepage as shown in Figure 2.2, Sato and Kuwano (2015). From the modeling tests, it indicates that soil adjacent to the pipe defect becomes loose, and the corresponding permeability is significantly increased, while the soil cavity would be formed due to seepage localization (Sato and Kuwano, 2013, 2015). Physical modeling using a defective pipe

with a rainfall simulator shows that water level is a dominant factor in sinkhole formation over ground compaction or relative density (Kim et al., 2016). A laboratory physical modeling was carried out by Indiketiya et al. (2017) to investigate soil erosion due to defective sewer pipe, and particle image velocimetry (PIV) was used to measure soil deformation during erosion. Preliminary visualization results show that particles less than 0.3 mm are vulnerable to erosion through an opening of 5 mm in diameter.
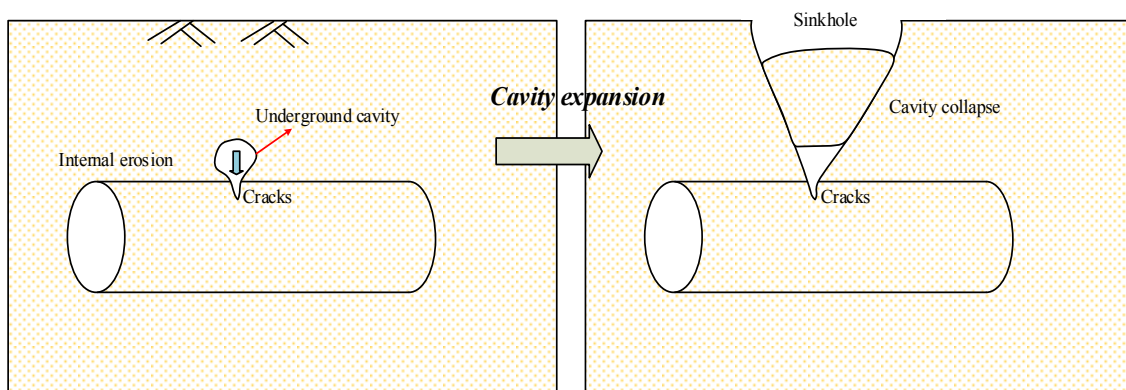
Figure 2.2 Schematic figure of internal erosion and sinkhole formation due to the defective pipes (Sato and Kuwano, 2015)

2.1.2   Soil erosion by water exfiltration

van Zyl et al. (2013) conducted a series of laboratory experiments to study the soil fluidization by leaking pipes. The progressive evolution of fluidization zone and head loss was monitored by controlling the inlet water flow rate as shown in Figure 2.3. From the visualization analysis, it was found that the fluidized and mobile zones were almost independent of the size of orifice. By monitoring the water head in the granular bed, the water head is mostly consumed within the fluidized and mobile zones.
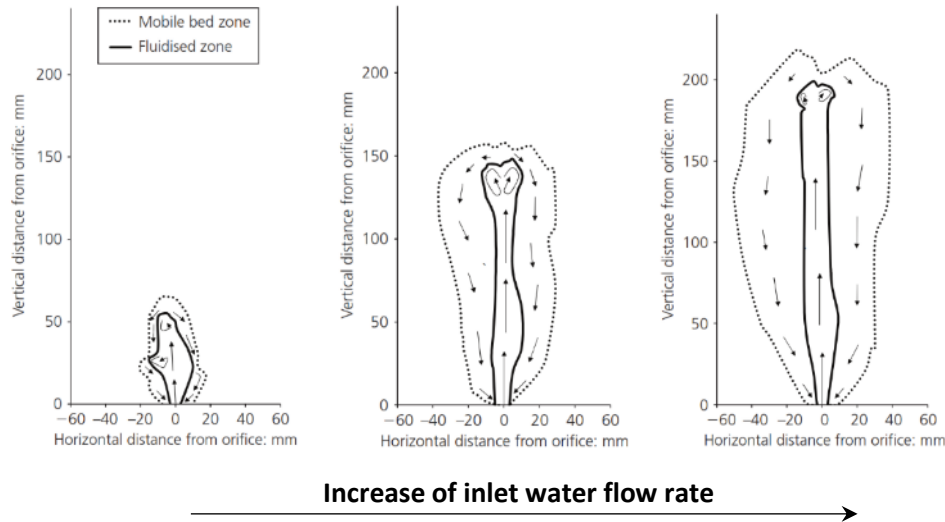
Figure 2.3 Geometry of the fluidized zone as the increase of inlet water flow rate (van Zyl et al., 2013)

Alsaydalani and Clayton (2014) investigated the mechanism of granular fluidization around leaking pipes by conducting small-scale laboratory experiments using similar setup as van Zyl et al. (2013). Failure was described as fluidization whereby granular material was transformed into a fluid-like state. The relationship between flow rate and pressure upstream of the orifice was analyzed. As the increase of inlet water flow rate, Darcy or non-Darcy flow around the orifice can be produced at the initial stage, while the orifice will be clogged due to the movement of granular particles. As the pressure inside the pipe increases to a certain magnitude, the buoyant weight of the granular bed would be equilibrated by the upward seepage force. After that, the grains can be loosened and the fluidization zone would be enlarged to the surface. The author also noted that the in-situ stress level and strength was necessary to be considered for the practical application of the equilibrium analysis method. Alsaydalani and Clayton (2014) also proposed an analytical model to predict the onset of sand-bed fluidization by an upward water jet as shown in Figure 2.4. The model was developed based on the force equilibrium. The force on the mobilized wedge can be either calculated as the boundary pressure or as the seepage force inside the wedge. Although the

model shows reasonable results in comparison with experiment measurements, the effect between the mobilized and static zone was not taken into account, and the upward motion of water jet was neglected.

(a) Boundary pressure method   (b) Gradient method
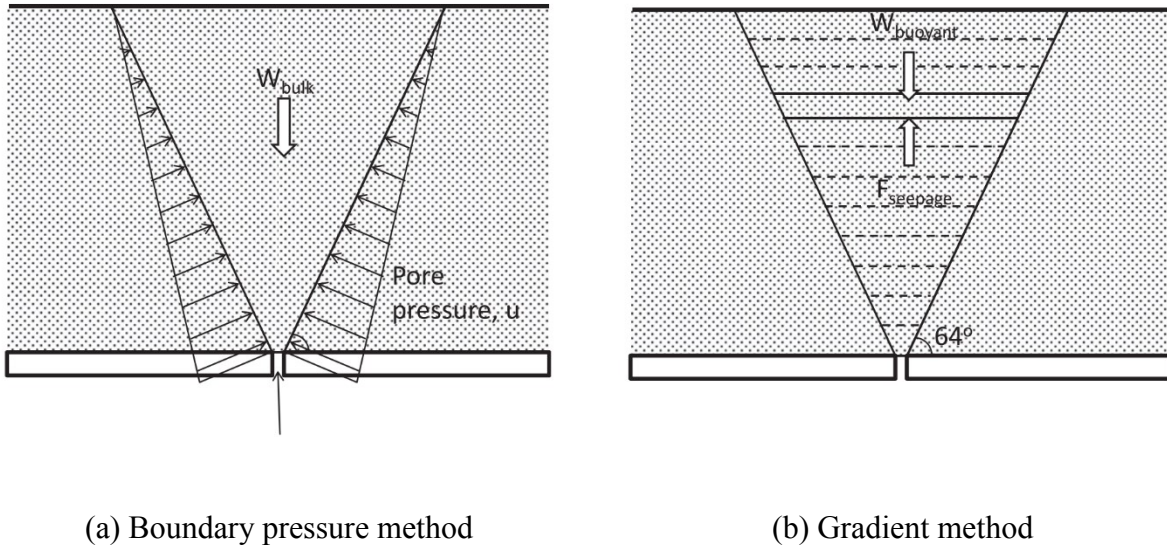
Figure 2.4 Analytical model of predicting onset of fluidization over an upward facing orifice (Alsaydalani and Clayton, 2014)

Cui et al. (2012) developed a two-dimensional numerical model based on discrete element method (DEM) and lattice Boltzmann method (LBM) to simulate the leaking process of pipe and corresponding effects on granular bed behavior. The granular material was described using DEM while fluid phase was simulated using LBM, and the interaction was incorporated by considering the drag force on solid particles and buoyant force. From the observation as shown in Figure 2.5, the cavity is firstly formed by the washing effect of water jet, and then there would be a stable stage, whereby the cavity is not evidently enlarged as the increase of flow velocity. The last step is 'blow-out' failure of the entire granular bed. Cui et al. (2013, 2014) studied the effects of parameters on the generation and evolution of cavity by the upward water flow based on the same numerical scheme as Cui et al. (2012). It was found that the pressure near the orifice would

15

decrease as the cavity growth, and particle bonding can increase the granular material resistance against the cavity expansion. The depth of soil bed can only slow the developing rate of the cavity without influencing the final shape of the cavity.
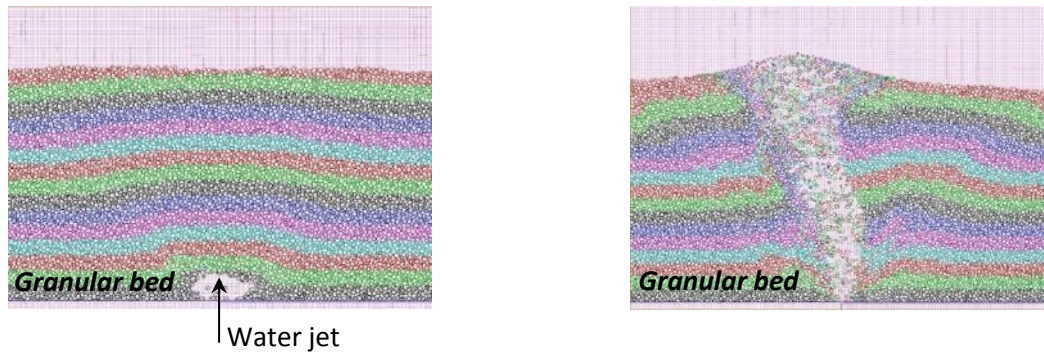
(a) Cavity formation   (b) 'Blow-out' failure

Figure 2.5 Stages of cavity formation and evolution (Cui et al., 2012)

Soil erosion by an upward water jet through a pipe defect was studied by He et al. (2017) using an experimental model. Different erosion stages were recognized by visualization analysis as shown in Figure 2.6, which is similar to the numerical simulations by Cui et al. (2012, 2014). A cavity is formed and expanded as the increase of inlet water flow rate, and the sand bed becomes finally fluidized at the flow rate that is defined as the critical flow rate. A simple analytical model was proposed based on the force equilibrium and Darcy's law to predict the critical flow rate leading to the sand bed fluidization.
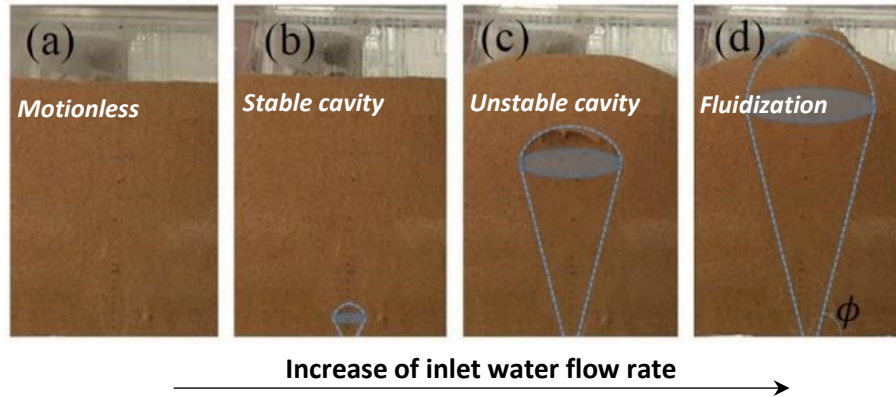
Figure 2.6 Different sand bed erosion stages by an upward water jet (He et al., 2017)

Fluidization of granular material due to the fluid flow has been studied by researchers in chemical engineering to investigate the mechanism of the reactor for improving chemical reactions (Benyahia et al., 2000; Cooper and Coronella, 2005; Taghipour et al., 2005; Chen et al., 2011). As the force generation by fluid flow inside the immersed granular bed, granular particles will be reorganized, and the internal structure of the multiphase medium is modified. Different regimes of fluidization as the increase of inlet flow rate was identified (Rigord et al., 2005; Zoueshtiagh and Merlen, 2007; Nermoen et al., 2010; Philippe and Badiane, 2013). At the low inlet flow rate, the particles remain at rest and fluid seepages through the granular media. As the increase of flow rate, the granular material is deformed while the seepage of fluid still follows Darcy's law. Finally, the granular bed is fluidized with voids. It has been found that the formation of an arch in the particle mobilization will cause the localized fluidization (Philippe and Badiane, 2013).

Numerical simulation makes it possible to investigate the mechanisms of sand-bed erosion. In a Lagrangian discrete framework, each particle can in principle be tracked by considering force equilibrium, but the computational demands for a realistic sand-bed erosion simulation is substantial. Consequently, previous simulations were conducted using much larger particles in studying granular behavior in the erosion process with reasonable accuracy (Tsuji et al., 1993; Cui

et al., 2012, 2014). Because of the computational limitations, the Lagrangian discrete approach is usually limited to a small number of particles (Taghipour et al., 2005), whereas the Eulerian continuum method based on the multiphase model is a more feasible alternative for simulating granular material behavior.

The Eulerian method was developed based on the granular kinetic theory (Gidaspow, 1994), assuming the fluidized bed consisting of two interpenetrating fluids. In this approach, the momentum balance equations for both phases are solved simultaneously, with the constraint that the volume fractions of the phases must sum to unity. The interphase momentum transfer between the fluid and solid phase can be taken into account by calculating the drag forces. The solid-phase momentum equation contains an additional term to account for momentum exchange attributable to particle-particle collisions. This Eulerian approach with granular kinetic theory has been widely employed in chemical engineering to study the gas-solid fluidization (Taghipour et al., 2005; Cooper and Coronella, 2005; Chen et al, 2011) and liquid-solid fluidization (Cheng and Zhu, 2005; Lettieri et al, 2006; Cornelissen et al., 2007). Sand/water two-phase flow was simulated to investigate the characteristics of slurry jet in water based on the numerical method using ANSYS CFX (Azimi et al., 2012).

From the studies on the granular bed fluidization by the injected fluid, the motion of granular particles is affected by the inlet fluid velocity. Therefore, the minimum fluid velocity leading to the fluidization is defined as a critical value (Chen et al., 2011; He et al., 2017). On the other hand, the difference in fluid pressure between the inlet and granular surface is studied (Taghipour et al., 2005; Chen et al., 2011) which also indicates a threshold value for granular bed fluidization. It has been proven that the pressure difference is dependent on the inlet fluid velocity, and various relationships or constitutive models were proposed such as Darcy's law, Ergun's model, Wen and

Yu's model. The constitutive model is affected by the granular bed property, which is the granular particle size, shape and porosity. In Darcy's law, these factors are simply combined as the permeability. Therefore, the granular bed fluidization can be simplified as the injected fluid causes the change of pressure difference which results in the granular particle motion, while the pressure difference is affected by the granular bed property.

2.2 Study on the Discrete Element Method and Solid-Fluid Coupling Model

Discrete element method (DEM) was firstly introduced by Cundall (1971) for simulating the discrete behavior of rock and then extended for soil (Cundall and Strack, 1979). Unlike the classical continuous numerical simulation approaches, such as, the finite element method (FEM), the finite difference method (FDM), DEM is an explicit method which is capable of tracking each particle and their interaction. Therefore, it is not necessary to take the sophisticated constitutive model into account especially for the high nonlinear properties of geomaterial. As an effective simulation technique, DEM can be used to investigate the detailed mechanism of soil deformation by simulating virtual physical experiments (Ng, 2004; Liu, 2006; Widuliński et al., 2009). Besides, the implementation of DEM does not rely on meshes, and DEM is capable of simulating large deformation problems.

The theoretical basis of DEM is Newton's 2nd law for each particle and the force-displacement law at the contact. The general DEM calculation scheme is as shown in Figure 2.7 (O'Sullivan, 2011). After the generation or definition of a specific simulation model, the particle parameters (e.g., density, dimensions) and the contact parameters, including stiffness and friction coefficient, are required to specify. At the beginning of each calculation cycle, the contacts between particles will be identified first. Based on the distance between particles, the inter-particle

force can be determined using the contact law. After that, the resultant force and moment or torque acting on each particle can be figured out. Except when particle rotation is inhibited, at each time increment two sets of equations for the dynamic equilibrium of the particles are solved to determine the translational movement and rotation motion. Both translational and rotational accelerations for each particle within current time-step can be calculated using Newton's law. From the incremental displacements and rotations, the particle positions and orientations can be updated. In the next time step, the contact forces will be recalculated using this updated geometry, and the calculation loop will repeat until reaching required conditions.
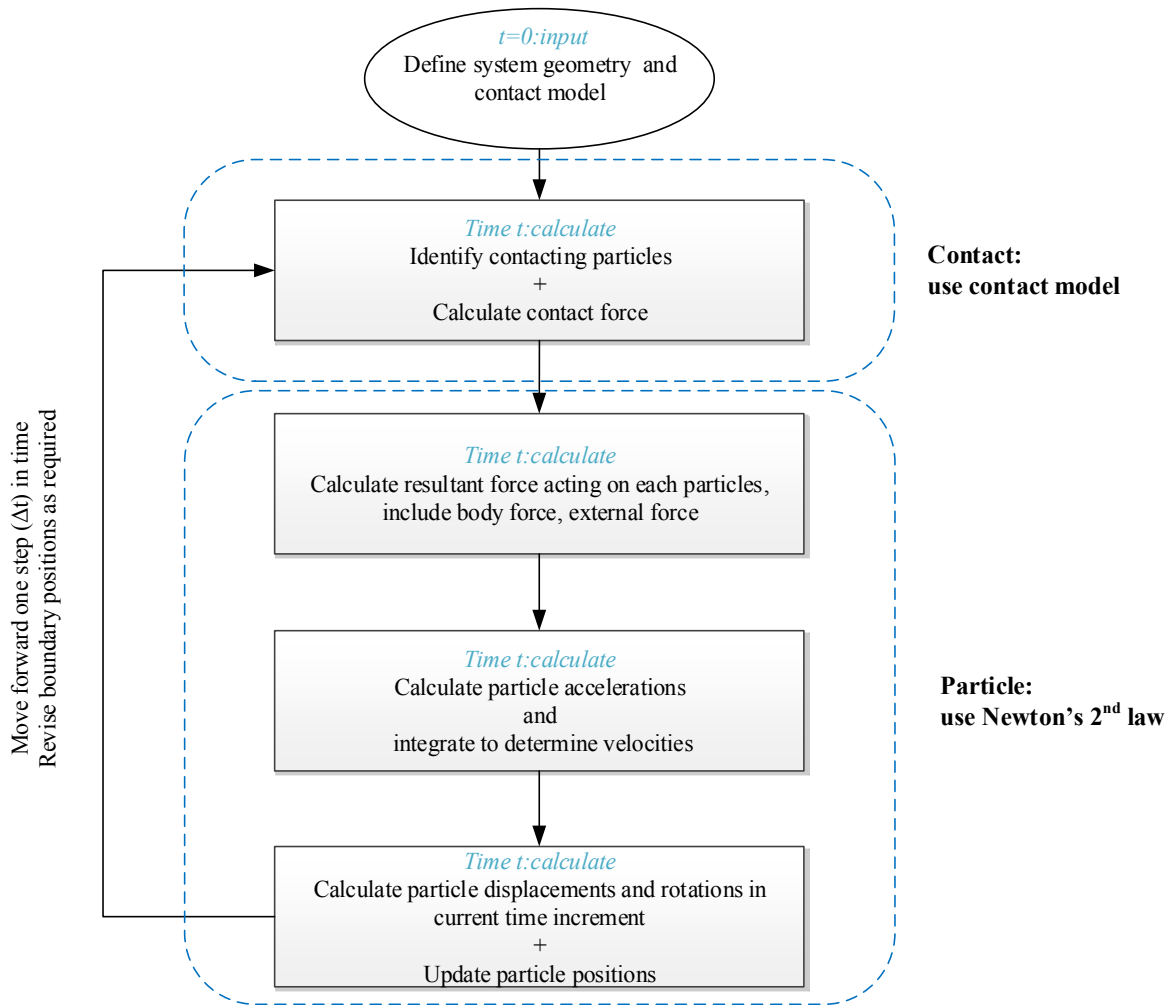
Figure 2.7 Schematic of calculation sequences in DEM simulation (O'Sullivan, 2011)

2.2.1 DEM model coupling with fluid flow

DEM originally was developed for simulating dry material. However, the effect of water in geomaterial cannot be neglected. Seepage theory based on Darcy's law provides a theoretical basis for pore water pressure prediction at either steady or transient states. Based on various fluid models, different coupling models have been developed and employed to simulate granular material considering the fluid effect.

Hakuno and Tarumi (1988) developed a two-dimensional fluid network model and coupled with the DEM model, which was applied to the analysis of sand liquefaction induced by seismic motion. Thallak et al. (1990, 1991) proposed a coupling DEM model to study the lateral growth and interaction of fluid-driven fractures. As shown in Figure 2.8, the flow channel between voids is assumed to follow the Hagen-Poiseuille pipe flow, which is:

$$q_{pipe} = -\frac{\pi D_{pipe}^{4}}{128\mu}\frac{\Delta p}{L_{pipe}} \tag{2.2}$$

where, q_{pipe} is the flow rate through the assumed pipe; D_{pipe} is the diameter of pipe and L_{pipe} is the length of pipe; Δp is the pressure difference between the two adjacent voids; μ is the fluid viscosity. Based on this flow network assumption, numerical simulations were conducted to account for the effects of particles crushing or ellipsoidal particle (Li and Holt, 2001, 2002; Bonilla, 2004). This flow network model was also incorporated in *PFC* by Itasca (2008) and was used to study the soil behavior (Shimizu, 2011; Liu et al., 2015; Chang and Huang, 2016). Catalano et al. (2011) and Chareyre et al. (2012) proposed a coupled three-dimensional DEM model with a fluid model based on finite volume method in a pore network, while the flow through the network was also assumed to be consistent with Hagen-Poiseuille equation.
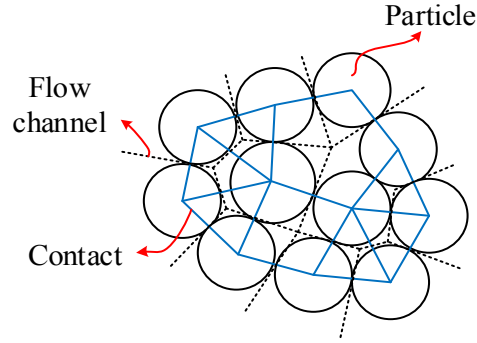
Figure 2.8 Network of flow channels between particles (Tallak et al., 1991)

Chan (1993) developed a coupled DEM model considering fluid flow using Darcy's law in an explicit finite difference scheme and the permeability at each numerical node was varied as the particle movement. Similar coupling method was used to simulate the sand production process in petroleum engineering (Preece et al., 1999; Jensen and Preeece, 2000; Cui et al., 2016). The pore-water pressure in soils was simulated using the coupling discrete element model to consider the soil deformation and water pressure dissipation (Goodarzi et al., 2015; Cui et al., 2017). In the coupling model based on Darcy's law, the fluid was assumed as a continuum media covering the calculation domain, and Darcy's law controlled the fluid flow with a varying permeability.

Navier-Stokes (N-S) equation provides a general description of fluid flow, which can be solved by various numerical methods. The difficulty in solving the N-S equation is the implicit pressure term, and the SIMPLE (semi-implicit method for pressure linked equation) algorithm using the staggered mesh is proved to be an effective numerical method as the development of computational fluid dynamics (CFD) (Anderson, 1995). The averaged N-S equation considering the solid particles was proposed by Anderson and Jackson (1968), which is:

$$\frac{\partial\left(\varepsilon\rho_f\right)}{\partial t}+\nabla\cdot\left(\varepsilon\rho_f\mathbf{u}\right)=0 \tag{2.3}$$

$$\varepsilon \rho_f \left(\frac{\partial \mathbf{u}}{\partial t} + \mathbf{u} \cdot \nabla \mathbf{u} \right) = -\nabla p + \mu \nabla \cdot \mathbf{u} - \mathbf{f}_f + \varepsilon \rho_f \mathbf{g} \qquad (2.4)$$

where, $\mathbf{u}$ is the fluid velocity; p is the fluid pressure; ε is the porosity; ρ_f is the fluid density; $\mathbf{f}_f$ is the coupling force on fluid. $\mu \cdot \nabla \mathbf{u}$ is the viscous force on fluid, and the fluid is assumed to be Newtonian fluid. Tsuji et al. (1993) proposed a coupled CFD-DEM model to simulate the gas flow within the granular material, and the behavior of gas flow was described by solving the averaged N-S equation (Anderson and Jackson, 1968) using finite difference method. Sand liquefaction was studied using the DEM-CFD model (Zeghal and El Shamy, 2004; El Shamy and Zeghal, 2005; 2007). Chan and Tipthavonnukul (2008) developed a numerical procedure with a coupling interaction of DEM solids and fluid flow, which used the general N-S equation and introduce a fluid velocity reduction factor to account for the effect of granular particles on fluid flow. Similar numerical methods were used to study the soil discrete behavior with the fluid flow (Suzuki et al., 2007; Jeyisanker and Gunaratne, 2009; Zou et al., 2013; Shan and Zhao, 2014).

Unlike the CFD approach, the smoothed particle hydrodynamics (SPH) was developed as a mesh-free method to solve N-S equation (Gingold and Monaghan, 1977). By introducing the equation of state, the fluid pressure can be determined explicitly, and the N-S equation can be solved (Monaghan, 1994; Morris e al., 1997). As a Lagrangian method, SPH can be simply applied to the complicated geometries without the requirement of high-quality mesh. A coupled DEM-SPH model was developed to simulate the solid-fluid interaction (Potapov et al., 2001; Li et al., 2007; Huang et al., 2012; Robinson et al., 2014).

As an alternative technique, lattice Boltzmann method (LBM) originated from Boltzmann equation was utilized to study the particulate suspensions, multiphase flow, energy transport, and turbulent flow. It has been proven that LBM can recover the N-S equation for nearly

incompressible fluids (Frisch et al., 1986). Since LBM can be implemented explicitly and avoid solving N-S equations, the coupled DEM-LBM model was developed to simulate solid-fluid coupling process (Cook and Noble, 2004; Feng et al., 2007; Cui et al., 2012, 2013, 2014; Han and Cundall, 2013; Lominé et al., 2013; Wang et al., 2016).

Various DEM models have been proposed to simulate the coupling behavior between the fluid and solid. The flow channel model is simple to be implemented without the numerical discretization and mesh generation, but the parameters are difficult to be determined. Only permeability is necessary for Darcy's model, and the governing equation is easy to be solved. The other coupling methods (DEM-CFD, DEM-SPH, and DEM-LBM) are based on the general governing equation of fluid flow, but the computational cost is expensive. In particular, the lattice size should be small enough in the DEM-LBM since each solid particle is treated as the 'wall' boundary.

2.2.2   Interaction between solid and fluid phase in the coupling model

In the coupled DEM model, solid particle motion is affected by fluid flow, and different types of forces act on the particles. These forces can be classified as hydrostatic or hydrodynamic forces (Zhu et al., 2007). The hydrostatic force is known as the buoyancy force, while the hydrodynamic forces are caused by the dynamic behavior of fluid flow which can include drag force, virtual mass force and lift force. Specifically, drag forces are due to the relative motion between the fluid and solid phase. Virtual mass force is the force to reach the acceleration of fluid motion, which is equivalent to increase of the mass of each particle. Viscous forces are related to the boundary layer and viscosity of fluid, while lift forces are due to the particle rotation. Morsi and Alexander (1972) stated that the lift forces are much smaller than the drag forces. Zhu et al. (2007) stated that the pressure gradient force and the drag force would be the dominant interaction forces and have a

measurable influence on the particle motion and flow pattern. Therefore, in this study, the other interactions will not be taken into account.

Hydrostatic forces

The hydrostatic force on each particle can be calculated (Tsuji et al., 1993; Kafui et al., 2002):

$$\mathbf{f}^{\text{hyrostatic}} = V_p \left(\rho_f \mathbf{g} \right) \tag{2.5}$$

where, V_p is particle volume, ρ_f is the fluid density; $\mathbf{g}$ is the gravitational acceleration.

Drag force

The drag force is dependent on the relative velocity between the fluid and solid phase, the relative velocity between the particle and fluid flow is:

$$\mathbf{u}_r = \mathbf{u}_f - \mathbf{u}_p \tag{2.6}$$

where, $\mathbf{u}_r$ is the relative velocity, $\mathbf{u}_f$ is the fluid velocity, $\mathbf{u}_p$ is the solid particle velocity.

The simplest drag force law is the Stokes' drag force (Batchelor, 1967):

$$\mathbf{f}_d = 3\pi\mu d_p \mathbf{u}_r \tag{2.7}$$

where d_p is the particle diameter, μ is the dynamic viscosity of fluid.

Chan and Tipthavonnukul (2008) used the following equation for drag force calculation:

$$\mathbf{f}_d = C_d \pi \rho_f d_p^2 |\mathbf{u}_r| \frac{\mathbf{u}_r}{8} \tag{2.8}$$

where C_d is the drag coefficient, ρ_f is fluid density. The drag coefficient can be determined for the sphere-shaped particle using the equation given by White (2005):

$$C_d = \frac{24}{R_e} + \frac{6}{1+\sqrt{R_e}} + 0.4, \ R_e < 2\times10^5 \tag{2.9}$$

where R_e is the Reynolds number determined by $\rho_f |\mathbf{u}_f| d_p/\mu$, this formulation will not be valid if the Reynolds number is greater than 2×10^5.

The drag forces from Eqs. (2.7) and (2.8) are derived from a single particle model, which cannot directly be applied to the particle assembly. Zhu et al. (2007) explained the presence of other particles would reduce the space for the fluid and lead to the steep gradient of the fluid velocity and an increased shear stress on the particle surface. Therefore, other drag laws are developed using a corrective function of porosity.

Tsuji et al. (1993) used the following equation to determine the drag force:

$$\mathbf{f}_d = \beta \frac{\mathbf{u}_r}{\rho_f} \tag{2.10}$$

If the porosity is less than 0.8, β is determined from Ergun equation (Ergun, 1952):

$$\beta = 150\mu \frac{(1-\varepsilon)}{d_p^2 \varepsilon^2} + 1.75 \frac{(1-\varepsilon)\rho_f |\mathbf{u}_r|}{d_p \varepsilon} \tag{2.11}$$

where ε is the porosity. If the porosity is larger than 0.8, β can be determined from Wen and Yu's expression (Wen and Yu, 1966):

$$\beta = \frac{3}{4}C \frac{|\mathbf{u}_r|\rho_f(1-\varepsilon)}{d}\varepsilon^{-2.7} \tag{2.12}$$

where C is a coefficient that depends on the Reynolds number,

$$C = \begin{cases} 24\left(1 + 0.15 R_e^{0.687}\right) & R_e < 1000 \\ 0.43 & R_e > 1000 \end{cases} \tag{2.13}$$

By introducing a corrective function of porosity, the drag force can be calculated based on the modification of Eq. (2.7) (Kafui et al., 2002; Robison et al., 2014):

$$\mathbf{f}_d = C_d f\left(\varepsilon\right) \pi \rho_f d_p^2 \left|\mathbf{u}_r\right| \frac{\mathbf{u}_r}{8} \tag{2.14}$$

The corrective function $f\left(\varepsilon\right)$ can be determined by Di Felice's voidage function based on experimental data of fluid flow through packed spheres (Di Felice, 1994):

$$f\left(\varepsilon\right) = \varepsilon^{-\xi} \tag{2.15}$$

$$\xi = 3.7 - 0.65 \exp\left[-\frac{\left(1.5 - \lg R_e\right)^2}{2}\right] \tag{2.16}$$

2.3   Study on Granular Flow through an Opening

2.3.1   Estimation of granular flow rate through an opening

As a significant difference from the fluid flow, granular flow through an opening is independent of the granular height, which is firstly explained as the Janssen effect (Janssen, 1895). The early experimental results also support this statement if the height is greater than a few multiples of the opening size (Beverloo et al., 1961; Al-Din and Gunn, 1984; Nedderman, 1992). It was found that the discharge rate would be varied with the outlet size to a power around 2.5. Franklin and

Johanson (1955) found the power of 2.93. Beverloo et al. (1961) proposed the particle discharge mass rate for a flat-bottomed, cylindrical silo with a circular opening:

$$\dot{M} = C\rho\sqrt{g}\left(W_0 \text{-} kd_p\right)^{2.5} \tag{2.17}$$

where: $\dot{M}$ is the mass rate of granular flow, ρ is the density of granular material, W_0 is the orifice diameter, d_p is the particle diameter. Parameters k and C are empirical dimensionless constants of order 1. The coefficient k accounts for the presence of boundary that can reduce its effective diameter. Experimentally k has been found to be independent of the particle size and take a value between 1 and 3, depending on the particle and container properties (Nedderman and Laohakul, 1980). The constant C is found to be a range of 0.55-0.65 (Nedderman, 1992).

Based on the experimental results and dimensional analysis, various correlations were proposed to estimate the granular flow rate through an opening under different conditions, and the correlations are in the similar form of Beverloo's equation in Eq. (2.16) (Khanam and Nanda, 2005; Ahn et al., 2008). Nedderman (1992) proposed a correlation considering the wall effect, and a modified equation for noncircular exit slots was proposed as well. Franklin and Johanson (1955) firstly studied the flow rate of granular matter from an orifice with an inclination angle, and the results showed that there is a linear relationship between the flow rate and the cosine of inclination angle. Sheldon and Durian (2010) studied the flow rate of glass beads with different sizes through a circular orifice with different inclination angles, and the correlation was proposed based on the experimental results. Liu (2014) presented a theoretical calculation method for the flow rate from the inclined orifice with different angles by modifying Beverloo's equation.

Another issue between the simplified model and the practical fact is the shape of the granular particle. Granular material naturally is non-spherical, while normally we assumed it is perfectly

28

spherical in numerical simulation. Wu et al. (2008) studied the flow pattern of three kinds of particles with different shapes. Li et al. (2004) examined the flow of sphere-disc particles. Zuriguel et al. (2005) found the material properties of the grains had little effect on the arch formation, but the particle shape influenced it significantly. Tao et al. (2010) studied the flow behaviors of four kinds of granular material (i.e. sphere, ellipsoid, hexahedron and a binary mixture of sphere and hexahedron).

Although Beverloo's correlation is in good agreement with experimental observations, this equation should be applied only for particle diameters in the range of 0.4 mm $< d_p < W_0/6$. The effect of air cannot be neglected if the particle is smaller than the lower limit, while mechanical interlocking of particles is likely to occur at the exit above the upper limit (Nedderman, 1992; Mankoc et al., 2007, 2009).

Beverloo's correlation and other modified correlations can accurately predict the granular flow rate for the specific conditions, while the theoretical prediction is necessary to examine the mechanism of granular flow through an opening. Brown (1961) firstly assumed the energy of granular particles would reach the minimum at a boundary adjacent to the opening, and granular particles will fall freely below this boundary. This boundary is named as 'free-fall arch' by Brown and Richards (1965) as show in Figure 2.9, and the hour-glass theory was proposed with similar assumptions to account for the effect of granular material head and stress distribution (Davidson and Nedderman, 1973).
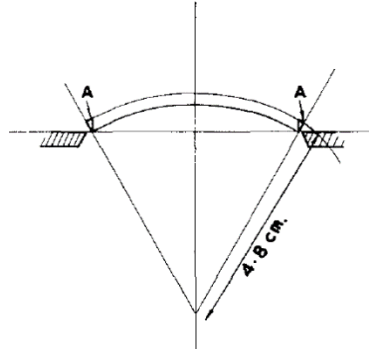
Figure 2.9 The free-fall arch (Brown and Richards, 1965)

Due to its simplicity and realistic mechanics, the free-fall arch theory has been widely accepted (Le Pennec et al., 1996; Janda et al., 2012; Rubio-Largo et al., 2015; Tian et al., 2015). Hilton and Cleary assumed that the particle velocity at the free-fall arch can be negligible, and the particle can fall out freely only under the gravitational acceleration as shown in Figure 2.10. Therefore, the granular flow through the opening can be theoretically derived, which is proved that the granular flow rate is theoretically in a similar form as Beverloo's equation. By assuming the granular material as a continuum, another analytical approach was proposed based on the continuity equation, equilibrium equation and related yield criteria (Savage, 1965; Drescher, 1991). Although the continuum method is proposed with the strict mathematic basis, the discrete characteristic of granular material cannot be taken into account.
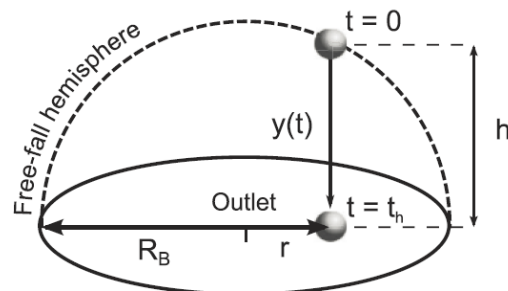
Figure 2.10 Assumptions of free-fall arch in the granular flow (Hilton and Cleary, 2011)

30

Various models have been proposed to investigate the multiphase granular flow. Ring et al. (1973) proposed an equation to estimate granular flow submerged in water based on the experimental results, and Donsì et al. (1997) provided a simple analytical model to account for the effect of air on the granular flow based on the laboratory tests. The essence to consider the fluid effect on granular flow is the interaction between the fluid and granular flow. The linear relationship between the pressure gradient and fluid velocity, which is the Carman-Kozeny equation, was introduced to the energy balance equation (Resnick et al., 1966). Similarly, Carman-Kozeny equation was used to modify the Beverloo's equation considering the effect of air on granular flow (Crewdson et al., 1977; Barletta et al., 2003). The linear relationship between the pressure gradient and velocity was also incorporated to modify Brown's minimum energy theory considering the fluid flow (Papazoglou and Pyle, 1969; Altenkirch and Eichhorn, 1981). The nonlinear relationship between pressure gradient and fluid velocity, which is Ergun's equation, was used to explore the effect of fluid on granular flow (de Jong and Hoelen, 1975; Lamptey and Thorpe, 1991). Hilton and Cleary (2011) used the Stokes law to improve the free-fall arch theory, and proposed an analytical solution to estimate the granular flow rate based on the free-fall arch theory.

The granular velocity distribution in the discharge was investigated using a kinetic model (Nedderman and Tüzün, 1979; Tüzün and Nedderman, 1979; Tüzün et al., 1982). By assuming the horizontal velocity of granular material is related to the vertical velocity, the continuity equation was simplified, and an analytical solution was proposed incorporating the boundary conditions. By linking the velocity field with stress field, a method of characteristics was proposed for the granular material discharging from a conical hopper (Moreea and Nedderman, 1996).

2.3.2 Jamming on the granular flow

Nedderman (1992) stated that the mechanical interlocking or jamming is likely to occur at the exit when the particle size is below a certain limit, which is an important property of granular flow (Drescher et al., 1995a, 1995b). Normally the goal is to eliminate the clogging effect and increase the output volume in chemical or food industries, while in geotechnical engineering this effect might be helpful for the stability or safety to prevent the soil loss around the defective pipe in this study.

Particle jamming can occur when a dense stream of solids competitively flows through an orifice. 'Jamming' is commonly used to describe the occurrence of this self-stabilizing dome or arch-like arrangement of particles immediately above a point of particle discharge (To et al., 2001; Zuriguel et al., 2003). Once a jam occurs, further particle flow is ceased until the jam is removed. To et al. (2001) developed a jamming probability model based on the experimental results, and the proposed jamming probability function is dependent on the ratio between the opening and granular particle size. Based on this framework, various experiments were carried out to study the influencing factors on the jamming probability (Zuriguel et al., 2003; Zuriguel et al., 2005; Pournin et al., 2007; Janda et al., 2008; Mankoc et al., 2009). Guariguata et al. (2012) studied the flow behavior of fluid-driven flow jamming. For practical purpose, experiments were carried out to study the dynamic mechanism of arch formation/breakup under the vibrated conditions (Hunt et al., 1999; Wassgren et al., 2002; Chen et al., 2006).

2.4 Case Studies of Sinkholes

Since most of the sinkholes occurred instantaneously without evident signs, very few case study papers can be found. To investigate the sinkhole formation and generalize an appropriate analysis

model, reports about the sinkhole accidents are collected from the news reports as listed in Table 2.1. The terminology, sinkhole, is originally used to describe the geological phenomenon due to the limestone erosion, while in this study sinkhole will be restricted to that by soil erosion in the urban area due to the defective pipes.

Table 2.1 Representative sinkhole accidents by defective sewer pipes

Time	Location	Water condition	Type of soil	Pipe condition and possible cause	Consequence	
					Sinkhole size	Loss
06/1993	Georgia, US[1*]	Heavy storm	Soil and construction rubble	A sewer tunnel with a diameter of 4 m failure, soil erosion	20 m in diameter, 10 m deep	2 killed
02/2007	Guatermala[2]	Heavy storm	Pumice and volcanic ash	Overloaded sewer or drainage pipe with a diameter of 3.75-4.50 m	20 m in diameter, 60 m in deep	3 killed
09/2009	Toronto, Canada[3]	Heavy rainfall	-	-	5 m wide, 14 m deep	
06/2010	Guatermala[4]	Heavy storm	Pumice and volcanic ash	Overloaded sewer or drainage pipe with a diameter of 3.75-4.50 m	18 m in diameter, 30 m deep	152 killed
09/2010	Texas, US[5]	Not reported but near a lake	Sandy soil	A pipe with a diameter of 1.2 m failure	2 m in diameter	-
01/2011	Austin, Texas, US[6]	-	-	Soil erosion into the storm sewer pipe	2.7 m deep	-
02/2011	Florida, US[7]	-	-	Corroded sewer line	1.5 m in diameter, 4 m deep	-
03/2011	Ohio, US[8]	Heavy rainfall	-	A defective 60-year-old sewer pipe, soil was washed away	-	-
03/2011	Connecticut, US[9]	-	-	broken sewer line	5 m deep	-
03/2011	New South Wales, Australia[10]	Heavy rainfall	-	Soil erosion into the sewer pipe	8 m wide, 6 m deep	-
04/2011	Saskatoon, Canada[11]	Freezing	-	Broken sewer line due to freezing	3 m deep	-
04/2011	New York, US[12]	Storm	-	199-year-old clay sewer pipe cracked, soil erosion	9 m wide, 6 m deep	$4.5 million

Table 2.1 Representative sinkhole accidents by defective sewer pipes (cont'd)

Time	Location	Water condition	Type of soil	Pipe condition and possible cause	Consequence	
					Sinkhole size	Loss
05/2011	Ohio, US[13]	-	-	Collapsed brick sewer line	4 m deep	-
05/2011	New Jersey, US[14]	-	-	Collapsed sewer line	10 m wide, 1.5 m deep	-
06/2011	New York, US[15]	Steady rain for a month	Sandy soil	Broken clay sewer pipe, soil loss	-	-
06/2011	Ohio, US[16]	-	-	Soil erosion into an 84-year-old brick tunnel with a diameter of 1 m	5 m deep	-
08/2011	Pennsylvania, US[17]	Extreme wet weather event, hurricane	Backfill granular material	A corrugated metal pipe with a diameter of 2.1 m deteriorated	2 m wide	$263,000
04/2012	Bangkok, Thailand[18]	-	Sand	Soil erosion into the broken drainage pipe	1 m wide, 1 m deep	-
09/2012	Ottawa, Canada[19]	Heavy rainfall	-	Soil loss into a 3.6 m wide storm sewer pipe	-	One car
09/2012	Shanghai, China[20]	-	Sandy soil	Sewer pipe beneath	3.5 m in diameter, 1.5 m deep	-
04/2013	Chicago, US[21]	Heavy storm	-	Defective sewer line, soil loss	3 m in diameter	-
05/2013	Ontario, Canada[22]	Increasing height of nearby river	Granular material	Soil erosion into the storm sewer pipe	Small sinkholes	-
05/2014	Edmonton, Canada[23]	Rainfall	-	Drainage issue	-	-
05/2014	Minnesota, US[24]	-	-	Broken sanitary sewer pipe	-	$2 million
01/2015	Scotland, UK[25]	-	Sand	Drainage issue	4 m deep	$ 30,000
04/2015	Mississippi, US[26]	-	-	Soil erosion into the culvert buried 9.5 m below ground	3 m in diameter	-

Table 2.1 Representative sinkhole accidents by defective sewer pipes (cont'd)

Time	Location	Water condition	Type of soil	Pipe condition and possible cause	Consequence	
					Sinkhole size	Loss
11/2015	Ohio, US[27]	Heavy rainfall	-	Soil erosion into the defective sewer pipes	1.5 m in diameter, 1 m deep	-
04/2016	California, US[28]	Heavy rainfall	-	Sewer pipe collapsed, soil erosion	5 m deep	-
04/2016	Hangzhou, China[29]	Heavy rainfall	Sand	Soil erosion into the defective storm pipe	2.5 m in diameter, 2 m deep	-
06/2016	Ottawa, Canada[30]	-	-	Soil erosion into defective pipes	28 m wide, 40 m long, 5 m deep	-
07/2016	Beijing, China[31]	Heavy rainfall	-	Soil erosion and fluidization due to the defective pipes	20 m long, 5 m wide, 1.5 m deep	-
08/2016	Cambridge, UK[32]	-	-	Erosion into the defective pipes	4 m deep	-
08/2016	Kentucky, US[33]	Heavy rainfall	-	Defective sewer pipes	0.6 m in diameter, 1.8 m deep	-
11/2016	Likas, Malaysia[34]	Earthquake	-	Cracked sewer pipe	1.5 m wide, 1.8 m deep	-
11/2016	Fukuoka, Japan[35]	-	Sand	Erosion into tunnel, defective sewer pipe	30 m long, 27 m wide, 15 m deep	-
11/2016	Shenzhen, China[36]	-	-	Erosion into defective sewer pipes 4 m below the ground	3 m in diameter, 2 m deep	-
01/2017	Michigan, US[37]	-	-	Soil erosion and collapsed pipe 15 m below the ground	Football field-sized	22 families moved

Note:

* sources of the information in this table are listed as an Appendix A.

'-' in this table indicates 'not reported'.

From these qualitative descriptions of the sinkhole accidents, the formation of sinkhole or ground collapse due to the defective sewer pipes can be generalized in a conceptual model as shown in Figure 2.11. As the deterioration of sewer pipes, cracks and defects are developed. If the groundwater level is above the defect position, soil adjacent to the defect will be washed into the defective pipe. On the other hand, the water in pipe can be exfiltrated if the sewer pipe is fully filled, which will cause the fluidization and erosion of surrounding soils. As the granular material, the soil arch can be formed as the soil loss through the pipe defect, which can prevent the subsequent erosion if the arch stable. The instability failure, such as the sinkhole or ground collapse, can occur as the soil erosion.
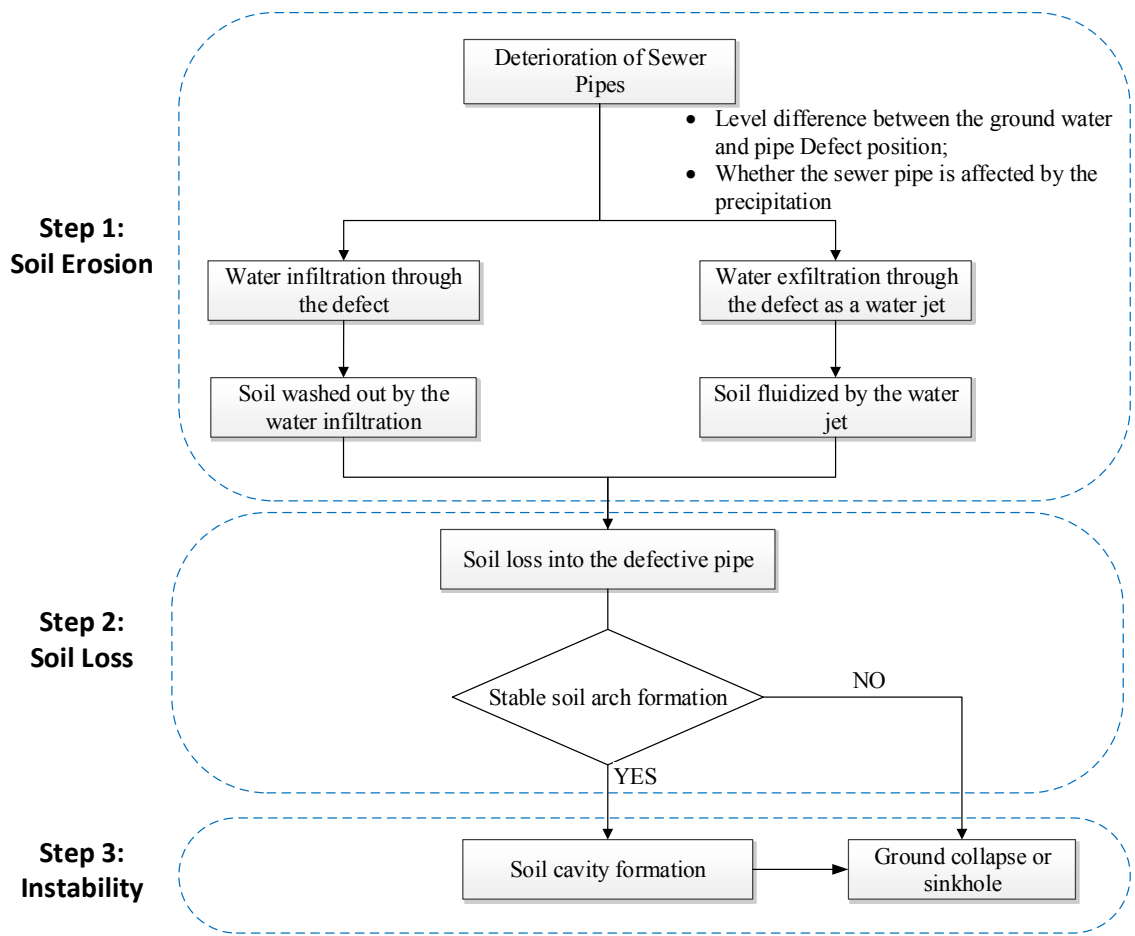
Figure 2.11 Conceptual model of sinkhole formation due to the defective sewer pipe

The consequence of the sinkhole problem is increasingly serious. From the accidents in Table 2.1, the cost of remediation is in millions of dollars since most of the accidents occurred in populated urban area. The direct consequence is severe, and rehabilitation measures are difficult. Besides the costs of the sewer pipes, there are additional indirect and social costs such as the interception of transport, damage of adjacent utilities, which has been summarized by Davies et al. (2001). The most severe consequence is human casualties and sinkhole hazard occurred rapidly in the populated urban area.

Most of the failures are induced by the change of water condition. Water condition can be affected by various factors. Heavy rainfall may increase the water level and wash soil through the pipe defect. From Table 2.1, most of the accidents on US eastern coast in 2011 were due to the serious hurricane at that time. Failures in Texas, US (2010) and Ontario, Canada (2013) were close to the river or lake where the groundwater condition was significantly affected by the water level in river or lake. From the accident in Saskatoon, Canada (2011), the sewer pipe was damaged due to the freeze while thaw caused the rapid increase in water level.

From the cases, the deterioration of sewer pipe is the prerequisite for sinkhole formation. Defects may be developed in the sewer pipe by various factors, such as corrosion, external loads, and internal pressure (Makar, 2000). Some old sewer systems were constructed using clay pipe or brick tunnel, which will easily result in the leaking and soil erosion problem even developed to sinkhole accidents (New York US, 2011; Ohio, US, 2011).

Sinkhole and ground collapse mostly occur in sandy soil. From the studies by WRC (Water Research Center) in 2001 as shown in Table 2.2, soils with little or no cohesion can be easily mobilized and washed out with higher risk.

Table 2.2 The effect of soil type on ground loss (WRc, 2001)

Soil type	Risk of ground loss
	High
Silts, silty fine sands or fine sands	
Medium to coarse sands	
Low plasticity clays (plasticity index < 15)	
Fine to medium gravels	
Well grade sandy gravels	
Medium to high plasticity clays (plasticity index > 15)	
All clays if sewer constructed by tunnelling	
	Low

Chapter 3 Experimental Study on Submerged Sand Erosion through a Slot on a Defective Pipe[1]

3.1   Introduction

The development of sinkholes can lead to the ground collapse or sinkhole formation in urban areas, resulting in serious personal injuries and casualties (Mukunoki et al., 2012; Guo et al., 2013a). One possible mechanism of sinkhole formation is soil loss into defective sewer pipes. Based on current accident reports and other qualitative analysis (Fenner, 1991; WRc, 2001), sandy soil without cohesion is easily eroded, leading to accidents. Therefore, sand erosion through a defect on a pipe is similar in mechanism to granular flow through an orifice. As a classic topic in chemical engineering, the flow rate of dry granular material through an orifice follows the correlation proposed by Beverloo et al. (1961). The flow rate is proportional to $D^{2.5}$ for a 3D outlet and $D^{1.5}$ for a 2D slot, where D is the orifice size or slot width.

Various studies have been conducted to investigate scour hole formation upstream of an orifice in hydraulic engineering. Lai and Shen (1996) conducted experiments to study the flushing process during drawdown flushing, and the erosion stages were identified based on the change in the water surface and sediment discharge. The size of the scour hole upstream of a circular orifice under constant water head was studied by Powell and Khan (2012) using dimensional analysis of the experimental results. The flow behavior upstream of a circular orifice was investigated, and the effects of the sediment size and water head were analyzed by Powell and Khan (2014).

Langford et al. (2015) conducted field measurements and numerical simulations to study the velocity field after creating a large scour hole upstream of a dam.

In this chapter, experiments are conducted to investigate the mechanism of sand erosion through a defect on a pipe, where the defect is modeled as a slot on the pipe to simplify sand erosion as a 2D problem. Sand erosion through a defect on the pipe is closely related to the particle size and opening size (Mukunoki et al., 2009, 2012; Guo et al., 2013a); therefore, the particle size and slot size are controlled to study the sand particle behavior, including erosion to arch formation conditions. In addition, the effect of the defect location and the water level on sand erosion are studied. The sand and water flow rate are measured during sand erosion, and visualization analysis using particle image velocimetry (PIV) is adopted to investigate the sand erosion process. In this experimental study, the mechanism of sand erosion due to defective sewer pipes is explored, and the corresponding effects of the controlling parameters are analyzed and evaluated. Based on the experimental results, a simple analytical model is developed for sand and water flow rate estimation.

3.2   Experiments

The experimental setup used to simulate sand erosion through a defect on a pipe with a 2D slot is shown in Figure 3.1. The model box was constructed using Plexiglas with dimensions of 500×80×500 mm (length × width × height). A pipe with a slot was used to simulate a defective sewer pipe with a different slot size and defect position. To prevent leakage of sand and water before the experiment, a water swelling strip, which is a special type of rubber that can be swelled with water, was used to seal the defect. The outflow sand and water mixture were collected using a sloped Plexiglas channel on the bottom of the model box.
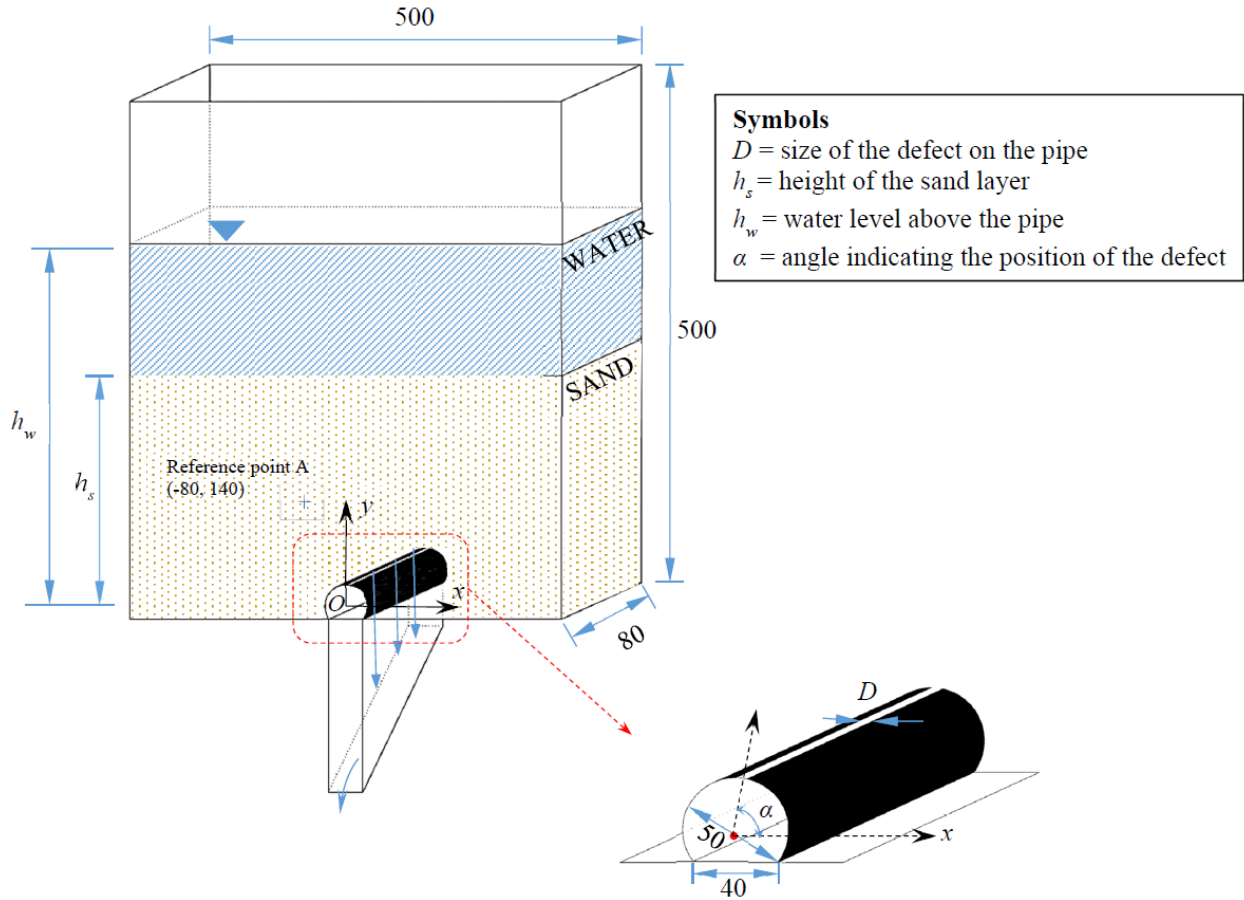
Figure 3.1 Schematic of experiment setup for the sand erosion through a 2D pipe defect (not to scale, unit: mm)

In this experiment, three different sizes of quartz sand were used, with a d_p of 1.52 mm (coarse), 0.96 mm (medium), and 0.17 mm (fine). The particle size distributions are plotted in Figure 3.2, and the detailed properties are listed in Table 3.1. The grain size distribution was tested based on American Society for Testing and Materials (ASTM) standard D422-63, while the specific gravity was based on the ASTM D854-14. The uniformity coefficient $C_u = d_{60}/d_{10}$ ranged from 1.31 to 2.14, indicating a relatively uniform distribution of sand particles. The angle of repose was determined by conducting the hopper flow of the dry sand. The specific gravity of the sand particles was fairly constant and was measured close to 2.6. Based on the images of these sand

particles under the microscope shown in Figure 3.2, the sands used in this test were subrounded and slightly elongated and flattened.

Table 3.1 Properties of the sand used in this test

Material	Specific Gravity	Angle of Repose (°)	Mean Particle Diameter d_p (mm)	Uniformity Coefficient $C_u=d_{60}/d_{10}$
Coarse Sand	2.6	36	1.52	1.31
Medium Sand	2.6	36	0.96	2.31
Fine Sand	2.6	36	0.17	2.14
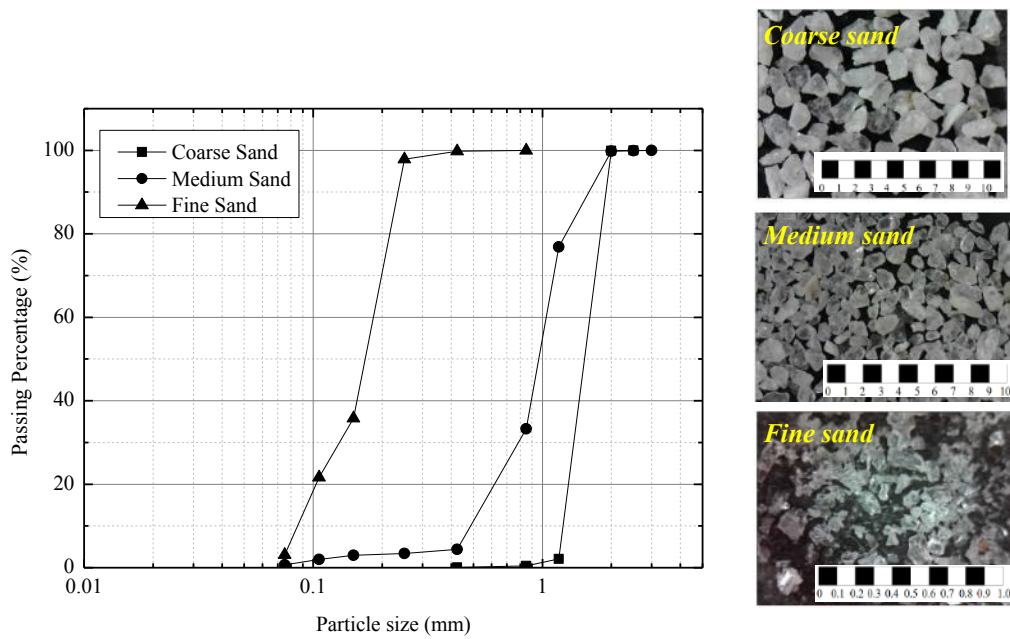
Figure 3.2 Particle size distributions of the sand and images under the microscope (unit: mm)

The experimental program is listed in Table 3.2. The effects of the defect size, defect position, sand particle size and water level above the pipe were studied.

Table 3.2 Experimental program for the sand erosion through a 2D pipe defect

RUN #*	Sand Type	Slot Position α (°)	Slot Size D (mm)	Water Level h_w (mm)	Sand Height h_s (mm)	Average Hydraulic Gradient $i = h_w/h_s$
2D-1$_{T**}$, 2D-1$_S$, 2D-1$_H$	medium	90, 45, 0	3	400	250	1.6
2D-2$_T$, 2D-2$_S$, 2D-2$_H$	medium	90, 45, 0	3	450	250	1.8
2D-3$_T$, 2D-4$_T$	medium	90	3	500, 600	250	2, 2.4
2D-5$_T$, 2D-6$_T$	medium	90	3	550, 650	300	1.8, 2.2
2D-7$_T$, 2D-7$_S$, 2D-7$_H$	medium	90, 45, 0	9	400	250	1.6
2D-8$_T$, 2D-8$_S$, 2D-8$_H$	medium	90, 45, 0	9	450	250	1.8
2D-9$_T$, 2D-10$_T$	medium	90	9	500, 600	250	2, 2.4
2D-11$_T$, 2D-11$_S$, 2D-11$_H$	coarse	90, 45, 0	3	400	250	1.6
2D-12$_T$, 2D-12$_S$, 2D-12$_H$	coarse	90, 45, 0	3	450	250	1.8
2D-13$_T$, 2D-13$_S$, 2D-13$_H$	coarse	90, 45, 0	9	400	250	1.6
2D-14$_T$, 2D-14$_S$, 2D-14$_H$	coarse	90, 45, 0	9	450	250	1.8
2D-15$_T$, 2D-15$_S$, 2D-15$_H$	fine	90, 45, 0	3	400	250	1.6
2D-16$_T$, 2D-16$_S$, 2D-16$_H$	fine	90, 45, 0	3	450	250	1.8
2D-17$_T$, 2D-17$_S$, 2D-17$_H$	fine	90, 45, 0	9	400	250	1.6
2D-18$_T$, 2D-18$_S$, 2D-18$_H$	fine	90, 45, 0	9	450	250	1.8

Note: * RUN # indicates test number in this experiment; ** the subscript T indicates the opening is at top of the pipe ($\alpha = 90°$), while S is for the side opening ($\alpha = 45°$) and H is the horizontal defect on the pipe ($\alpha = 0°$).

The initial porosity of the sand was controlled to be 0.4 by calculating the amount of water and sand needed for the total volume. The model box was firstly filled with the water, and sand was then gradually added to the model box. After adding a weighted amount of the sand, the sand layer was slightly compacted to the calculated thickness for a porosity of 0.4. The sand was added layer-by-layer until the desired thickness was reached (250 mm). After placing the sand in water, the tank was finally filled with water to the desired depth. Some dyed sand with the same particle size was added to allow visualization of the sand movements and velocity analysis using PIV, and the dyed sand particles were only placed close to the front of the model. After removing the rubber strip at the defect, sand began to erode, and the experiment was initiated. A video camera (SONY

HDR-PJ580E) was used to record the experiment at a rate of 50 frames per second to determine the time and duration of the flow rate measurements.

PIV was used to study the sand particle mobilization. PIV was first developed in experimental fluid mechanics to study the velocity field of fluids based on image analysis (Adrian, 1991) by analyzing the motion of seeded tracer particles inside a laser sheet. Because of the natural texture of geomaterial, PIV was applied in geotechnical engineering (White et al., 2003). To measure the sand velocity, only a camera is necessary, and the sand particle motion can be detected and calculated based on the color difference between two neighboring pixels. In this experiment, dyed sand particles were added to increase the color difference. Considering the requirement of image quality, a DSLR camera (Canon EOS 50D) with a resolution of 1920×1080 pixels at 25 frames per second was used to record the experiment, and a spot light was used as a stable light source. A ruler was placed in the camera view, and a cross mark was drawn in front of the model box for image calibration. The recorded video was digitized and calibrated for processing. The images were analyzed using open source PIV code named *OpenPIV*, which was developed based on MATLAB for high efficiency and flexibility (Taylor et al., 2010). A microscopic camera (Andonstar-A1; Shenzhen Andonstar Tech Co., Ltd, Shenzhen, China) was used to observe sand erosion at selected locations. Although the magnification of this microscopic camera can reach 500x, the camera field is fairly small and only certain small areas can be recorded (shown as reference point A in Figure 3.1).

During the experiment, the outflow mixture was captured using beakers at different time intervals. The total volume and weight of the outflow mixture were measured, and the corresponding sand volume and water volume were calculated. The volumetric flow rates for the

sand and water were calculated by dividing the time duration obtained from the video of the experiment.

3.3 Results and Discussions

3.3.1 Observation of sand erosion

A general overview of the experiments is presented as a detailed description of a representative run, Run 2D-2$_T$, in this section. Photos of sand erosion into the defective pipe at various times are shown in Figure 3.3, where some black sand particles were added for observation. The mobilized zone, slip surface and eroded zone shape are shown in the photos using various color lines, and the corresponding dimensions are labeled in Figure 3.3. The sand layer began to move towards the outlet after opening the slot. The mobilized zone in the sand layer was restricted to a narrow zone immediately above the slot. The width of the mobilized zone was almost constant at approximately 80 mm in the first three photos before 54 seconds, while the height of the mobilized zone decreased from 152 mm to 40 mm. At 27 seconds, the movement of dyed sand particles in the narrow mobilized zone was directly towards the outlet, whereas the pattern of dyed sands was horizontally layered at 13 seconds. Therefore, the sand particles at the original narrow mobilized zone had been washed out, and the sand particles in this narrow mobilized zone were composed of surface sand. In other word, this narrow mobilized zone acted as a channel between surface erosion and the slot opening. At 54 seconds, the mobilized core was fairly small and dyed sand was hardly observed in the mobilized core, which indicated that the particles in this zone were fed by the particles above. At 69 seconds, the water level was significantly decreased, and the narrow mobilized sand zone disappeared.
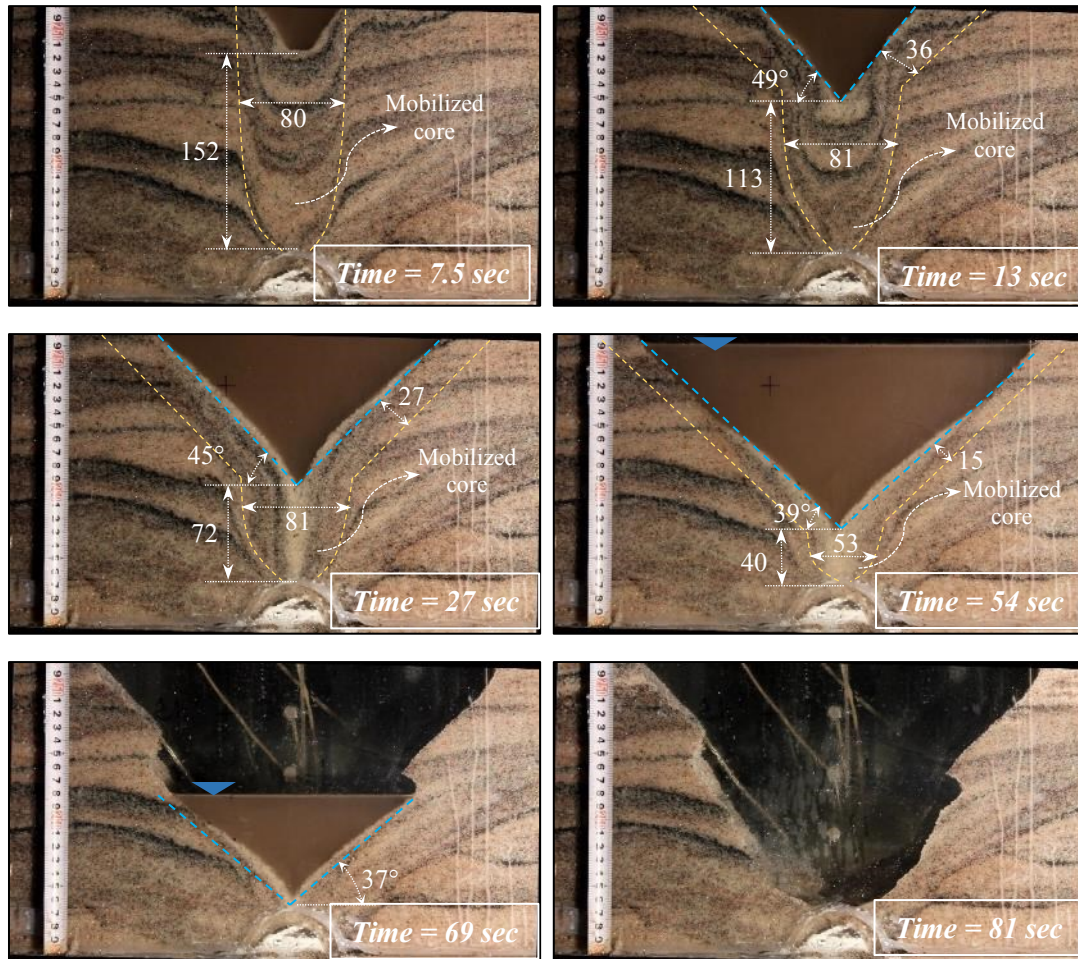
Figure 3.3 Representative photos of the sand erosion around the defective pipe (Run 2D-2$_T$; blue dash lines are sketching the eroded zone shape; orange dash lines are sketching the slip surface in sand layer; Unit: mm)

With the loss of sand particles, an eroded zone was formed at the sand surface at 7.5 seconds. The eroded zone increased due to the continuous discharge of sand, and the slope of the eroded zone decreased during the erosion process, as shown in Figure 3.3. At 13 seconds, the slope was approximately 49°, which was steeper than the angle of repose of the sand. The thickness of the slip surface at 13 seconds was greater than that in the subsequent time intervals, and the slope of the eroded zone flattened as the particles gradually slid into the mobilized zone. As mentioned

above, sliding sand particles formed the narrow mobilized zone. Eventually, the slip surface in the sand layer disappeared at 69 seconds, and the slope of the eroded zone decreased to 37°, which was close to the sand repose angle. Therefore, the slope of the eroded zone during the erosion process tended to become flat and reach the angle of repose of sand by gradually sliding into the narrow mobilized zone.

During water drawdown, the shape of the eroded zone changed. Before 54 seconds, the eroded zone was smooth, although the slope became flat, and the shape of the eroded zone was similar to the scour hole (Lai and Shen, 1996; Powell and Khan, 2012). At 69 seconds, the rapid decrease in the water level created an unsaturated zone above the water level, and the suction at this unsaturated zone resulted in the zigzag eroded zone shape. Nevertheless, most of the water was discharged after 69 seconds, and only a small amount of sand particles was eroded. The water was completely drained at 81 seconds. Sand particles were significantly cut and eroded when the water level decreased near the opening. Therefore, the final eroded zone had a 'bowl' shape rather than a 'cone' shape at 81 seconds, as shown in Figure 3.3.

From the observations of the experiments, the mechanism of sand erosion and water flow was fairly complicated considering the interaction of the two phases and the effect of the outlet boundary on the erosion process. As most of the sand particles were eroded before the eroded zone reached the opening, the following analysis focuses on this erosion stage.

Using PIV, the measured sand velocity contours at various times are plotted in Figure 3.4. For the test with a slot at the top of the pipe (Run 2D-2_T), sand particles near the opening were mobilized at 0.08 seconds. At 5 seconds, the maximum sand velocity increased to 0.01 m/s from 0.005 m/s at 0.08 seconds. Based on the velocity contour at 5 seconds, sand particles above the slot were mobilized in a narrow zone, consistent with the observation in Figure 3.3, and the

velocity of the mobilized zone was almost identical. Therefore, this mobilized zone behaved as a 'block' at this stage. At 10 seconds, an eroded zone was formed at the surface of the sand layer, and the width of the mobilized core increased slightly, which resulted in decreased sand velocity from approximately 0.01 m/s to 0.007 m/s. Similarly, the mobilized core was still in a narrow zone above the opening. At 15 seconds, the eroded zone was significantly expanded, and the narrow mobilized core decreased in height, as observed in Figure 3.3. Sand particles above the mobilized core at the sand/water interface gradually slid into the mobilized core. Some parts of the sand/water interface in the contour showed zero sand velocity due to the loss of dyed sand particles without significant color differences. At 20 seconds, the eroded zone was expanded, and the boundary between the mobilized and static zones in the contour was consistent with the observations in Figure 3.3 at 13 and 27 seconds. Although the narrow mobilized zone decreased, the maximum sand velocity within the mobilized core was approximately 0.01 m/s. Above the mobilized zone, the sand at the sand/water interface eroded almost parallel to the erosion surface. The maximum sand velocity in the erosion process was approximately 0.01 m/s, except at the onset of erosion.

Based on the velocity contours of the tests with a side slot (Run 2D-2$_S$) and horizontal slot (Run 2D-2$_H$), the sand movement and eroded zone development were similar to the results of Run 2D-2$_T$. After the onset of erosion, a narrow zone above the slot was mobilized and shifted due to the change in the opening position. The maximum sand velocity decreased as the slot moved from the top to horizontal. At 20 seconds, the maximum velocity of Run 2D-2$_T$ was 0.01 m/s, whereas it decreased to 0.008 m/s for Run 2D-2$_S$ and 0.005 m/s for Run 2D-2$_H$. The reduction in sand velocity was not significant from Run 2D-2$_T$ to Run 2D-2$_S$, and the maximum sand velocity was fairly close due to the small size of the model pipe.
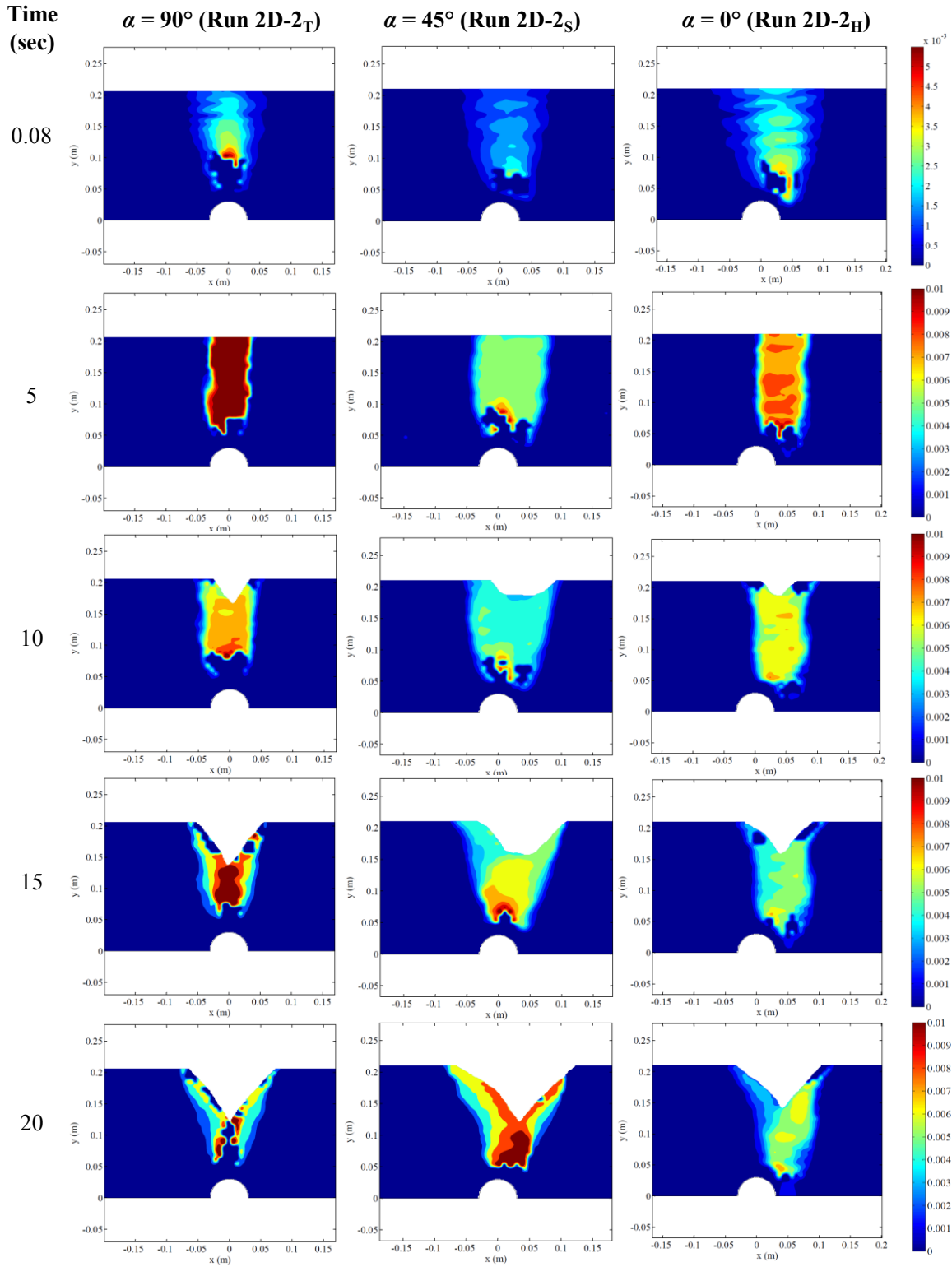
Figure 3.4 Contours of the sand velocity magnitudes (velocity unit: m/s; the color bar is the same at the same time for the different conditions)

To obtain the sliding velocity, a microscopic camera focused on reference point A (see Figure 3.1) was used, and the velocity contour and vectors are shown in Figure 3.5. The sand particles in this zone began to mobilize 25 seconds after opening the slot, and some particles at the sliding surface were washed out at 45 seconds. At 25 seconds, sand particles were mobilized downward, while the motion was parallel to the erosion surface at 45 seconds. At 25 seconds, the sand particles within the camera field were in the mobilized core and moved towards the slot, while the sand particles in the visual field were mobilized by the surface erosion with the expansion of the eroded zone at 45 seconds. Moreover, the sliding layer was approximately 19-21 mm at 25 seconds, as shown in Figure 3.5.
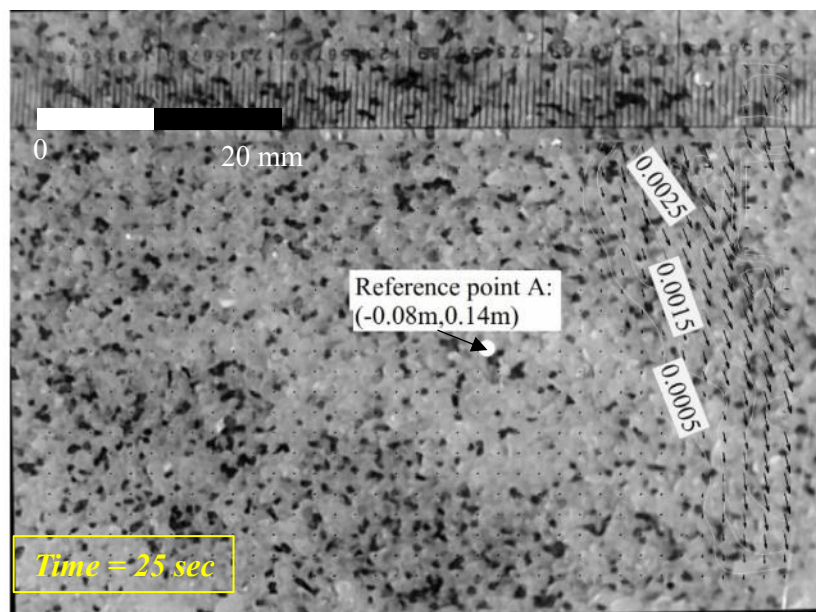
(a) Time = 25 sec
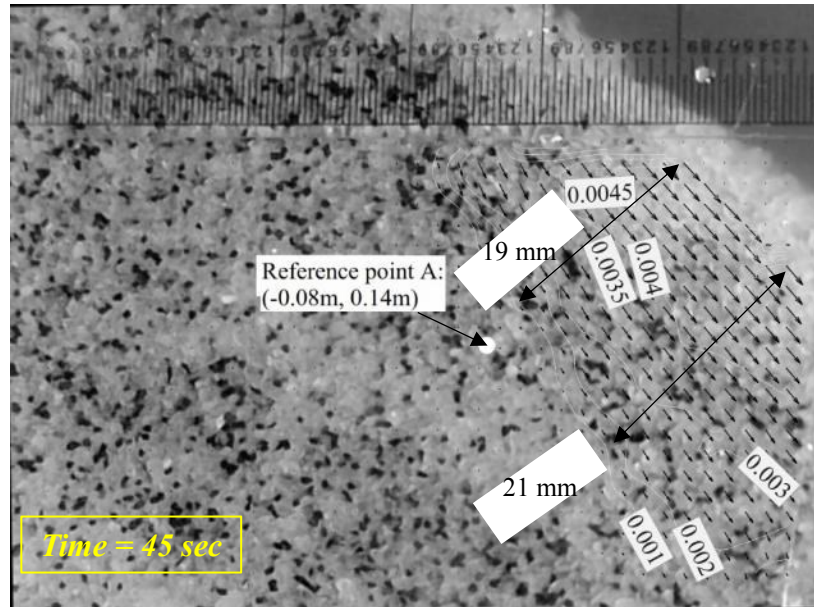
(b) Time = 45 sec

Figure 3.5 Microscopic image analysis at Reference point A using PIV (Run 2D-2$_T$; the velocity contour is labeled while the arrows are for the velocity vectors; unit: m/s)

3.3.2   Effect of the water level above the pipe

Since the sand layer erosion in this study was accelerated by flowing water, the effect of water level above the pipe was evaluated. In Figure 3.6, the changes in both the sand and water flow rates are plotted at different water levels. q_s is used for the sand volumetric flow rate per unit width, whereas q_w represents that of water. The curves of both the sand and water flow rates at the initial stage were almost flat with a slight decrease. For the results of Run 2D-2$_T$ in Figure 3.6, the sand and water flow rates began to decrease significantly at approximately 40 seconds. This is the time when the eroded zone is close to the slot, as shown in Figure 3.3. When the slot was at the top of the pipe ($\alpha = 90°$), the sand and water flow rates increased with increasing water level (Figure 3.6 (a) and (b)), but the effect of the water level was not highly significant. The initial sand flow rate increased from approximately 550 ml/(s·m) (1 ml = 10^{-6} m^3) to 900 ml/(s·m) as the water head above the pipe increased from 0.4 m to 0.6 m. A 'free-fall arch' forms near the slot as sand particles

52

discharge through an opening (Altenkirch and Elchhorn, 1981; Donsì et al., 1997; Hilton and Cleary, 2011). Above this 'free-fall arch', water flow is assumed to be fluid flow through porous media. If the average hydraulic gradient above the defective pipe is roughly defined as $i = h_w/h_s$, the water flow rate is almost proportional to the hydraulic gradient i, which is increased from 1.6 to 2.4. Although the water flow rate increased with increasing water level, the corresponding effect on the sand flow rate was not obvious. Based on the 'free-fall arch' theory (Davidson and Nedderman, 1973; Hilton and Cleary, 2011), the driving effect of water mostly occurs below the 'free-fall arch' near the opening, which is a small zone that depends on the opening size.

(a) Water flow rate   (b) Sand flow rate
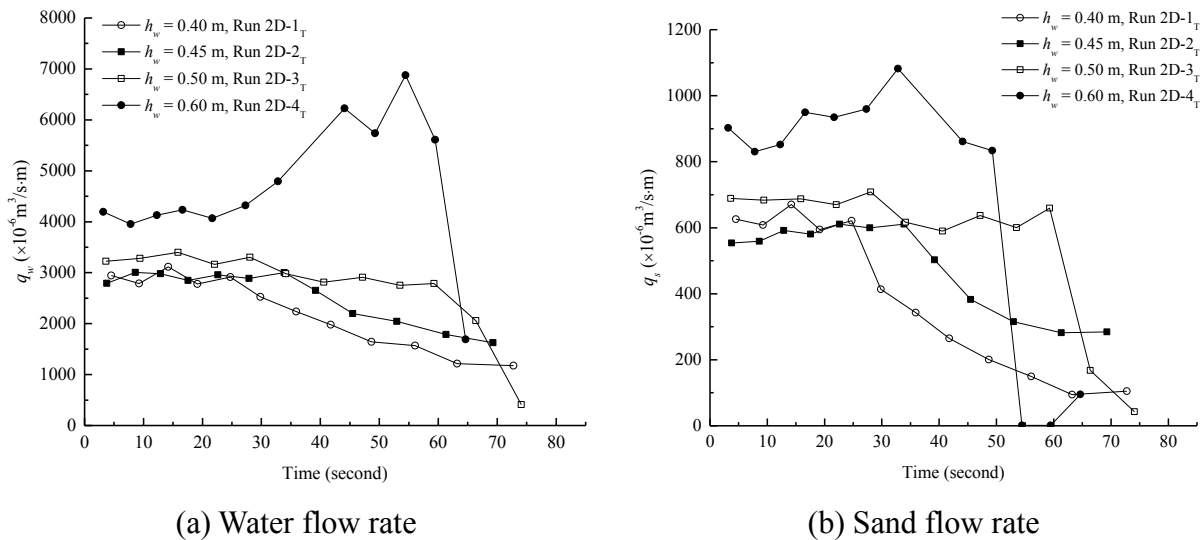
Figure 3.6 Variation of the flow rate with time under various water layer heights

The effect of the slot position on sand erosion was investigated. Although deterioration at the top or crown of a sewer pipe is most common, defects at other positions have been reported (Davies et al., 2001). The changes in the sand and water flow rates with time are plotted in Figure 3.7 (a) and (b), showing that the flow rate decreased as the defect moved from $\alpha = 90°$ (top) to $0°$ (horizontal). As the defect shifted from the top to horizontal position, the mobilization of sand particles was resisted by gravity, which resulted in decreased sand permeability near the defect.

As the water flow rate decreased, the erosional effect on the sand particles also decreased. On the other hand, the duration of the erosion process increased as α shifted from 90° (top) to 0° (horizontal).

(a) Water flow rate　　　　　　　　　　(b) Sand flow rate
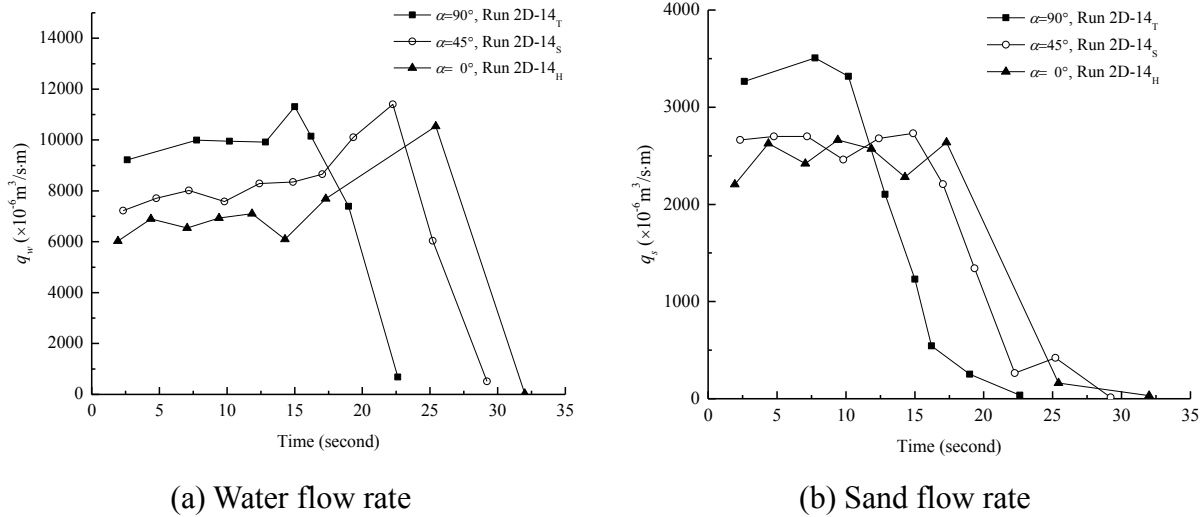
Figure 3.7 Variation of the flow rate with time under various slot positions

3.3.3　Effects of the slot size and particle size

Studies on dry granular flow through an opening have shown that the granular discharge rate is proportional to $D^{1.5}$ for a 2D slot because the granular velocity at the outlet is proportional to the square root of D, where D is the slot size (Beverloo et al., 1961). The arch adjacent to the outlet may be formed stably, ceasing granular flow if the ratio between the opening size and the particle size D/d_p is smaller than a critical value of approximately 3 to 6 (Nedderman et al., 1982; Sheldon and Durian, 2010). Therefore, the ratio is controlled between 3.1 and 53.6 in this experiment to investigate sand particle behavior through a slot on a pipe.

In the tests under dry conditions, the sand particles jammed if D/d_p was less than 3.1 for $\alpha =$ 90° or 45°, while the discharge stopped if D/d_p was less than 9.3 for $\alpha = 0°$. Sheldon and Durian (2010) found a critical ratio of approximately 3 for $\alpha = 90°$ and 6 for $\alpha = 0°$. The difference may

be due to the tested material: glass beads were used in Sheldon and Durian's experiment while quartz sand was used in this study. After immersing sand under water, the critical ratios for the three α angles were all 3.1. Although water flow can destroy the sand arch and assist sand erosion, the critical ratio remained approximately 3.1, which indicates that the sand arch is difficult to break after it has been created in a stable configuration. In this experiment, the arch can be reformed after being destroyed using a small screwdriver. This phenomenon is supported by the theoretical analysis of Davidson and Nedderman (1973), which showed that it is difficult to break the arch formed by granular material.

Comparing the experiment results of Run 1_T and Run 7_T, the water flow rate increased from 3,000 ml/(s·m) to 9,000 ml/(s·m) as the slot width increased from 3 mm to 9 mm, and the sand flow rate increased significantly from 600 ml/(s·m) to 4,500 ml/(s·m). Because the sand flow rate is approximately linearly dependent on the water flow rate before the formation of the connected eroded zone (Barletta et al., 2003; Hilton and Cleary, 2011; Guo et al., 2013a), the relationship varies with the width of the slot and sand particle size. In Figure 3.8, the relationships between the sand and water flow rates in this experiment are plotted for various D/d_p, and the flow rates at different defect positions are plotted with the same linear relationship. Figure 8 shows that the ratio q_s/q_w increased from 0.21 to 0.66 as D/d_p increased, similar to the studies by Guo et al. (2013a). When D/d_p is very small, sand particles are hard to erode because of the arch formation, and there is no sand flow, which means q_s/q_w is equal to zero.
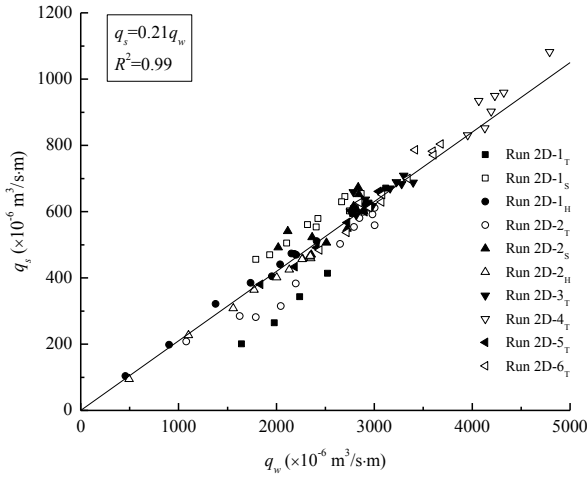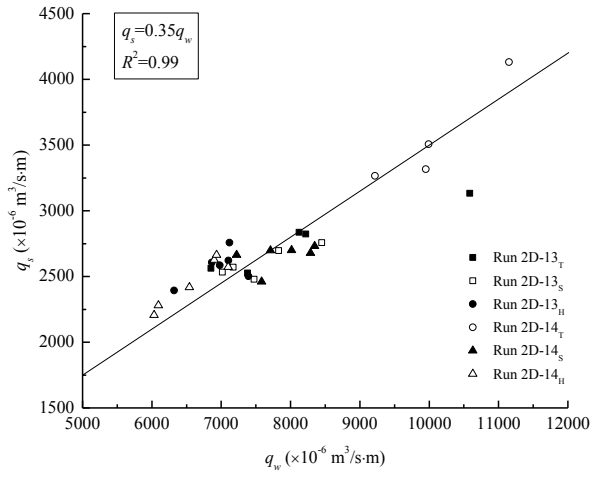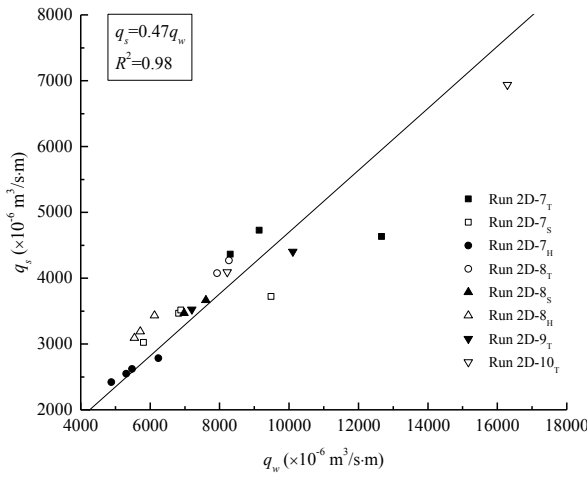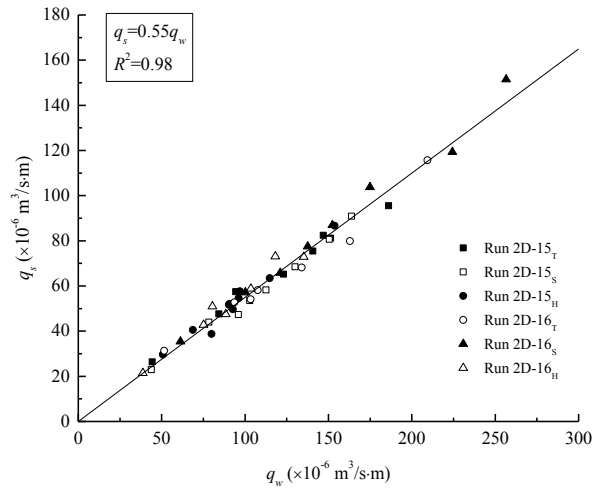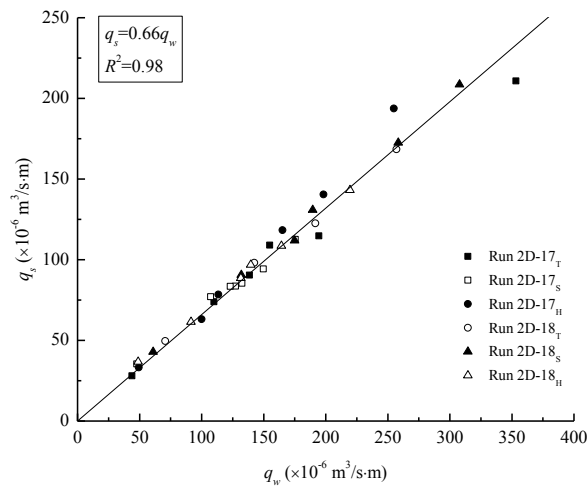
Figure 3.8 Relationship between q_s and q_w for all the experiments under different D/d_p values

As shown in Figure 3.8, the sand flow rate is linearly dependent on the corresponding water flow rate for different D/d_p. The approximate relationship between q_s/q_w and D/d_p can be plotted and fitted by the following equation, as shown in Figure 3.9:

$$\frac{q_s}{q_w} = 0.18 \ln\left(\frac{D}{d_p}\right) \qquad (3.1)$$
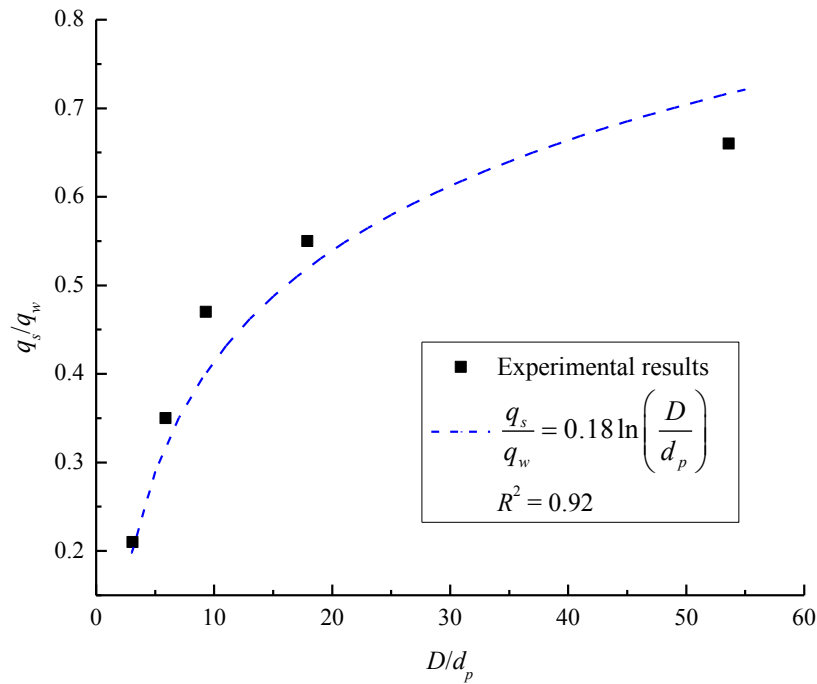
Figure 3.9 Relationship between q_s/q_w and D/d_p

This equation is directly obtained from the experimental results and is valid for 2D sand erosion conditions with D/d_p ranging from 3.1 to 53.6.

The sand velocity distributions obtained from the PIV analysis are plotted in Figure 3.10. The effect of the slot width on the sand velocity distribution is shown in Figure 3.10 (a) and (b), which are for 3 mm and 9 mm slot widths using medium sand with the same mean particle size of $d_p = 0.96$ mm. At the beginning of erosion (0.08 seconds), the sand velocity close to the opening

is greater than the sand velocity above. After the onset of sand erosion, the sand layer is mobilized with almost the same velocity in a narrow zone above the opening. The width *w* of the narrow mobilized zone is increased slightly from 0.053 m to 0.065 m, as shown in Figures 3.10 (a) and (b). Although the width *w* increases as expected, the change is not significant due to arch formation between the mobilized and static zones during sand erosion. Only two slot sizes were tested in this experiment; future research will be conducted to explore the effect of the opening size on the mobilized zone width. As the slot width increased from 3 mm to 9 mm, the velocity of the mobilized core increased from 0.011 m/s to 0.052 m/s. With the growth of the slot width, the water flow and sand velocity also increased. Correspondingly, the sand flow rate increased significantly from 600 ml/(s·m) to 4500 ml/(s·m). In contrast, the decreased resistance near the slot as slot width increases also assists sand flow.
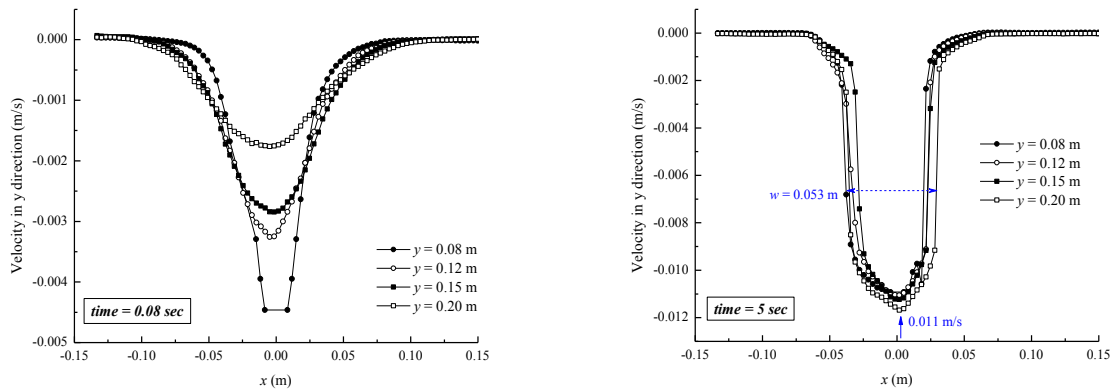
(a) d_p = 0.96 mm; D = 3 mm; h_w = 200 mm (Run 2D-2$_T$)
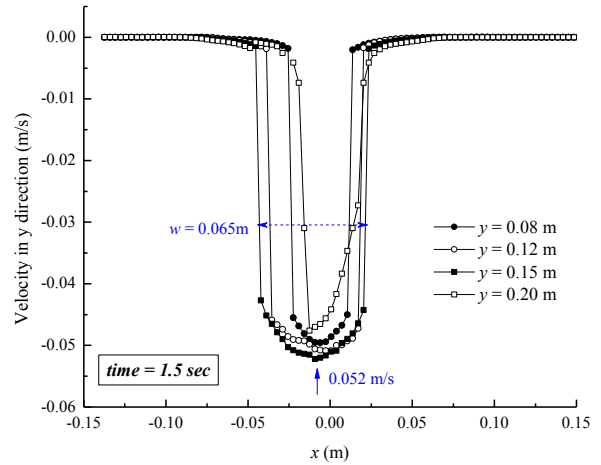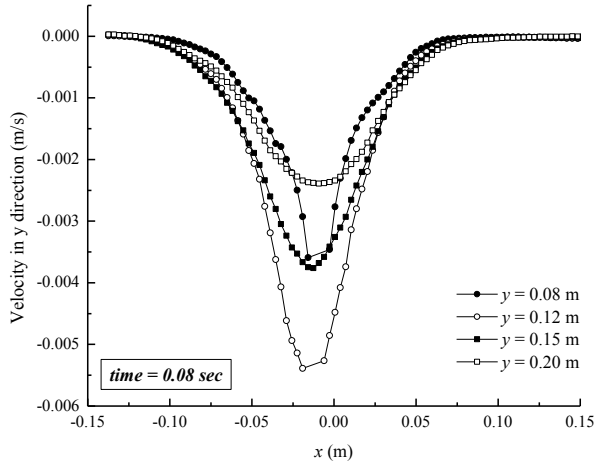
(b) d_p = 0.96 mm; D = 9 mm; h_w = 200 mm (Run 2D-8$_T$)
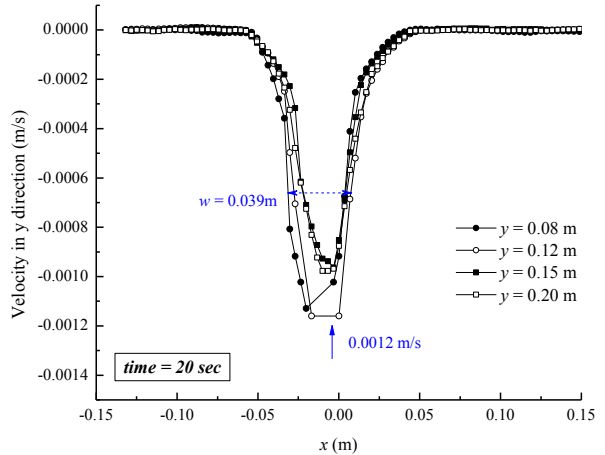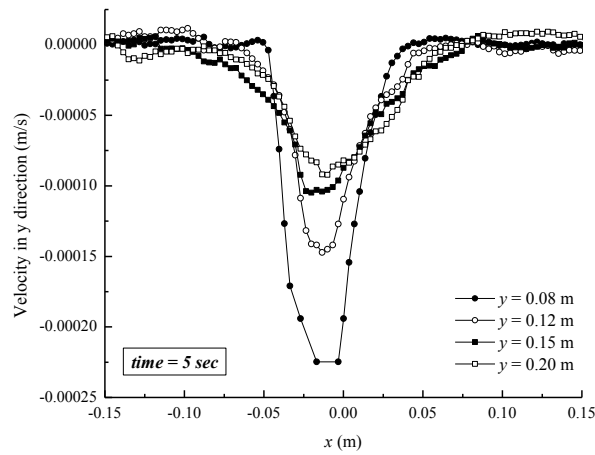
(c) d_p = 0.17 mm; D = 9 mm; h_w = 200 mm (Run 2D-18$_T$)
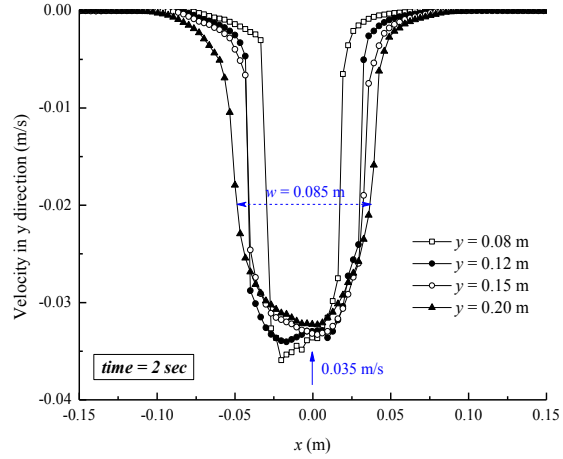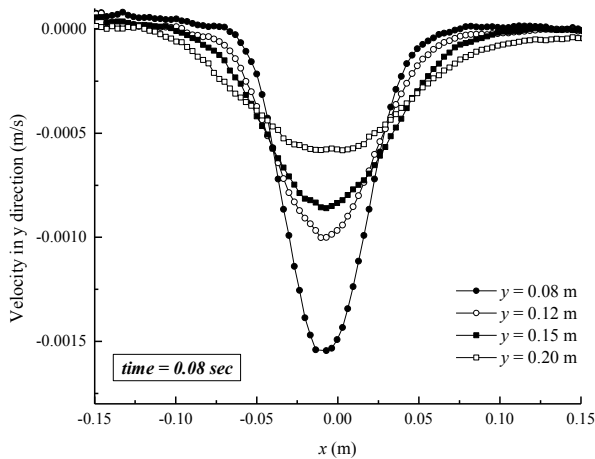
(d) d_p = 1.52 mm; D = 9 mm; h_w = 200 mm (Run 2D-14$_T$)

Figure 3.10 Sand velocity distributions for various conditions

The sand velocity distributions for fine sand with a mean particle size of $d_p = 0.17$ mm are plotted in Figure 3.10 (c), and the results for coarse sand with a mean particle size of $d_p = 1.52$ mm are shown in Figure 3.10 (d). Comparing Figure 3.10 (b) with 10 (c), velocity of the mobilized core is decreased from 0.052 m/s to 0.0012 m/s as d_p decreases from 0.96 mm to 0.17 mm. The permeability of the sand layer is decreased as the particle size decreases since the permeability is proportional to the square of the particle size based on Kozeny-Carman's equation (Lambe and Whitman, 1969). Therefore, the driving force effect of flowing water is weaker for fine sand than for medium sand. In contrast, the velocity of the mobilized core decreases from 0.052 m/s to 0.035 m/s as d_p increases from 0.96 mm to 1.52 mm, as shown in Figure 3.10 (b) with (d). This opposite effect on particle size is due to the flow resistance caused by sand arching. With increasing particle size, arching becomes easier, resulting in greater stability and making sand particles more difficult to erode. In general, sand erosion in this study is controlled by two factors: the driving force of flowing water and the resisting effect of sand particle arching. On the other hand, the width w of the mobilized zone increases from 0.039 m to 0.085 m as d_p increases from 0.17 mm to 1.52 mm. Based on this experiment, w increases significantly as the particle size increases.

According to the conservation of mass, the sand flow rate through the slot can be approximated by multiplying the mobilized zone width w by the corresponding sand velocity. Using the width w and sand velocity obtained from the PIV analysis in Figure 3.10, the calculated sand flow rates are in agreement with the measured sand flow rates shown in Figure 3.11, suggesting that these two measurements are reliable. A simple analytical model is proposed to estimate the sand flow rate in the following sections. The width w of the mobilized zone in this experiment is dependent on the particle size and opening size. As the opening size increases from 3 mm to 9 mm, w increases from 53 to 65 mm. Considering the sand particle size is 0.97 mm

(medium sand), the opening size is close to the critical condition and the sand flow may be jammed if the defect size is less than 3 mm. Therefore, there is a limiting mobilized zone width of approximately 53 mm for the medium sand used in this test. This width decreases significantly as the sand particle size decreases.
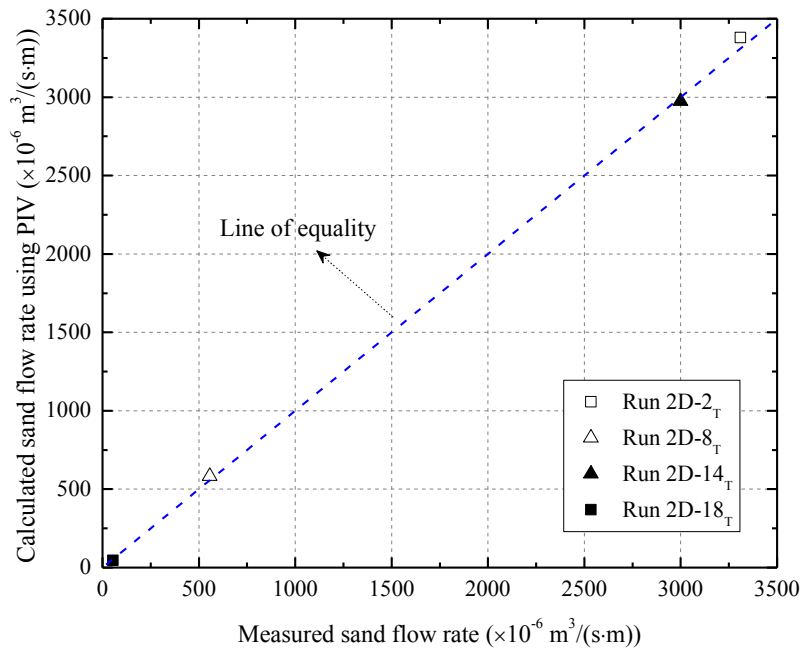
Figure 3.11 Predicted sand flow rate from PIV results compared with measurements

In Figure 3.12, the final shapes of the eroded zone are plotted for different slot sizes. The eroded zone is significantly expanded as the slot width increases. Additionally, the velocity of water increases as the slot width increases and more sand particles at the sand/water interface are eroded during water drawdown. The final eroded zones for different particle sizes are plotted in Figure 3.12. The slope of the eroded zone when using coarse sand is approximately 36°-37°, which is consistent with the measured angle of repose for sand. This finding agrees with the conclusions of Guo et al. (2013a) and can be explained using the Mohr-Coulomb theory (Rao and Nott, 2008). The eroded zone is formed by surface erosion and the sliding of sand particles along the sand/water

interface, while the slope of the eroded zone cannot always reach the angle of repose since matrix suction in the sand increases its stability. Although the water was drained, pore water remained in the sand layer, especially for fine sand with lower permeability, which led to the steeper slope angle for the eroded zone, as shown in Figure 3.12. Therefore, the angle of the final eroded zone cannot be less than the angle of repose of sand.
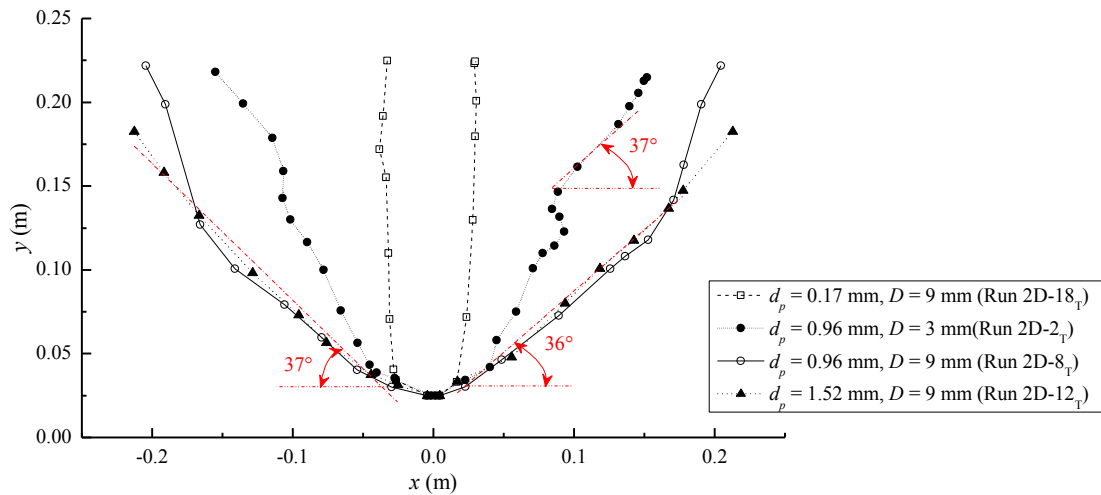
Figure 3.12 Final eroded zone shapes of different defect sizes and particle sizes

Based on the above analysis, sand erosion due to a defective pipe can be simplified using the schematics shown in Figure 3.13. At the beginning of the erosion process, as shown in Figure 3.13(a), a layer of sand moves towards the slot. The mobilized core of the sand layer acts as a 'block' with the same velocity, and the width of the block decreases near the opening. As shown in Figure 3.13(b), the mobilized core is reduced in height due to the loss of sand particles, and a triangular eroded zone is formed starting at the surface of the sand layer. This eroded zone gradually expands due to surface erosion and the sliding of sand particles at the sand/water interface, and these eroded particles flow in the mobilized core and are then washed out. Finally, the mobilized core disappears, as shown in Figure 3.13(c), and the slope of the eroded zone flattens due to surface erosion. Based on the analysis of Guo et al. (2013a), the slope of the eroded zone

eventually reaches the angle of repose of sand φ. This schematic analysis and following calculation approach are based on experiments with an opening at the top of the pipe.
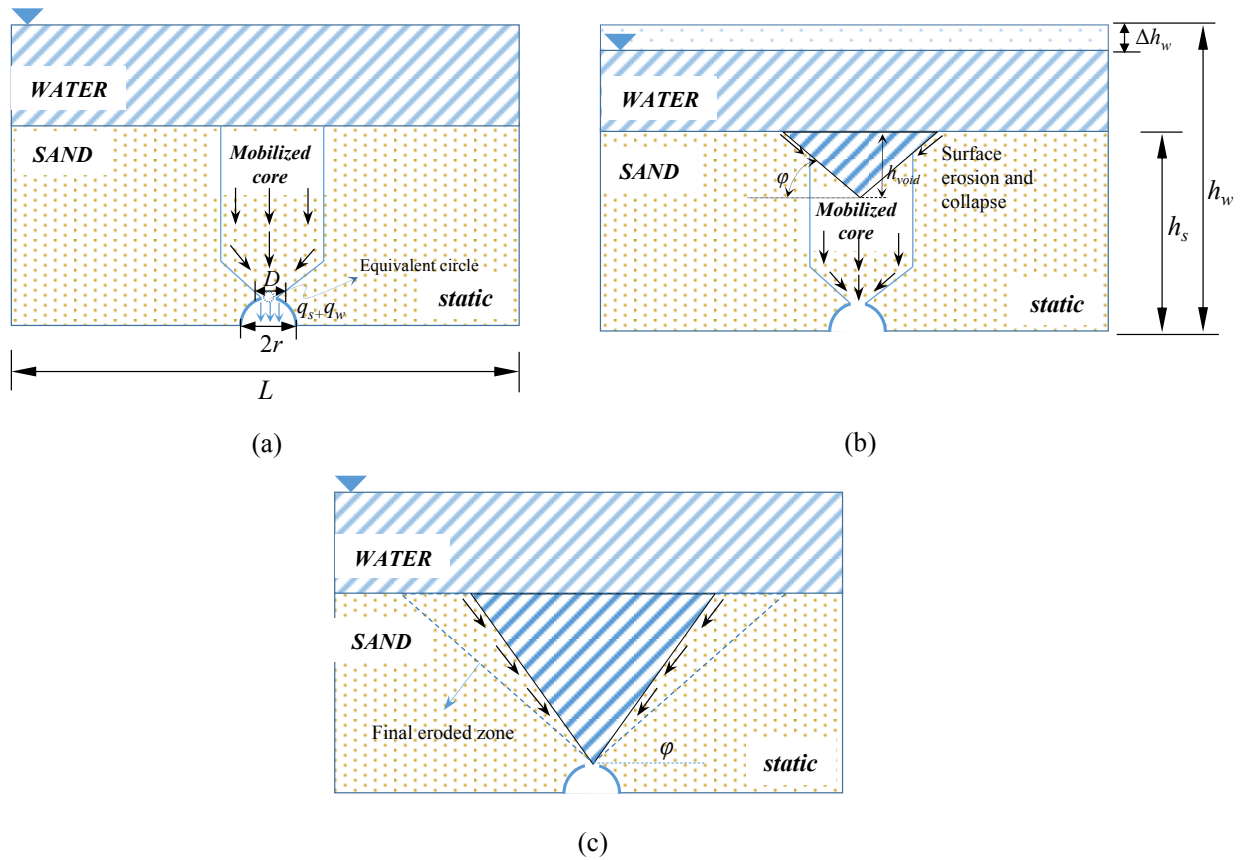
Figure 3.13 Schematics of the sand erosion around a defective pipe

According to Eq. (3.1), the sand flow rate can be predicted if the water flow rate is known. The calculation model and main symbols are shown in Figure 3.13(a). In studies of inflow into a drained circular tunnel (El Tani, 2003; Park et al., 2008), the domain was simplified as a semi-infinite aquifer, while the full tunnel is considered permeable with a Dirichlet boundary condition. Therefore, the domain can be mapped onto two circles using conformal mapping, and the constants in the general solution can be determined by incorporating the boundary conditions. The boundary conditions on the pipe in this study are the Dirichlet boundary conditions at the defect, while the impermeable pipe uses the Neumann boundary conditions for the rest of the pipe. Guo et al. (2013b)

proposed an approximate solution using the equivalent circle assumption, which simplified the pipe defect as a small fully drained pipe with the perimeter of the pipe equal to the defect size. Therefore, the water flow rate when the opening is at the top of the pipe can be calculated as:

$$q_w^T = \frac{2\pi k}{\ln\left[\frac{h_s-r}{r'}+\sqrt{\frac{(h_s-r)^2}{r'^2}-1}\right]}\left[(h_s-r)\frac{r'^2-\left(h_s-r-\sqrt{(h_s-r)^2-r'^2}\right)^2}{r'^2+\left(h_s-r-\sqrt{(h_s-r)^2-r'^2}\right)^2}+(h_w-h_s)\right], \qquad (3.2)$$

where k is the permeability of sand; r is the radius of the pipe; and r' is the radius of the equivalent circle, which and can be determined using $r' = D/(2\pi)$, where D is the defect size.

If the opening size on the pipe is smaller than the burying depth of the pipe, which means r' $\ll (h_s-r)$, Eq. (3.2) can be simplified to the following equation (Guo et al., 2013b):

$$q_w^T = \frac{2\pi k}{\ln\left(2\frac{h_s-r}{r'}\right)}(h_w-r) \qquad (3.3)$$

The permeability k can be estimated using the Kozeny-Carman equation (Lambe and Whitman, 1969):

$$k = \frac{1}{C_S S_S^2 T^2}\frac{\gamma_w}{\mu}\frac{e^3}{1+e}, \qquad (3.4)$$

where, C_S is the shape factor of the granular material and is approximately equal to 2.5; S_S is the surface area per unit volume of soil solids, which is $6/d_p$, assuming the sand particles are spheres; T is the tortuosity factor and is approximately equal to $\sqrt{2}$; γ_w is the unit weight of water, which can be taken as 10 kN/m^3; μ is the dynamic viscosity of water, which can be taken as 0.001 Pa·s; e is the void ratio of sand, which can be calculated using the porosity n, $e = n/(1-n)$. The

permeability of sand in this study can be estimated using Eq. (3.4) and is equal to 2.2×10^{-2} m/s for coarse sand, 9.1×10^{-3} m/s for medium sand and 2.8×10^{-4} m/s for fine sand.

The water flow rate at the beginning of sand erosion, based on Figure 3.13(a), can be predicted using Eq. (3.3), and the corresponding sand flow rate can be estimated using the correlation in Eq. (3.1). The proposed method can be verified by comparison with the experimental results, as shown in Figure 3.14.
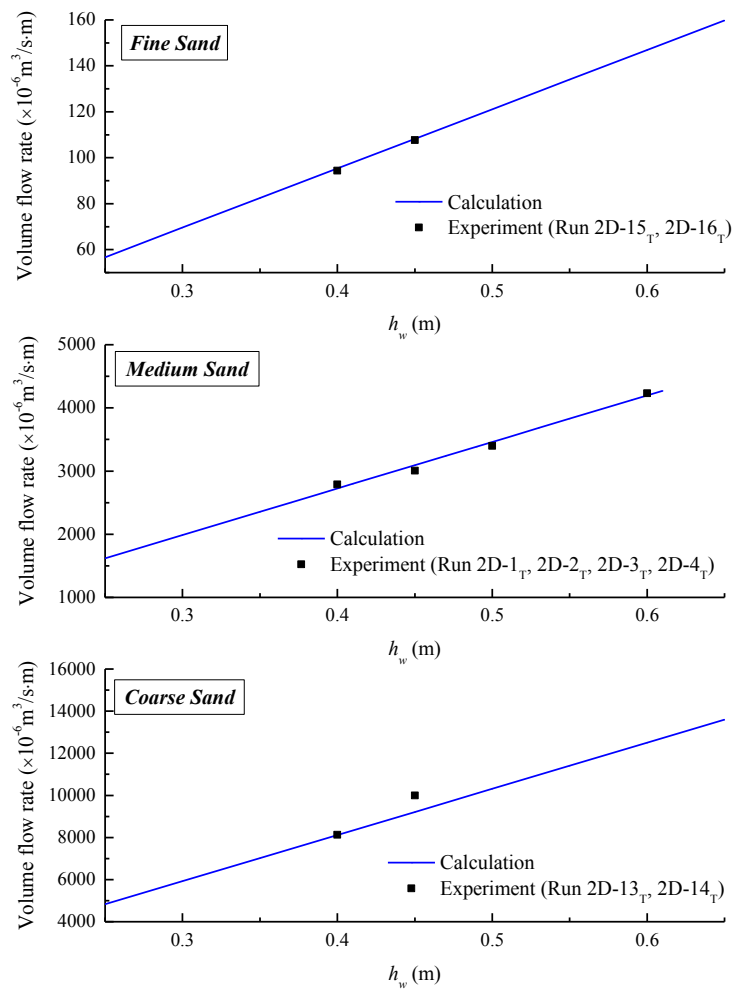
Figure 3.14 Verification of the analytical method for the water flow rate

Figure 3.3 shows that the eroded zone is formed from the sand surface and gradually expands towards the opening, as demonstrated in Figure 3.13(b). Guo et al. (2013a) stated that the slope of

65

the eroded zone is approximately consistent with the angle of repose of sand. However, erosion process in this study is transient at each time step, and the slope of the eroded zone cannot always reach the angle of repose during erosion. According to the experimental results in Figure 3.15, it is acceptable to assume that the slope of the eroded zone is equal to the angle of repose of sand, which is 36° in this experiment. Therefore, the gradual formation of the eroded zone and the decrease in the water level can be simplified, as shown in Figure 3.13(b).
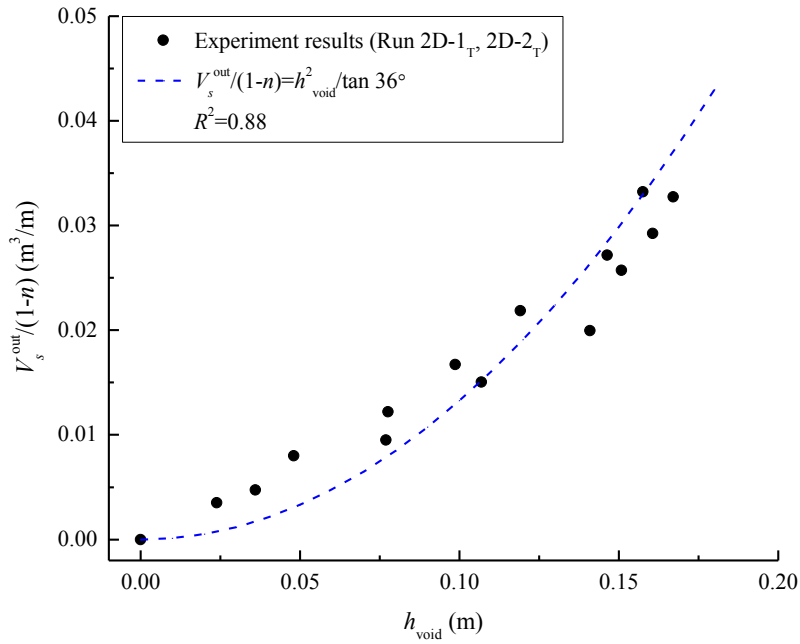
Figure 3.15 Relationship between the eroded zone shape and outflow sand volume

Based on the conservation of mass and the correlation in Figure 3.15, the formation of the eroded zone and the decrease in water level can be predicted:

$$\sum_{t=t_1}^{t_m} q_s^T(t_i) \cdot \Delta t = \left(\frac{1}{2} \cdot h_{void}^m \cdot \frac{2h_{void}^m}{\tan \varphi}\right)(1-n) \tag{3.5}$$

$$q_w^T(t_m) \cdot \Delta t = \Delta h_w^m \cdot L \tag{3.6}$$

where $q_s^T(t_i)$ is the sand flow rate at time t_i; $q_w^T(t_m)$ is the water flow rate at time t_m; h_{void}^m is the eroded zone height after m time steps; Δt is the time step;   is the decrease in the water level at the mth time step; and L is the length of the calculation model, as shown in Figure 13(a).

Eqs. (3.5) and (3.6) can be used to calculate the height of the eroded zone at the mth time step and the corresponding change in the water level:

$$h_{void}^m = \sqrt{\frac{\sum_{t=t_1}^{t_m} q_s^T(t_i) \cdot \Delta t \cdot \tan \varphi}{1-n}} \tag{3.7}$$

$$\Delta h_w^m = \frac{q_w^T(t_m) \cdot \Delta t}{L} \tag{3.8}$$

The sand layer height at the mth time step can be assumed to be the initial sand layer height h_s^{ini} reduced by h_{void}^m:

$$h_s^m = h_s^{ini} - h_{void}^m \tag{3.9}$$

The water level at the mth time step is decreased by Δh_w^m:

$$h_w^m = h_w^{m-1} - \Delta h_w^m \tag{3.10}$$

Using Eqs. (3.3) and (3.1) with the updated water level and sand layer height from Eqs. (3.9) and (3.10), the sand and water flow rates can be calculated for the next time step. The calculation results are plotted and compared with the experimental results in Figure 3.16. The proposed simple analytical model reasonably predicts the water and sand flow rates during submerged sand erosion through a defect on a sewer pipe. It should be noted that this analytical model is developed based

on the two-dimensional condition, and the experimental fitting formula is used to determine the sand flow rate using the water flow rate. Therefore, this analytical model is valid if D/d_p is between 3.1 and 53.6, and sand permeability should be accurately determined if Darcy's law was used to calculate the water flow rate.
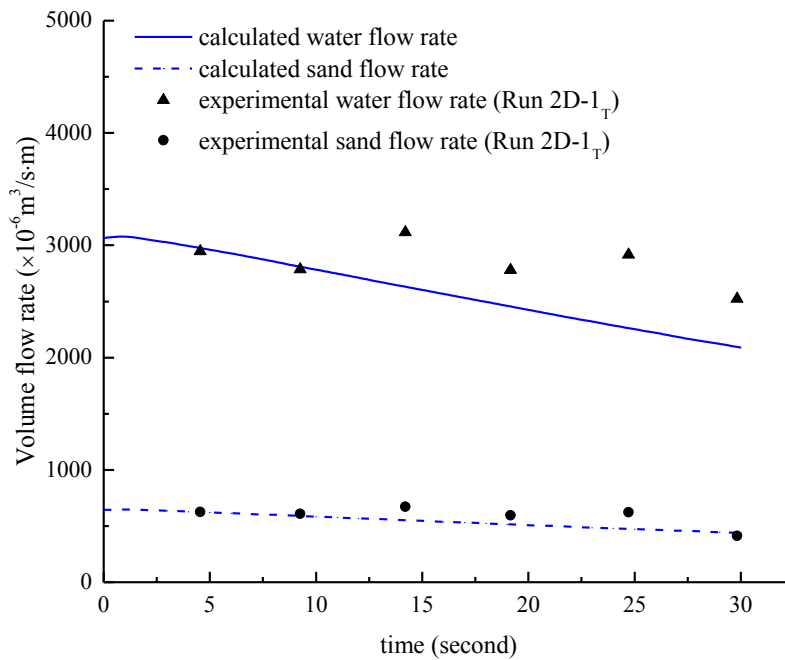
Figure 3.16 Predicted water and sand flow rate with time compared with experiment results

3.4   Summary and Conclusions

In Chapter 3, a physical model was designed to simulate submerged sand erosion through a slot on a defective pipe. The sand and water flow rates through the defect were measured, and PIV was used to analyze the sand movement. Based on the experimental results and analysis, the following conclusions are obtained:

- The process of sand erosion into a defective pipe occurs in several stages. First, sand particles are washed out by flowing water, and the mobilized core of the sand layer moves towards the slot as a vertical 'block'. As the sand particles are discharged, an eroded zone above the

mobilized core is formed and expanded. When the eroded zone reaches the opening, the sand flow rate gradually decreases, and sand erosion eventually stops.

- The sand particle size and slot size significantly affect sand erosion. The sand and water flow rates increase as the opening size increases. The sand flow rate decreases as the sand particle size decreases from 0.96 mm to 0.17 mm due to the significant decrease in water flow, while the sand flow rate increase as the sand particle size decreases from 1.52 mm to 0.17 mm because of the arching effect of the larger particles. The increase in the water level and the change in the slot position from the horizontal to the top increase the sand and water flow rates.

- The sand flow rate is linearly related to the water flow rate during sand erosion, and the ratio between the sand and water flow rates, q_s/q_w, is dependent on the ratio between the slot width and particle size, D/d_p. As D/d_p increases, q_s/q_w also increases. When D/d_p is less than 3.1, sand flow stops due to jamming near the opening.

- Based on the experimental results, a simple analytical model is proposed to estimate the water and sand flow rates. By considering the decrease in the sand layer thickness and water level during the erosion process, the method can be improved to predict the change in flow rate with time to predict the process of sand erosion through a defect on a sewer pipe.

List of Symbols

The following symbols are used in this chapter:

C_u	uniformity coefficient
C_s	shape factor of granular material
D	size of the defect on the pipe, m
d_p	particle size, m
e	void ratio

h_s	height of the sand layer, m
h_{void}	height of the erosion void, m
h_w	water level above the pipe, m
i	hydraulic gradient
k	soil permeability, m/s
n	porosity
q_s	sand flow rate per unit width, m^3/s/m
q_s^T	sand flow rate per unit width if the defect is at the top of pipe, m^3/s/m
q_w	water flow rate per unit width, m^3/s/m
q_w^T	water flow rate per unit width if the defect is at the top of pipe, m^3/s/m
r	radius of the pipe, m
r'	radius of the equivalent circle, m
S_S	surface area per unit volume of soil solids, m^{-1}
T	tortuosity factor
V_s^{out}	outflow sand volume, m^3
w	width of mobilized zone, m
α	angle indicating the position of the defect, °
γ_w	unit weight of water, kN/m^3
μ	dynamic viscosity of water, Pa·s
φ	sand angle of repose, °

Chapter 4 Experimental Study on Submerged Sand Erosion through an Orifice on a Defective Sewer Pipe[2]

4.1   Introduction

Accidents caused by the sinkhole and ground collapse in the urban area have frequently been reported and may result in severe consequences. The soil erosion through the pipe defect is found to be one of the possible reasons. In Chapter 3, the submerged erosion process was studied based on the two-dimensional experimental studies. Sand/water flow rate in the erosion process was analyzed, and the sand mobilization was investigated using the PIV technique. In this chapter, experiments are carried out to study the sand erosion due to the defective pipe, and the pipe is modeled with a three-dimensional orifice and can simulate various defect positions. The mechanism of sand erosion is analyzed based on the observational analysis, and various stages of sand erosion are identified. The formation of erosion void is quantitatively analyzed, and the assumed erosion void shape can be used to predict the erosion void formation based on the change of sand flow rate. The sand velocity can be measured using particle image velocimetry (PIV) technique, and the mobilization of the sand layer during erosion process is analyzed. An analytical solution is suggested to calculate the sand velocity distribution. Finally, an analytical model is developed for the sand and water flow rate calculation.

---

[2] This chapter is currently being prepared as a journal manuscript: Tang, Y., Chan, D. H. and Zhu, D. Z. (2017). "Experimental Study on Submerged Sand Erosion through an orifice on a Defective Sewer Pipe." *ASCE Journal of Engineering Mechanics,* to be submitted.

4.2   Experiments

Figure 4.1 shows the experimental setup to study the sand erosion due to the defective sewer pipe. The model box was made of Plexiglas with a dimension of 500×300×600 mm (length × width × height). The defective pipe was 50 mm in diameter with a square shape defect, and two circular holes with the same diameter as the defective pipe were drilled in the front and back wall of the model box. By inserting the defective pipe into the model box, the pipe can be rotated to various positions simulating the defective pipe with different defect positions. Three different types of sand were used in this experiment with a mean particle size d_p of 1.52 mm (coarse), 0.96 mm (medium), and 0.17 mm (fine). The particle size distribution and microscopic images of sand are shown in Figure 3.2, and detailed parameters of sand can be found in Table 3.1. The experimental program is listed in Table 4.1, and the defect size, defect position, sand particle size and water layer height were controlled in this study. From the studies by Davies et al. (2001), the soil loss cannot be neglected if the defect size is greater than 2 mm. On the other hand, the sand particle might be jammed with only water flow if the defect size is too small (Guo et al., 2013b), and typically the defect size can cause the jamming is about 1/6 of the particle size (Sheldon and Durian, 2010). Therefore, the defect sizes in this study are from 3 mm to 9 mm considering the particle size in this test.
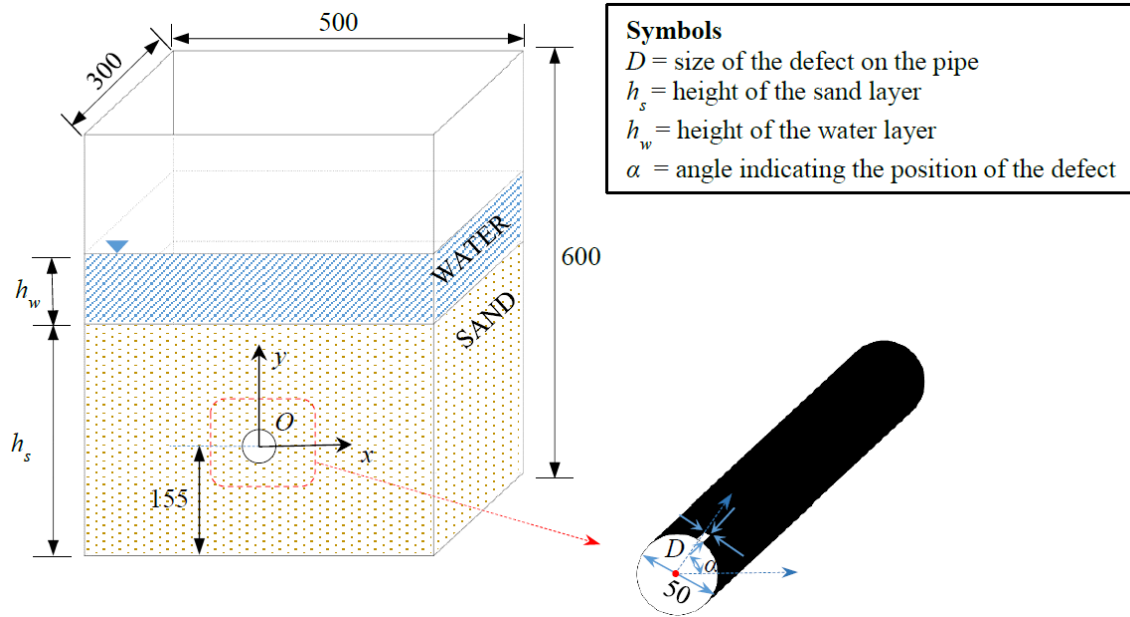
Figure 4.1 Schematic of experiment setup for the 3D condition (not to scale, unit: mm)

Table 4.1 Experimental program for the 3D condition

RUN #*	Sand Type	Orifice Position α (°)	Orifice Size D (mm)	Sand Height h_s (mm)	Water Height h_w (mm)
3D-1$_{T**}$, 3D-1$_{TS}$, 3D-1$_H$, 3D-1$_{BS}$, 3D-1$_B$	medium	90, 45, 0, -45, -90	9	150	50
3D-2$_T$, 3D-2$_{TS}$, 3D-2$_H$, 3D-2$_{BS}$, 3D-2$_B$	medium	90, 45, 0, -45, -90	9	150	100
3D-3$_T$, 3D-3$_{TS}$, 3D-3$_H$, 3D-3$_{BS}$, 3D-3$_B$	medium	90, 45, 0, -45, -90	6	150	50
3D-4$_T$, 3D-4$_{TS}$, 3D-4$_H$, 3D-4$_{BS}$, 3D-4$_B$	medium	90, 45, 0, -45, -90	6	150	100
3D-5$_T$, 3D-5$_{TS}$, 3D-5$_H$, 3D-5$_{BS}$, 3D-5$_B$	medium	90, 45, 0, -45, -90	3	150	50
3D-6$_T$, 3D-6$_{TS}$, 3D-6$_H$, 3D-6$_{BS}$, 3D-6$_B$	medium	90, 45, 0, -45, -90	3	150	100
3D-7$_T$, 3D-7$_{TS}$, 3D-7$_H$, 3D-7$_{BS}$, 3D-7$_B$	coarse	90, 45, 0, -45, -90	9	150	50
3D-8$_T$, 3D-8$_{TS}$, 3D-8$_H$, 3D-8$_{BS}$, 3D-8$_B$	coarse	90, 45, 0, -45, -90	9	150	100
3D-9$_T$, 3D-9$_{TS}$, 3D-9$_H$, 3D-9$_{BS}$, 3D-9$_B$	coarse	90, 45, 0, -45, -90	6	150	50
3D-10$_T$, 3D-10$_{TS}$, 3D-10$_H$, 3D-10$_{BS}$, 3D-10$_B$	coarse	90, 45, 0, -45, -90	6	150	100
3D-11$_T$, 3D-11$_{TS}$, 3D-11$_H$, 3D-11$_{BS}$, 3D-11$_B$	coarse	90, 45, 0, -45, -90	3	150	50
3D-12$_T$, 3D-12$_{TS}$, 3D-12$_H$, 3D-12$_{BS}$, 3D-12$_B$	coarse	90, 45, 0, -45, -90	3	150	100
3D-13$_T$, 3D-13$_{TS}$, 3D-13$_H$, 3D-13$_{BS}$, 3D-13$_B$	fine	90, 45, 0, -45, -90	9	150	50
3D-14$_T$, 3D-14$_{TS}$, 3D-14$_H$, 3D-14$_{BS}$, 3D-14$_B$	fine	90, 45, 0, -45, -90	9	150	100
3D-15$_T$, 3D-15$_{TS}$, 3D-15$_H$, 3D-15$_{BS}$, 3D-15$_B$	fine	90, 45, 0, -45, -90	6	150	50
3D-16$_T$, 3D-16$_{TS}$, 3D-16$_H$, 3D-16$_{BS}$, 3D-16$_B$	fine	90, 45, 0, -45, -90	6	150	100
3D-17$_T$, 3D-17$_{TS}$, 3D-17$_H$, 3D-17$_{BS}$, 3D-17$_B$	fine	90, 45, 0, -45, -90	3	150	50
3D-18$_T$, 3D-18$_{TS}$, 3D-18$_H$, 3D-18$_{BS}$, 3D18$_B$	fine	90, 45, 0, -45, -90	3	150	100

Note: * RUN # indicates the test number in this experiment; ** the subscript T indicates the opening is at top of the pipe ($\alpha = 90°$); TS indicates the opening is at top side of the pipe ($\alpha = 45°$); H is the horizontal defect on the pipe ($\alpha = 0°$); BS indicates the opening is at bottom side of the pipe ($\alpha = -45°$); B indicates the opening is at bottom of the pipe ($\alpha = -90°$);

For each test in this experiment, sand was placed layer by layer until reaching the desired height, and the porosity of the sand layer was controlled about 0.4. Dyed sand particles with the same size were added into the sand layer to increase the color difference for the visualization analysis. After that, the model was filled with water to the desired height. Sand erosion in this experiment would be started after opening the defect. The overall process of each test was recorded using a video camera (SONY HDR-PJ580E).

The particle image velocimetry (PIV) technique was used to investigate the sand mobilization during sand erosion, which was firstly developed in experimental fluid mechanics (Adrian, 1991) and then extended to the study of geomaterial (White et al., 2003). Because of the natural color difference, the motion of sand particles can be directly captured and calculated using PIV, while the color difference was increased by adding dyed sand in this experiment as mentioned above. Considering the requirements of image quality in PIV analysis, a DSLR camera (Canon EOS 50D) with a resolution of 1920×1080 pixels at 25 frames per second was used. After calibration, the images were analyzed using an open source *MATLAB*-based code *OpenPIV* (Taylor et al., 2010) to investigate the sand mobilization. During the experiment, sand and water flow rate can be measured using the beakers, and the corresponding measurement time was determined from the recorded video.

4.3   Results and Discussions

4.3.1   Observation of the sand erosion

Photos of the experiments under various conditions are shown in Figure 4.2. By rotating the model pipe, the defect at different positions was simulated. For the test with a defect at the top of pipe (α = 90°), sand particles started to move towards the defect at 3 seconds, and the mobilized sand particles were restricted in a narrow zone just above the defect. As the loss of sand particles, an erosion void in a triangular shape was formed from the sand layer surface at 15 seconds. The slope of the erosion void was about 39°, which was approximately consistent with the repose angle of sand. As the gradual loss of sand particles, erosion void was expanded. Finally, the erosion void would reach the defect. As shown in the photos from 3 to 70 seconds, the width of mobilized zone was suddenly increased just close to the defect while the width was not significantly changed above the defect during the erosion. If the defect was rotated to the top side (α = 45°) or horizontal position (α = 0°), there was no obvious difference in comparison with the condition with a defect at the top. The narrow mobilized zone was just above the defect while erosion void was formed towards defect. From the measurements based on the photos, the width of mobilized zone in the sand layer was not significantly changed.

As the defect changing to the bottom side position (α = -45°), the mobilized zone was not just above the defect. Sand particles close to the pipe was mobilized directly downwards, and the width of mobilized area was approximately equal to other tests as shown using the dash lines. On the other hand, sand particles at the left of pipe as pointed by the arrow were mobilized slowly towards the defect. Due to the longer flow path, sand particles at this zone were not rapidly mobilized. As the loss of sand particles, the formation of erosion void was similar with other

conditions, and erosion void was in a triangular shape with a slope angle equaling to sand repose angle. When the defect was at the bottom of the defective pipe (α = -90°), erosion process was different. The width of the mobilized zone above pipe was significantly increased due to the impeding effect of pipe on sand mobilization. Unlike the triangular erosion void, the erosion void was formed in the shape of a trapezoid, while the slope of erosion void was still close to sand repose angle.

From observations, the sand erosion process for different defect positions can be generalized within a similar scheme. Sand particles above the defect are firstly mobilized, and an erosion void is formed from the sand layer surface. As the loss of sand particles, the erosion void is expanded. Finally, the erosion void reaches the defect. During the erosion process, the width of mobilized zone is not apparently changed, and only the height of mobilized zone is decreased. Except defect is at the bottom of pipe, erosion void is expanded in a shape of triangular, and the slope of erosion void is always close to sand repose angle. The pipe hinders the sand mobilization if the defect is at the bottom of the pipe, and the width of mobilized zone is significantly increased at this condition.
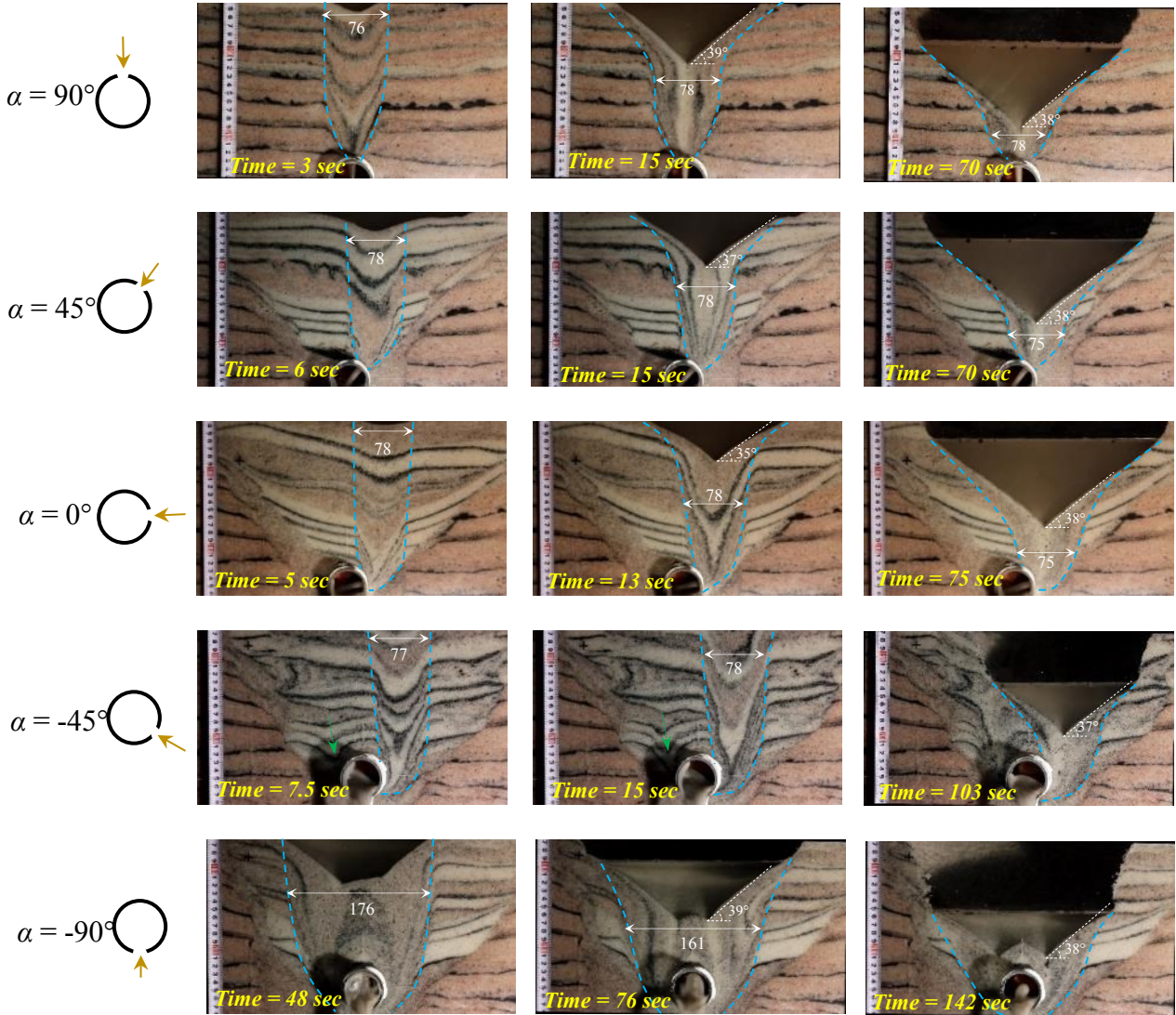
Figure 4.2 Photos of sand erosion around the defective pipe with different defect positions (Run 3D-1$_T$, 3D-1$_{TS}$, 3D-1$_H$, 3D-1$_{BS}$, 3D-1$_B$; dash lines are sketching the slip surface in sand layer; unit: mm)

4.3.2 Variation of sand and water flow rate during sand erosion

The change of sand and water flow rate with time during erosion process for various conditions are plotted in Figure 4.3. It can be found sand flow rate is always less than water flow rate during the erosion process, while the sand and water flow rate keeps a steady relationship with a slight decrease after the initiation of erosion. After a transitional point, sand flow rate suddenly decreases

and finally reaches zero, while water flow rate is significantly increased and then gradually decreased. This trend of flow rate change with time is consistent with the experimental results by Guo et al. (2013a). From the video of experiments, the transitional time is the time when erosion void reaches the defect. Afterward, only pure water is discharged through the defect without sand erosion, which leads to the significant increase in water flow rate and a decrease of sand flow rate. In the steady erosion stage, water flow rate is slightly decreased due to the decrease in water level. Since sand particles are washed out by the water flow, the sand flow rate will inevitably be reduced as the decrease of water flow rate.
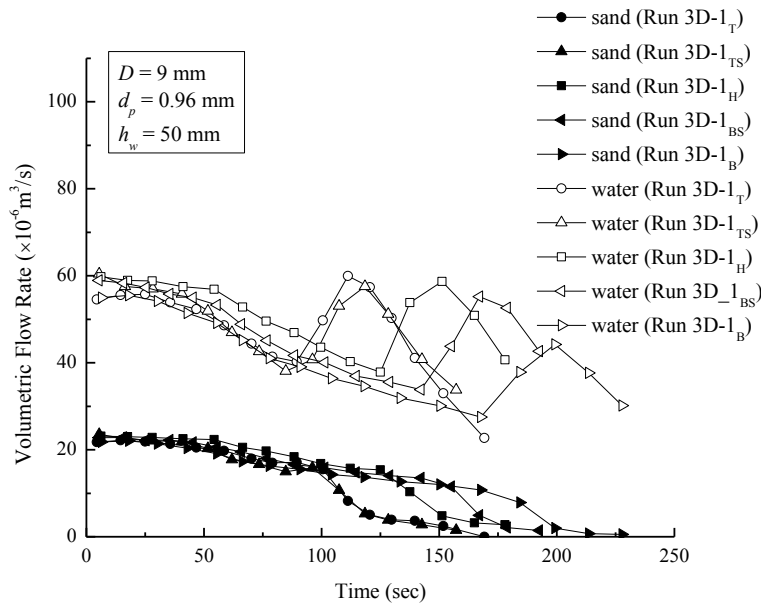
(a)
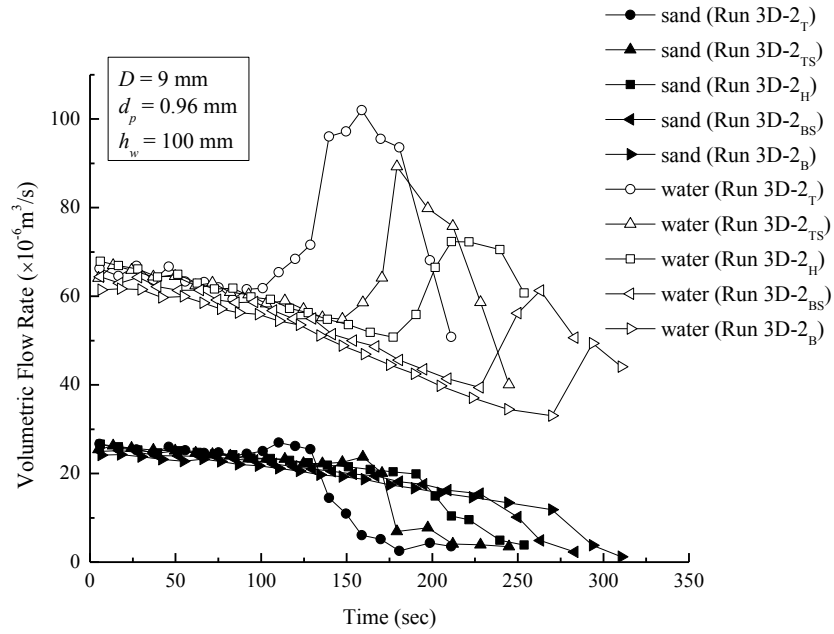
(b)
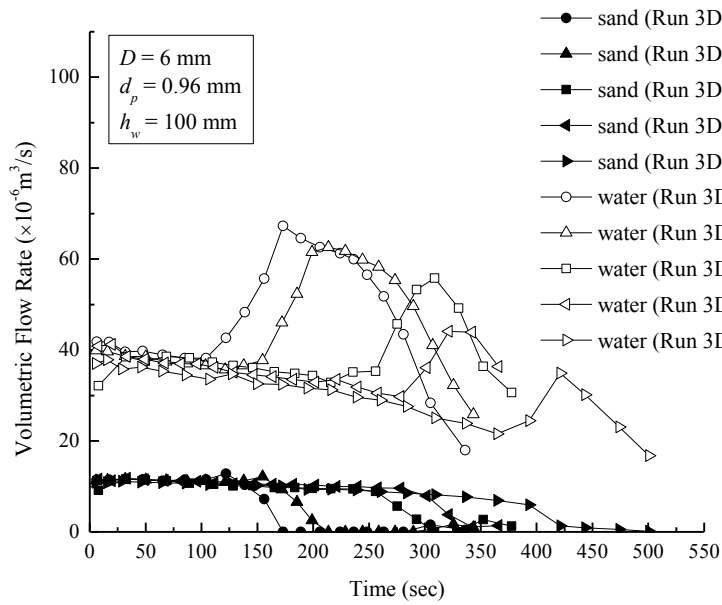
(c)
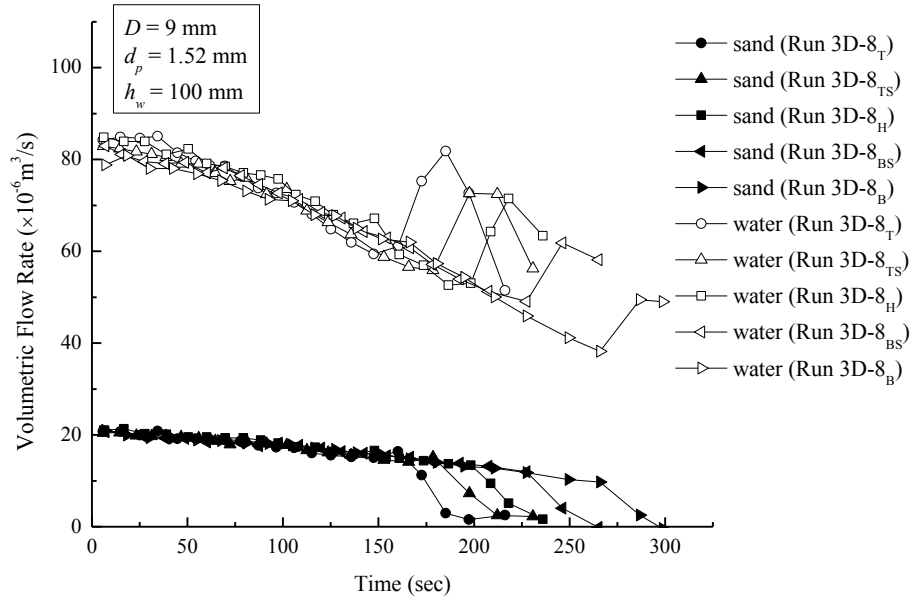
(d)

Figure 4.3 Variation of sand and water flow rate with time during the sand erosion

In Figure 4.3, there is no significant effect of defect position on the flow rate. On the other hand, the duration of erosion process is increased as the defect is rotated from top to bottom on the pipe. In Figure 4.3(a), the sand erosion is stopped at about 150 seconds when the defect is at the top of the pipe ($\alpha = 90°$) while it is extended to 200 seconds when the defect is at the bottom ($\alpha = -90°$).

The effect of water layer height on the flow rate is shown in Figure 4.3(a) and 4.3(b). As the water layer height h_w is increased from 50 mm to 100 mm, the initial water flow rate is increased from less than 60 ml/s (1 ml = 10^{-6} m^3) to 70 ml/s when the defect is at the top of the pipe. The sand flow rate is increased about from about 22 ml/s to 26 ml/s. Although both sand and water flow rates are increased as the increase of water layer height, the ratio between sand flow rate Q_s and water flow rate Q_w keeps almost the same which is about 0.37. Therefore, the change of water layer height will not affect the ratio between sand and water flow rate in the erosion.

Comparing Figure 4.3(b) with 4.3(c), both sand and water flow rates will be decreased as the decrease of defect size. For the dry granular flow, it has been proved the granular flow rate is proportional to $D^{2.5}$ (Beverloo et al., 1961). In this experiment, the sand flow rate is decreased from 26 ml/s to 10 ml/s as the defect size is decreased from 9 mm to 6 mm, which is approximately proportional to $D^{2.5}$. Unlike the effect of water layer height, the ratio between Q_s and Q_w is decreased as the decrease of orifice size. Sand particles are easy to be jammed as the decrease of defect size due to the arching effect. The mobilization of sand particles around the defect will be resisted resulting in the lower sand volume fraction in the outflow mixture.

As the increase of sand particle size d_p from 0.96 mm to 1.52 mm, the water flow rate will be increased from 65 ml/s to 85 ml/s as shown in Figure 4.3(b) and 4.3(d). If the water flow is assumed to follow Darcy's law, the permeability of sand layer is significantly increased as the increase of particle size (Lambe and Whitman, 1969). On the other hand, the sand flow rate is decreased from 26 ml/s to 20 ml/s as the increase of sand particle size, which is due to the resistance by the arch formation close to the defect. Therefore, the increase of sand particle size can increase the water flow and assist the sand erosion. On the other hand, the sand erosion is resisted by the arching effect due to larger particles.

From above analysis, the sand erosion is affected by water layer height, defect size and particle size, and it can be found the ratio Q_s/Q_w is not significantly affected by the water layer height. Therefore, the sand flow rate and water flow rate for various D and d_p are plotted in Figure 4.4. Similar to studies by Guo et al. (2013a), Q_s is linearly dependent on Q_w for different D and d_p. The tests with different water layer heights and defect positions are plotted in the same figure. As D/d_p increases from 3.1 to 53.6, the flow rate ratio Q_s/Q_w is increased from 0.20 to 0.63. In another word, for the larger D/d_p, sand particles will be eroded at a higher flow rate for the same water

flow rate. This finding is consistent with the experimental results by Papazoglou and Pyle (1970) on the air assisted granular flow, and the ratio between sand and water flow rate is increased as the increase of orifice size while it is increased as the decrease of granular particle size. The experimental results of solid-liquid mixture flow by Lamptey and Thorpe (1991) also indicates the ratio between sand and water flow rate is increased as the increase of orifice size, and the effect was explained by the 'displacement thickness' theory (Beverloo, 1961). As the increase of orifice size, the effect of displacement thickness close to the orifice is reduced while the effect on fluid outflow is not changed. Based on these experimental results, the fitting relationship between D/d_p and Q_s/Q_w can be obtained as shown in Figure 4.5 using following Eq. (4.1):

$$\frac{Q_s}{Q_w} = 0.18 \ln\left(\frac{D}{d_p}\right) \tag{4.1}$$

This equation is valid for the two-dimensional condition as shown in Figure 4.5 in comparison with the 2D experiment results, and the experiment results by Guo et al. (2013a) are plotted in Figure 4.5 as well. Eq. (4.1) provides an approach to estimate the sand flow rate if the water flow rate can be determined.

(a) $D/d_p = 3.1$

(b) $D/d_p = 5.9$

$Q_s = 0.30Q_w$
$R^2 = 0.99$
$D = 6$ mm
$d_p = 0.96$ mm

- ■ Run 3D-3$_T$
- □ Run 3D-4$_T$
- ● Run 3D-3$_{TS}$
- ○ Run 3D-4$_{TS}$
- ▲ Run 3D-3$_H$
- △ Run 3D-4$_H$
- ◀ Run 3D-3$_{BS}$
- ◁ Run 3D-4$_{BS}$
- ▶ Run 3D-3$_B$
- ▷ Run 3D-4$_B$

(c) $D/d_p = 6.2$

$Q_s = 0.39Q_w$
$R^2 = 0.99$
$D = 9$ mm
$d_p = 0.96$ mm

- ■ Run 3D-1$_T$
- □ Run 3D-2$_T$
- ▲ Run 3D-1$_{TS}$
- △ Run 3D-2$_{TS}$
- ● Run 3D-1$_H$
- ○ Run 3D-2$_H$
- ◆ Run 3D-1$_{BS}$
- ◇ Run 3D-2$_{BS}$
- ▼ Run 3D-1$_B$
- ▽ Run 3D-2$_B$

(d) $D/d_p = 9.3$

(e) $D/d_p = 17.8$

(f) $D/d_p = 35.7$

(g) $D/d_p = 53.6$
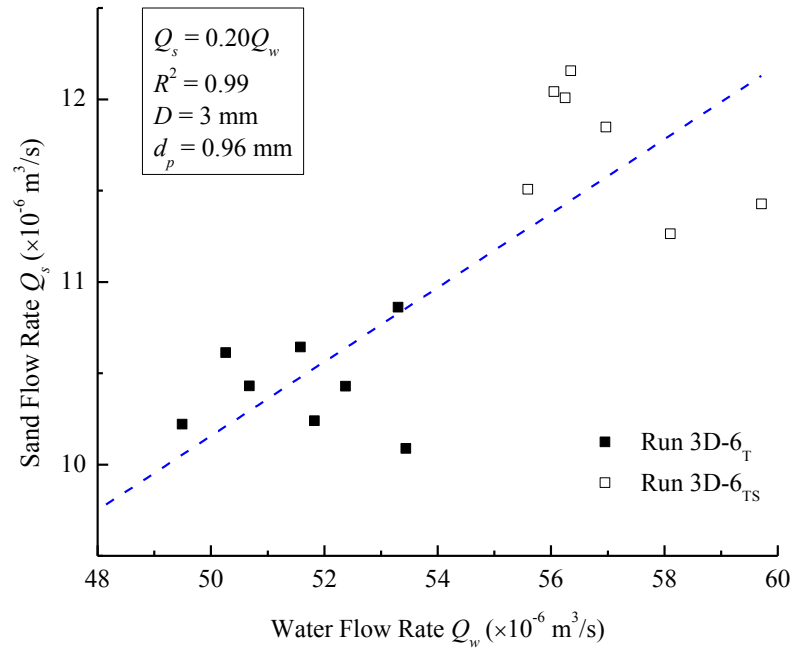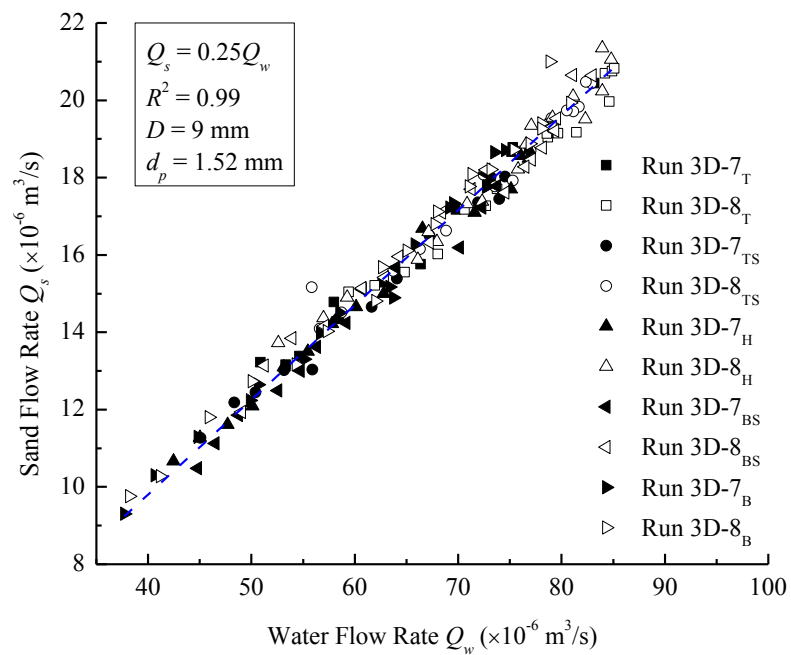
Figure 4.4 Relationship between Q_s and Q_w for various conditions: (a) $D/d_p = 3.1$; (b) $D/d_p = 5.9$;
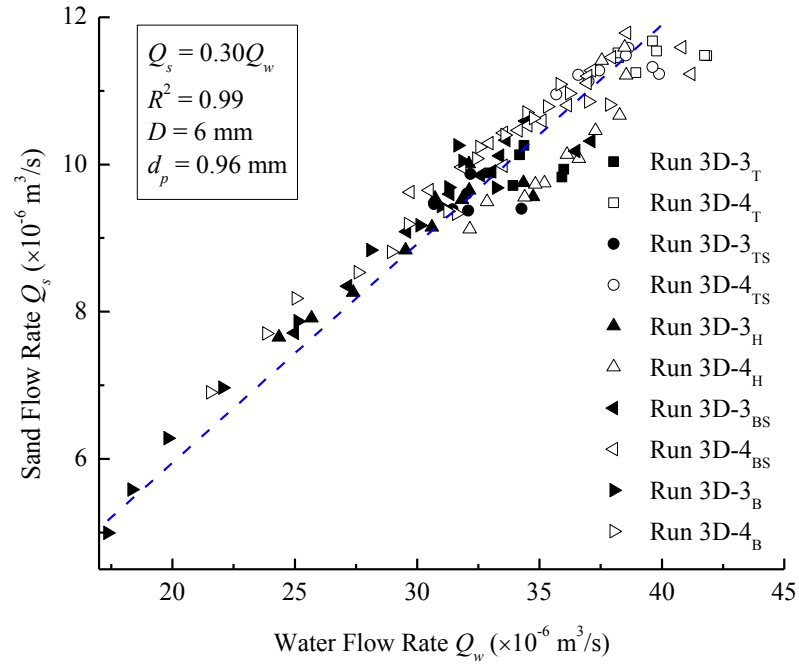
(c) $D/d_p = 6.2$; (d) $D/d_p = 9.3$; (e) $D/d_p = 17.8$; (f) $D/d_p = 35.7$; (g) $D/d_p = 53.6$;
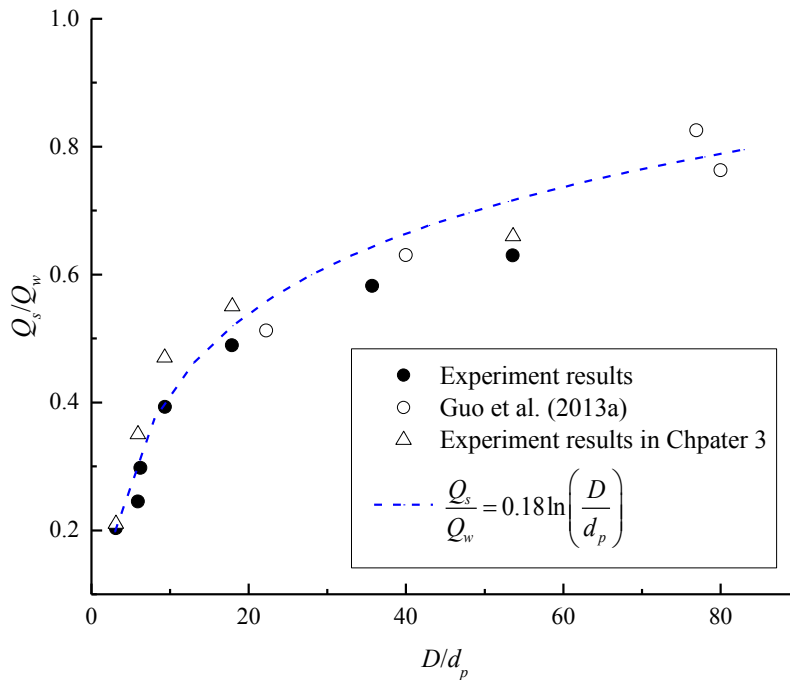
Figure 4.5 Relationship between Q_s/Q_w and D/d_p

4.3.3 Formation of the erosion void

The erosion void shapes are mapped in Figure 4.6 for different defect positions. When the defect is at the top of pipe as shown in Figure 4.6(a), the erosion void is formed at 5.5 seconds. After that, the erosion void is gradually expanded as observed in Figure 4.2. At approximately 100 seconds, the erosion void reaches the defect. During the expansion of erosion void, the slope of erosion voids at the various time are almost the same, which is equal to the sand repose angle 36-37°. When the defect is changed to the top side position ($\alpha = 45°$) in Figure 4.6(b), the formation and expansion of erosion void are similar with that in Figure 4.6(a). The only difference is the erosion void is shifted while it is still directly towards the defect. When the defect is at the horizontal position ($\alpha = 0°$) in Figure 4.6(c), the erosion void is similarly expanded in a triangular shape towards the defect. At 190 seconds in Figure 4.6(c), one side of erosion void reaches the defect while the other side reaches the top of the pipe. As the defect is changed to the bottom side position ($\alpha = -45°$) in Figure 4.6(d), the erosion void is expanded while the erosion void is not always towards the defect. As shown by the arrow in Figure 4.6(d), the lowest point of erosion void starts to be away from the pipe at 17 seconds. Since the motion of sand particles are hindered by the pipe towards the defect, the lowest point of erosion void is moved closer to the defect as the expansion of erosion void. When the defect is at the bottom of the pipe ($\alpha = -90°$) in Figure 4.6(e), the shape of erosion void is more like a trapezoid. Initially, the erosion void is formed with a flat bottom at 30 seconds while the bottom is bulged up since erosion void is close to the pipe at 135 seconds. In the erosion process, the slope of erosion void is still approximately equal to sand repose angle while the bottom zone of erosion void is restricted just above the pipe as shown in Figure 4.6(e).
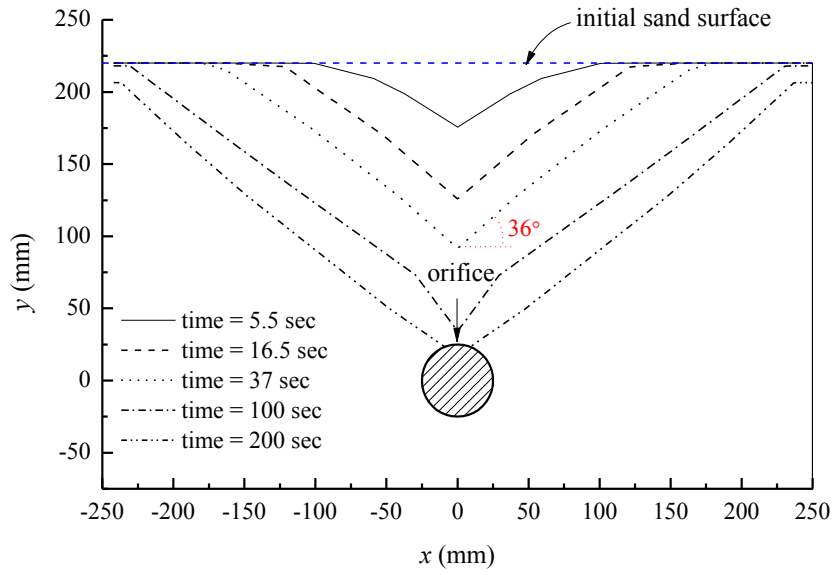
(a) Run 3D-2$_T$ ($\alpha = 90°$)
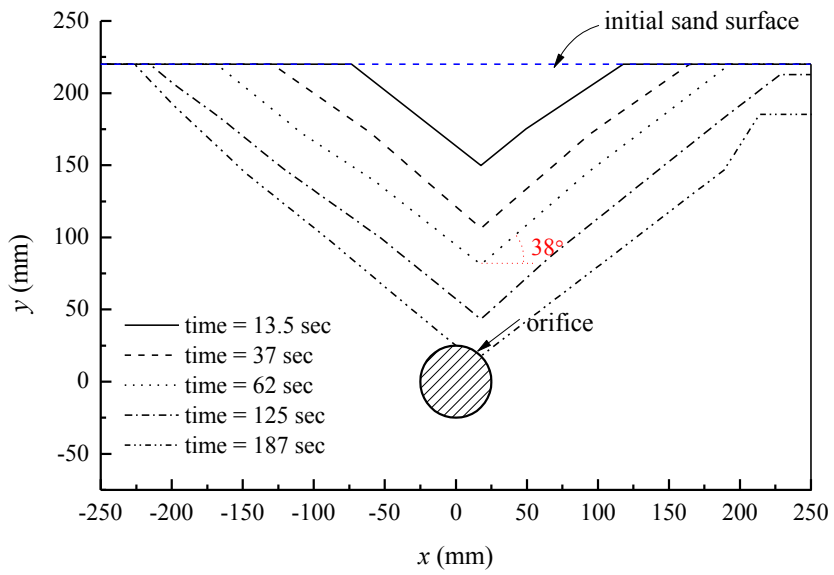
(b) Run 3D-2$_{TS}$ ($\alpha = 45°$)
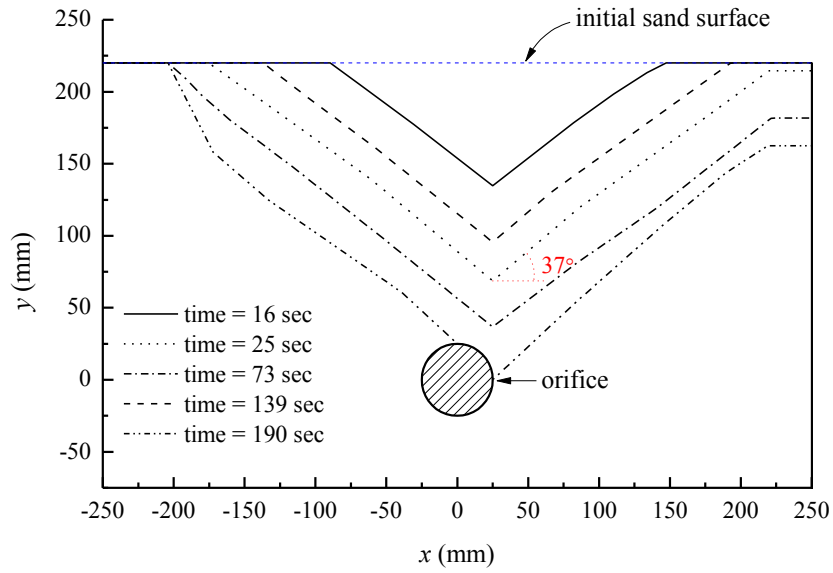
(c) Run 3D-2$_H$ ($\alpha = 0°$)
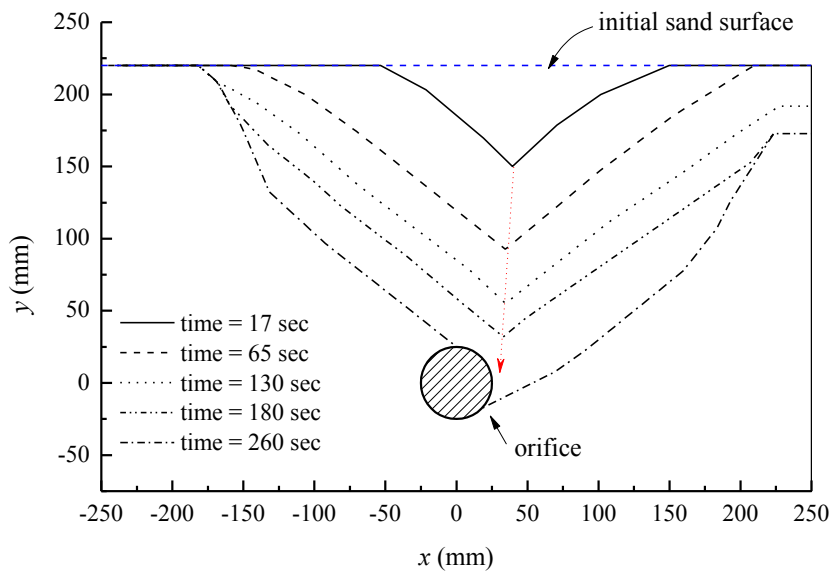
(d) Run 3D-2$_{BS}$ ($\alpha = -45°$)
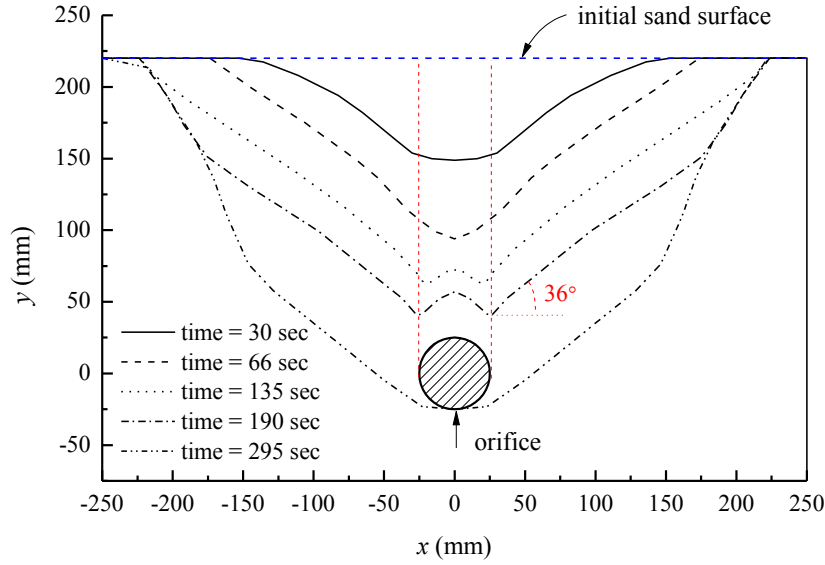
(e) Run 3D-2$_B$ (α = -90°)

Figure 4.6 Development of the erosion void at different time in 3D condition: (a) Run 3D-2$_T$ (α = 90°); (b) Run 3D-2$_{TS}$ (α = 45°); (c) Run 3D-2$_H$ (α = 0°); (d) Run 3D-2$_{BS}$ (α = -45°); (e) Run 3D-2$_B$ (α = -90°)

From Figure 4.6, the erosion void can be assumed to be a triangular shape on the cross section or to be a trapezoidal shape if the defect is at the bottom of the pipe. These experimental results are consistent with the studies by Fathi-Moghadam et al. (2010) and Guo et al. (2013a), while the slope angle of erosion void in the erosion keeps constant and is close to the sand repose angle. Theoretically, this can be proved by Coulomb's theory (Rao and Nott, 2008). Because of the symmetry and effect of pipe on the erosion void formation, the erosion void in three-dimensional can be assumed to be a cone or a truncated cone as shown in Figure 4.7(a) depending on the defect position. Therefore, the outflow sand volume V_s^{out} can be determined using the erosion void height h_{void} based on the geometric relationship:

$$\text{Cone shape erosion void: } V_s^{out} = \frac{\pi}{6} \frac{h_{void}^3}{\tan^2 \varphi}(1-n) \qquad (4.2)$$

90

Truncated cone shape erosion void: $V_s^{out} = \dfrac{\pi}{6}\left[\left(\dfrac{h_{void}}{\tan\varphi}+r_{pipe}\right)^2 + \left(\dfrac{h_{void}}{\tan\varphi}+r_{pipe}\right)r_{pipe}+r_{pipe}^2\right](1-n)$

$$(4.3)$$

where n is the porosity of sand layer; φ is the sand repose angle; r_{pipe} is the radius of pipe.

In this experiment, the outflow sand volume V_s^{out} can be calculated based the measured sand flow rate while the corresponding erosion void height h_{void} can be determined from the experiment videos. By comparing the experimental measurements with the estimated outflow sand volume from Eqs. (4.2) or (4.3), the assumption of cone shape erosion void is reasonable except for Run 3D-2B with a bottom defect, which is close to the truncated cone shape assumption. Although the difference between the cone and truncated cone shape assumption is not significant in Figure 4.7(b), this is due to the small pipe size in this experiment. Therefore, the size of erosion void can be predicted after determining the outflow sand volume.

Cone shape erosion void   **Truncated cone shape erosion void**
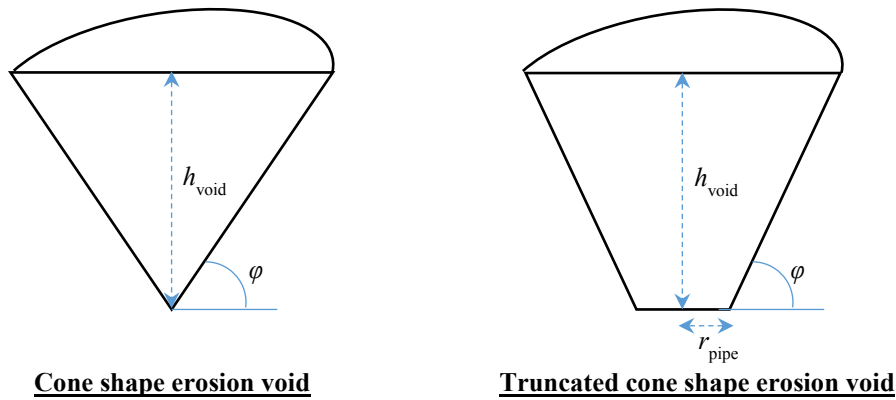
(a) Schematic of the erosion void shape assumptions
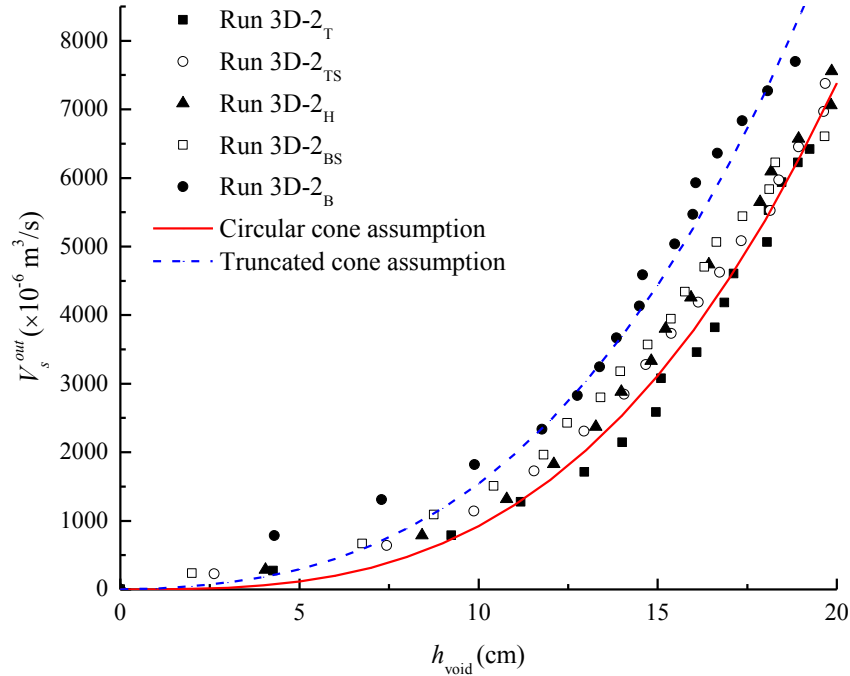
(b) Experiment results of the erosion void shapes comparing with predictions

Figure 4.7 Erosion void shape in 3D condition

4.3.4 Sand velocity distribution

The sand velocity is measured using PIV technique. Sand velocities in y-direction at various elevations are plotted in Figure 4.8, and the boundary between mobilized and static zone in the sand layer is determined. The sand velocity close to the defect is approximately 0.04 m/s in Figure 4.8(a) when the defect is at the top of the pipe ($\alpha = 90°$), and sand velocity is decreased from the defect to sand surface. The width of sand layer is significantly increased from 0.009 m to about 0.05 m at 0.025 m above the defect. On the other hand, the width of mobilized zone is slightly increased when $y > 0.05$ m, which accounts for the small decrease of corresponding sand velocity based on mass conservation.

When the defect is at the top side of the pipe ($\alpha = 45°$) in Figure 4.8(b), the sand velocity is also decreased from the defect to the sand surface while the width of mobilized zone is increased.

In comparison with the sand velocity distribution in Figure 4.8(a), the sand velocity at the same elevation is decreased while the width of mobilized zone is increased. The maximum sand velocity is approximately 0.02 m/s at $y = 0.075$ m in Figure 4.8(b) while it is 0.03 m/s in Figure 4.8(a), and the width of mobilized zone is decreased from 0.10 m ($\alpha = 90°$) to 0.08 m ($\alpha = 45°$).

The sand velocity in y-direction continues to decrease as the defect is changed to the horizontal position ($\alpha = 0°$) as shown in Figure 4.8(c). As the defect on the pipe is changed from the top to horizontal, the mobilization of sand particles is shifted. Sand particles are always tended to move through the defect in the erosion, which can account for the decrease in sand velocity in y-direction from Figure 4.8(a) to 4.8(c).

As the defect changing to the bottom side position ($\alpha = -45°$) in Figure 4.8(d), the sand velocity in y-direction is significantly decreased in comparison with results of first three conditions, while the width of mobilized zone is slightly decreased. The mobilization of sand particles is hindered by the pipe which will reduce the width of mobilized zone, while sand particles at the left side of pipe are also mobilized as shown in Figure 4.2.

As the defect rotating to the bottom position ($\alpha = -90°$) in Figure 4.8(e), the mobilized zone is significantly expanded while sand velocity is decreased. Due to the impeding effect of pipe on sand mobilization, the sand velocity directly above the pipe is relatively small especially close to the pipe ($y = 0.05$ m).
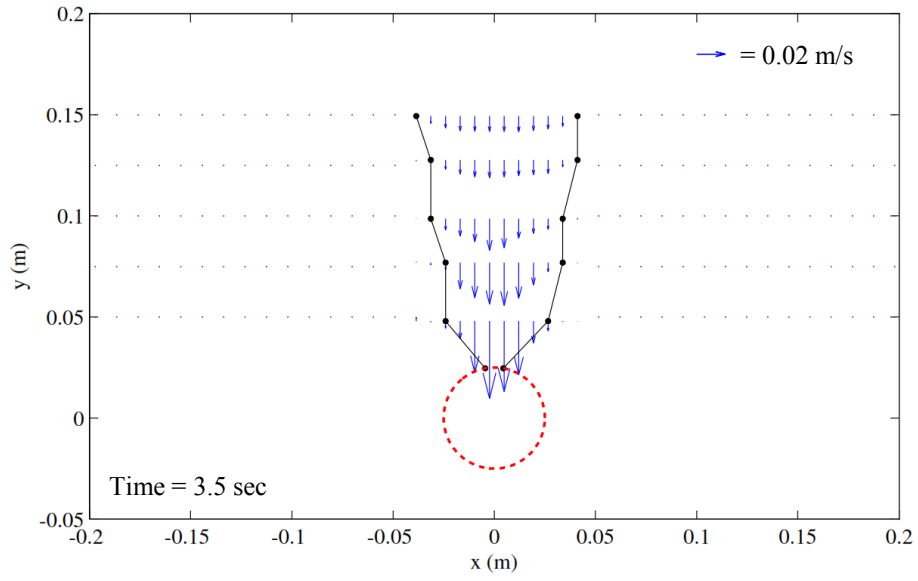
(a) Run 3D-2$_T$
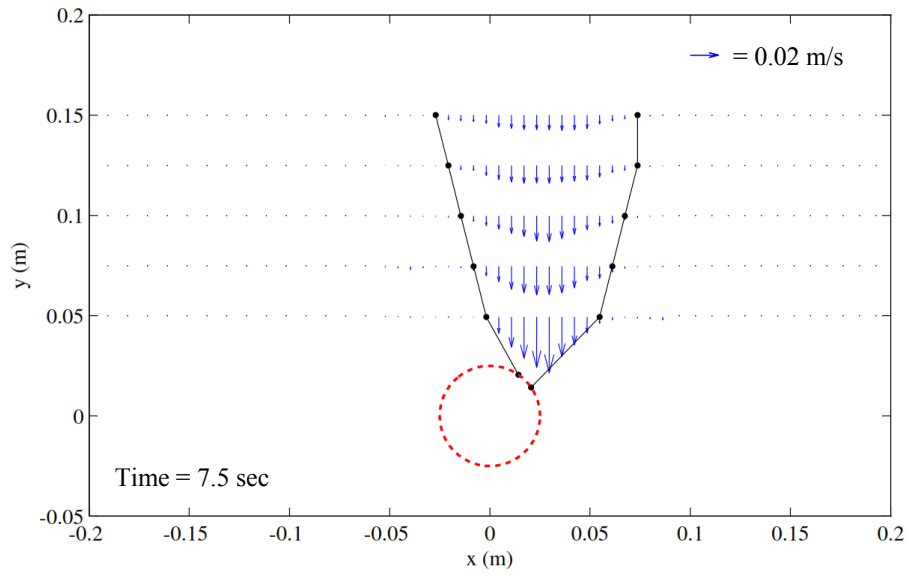
(b) Run 3D-2$_{TS}$
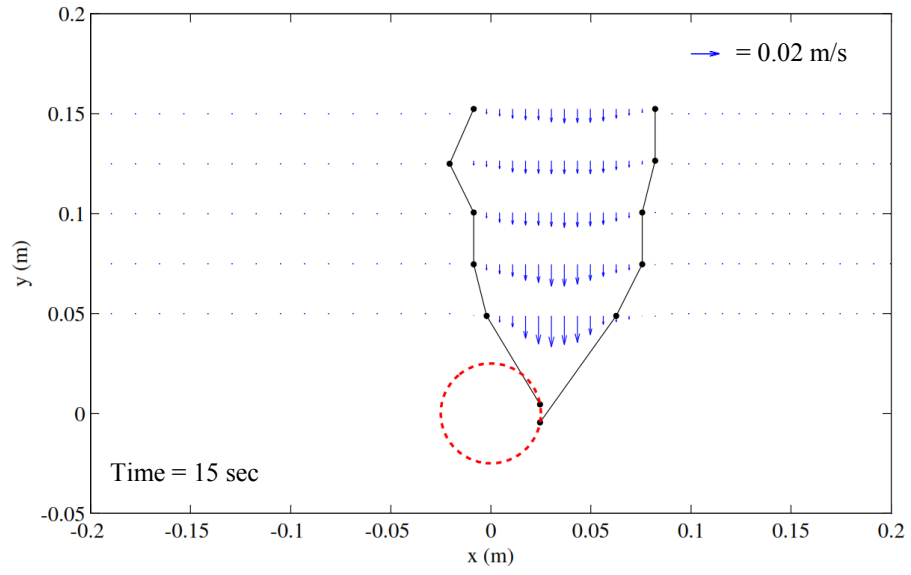
(c) Run 3D-2$_H$

(d) Run 3D-2$_{BS}$

95
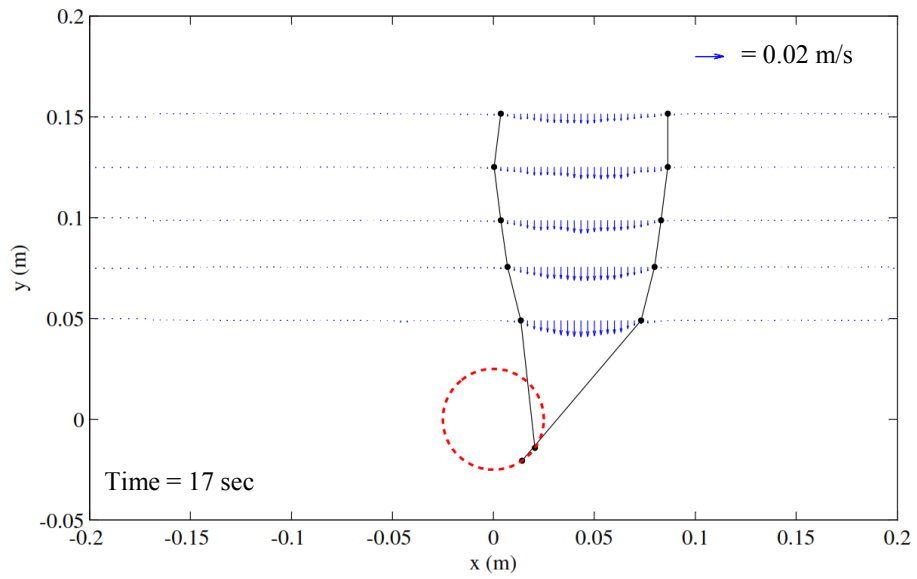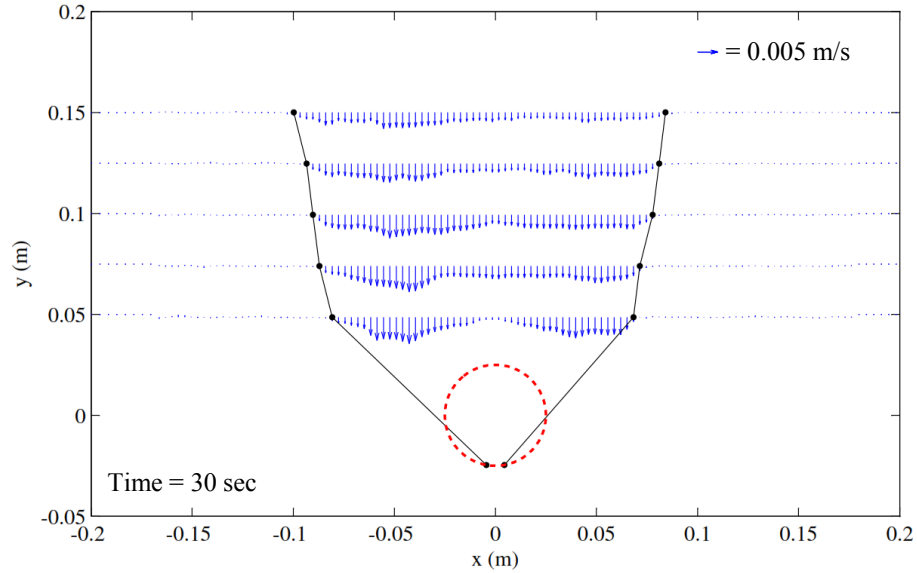
(e) Run 3D-2$_\mathrm{B}$

Figure 4.8 Sand velocity distributions in y-direction for various conditions (black dots are the boundary between mobilized and static zone)

From the sand velocity distribution for various defect positions, the downward sand velocity is always decreased as the defect is changed from the top to bottom on the pipe. The mobilization of sand particles in the erosion is always towards the defect. As the defect changing from the top to horizontal position, the width of mobilized zone in the sand layer is slightly increased. From the flow rates in the erosion under various conditions in Figure 4.3, it has been found the defect position has little effect on the sand flow rate. The horizontal component of sand velocity is increased as the defect is changed from the top to horizontal, which results in a wider mobilized zone. If the defect is at the bottom part of the pipe, the impeding effect of pipe on sand mobilization needs to be taken into account. The mobilized zone is the largest when the defect is at the bottom of pipe (α = -90°) since a static zone is formed above the pipe.

Figure 4.9 shows the boundary between mobilized and static zone in the erosion, and the sand velocity at the centerline of the defect is plotted in Figure 4.10. It can be found the boundary

between mobilized and static zone keeps consistent during the erosion process in Figure 4.9(a) from 2 seconds to 42 seconds. Although the erosion void is gradually expanded as shown in Figure 4.6, the boundary between mobilized and static zone in the sand layer is not changed. The width of mobilized zone is significantly increased from the defect to $y = 0.06$ m while the width is only slightly increased at $y > 0.06$ m. From the qualitative observations (Nedderman and Tüzün, 1979), this change of mobilized zone is the transition from 'converging flow' to 'plug flow'. From sand velocity distribution at the centerline in Figure 4.10(a), the velocity is decreased from the position close to the defect to the sand surface. Another fact is that the sand velocity is significantly changed at $y < 0.06$ m while it is slightly varied at $y > 0.06$ m, which is consistent with the change of mobilized zone width.
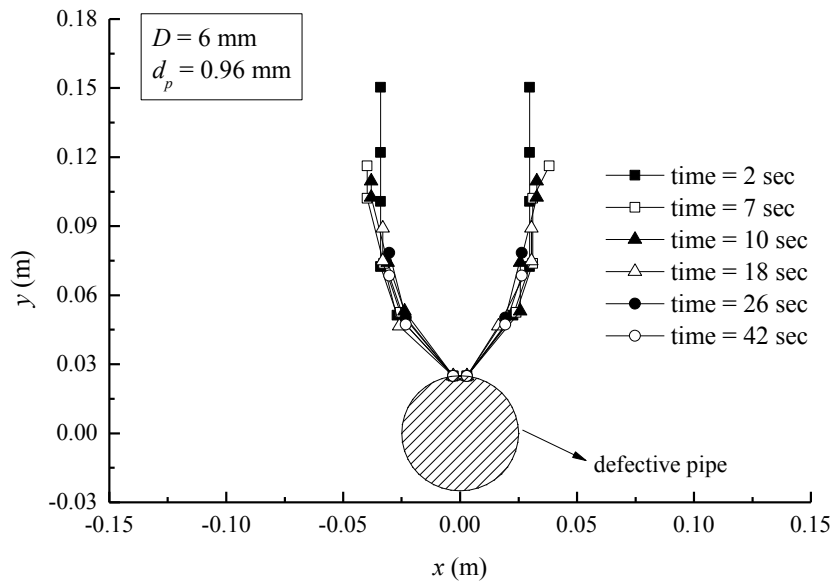
(a) Run 3D-3$_T$
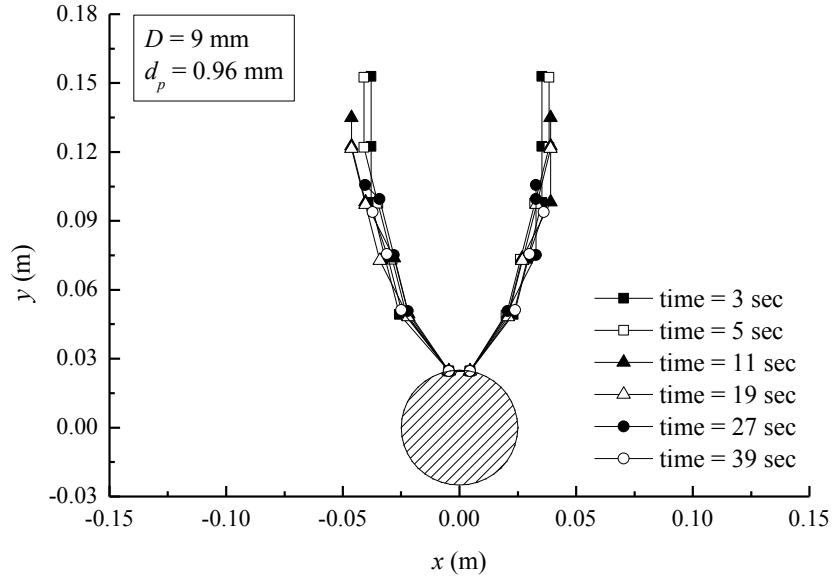
(b) Run 3D-1$_T$
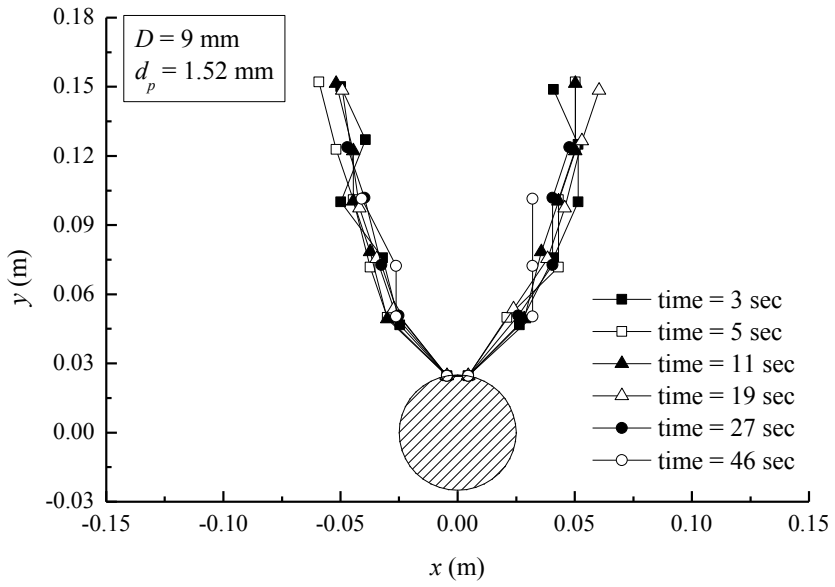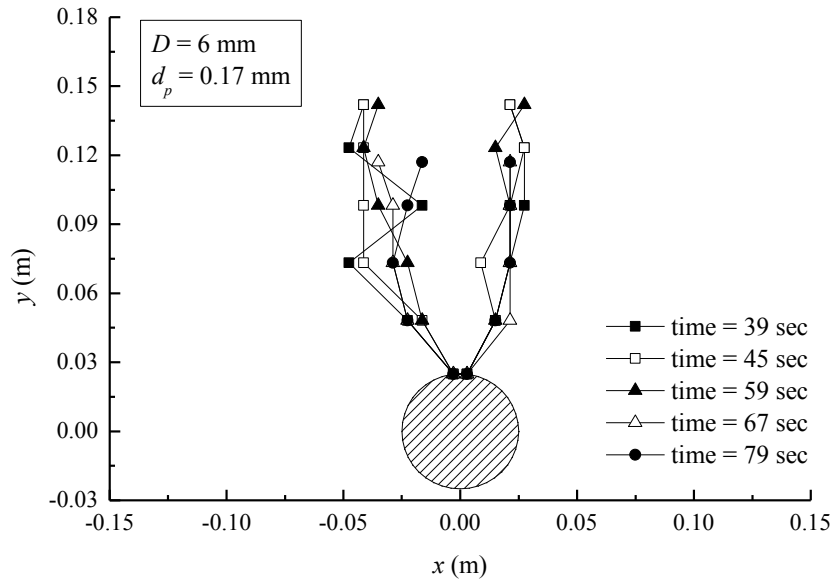
(c) Run 3D-7$_T$

(d) Run 3D-15$_T$

Figure 4.9 Change of the boundary between mobilized and static zone in sand layer
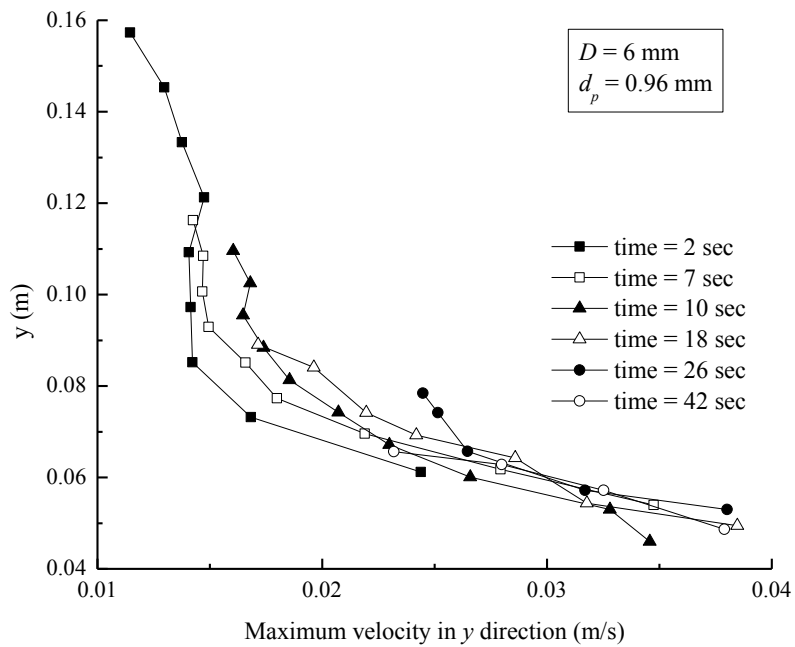
(a) Run 3D-3$_T$
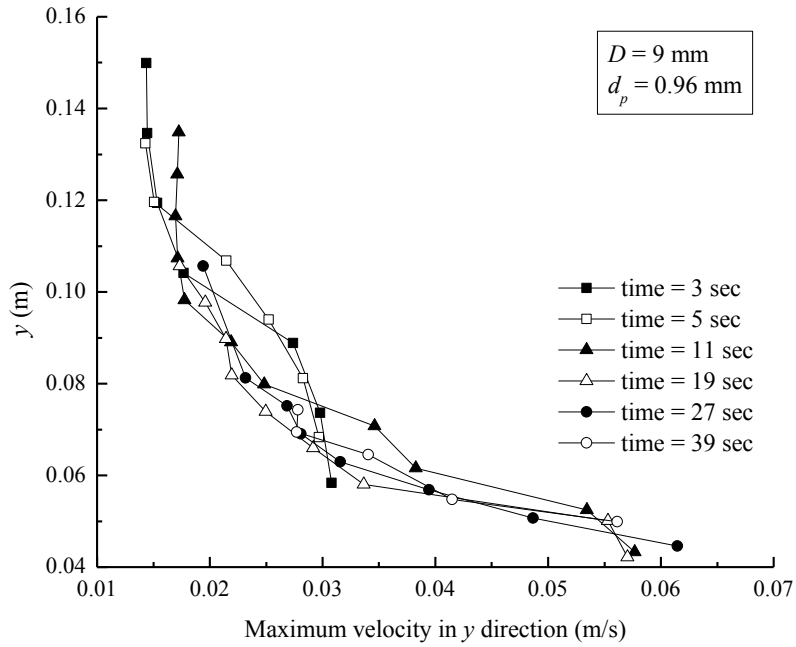
(b) Run 3D-1$_T$
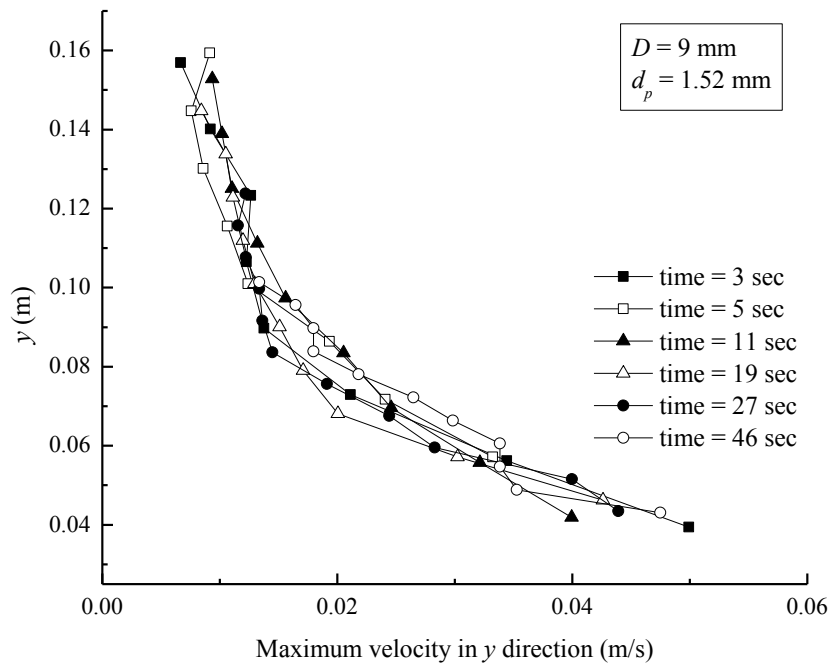
(c) Run 3D-7$_T$
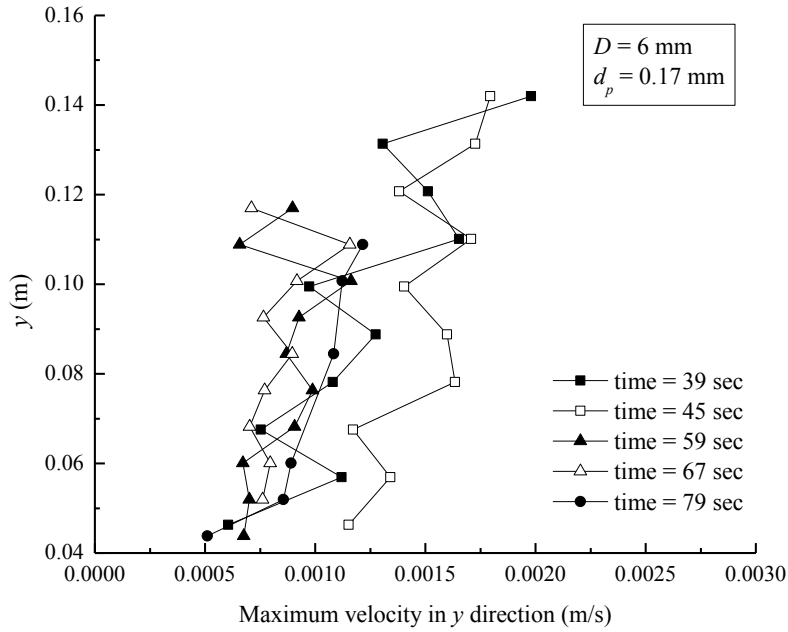
(d) Run 3D-15$_T$

Figure 4.10 Change of the sand velocity at the center line

As the increase of defect size from 6 mm to 9 mm in Figure 4.9(b), the boundary between mobilized and static zone still keeps consistent in the erosion while the width is slightly increased in comparison with Figure 4.9(a). The sand velocity at centerline is increased from 0.01 m/s-0.04 m/s in Figure 4.10(a) to 0.015 m/s-0.06 m/s in Figure 4.10(b). For the dry granular flow, it has been proved that the granular flow rate is proportional to $D^{2.5}$. Nevertheless, the sand velocity at $y > 0.8$ m is approximately 0.015 m/s which is almost the same with the sand velocity in Figure 4.9(a). Based on the free-fall arch theory (Hilton and Cleary, 2011), the granular flow rate is dominantly affected by the granular flow below the free-fall arch.

As the increase of sand particle size from 0.96 mm to 1.52 mm in Figure 4.9(c), the width of mobilized zone is significantly increased, while the sand velocity at the centerline is slightly decreased from 0.015-0.06 m/s to 0.01-0.05 m/s as shown in Figure 4.10(c). For the dry granular flow, the granular flow rate is decreased as the increase of particle size due to the increase of resistance adjacent to the defect by the arching effect. In this experiment, sand particles are

mobilized by water flow while the drag force is proportional to the relative velocity between the water and sand phase. Water velocity will significantly increase as the increase in particle size. Therefore, the increase of sand particle size can cause two different effects on the sand erosion.

The mobilized zone and sand velocity at the centerline using fine sand ($d_p = 0.17$ mm) are shown in Figure 4.9(d) and 4.10(d). It can be found the width of mobilized zone is decreased as the decrease of sand particle size while the boundary fluctuates. Sand velocity distribution at the centerline is fluctuated as shown in Figure 4.10(d), while the velocity is approximately 0.0005-0.0015 m/s and much smaller than the sand velocity using coarse or medium sand. Considering the measuring error based on image analysis, the small sand velocity in this condition is easy to be affected causing the fluctuation. However, the measured mobilized zone and magnitude of sand velocity indicate the reasonable trend as the decrease of sand particle size.

The boundaries between the mobilized and static zone are summarized in Figure 4.11 for various defect sizes and sand particle sizes. As expected, the width of mobilized zone will be increased as the increase of defect size. The experimental results also indicate that the mobilized zone will be significantly expanded as the increase of sand particle size. The experimental studies by Tüzün and Nedderman (1979) indicated that the width of mobilized zone during granular flow was proportional to the granular particle size, which is consistent with results of this study.
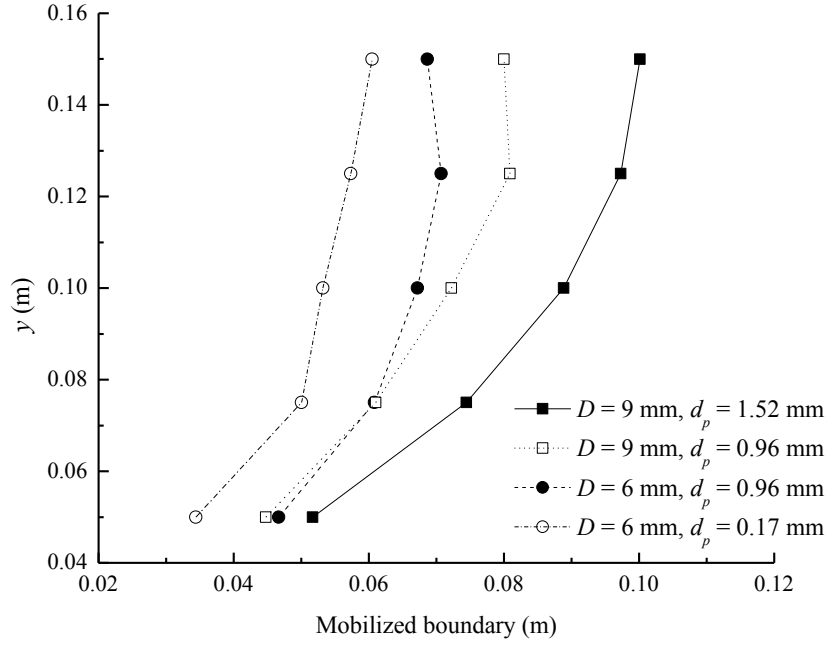
Figure 4.11 Comparison of the boundary between mobilized and static zone in sand layer with different particles sizes and opening sizes

A kinematic model was developed to estimate the velocity distribution of granular flow (Nedderman and Tüzün, 1979; Tüzün and Nedderman, 1979; Tüzün et al., 1982). By assuming the horizontal velocity is linearly proportional to the gradient of vertical velocity, the continuity equation can be simplified, and an approximated solution was provided for the granular flow in a bin. For the axisymmetric situation, the analytical solution is (Nedderman and Tüzün, 1979):

$$v = V_p + \sum_{n=1}^{\infty} \frac{2WV_p}{n\pi D} \exp\left(-4n^2\pi^2 By / W^2\right) \sin\left(n\pi D / W\right) \cos\left(2n\pi x / W\right) \tag{4.4}$$

where V_p is the sand velocity at great heights and can be estimated using the sand flow rate: $V_p = Q_s/D^2$; W is the width of bin; B is the kinetic constant with a dimension of length and dependent on the nature of material, which is defined from the simplified relationship: $u = -B\dfrac{\partial v}{\partial x}$ and u is the horizontal component of granular velocity. From the experimental studies (Tüzün and

Nedderman, 1979), B is proportional to the granular particle size d_p and suggested to be $2.3d_p$, while it will be larger for the axisymmetric flow and $2.8d_p$ is used in this study.

Sand velocity distribution can be calculated using the measured sand flow rate and Eq. (4.4), which is compared with the measurements as shown in Figure 4.12. The analytical results are consistent with the experimental results. Therefore, the sand velocity distribution during erosion process can be calculated once the sand flow rate through the defect is determined. Figure 4.13 shows the comparison of analytical results with the sand velocity measurements for $y/D = 10$. In Figure 4.13, the distance x is normalized with the width b (defined as the distance where the velocity is half of the maximum velocity), and the velocity v is normalized with the maximum velocity v_{max}. The measurements and calculations are approximately consistent, while the measured mobilized width is slightly narrower than the calculated width. In the erosion, the mobilization of sand particles cannot always keep steady in the erosion as assumed in the analytical model. Therefore, the predicted mobilized zone using the analytical solution will be slightly wider than that in the actual erosion.
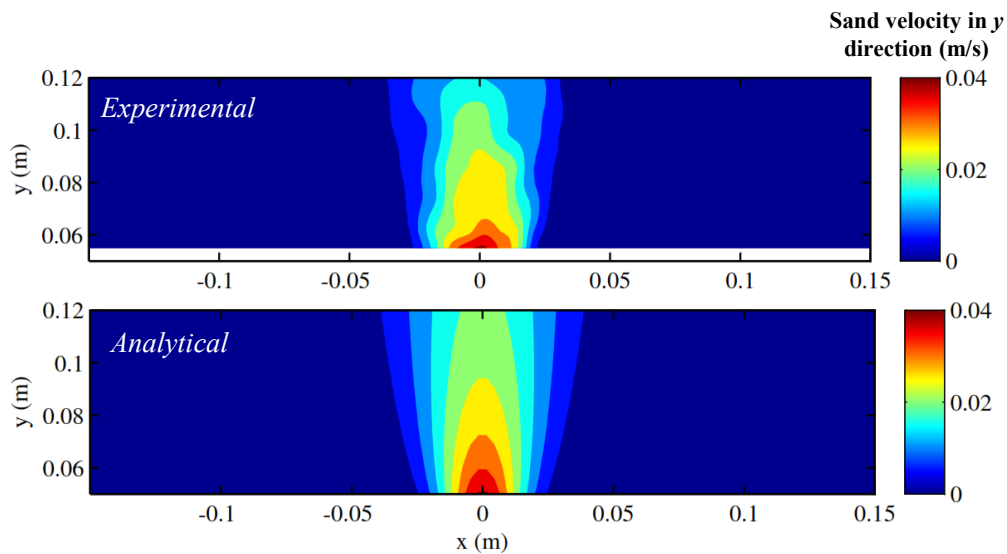
(a) Run 3D-1_T (time = 5 sec)

(b) Run 3D-2$_T$ (time = 7 sec)
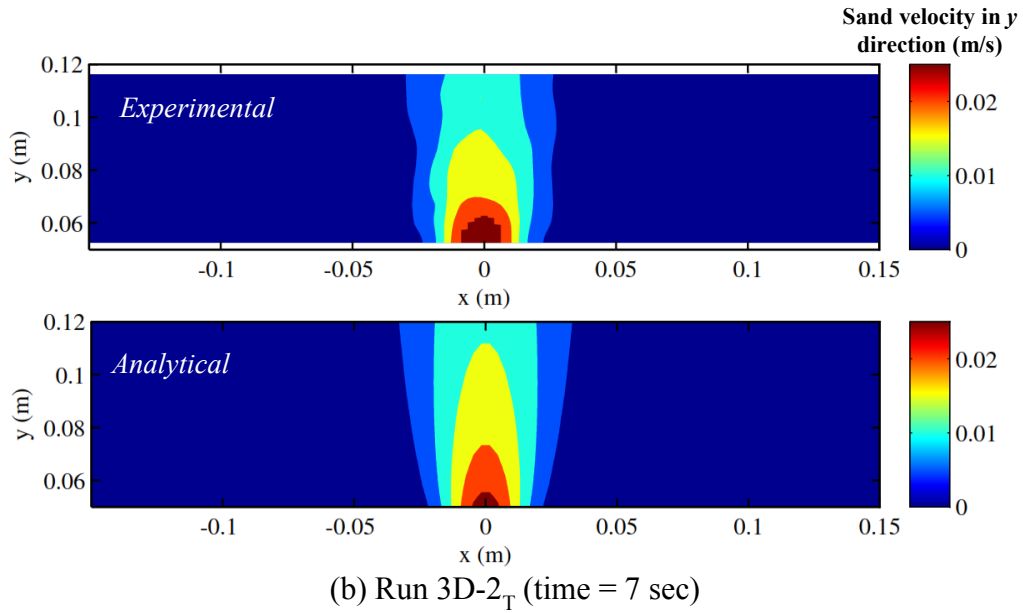
Figure 4.12 Sand velocity distribution and the predicted sand velocity distribution
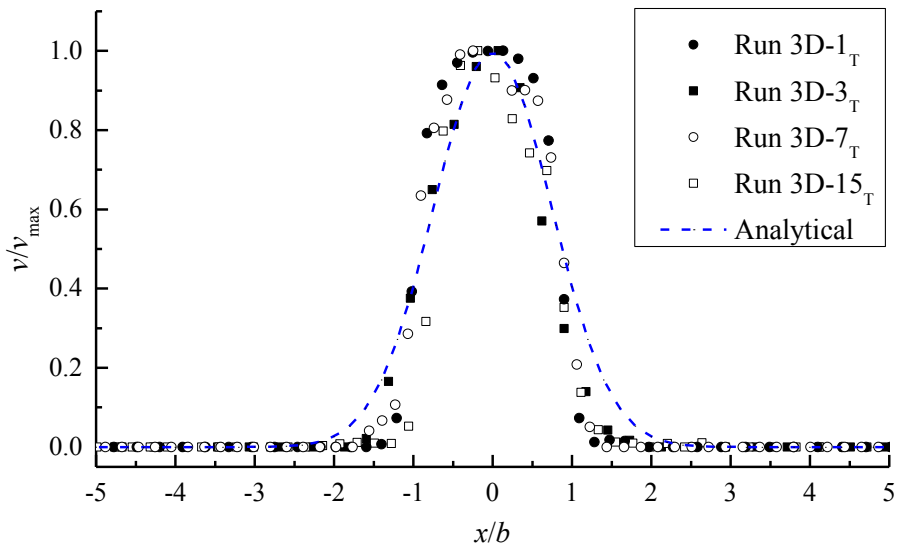
Figure 4.13 Comparison of the sand velocity profile using the analytical result with measurements ($y/D = 10$)

4.3.5 Analytical model for the 3D sand erosion

As shown in Figure 4.14, sand erosion in this study with a defect at the top of pipe can be simplified as an axisymmetric condition, which has been accepted in the calculation of sand velocity

distribution in this chapter. Therefore, the two-dimensional solution can be improved to estimate the water flow rate. Based on the studies of inflow through drained circular tunnel (El Tani, 2003; Park et al., 2008), the water flow rate through a slot can be estimated based on an equivalent circle assumption (Guo et al., 2013b). For the small opening condition, which means $r << (h_s\text{-}r_{\text{pipe}})$, the water flow rate per unit length can be simply calculated (Guo et al., 2013b):

$$q_w = \frac{\pi k}{\ln\left(2\dfrac{h_s - r_{\text{pipe}}}{r}\right)}\left(h_s - r_{\text{pipe}} + h_w\right) \tag{4.5}$$

where r is the opening size in two-dimensional condition, and can be approximately calculated as $r = \sqrt{2/\pi}D$ since the defect in this experiment was in a square shape; h_s is the sand layer height; h_w is the water layer height; r_{pipe} is the radius of defective pipe; k is the permeability of sand layer and can be estimated using Kozeny-Carman equation (Lambe and Whitman, 1969).

Based on Eq. (4.5), the water flow rate in an axisymmetric condition can be estimated:

$$Q_w = \int_0^\pi \frac{1}{2}q_w r \, \mathrm{d}\theta = \frac{\pi^2 k r}{2\ln\left(2\dfrac{h_s - r_{\text{pipe}}}{r}\right)}\left(h_s - r_{\text{pipe}} + h_w\right) \tag{4.6}$$

After estimating the water flow rate using Eq. (4.6), the sand flow rate can be calculated from Eq. (4.1). The sand velocity distribution can be predicted by Eq. (4.4) using the estimated sand flow rate, and the mobilized zone in the sand layer can be determined. During the discharge of sand and water, the water level is decreased while the sand surface is changed by forming an erosion void. In Eqs. (4.2) and (4.3), the shape of erosion void is simplified as a cone. If the lowest point of erosion void is used to determine the sand layer height, the sand and water flow rate can

be calculated using the updated parameters. Based on the mass conservation and assumption of the cone shape erosion void, following equations are obtained after m time steps:

$$\sum_{t=t_1}^{t_m} Q_s\left(t_i\right)\cdot\Delta t = \left(\frac{1}{6}\pi\cdot\frac{\left(h_{void}^m\right)^3}{\tan^2\varphi}\right)\left(1-n\right) \tag{4.7}$$

$$Q_w\left(t_m\right)\cdot\Delta t = \Delta h_w^m\cdot L\cdot W \tag{4.8}$$

where $Q_s\left(t_i\right)$ is the sand flow rate at time t_i; $Q_w\left(t_m\right)$ is the water flow rate at time t_m; h_{void}^m is the erosion void height after m time steps; Δt is the timestep; Δh_w^m is the decrease of the water layer height at the mth timestep; L is the length and W is the width of the calculation model as shown in Figure 4.14.
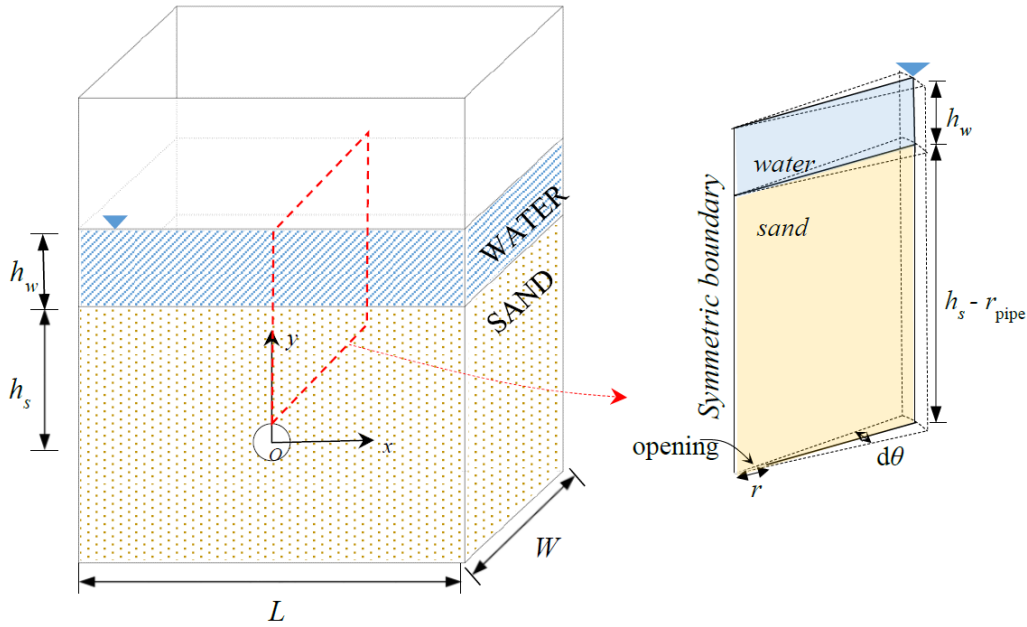
Figure 4.14 Schematics of the analytical model for 3D sand erosion

From Eqs. (4.7) and (4.8), the height of erosion void at m^{th} timestep and the corresponding change of water layer height can be calculated:

$$h_{void}^m = \sqrt[3]{\frac{6\left(\sum_{t=t_1}^{t_m} Q_s\left(t_i\right)\cdot\Delta t\right)\cdot\tan^2\varphi}{\left(1-n\right)\pi}} \tag{4.9}$$

$$\Delta h_w^m = \frac{Q_w\left(t_m\right)\cdot\Delta t}{LW} \tag{4.10}$$

The sand layer height at m^{th} timestep can be simply assumed to be the initial sand layer height h_s^{ini} reduced by h_{void}^m :

$$h_s^m = h_s^{ini} - h_{void}^m \tag{4.11}$$

The water layer height at the mth timestep is decreased by Δh_w^m :

$$h_w^m = h_w^{m-1} - \Delta h_w^m \tag{4.12}$$

Backing to Eqs. (4.6) and (4.1) with the updated water and sand layer height from Eqs. (4.11) and (4.12), the sand and water flow rate can be calculated for the next timestep. As shown in Figure 4.15, the calculated results using this analytical model are compared with the measurements and the results by Guo et al. (2013a), and this analytical model is proved to be effective estimating water and sand flow rate in the submerged sand erosion due to the defective sewer pipe. Besides, the sand velocity distribution can be calculated from Eq. (4.4) after determining the sand flow rate.

The chart displays data with axes labeled "Volumetric flow rate ($\times 10^{-6}$ m^3/s)" (y-axis, 0 to 120) and "Time (sec)" (x-axis, 0 to 80).

Legend box:
$D = 9$ mm
$h_s = 150$ mm
$h_w = 100$ mm

Legend:
△ sand (experimental, Run 3D-2$_T$)   ▲ sand (experimental, Run 3D-8$_T$)
○ water (experimental, Run 3D-2$_T$)   ● water (experimental, Run 3D-8$_T$)
------- sand (analytical, Run 3D-2$_T$)   ·········· sand (analytical, Run 3D-8$_T$)
------- water (analytical, Run 3D-2$_T$)   ——— water (analytical, Run 3D-8$_T$)

(a) Analytical results in comparison with experimental results

The figure contains the following legend text:

- ■   sand (Guo et al., 2013a; h_w = 20 mm)   □   water (Guo et al., 2013a; h_w = 20 mm)
- - - - - sand (analytical, h_w = 20 mm)   ——— water (analytical, h_w = 20 mm)
- ▲   sand (Guo et al., 2013a; h_w = 40 mm)   △   water (Guo et al., 2013a; h_w = 40 mm)
- —·—· sand (analytical, h_w = 40 mm)   ······· water (analytical, h_w = 40 mm)
- ●   sand (Guo et al., 2013a; h_w = 60 mm)   ○   water (Guo et al., 2013a; h_w = 60 mm)
- ········ sand (analytical, h_w = 60 mm)   —··—·· water (analytical, h_w = 60 mm)

Inset box: D = 10 mm, d_p = 0.45 mm, h_s = 200 mm

(b) Analytical results in comparison with the experimental results by Guo et al. (2013a)

Figure 4.15 Comparison of estimated flow rate using the analytical model with experimental measurements

4.4   Summary and Conclusions

Sand erosion due to defective sewer pipe was studied using a physical model in this chapter. The sand and water flow rate during sand erosion were measured while the sand velocity is obtained using image analysis. From this study, following conclusions are obtained:

- After the onset of sand erosion, a narrow mobilized zone in the sand layer was formed just above the defect for various defect positions except the defect is at the bottom of the pipe. Because of the impeding effect of pipe on the sand mobilization when the defect is at the

bottom, sand particles are mobilized around the pipe with a wider mobilized zone. As the loss of sand particles, an erosion void was formed from the sand surface, and the void would be expanded till reaching the defect.

- The sand and water flow rate will quickly reach a steady state without significant changes after the initiation of sand erosion. As the decrease of water level, both sand and water flow rate are decreased while the flow rate will be changed dramatically when the erosion void reaches the pipe defect. The defect position on the pipe has little effect on the flow rate. As the increase of defect size, both the sand and water flow rate increase. As the sand particle size is increased from medium to coarse, the water flow rate is increased while sand flow rate is decreased. As the particle size is decreased from medium to fine, both sand and water flow rate are decreased. The water flow rate is always increased as the increase of particle size, which will assist the sand erosion. On the other hand, the sand flow is resisted by the larger particles because of the arching effect. Therefore, the sand flow rate can be either increased or decreased as the increase of sand particle size. It has been found the flow rate ratio between sand and water is dependent on the ratio between defect size and particle size.

- The erosion void is formed from the sand surface and expanded towards the pipe defect. From the visualization analysis, the cone and truncated cone shape erosion void are proposed to predict the development of erosion void for various defect positions, which are verified by the experimental results. Therefore, the size and shape of erosion void in the erosion can be predicted if the sand flow rate is determined.

- From the sand velocity distribution, the mobilization zone in the sand layer can be determined. Adjacent to the defect, the width of mobilized zone is significantly increased while the mobilized zone is restricted to a narrow zone above the opening. Either the increase of defect

size or sand particle size will increase the width of mobilized zone in the sand layer. An analytical solution based on a kinetic model is proposed to estimate the sand velocity distribution.

- By improving the two-dimensional analytical model, a model is developed to estimate the sand and water flow rate through a 3D defect on the pipe. The change of flow rate with time can be effectively predicted using the assumption of cone shape erosion void.

List of Symbols

The following symbols are used in this chapter:

B	kinetic constant for the sand velocity distribution, m
b	width where the sand velocity is half of the maximum velocity, m
D	size of the orifice on the pipe, m
d_p	particle size, m
h_s	height of the sand layer, m
h_{void}	height of the erosion void, m
h_w	height of the water layer, m
k	soil permeability, m/s
n	porosity
Q_s	sand flow rate, m³/s
Q_w	water flow rate, m³/s
r	pipe defect size in the two-dimensional condition, m
r_{pipe}	radius of the pipe, m
r'	radius of the equivalent circle, m
u	sand velocity in the horizontal direction, m/s
V_p	sand velocity at great heights, m/s
V_s^{out}	outflow sand volume, m³
v	sand velocity in the vertical direction, m/s
W	width of bin, m

α angle indicating the position of the defect, °

φ sand angle of repose, °

Chapter 5 A Coupled Discrete Element Model for the Simulation of Soil and Water Flow through an Orifice[3]

5.1　Introduction

Although the experimental program presented in Chapters 3 and 4 provides the opportunity to study the physical process of soil erosion, it is difficult to comprehensively analyze the effects of many factors and study the erosion process at the micro scale. Numerical techniques are convenient tools for investigating erosion processes and can determine physical process depending on the selection of the input parameters (Cui et al., 2012, 2014). As an effective numerical technique for simulating granular material, the discrete element method (DEM) was first introduced by Cundall (1971) to simulate rock behavior and was then extended to analyze soils (Cundall and Strack, 1979). Unlike the classical continuum approach, DEM is an explicit method that is capable of simulating the discrete behavior of geomaterials. Accordingly, it is not necessary to incorporate a sophisticated constitutive model at the micro-mechanical level, especially for the highly nonlinear macro-characteristics of some geomaterials. In addition, the implementation of the DEM does not require a mesh or grid, and the DEM is capable of simulating large deformation problems.

In this chapter, soil erosion is simulated using the DEM, while Darcy's law was used to determine the fluid flow through the porous media. Based on this theory, a coupled model is developed by implementing the DEM and fluid model calculation sequentially while accounting for the interaction between fluid and solid. On one hand, fluid flow will impose drag forces on soil particles, and on the other hand, the movement of soil particles will change the void size of the

---

porous media and affect the fluid flow regime. This two-way coupling effect will be calculated quantitatively and then implemented between the DEM and fluid flow calculation step. The detailed implementation of this model will be presented in the following sections. The model will be verified using simulating physical experiments, and factors will be explored that are difficult to obtain experimentally.

5.2 Formulation of the Coupled Numerical Model

5.2.1 DEM model for soil

The theoretical basis of DEM is Newton's 2nd law and the force-displacement law at the contact. In this study, *PFC*^{3D} 4.0 is used with linear contacts and spherical particles with uniform size will be used for the simulation. The DEM calculation is initialized by identifying the contacts after generating the DEM and specifying the input parameters. Based on the distance between particles and the contact law, inter-particle forces can be determined. Next, the resultant force on each DEM particle will be determined. The movement of each particle will be calculated using Newton's 2nd law, and the position of the particle will be updated after each calculation step.

5.2.2 Governing equations for fluid flow

The governing equation for transient fluid flow through a saturated porous media based on Darcy's law and mass conservation is expressed as follows (Desai and Christian, 1977; Chan, 1993):

$$\frac{\partial}{\partial x}\left(k_x\frac{\partial \phi}{\partial x}\right)+\frac{\partial}{\partial y}\left(k_y\frac{\partial \phi}{\partial y}\right)+\frac{\partial}{\partial z}\left(k_z\frac{\partial \phi}{\partial z}\right)+\bar{Q}=n\beta_f\gamma\frac{\partial \phi}{\partial t} \tag{5.1}$$

where k_x, k_y, and k_z are the coefficients of permeability in the x, y, and z directions, respectively; t indicates time; ϕ is the total fluid head, which consists of the pressure head p/γ and elevation head

z, where γ is the unit weight of water; $\overline{Q}$ is the specified fluid flux; n is the porosity of the porous media; and β_f is the fluid compressibility, which is normally considered as 4.4×10^{-10} Pa^{-1} when water flows through porous media (Freeze and Cherry, 1979).

Two types of boundary conditions will be specified to solve Eq. (5.1):

- Head boundary conditions: $\phi = \overline{\phi}(t)$;

- Flow boundary conditions: $k_x \dfrac{\partial \phi}{\partial x} l_x + k_y \dfrac{\partial \phi}{\partial y} l_y + k_z \dfrac{\partial \phi}{\partial z} l_z + \overline{q}(t) = 0$.

where $\overline{\phi}(t)$ is the prescribed water head at the head boundary and can vary with time; $\overline{q}(t)$ is the prescribed flow rate at the flow boundary; l_x, l_y and l_z are the direction cosines of the outward unit vector normal to flow boundary.

Eq. (5.1) is derived based on the following assumptions: the flow is continuous and irrotational and the fluid is homogeneous and incompressible; capillary and inertial effects are negligible; the magnitudes of the velocities are small; Darcy's law is valid. Eq. (5.1) can be solved numerically using the finite difference method, which can be found in the Appendix B.

5.2.3 Coupling effects

As the fluid flows through saturated soil, coupling forces will act on the soil particles (Zhu et al, 2007; O'Sullivan, 2011). Both hydrostatic and hydrodynamic forces act on the soil particles. The hydrostatic force is normally known as the buoyancy force, which can be calculated using (O'Sullivan, 2011):

$$\mathbf{f}_b = \rho_f \mathbf{g} V_p \tag{5.2}$$

where ρ_f is the fluid density, $\mathbf{g}$ is the gravitational acceleration, and V_p is the particle volume.

Hydrodynamic forces on soil particles are caused by the dynamic behavior of fluid. Based on recent studies of hydrodynamic forces on soil particles (Morsi and Alexander, 1972; Zhu et al., 2007), the hydrodynamic forces are small compared to the drag forces caused by the relative motion between the fluid and a particle. Therefore, the virtual force due to the acceleration of fluid motion and the viscous force related to the viscosity of fluid and boundary layer can be negligible. Consequently, only the drag force will be considered in this simulation.

The simplest drag force estimation method is based on Stokes Law; however, this method is only valid for limited particle conditions. Fluid flow will be affected by other adjacent solid particles; the fluid velocity gradient will become steep and the shear stress on the particle surface will increase as the void space decreases. Therefore, Ergun's method will be used in the drag force calculation (Tsuji et al., 1993):

$$\mathbf{f}_d = \frac{n}{1-n} \beta V_p \mathbf{u}_r \tag{5.3}$$

where $\mathbf{u}_r$ is the vector of relative velocity between fluid and particle. If the porosity n is less than 0.8, then β can be determined from Ergun's equation as follows (Ergun, 1952):

$$\beta = 150 \mu \frac{(1-n)^2}{d_p^2 n^2} + 1.75 \frac{(1-n) \rho_f |\mathbf{u}_r|}{d_p n^2} \tag{5.4}$$

where d_p is the particle diameter and μ is the fluid viscosity.

If the porosity is larger than 0.8, then β can be determined from Wen and Yu's expression as follows (Wen and Yu, 1966):

$$\beta = \frac{3}{4} C_d \frac{|\mathbf{u}_r| \rho_f (1-n)}{d_p} n^{-2.7} \tag{5.5}$$

where C_d is a coefficient that depends on the particle Reynolds number R_e, $R_e = n\,\rho_f|\mathbf{u}_r|d_p/\mu$, which can be determined as (Tsuji et al., 1993):

$$C_d = \begin{cases} 24\left(1+0.15R_e^{0.687}\right)/R_e & R_e < 1000 \\ 0.43 & R_e > 1000 \end{cases} \tag{5.6}$$

However, movement of the soil particles will change the void size of the porous media, which will subsequently alter the flow pattern. Mathematically, this effect is described as the relationship between the porosity and the coefficient of permeability. The porosity can be determined after each DEM calculation cycle, from which the coefficient of permeability is determined using a certain relationship. Currently, various models are proposed for permeability calculations, including the Kozeny-Carman equation (Kozeny, 1927; Carman, 1956), which is a commonly accepted method for calculating the permeability for granular materials.

$$k = \frac{1}{C_S S_S^2 T^2} \frac{\gamma_w}{\mu} \frac{e^3}{1+e} \tag{5.7}$$

where C_S is the shape factor of the granular material; S_S is the surface area per unit volume of soil solids; T is the tortuosity factor; and e is the void ratio of soil, which can be calculated from the porosity n, $e=n/(1-n)$.

Although the Kozeny-Carman equation is well correlated with experimental results, the calculated permeability is still not sufficient in some cases. In Eq. (5.7), S_S becomes $6/d_p$ for spherical particles, and the permeability should vary directly with $e^3/(1+e)$ and d_p^2 when compared with experimental observations (Mitchell and Soga, 2005). Early works by Taylor (1948) also supported this relationship. Therefore, the parameters for this linear relationship should be

calibrated using experimental results if possible. If not, Eq. (5.7) provides an alternative method for determining permeability with high accuracy.

Based on the discrete element method and Darcy's model, this coupled model can be implemented considering the coupling effect, and the detailed numerical scheme can be found in Appendix B.

5.3   Simulation of the Experiment

In previous experimental studies of soil erosion around a defective sewer pipe (e.g., Guo et al., 2013a), the erosion process was simplified as sand was discharged through a lateral orifice driven by water flow, as shown in Figure 5.1. In this experimental study, coarse and fine sands with particle diameters of 0.13 mm and 0.25 mm, respectively, were used. However, if the actual particle size and the experimental domain were to simulated using a DEM model, then billions of soil particles would exist in the simulated domain. Performing a calculation with such a domain is practically impossible given the present day commonly available computational capacity. To simulate the experiment using the current computing capacity, the numerical model is reduced to a small region around the orifice zone, as shown in Figure 5.1.
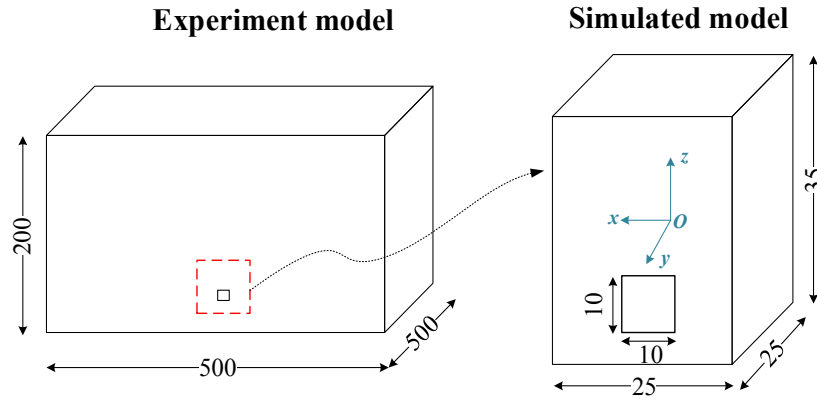
Figure 5.1 Experiment setup of Guo et al. (2013a) and the domain of the numerical model. (The red rectangle indicates the simulated zone, and the black square represents the orifice; the origin is at the center of the simulated model; Units: mm)

Because fluid flow through a porous media is governed by the hydraulic gradient, the water head contours change dramatically around the orifice. Therefore, it makes sense to simulate the orifice zone. While sand will be collapsed to fill the eroded space during the removal of particles around the orifice, this 'supply' process continues until the top-most layer collapses, leading to pure water outflow, as observed in the experiments. To simulate this continuous erosional process, a 'supply layer' is placed at the top of the simulated model, as shown in Figure 5.2 by the blue DEM elements. This 'supply layer' will be generated at the top within this model, and the original particles are marked in yellow. As the yellow particles are washed, the 'supply layer' particles move downward to fill the eroded space. After a certain number of calculation steps (10,000 steps in this simulation), which depends on the model size and estimated flow rate, the top layer will be replaced by an integral 'supply layer'. This calculation procedure is also shown in Figure 5.2.
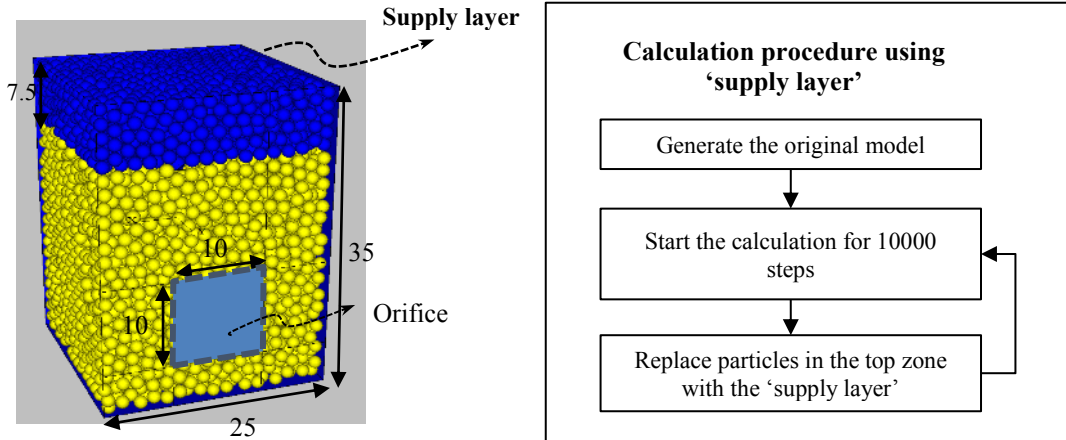
Figure 5.2 Numerical simulation setup with a 'supply layer' (Units: mm)

The parameters used in the numerical simulation are listed in Table 5.1. Because the sand particles are not significantly compacted in the erosion process, the focus of this study is the movement of particles under fluid flow. Thus, the stiffness between particles is specified based on the calibration and the density is the same as that in the experiment, as listed in Table 5.1. To simulate the sand particles and avoid unreasonable collision behavior between particles, the damping is set at 0.1. The detailed calibration process and effects of these factors will be presented in the following result section. In the experiment, the internal friction angle of the sand is 35°; thus, the friction coefficient is set as 0.5 based on the theoretical equation by Caquot (1937). To minimize the boundary effects, the friction coefficient between the wall and the particle is set to 0.5. The initial porosity was controlled at 0.4 in the experimental studies, and the same porosity is applied in the numerical model. As discussed above when determining the permeability, the initial permeability is calibrated to 0.025 m/s in this simulation, based on the initial water flow rate from the experiments. The permeability directly changes, with $e^3/(1+e)$ (Mitchell and Soga, 2005), and the coefficient was determined from the initial condition.

The particle size in the numerical simulation is 1.5 mm in diameter, which is larger than the real particle size. In this simulation, the numerical particle indicates a cluster of actual sand particles, which can make a difference in the erosion process. The contact property between these DEM elements was calibrated, and the effect of sand particle on the fluid regime was indicated by the permeability in Darcy's model. Therefore, the permeability was also calibrated based on experimental results to simulate the fluid flow. In this simulation, the uniform distributed particles are used to simulate the non-uniform sized experimental sample by calibrating the parameters. It has been found the distribution of particle size affects granular flow since the smaller particles can easily flow through the pores, while the larger particles are predominant in the granular flow through an orifice. Since the simulated elements can hardly reach the real particle size, the non-uniform distributed sample may introduce additional calibrations. Additionally, the particle size distribution in experiment (Guo et al., 2013a) is quite uniform (uniformity coefficient = 1.2). Therefore, the selection of DEM element size in this simulation is to avoid jamming at the orifice with lower computing cost.

Table 5.1 Parameters in numerical simulation

Soil phase	
Particle density (kg/m^3)	2650
Friction coefficient	0.50
Cohesion (kPa)	0.00
Particle normal stiffness (N/m)	1.00×10^8
Particle shear stiffness (N/m)	1.00×10^8
Damping	0.10
Particle size in diameter (mm)	1.5
Porosity of granular material	0.40
Wall normal stiffness (N/m)	1.00×10^8
Wall shear stiffness (N/m)	1.00×10^8
Wall friction	0.50
Fluid phase	
Density (kg/m^3)	1000
Viscosity (Pa·s)	0.001

The coupled fluid field is simulated using the Darcy fluid model via the finite difference technique. To simulate the water condition in this experiment, the top boundary in the model was set as a head boundary condition. The initial fluid field was calculated based on the initial particle distribution and is shown in Figure 5.3, from which the contour of the water head at different cross sections can be plotted.

The Reynolds number is calculated using the characteristic length, which is the pore size between the granular particles in this simulation. The Reynolds number inside the porous media can be determined as: $R_e = \rho_f |\mathbf{u}_f| L_{pore}/\mu$, where $|\mathbf{u}_f|$ is the fluid velocity. L_{pore} is the characteristic length of pore size, and can determined as $L_{pore} = 0.5 d_p \left[\left(\frac{4}{3} \right) \pi \left(\frac{n}{1-n} \right) \right]^{1/3}$. In this simulation, n is 0.4, and the $L_{pore} = 0.7 d_p$. The maximum fluid velocity is 0.006 m/s at 0.01 m away from the orifice into the model, and the Reynolds number can be calculated: $R_e = \rho_f |\mathbf{u}_f| L_{pore}/\mu = 1000 \times 0.006 \times (0.7 \times 0.0015) / 0.001 = 6.3$. In practical cases, the Darcy's law in Eq. (5.1) is valid as long as the Reynolds number is less than 10 (Bear, 1972), and has been widely used to simulate water flow around the defective pipe (DeSilva et al., 2005; Karpf and Krebs, 2013).
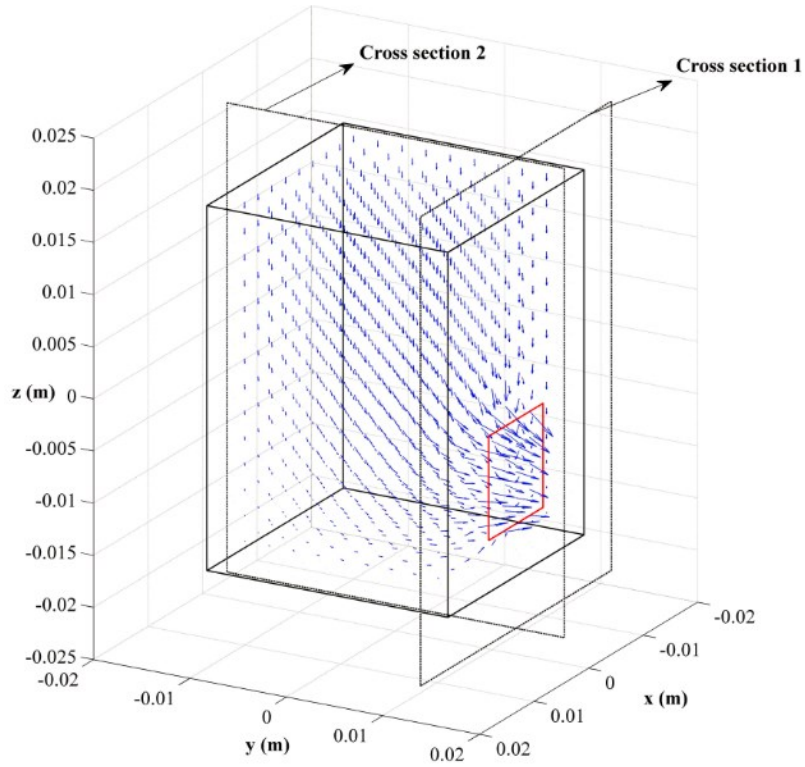
(a)
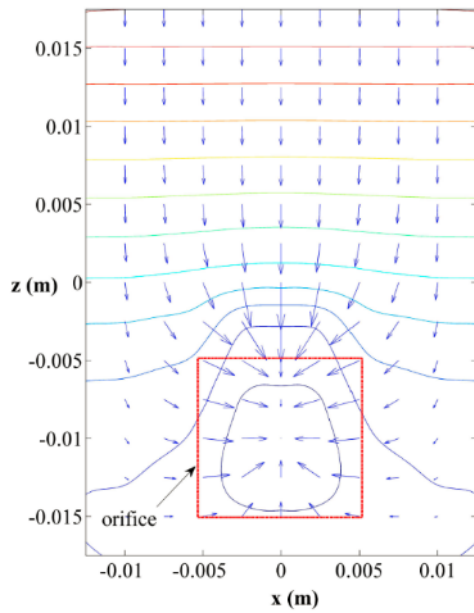
(b)
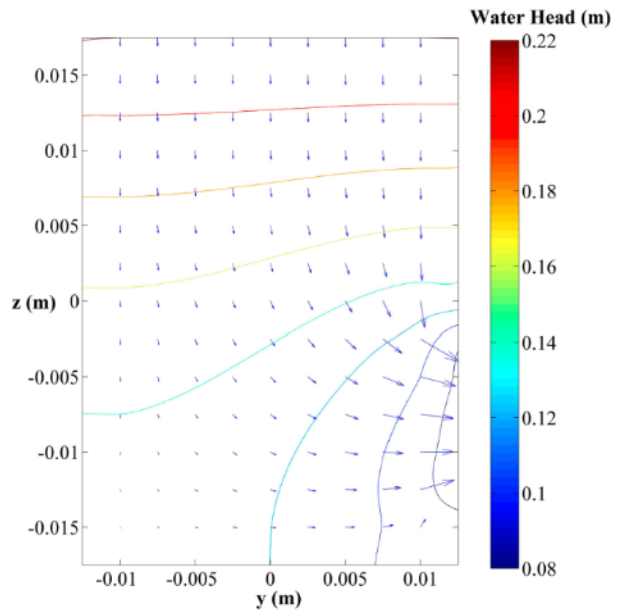
(c)

Figure 5.3 Fluid velocity vector and water head contour through different cross sections (time = 0.5 sec): (a) 3D view; (b) cross section 1; (c) cross section 2

Guo et al. (2013a) conducted experimental studies of soil erosion around defective sewer pipes, and six tests were performed using the setup with a lateral orifice by changing the water level and sand size. This numerical simulation is based on experiment 'Run 4' using the same setup, and the water level is 20 mm higher than the granular material height. Therefore, the water head will be prescribed as the head boundary condition in the Darcy fluid model. From this experiment, the erosion rate follows a similar pattern, and it is reasonable to choose this test to verify this coupling numerical model. In this simulation, the time step for the water flow simulation is 1×10^{-10} sec, which is determined based on the criterial in Eq. (B.2). The time step for the DEM simulation is determined by the default approach in PFC^{3D}, which is depended on the particle size. In this coupling model, the coupling time is 0.01 sec. The numerical calculation was conducted using an i7-4770 CPU and 24 GB RAM computer. There are 7,247 particles in the initial model and it took 141.5 hours (almost 6 days) to carry out 3.0 seconds real time simulation.

5.4   Results and Discussion

5.4.1   Analysis of the visualization results

From the numerical simulation, sand particles will be driven by the seepage force and washed out. With the progressive loss of sand particles, particles above the orifice will collapse downward, leading to an erosional space that will be filled with blue particles from the 'supply layer', as shown in Figure 5.4(a). Initially, only a small quantity of sand particles is replaced by the blue particles, and this zone gradually expands with the mobilization of the particles. A connected erosional space or erosional void towards the orifice begins to form at approximately 0.25 seconds in this case. From Figure 5.4(a), the sand particles adjacent to the wall or far from the orifice are found to form a steep erosional surface, which can be seen as the boundary between the yellow particles and blue

particles. This erosion surface becomes gentle with the mobilization of the particles until reaching

a steady erosion shape, as shown in Figure 5.4(b), which shows the variations of the erosion void.

In this erosion scheme, the driving forces include the gravity on the soil particles and the drag

force from fluid flow, while the resisting forces include the friction between soil particles and the

pressure by the adjacent particles, especially the particles above. The relatively stable erosional

void results from the equilibrium of these forces on the soil particles, the steady erosion state is

indicated by results in the following sections.

| Time: 0.05 sec | Time: 0.25 sec |

(a)

0.5 sec	1.0 sec	1.5 sec
36.83º 38.55º	32.77º 34.54º	33.58º 37.41º
2.0 sec	**2.5 sec**	**3.0 sec**
35.73º 34.40º	34.18º 32.38º	32.60º 36.13º
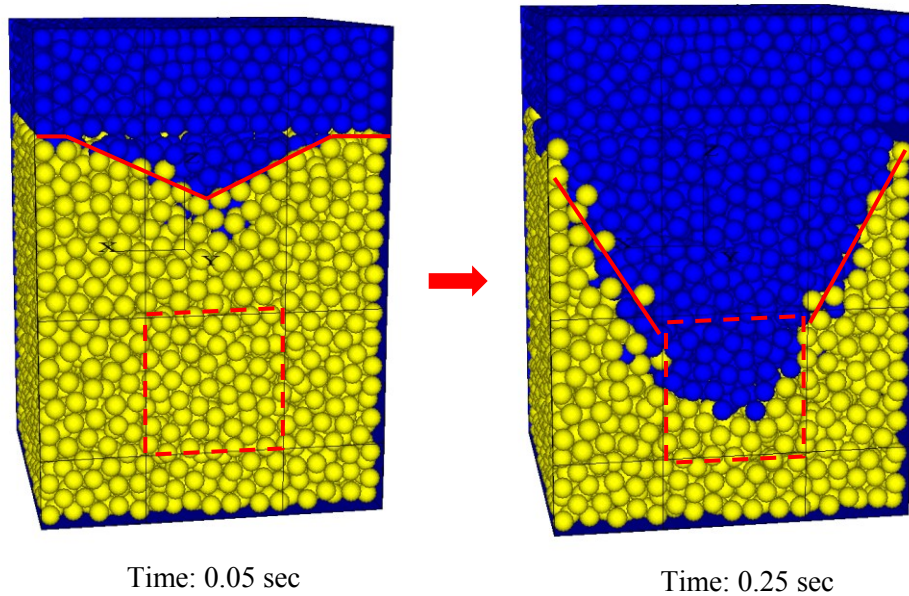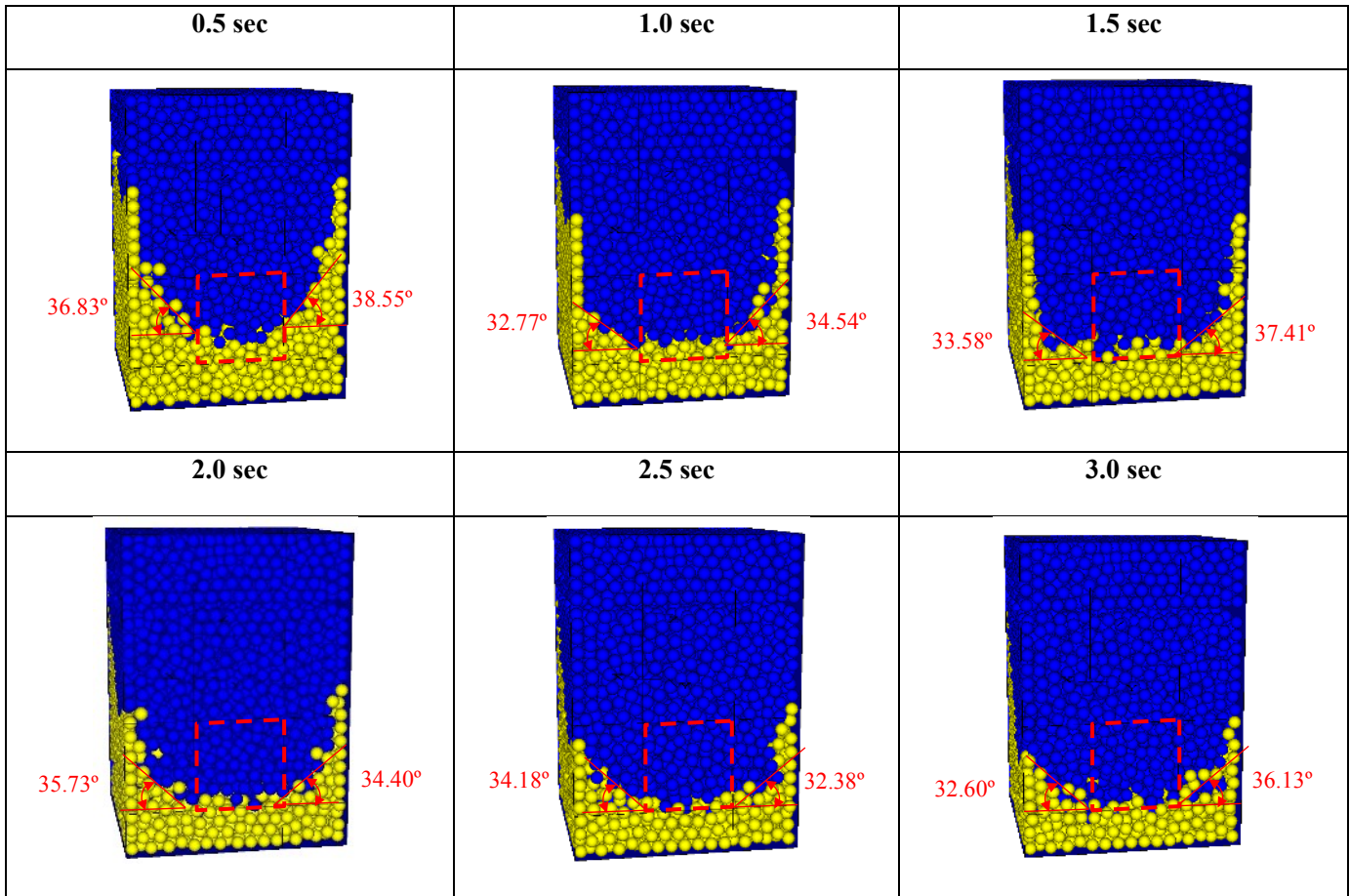
(b)

Figure 5.4 Evolution of the erosion void with time. (a) Initial erosion state; (b) Steady erosion state (the orifice is outlined by the red dash lines)

Because the particle information can be exported after each calculation step, the variation of the erosion surface, which is marked by the boundary between the yellow and blue particles, is plotted as shown in Figure 5.5. The erosion surface decreases very rapidly at the beginning and subsequently reaches a stable surface. The internal erosional void shape is like a 'cone' with a constant angle at steady state. Unlike the experimental studies, the numerical model allows for easy reconstruction and measurement of the internal void, while a special measurement technique is required in a physical experiment, such as an X-ray CT scanner (Mukunoki et al., 2009; Mukunoki et al., 2012).
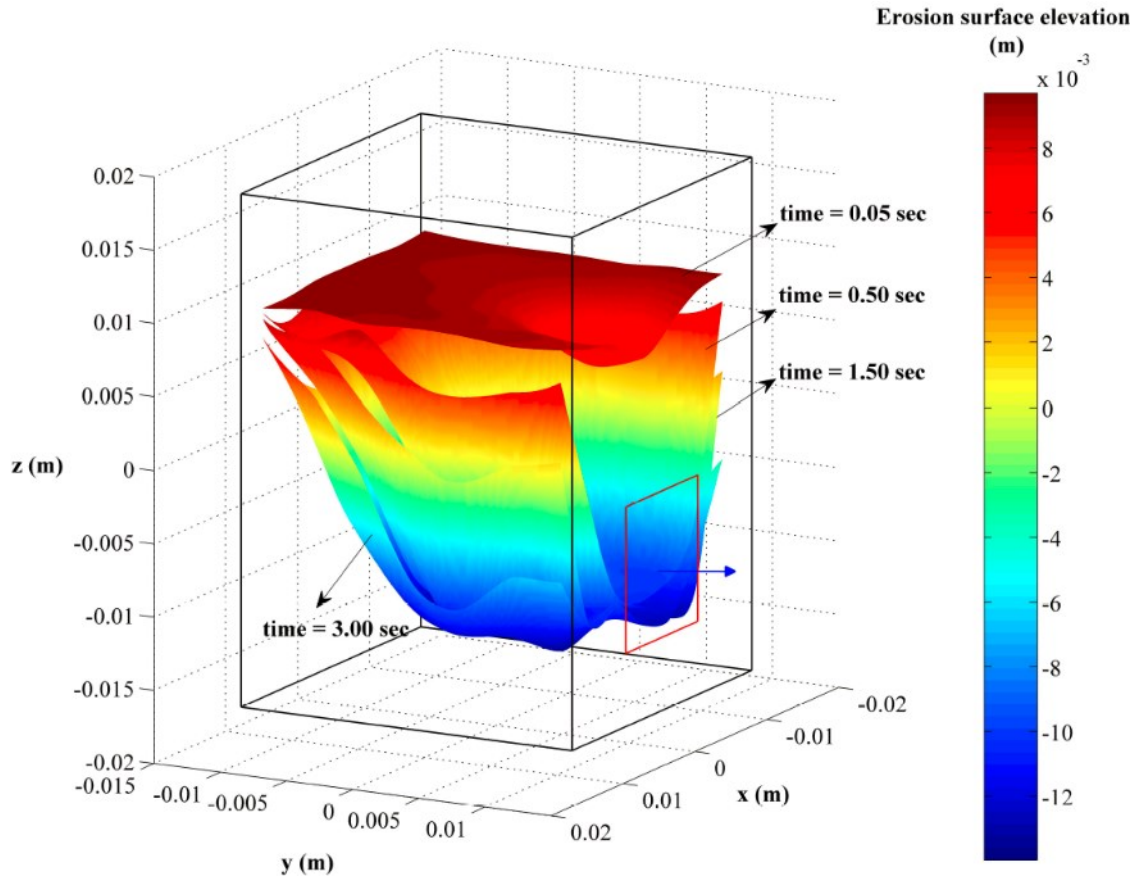
Figure 5.5 Erosion surface at various times

The particle velocities at different elevations are plotted in Figure 5.6. Near the model surface at $z = 10$ mm, 5 mm and 2 mm, the particle velocity is larger compared to that at $z = 0$ mm (at the edge of the orifice) and -7.5 mm (the orifice level). At each elevation, the maximum velocity occurs at the center of the orifice at $x = 0$, as expected. The particle velocity profile at $z = 10$ mm is very different from that of the fluid velocity, which is nearly uniform, as shown in Figure 5.3. At the orifice level, the particle velocity is the smallest among the three elevations, mainly because the particles flow out of the orifice. The small velocity fluctuation observed in the orifice region is likely due to the relatively large particle sizes used in the simulation and the particle collisions adjacent the orifice. From Figure 5.6, the sand erosion through the orifice will clearly lead to the sand loss at the surface, and the surface particle loss is restricted to a narrow zone, which is

128

immediately above the orifice. As granular particles are lost through the orifice, the particles above will naturally move to fill the erosion void due to gravity. From the distribution of the particle velocity, especially above the orifice, the velocity distribution shows the inflection point as marked in Figure 5.6 near the orifice, which implies a different particle motion pattern. Soil particles can be washed out freely with larger velocities at the narrow zone immediately above the orifice, while the particle mobilization is restricted by the adjacent particles beyond this narrow zone.
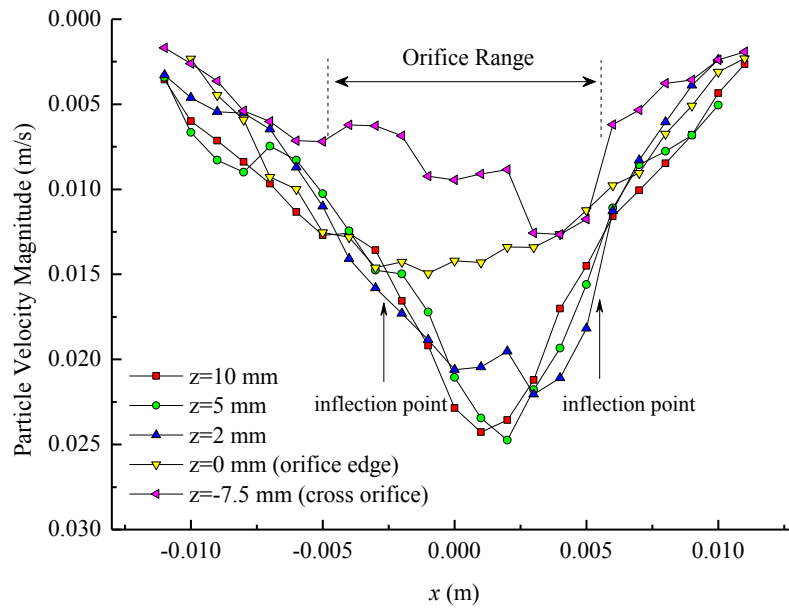
Figure 5.6 Distribution of granular particle velocity magnitude (time = 0.5 sec; y = 12.5 mm)

5.4.2 Flow rate in the erosion process

Figure 5.7 shows the variations of sand and water flow rate with time, which are consistent with the experimental results, although the DEM model causes some fluctuations. In the experiment studies, the flow rate was measured at certain time intervals and was constant at the steady erosion stage, as indicated by the horizontal line in Figure 5.7. For the fluid phase, the fluid behavior is governed by the permeability of the porous media and the hydraulic gradient, while the permeability is directly determined by the granular porosity. In non-homogeneous porous media,

the distribution of the water head is also affected by the differences in permeability. If the porous media is homogeneous, then the water head distribution will remain the same in the steady flow condition, which is governed by the Laplace equation. In this simulation of the erosion process, the water flow rate and water head distribution remain nearly unchanged during erosion, which means that the porous media can retain the constant porosity due to the continuous supply of the top granular particles, even though sand particles are washed out.
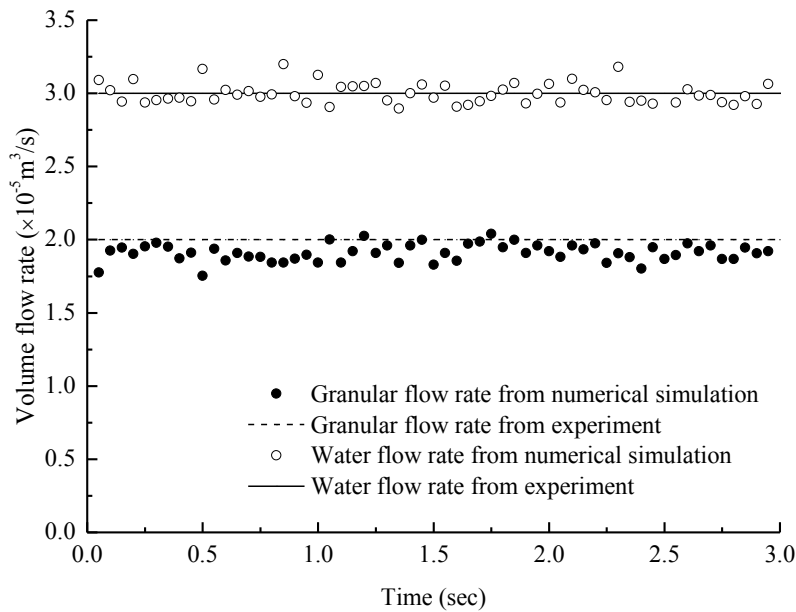
Figure 5.7 Sand and water flow rate at various times

The sand flow rate in the erosion process is mostly affected by the fluid flow, which provides the drag force, and will certainly be affected by the orifice and particle size. The sand discharge rate in the dry condition can be predicted using Beverloo's correlation (Beverloo et al., 1961), as described in Eq. (5.8):

$$\dot{M} = C\rho\sqrt{g}\left(W_0\text{-}kd_p\right)^{2.5} \tag{5.8}$$

where $\dot{M}$ is the mass rate of granular flow, ρ is the bulk density of granular material, and W_0 is the orifice size 10 mm. For a lateral orifice discharge condition, the following parameter values are valid: k_p = 2.5, and C = 0.264 (Sheldon and Durian, 2010). The theoretical studies were based on the glass bead experiments at steady discharge condition, while this numerical study was simulated for the dynamic discharge of sand with a friction coefficient of 0.5, which causes the slight differences between the numerical and theoretical results. The flow rate calculated from the numerical simulation is in reasonable agreement with the theoretical prediction, as shown in Figure 5.8, which validates the DEM model for the dry sand discharge condition.
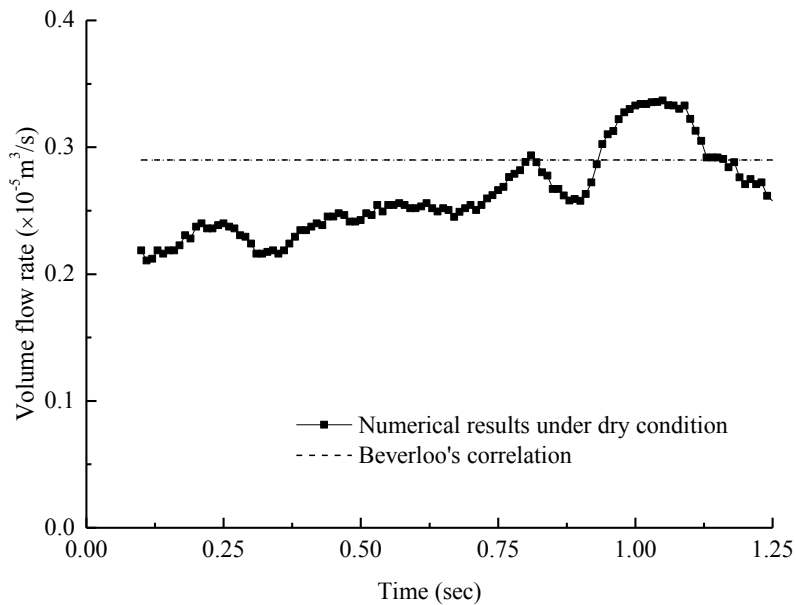
Figure 5.8 Sand discharge rate in the dry condition

When comparing Figure 5.8 with Figure 5.7, the sand erosion rate driven by fluid flow is 2×10^{-5} m^3/s and is reduced to 0.3×10^{-5} m^3/s under dry conditions, which shows that the dry discharge rate has a smaller order of magnitude than the coupling sand erosion rate. Therefore, fluid flow is the governing factor in the sand erosion process.

The flow rates will be changed as the variation of parameters as shown in following Figure 5.9. As shown in Figure 5.9(a) and 5.9(b), both granular and water flow rates are increased as the initial permeability is increased from 0.015 m/s to 0.035 m/s. Since Darcy's Law is used in this simulation, the water flow rate is proportional to permeability, while the loss of granular particles is intensified as the increase of water flow. To calibrate the experimental results, the initial permeability used in this simulation is 0.025 m/s.

The effect of the normal and shear stiffness on the granular flow is shown in Figure 5.9(c) and 5.10(d). Since the 'supply layer' was placed at the top of sample in this simulation, the water flow rate is not significantly changed during the erosion process. Therefore, only the granular flow rate is compared with the variation of contact parameters. As the normal stiffness between particles is increased from 5×10^7 N/m to 5×10^8 N/m, the granular flow rate is decreased from approximately 2.0×10^{-5} m^3/s to 1.5×10^{-5} m^3/s. As the increase of normal stiffness, the normal component of contact force between particles is increased, which results in the growth of interparticle friction and resist the erosion of granular particles. Similarly, the increase of interparticle shear stiffness will lead to the increase of shear force between particles as shown in Figure 5.9(d).

As shown in Figure 5.9(e), the granular flow rate is approximately decreased from 2.0×10^{-5} m^3/s to 1.0×10^{-5} m^3/s as the increase of local damping between particles from 0.1 to 0.5. Because of the increase of damping force on each particle, the motion of particles is slowed down with smaller granular flow rate. Since the quartz sand is used in the experiment, the local damping is small between particles, and 0.1 is used in this simulation.
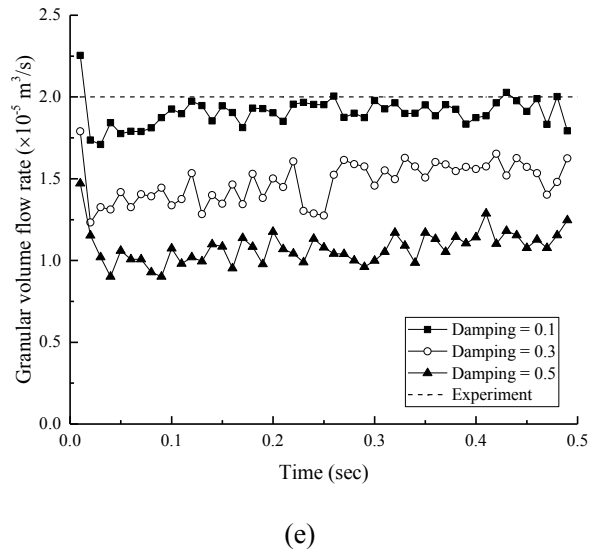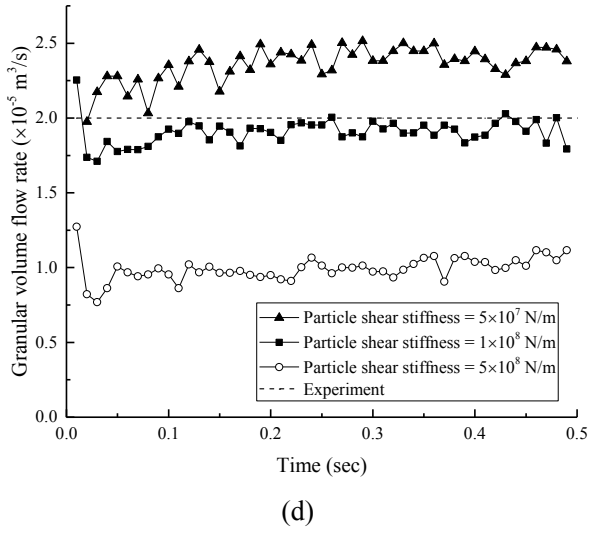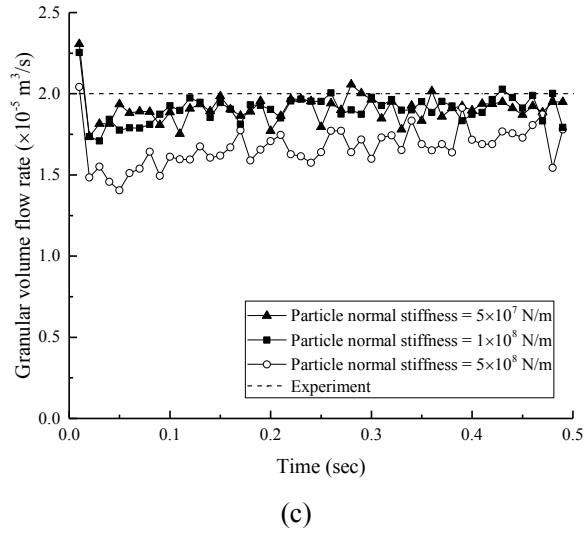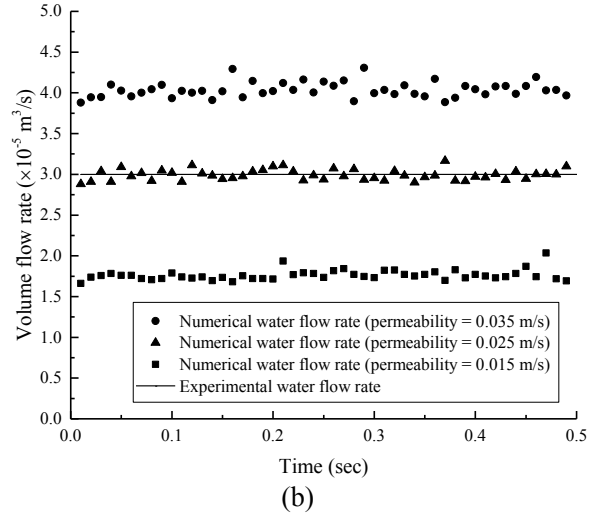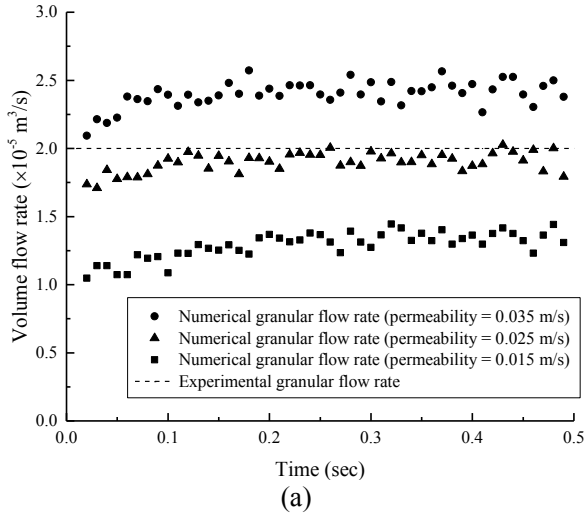
Figure 5.9 Variation of the flow rate with different parameters

5.4.3 Erosion void analysis

The erosional void shown in Figure 5.4 was formed progressively in the shape of a cone and achieved a constant cone angle, which is consistent with the internal friction angle of the granular material according to the theoretical analysis (Rao and Nott, 2008). In Figure 5.4(b), the erosion angle finally reaches a steady value, as shown in Figure 5.10. The erosion angle is approximately 35º, which is identical to those of the experimental and theoretical results (Guo et al., 2013a). Finally, the particles forming this erosion surface reach an equilibrium state, and these particles will not be eroded and stay at fixed positions due to the balance forces on them. This steady state can be achieved after the redistribution of the particles due to the unbalanced force.

Another observation worth noting is the percentage occupied by the original particles (yellow particles) in the total sand particles volume of the model. If the initial particle volume in the model is defined as V_0, then the particle volume with different colors in the erosion process is defined as $V_{particle}$. As shown in Figure 5.11, the percentage of supplied blue particles increases while the volume of the original yellow particles decreases due to erosion. After approximately 2 seconds, the percentage of the yellow particles becomes constant as the granular outflow comes from the supplied blue particles without further erosion of the yellow particles. Under this steady state condition, the erosion process can be assumed to occur by wedge movement with a constant angle, and this wedge becomes smaller as the supply of particles from the top layers is diminished. In Figure 5.4(a), although the erosion angle remains constant, the erosion surface is not as smooth as the theoretical analysis due to the discontinuous property of the DEM model. The arrangement of the particles is random at the beginning, which causes slight differences in the local porosity and influences the flow pattern of fluid at this zone. Therefore, some local particles may be subjected to larger drag forces without the formation of the ideal erosion surface.
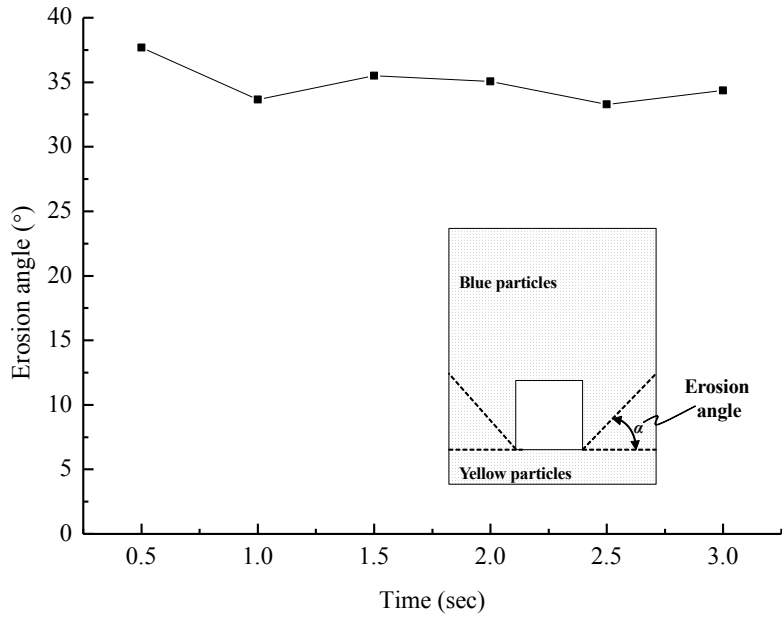
Figure 5.10 Variations of the erosion angle with time
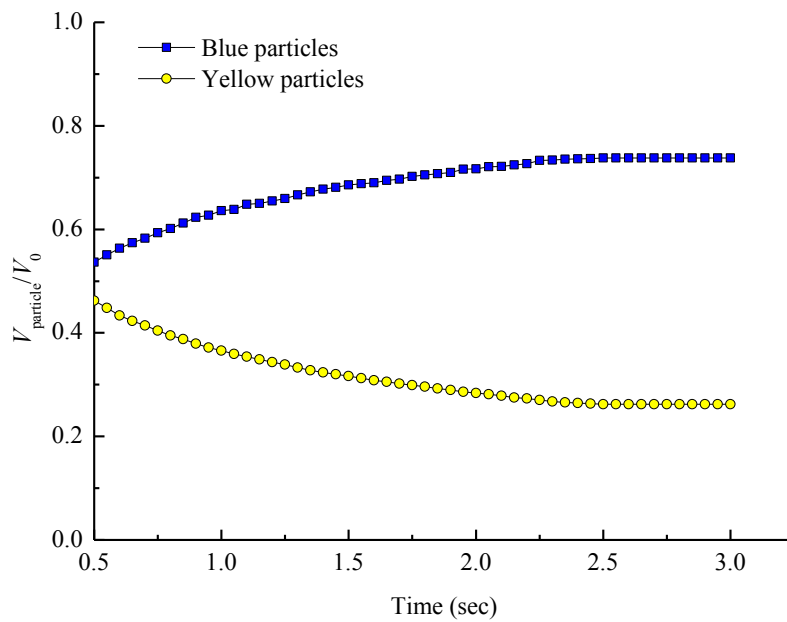
Figure 5.11 Variations of the particle volume percentage within the model at different times

From the above numerical simulation and analysis, this coupling model can satisfactorily predict the steady erosion stage of experimental Run 4 using setup 2 described by Guo et al. (2013a). This proposed numerical model can accurately predict the mixed outflow of sand and

water. From the experimental studies of Guo et al. (2013a), the sand will be eroded steadily for 150 seconds, depending on the dimensions of the erodible layer. Subsequently, water can freely flow through the opening on the pipe, and soil particles on the erosion surface will be washed progressively until the water level falls below the orifice. This process is the cause of the 'bowl' shape erosion void observed at the final stage of the experiment. Consequently, it is reasonable to anticipate that most of the sand particles will be washed out if there is enough water.

Based on the above explanation, the initial steady erosion stage provides enough information to predict the erosion void space evolution. This proposed numerical technique is an effective tool for calculating granular and water flow. The erosional cavity was shown to depend on the internal friction angle of the granular material. Based on mass conservation, the erosional time can be estimated using knowledge of the flow rate and the dimensions of the erosional cavity.

This proposed numerical model is based on the discrete element method and Darcy's law. Therefore, it is valid only if the Reynolds number is less than 10, and the permeability should be carefully determined either by the calibration or the appropriate analytical model. The parameters in the discrete element method are difficult to be determined, and there is no reliable relationship between the micro and macro properties. Therefore, it will be better to determine the parameters in this coupled numerical model by calibration for the reliable application.

5.5 Summary and Conclusions

To predict the behavior of granular material during erosion due to fluid flow, a coupling model combining the discrete element method (DEM) with Darcy's fluid model was proposed for the soil erosion studies. Through the numerical simulation, both the erosion angle and the sand flow rate

were compared with the experiment results to verify this coupled 3D discrete element model and Darcy's flow model. Based on the results, the following conclusions can be obtained:

- This proposed discrete element method coupled with the Darcy fluid model was shown to be an effective and efficient tool to study the dynamics of sand/water flow in the case of sand erosion around an orifice. The erosional flow rate and erosion void space can be estimated using this numerical technique by incorporating a 'supply layer' in the model.

- This numerical technique makes it possible to investigate sand mobilization during the erosion processes at the micro-scale. Sand particles are eroded around an opening, which could be a defect or crack in a sewer pipe. This erosion may eventually lead to surface collapse. The process is simulated as a depression from the soil surface to the orifice until the formation of an erosional cavity. When the steady state is reached, the erosional cavity will achieve a stable shape with a constant side slope angle.

- Fluid flow is the driving force in the mobilization of sand particles in this case and provides the drag force on the adjacent soil particles. According to Darcy's flow, permeability is the key factor controlling the fluid flow regime, which also influences the soil erosion process. Calibration from experimental observations is a more reliable method for determining the permeability than a small-scale permeameter test. The current model also considers permeability changes due to porosity changes.

- From the numerical simulation of the soil and the water flow through the orifice at a microscopic scale, the soil particles are washed out at a higher flow rate ($2 \times 10^{-5} \text{m}^3/\text{s}$) than the flow rate ($0.3 \times 10^{-5} \text{m}^3/\text{s}$) in the dry condition, which shows the driving effects of the fluid flow on granular erosion. The erosion zone is restricted in a narrow zone immediately above the

orifice, and the steady erosion stage retains a steady erosion surface shape and steady erosion flow rate.

- The proposed approach can be used to calculate the flow rate. Based on the flow rate and time, the size of the erodible zone can be estimated.

List of Symbols

The following symbols are used in this chapter:

C	coefficient in Beverloo's equation
C_d	drag force coefficient
C_s	shape factor of granular material
d_p	particle size, m
$\mathbf{f}_d$	drag force vector, N
g	gravitational acceleration, m/s^2
k_p	coefficient in Beverloo's equation
k_x	soil permeability in x-direction, m/s
k_y	soil permeability in y-direction, m/s
k_z	soil permeability in z-direction, m/s
L_{pore}	pore size in soils, m
l_x	direction cosine of the outward unit vector to flow boundary in x-direction
l_y	direction cosine of the outward unit vector to flow boundary in y-direction
l_z	direction cosine of the outward unit vector to flow boundary in z-direction
$\dot{M}$	mass rate of granular flow, kg/s
n	porosity
p	water pressure, Pa
$\overline{Q}$	specified fluid flux, m^3/s
$\overline{q}$	prescribed flow rate at the boundary, m^3/s
Re	Reynolds number
S_S	surface area per unit volume of soil solids, m^{-1}

T	tortuosity factor
$\mathbf{u}_r$	vector of relative velocity between fluid and particle, m/s
V_p	soil particle volume, m^3
W_0	orifice size, m
β	coefficient from Ergun's equation, Pa·s/m^2
β_f	fluid compressibility, Pa^{-1}
γ_w	unit weight of water, kN/m^3
Δt	timestep, s
μ	fluid dynamic viscosity, Pa s
ρ	bulk density of granular material, kg/m^3
ρ_f	fluid density, kg/m^3
ϕ	total water head, m
$\bar{\phi}$	prescribed total water head, m

Chapter 6 Analytical Model for the Granular Flow through a Two-dimensional Opening[4]

6.1 Introduction

Form the experimental and numerical studies, the soil erosion process due to the defective sewer pipe can be attributed to a simplified model which is granular flow through an opening on the defective underground sewer pipe (Guo et al., 2013a). Differ from fluid flow, granular flow through an opening is independent of the granular height, which is firstly explained as the Janssen effect (Janssen, 1895). Brown (1961) firstly proposed the minimum energy theory to explain the physics of granular flow. The energy within the granular material is assumed to be decreased along the stream tube of granular flow, and it will reach the minimum value close to the opening. After that, granular particles will freely fall under gravity. This minimum energy boundary is called the free-fall arch by Brown and Richards (1965).

Although the free-fall arch theory provided a reasonable theoretical basis for studying granular flow, there is no analytical model of the free-fall arch, while most of the free-fall is obtained from assumptions and simplifications. In this chapter, an analytical model of free-fall arch is proposed. The location and size of free-fall arch close to the opening can be predicted, and the granular flow rate can be estimated using this analytical model. Experimental results are used to verify this analytical model, and numerical simulation based on discrete element method can justify the assumption of free-fall arch theory and this proposed analytical model.

---

[4] This chapter is currently being prepared as a journal manuscript: Tang, Y., Chan, D. H. and Zhu, D. Z. (2017). "Analytical Model for the Granular Flow through a Two-dimensional Opening." *Physical Review E*, to be submitted.

6.2   Analytical Model

6.2.1   Model of the free-fall arch

From the free-fall arch theory, the granular flow is assumed to be transformed from slow dense flow to dilute flow due to inter-particle friction. The boundary between these two types of flow is the so-called free-fall arch. The free-fall arch is not always formed with the two ends at the opening boundary, and the potential arches might be formed when the granular flow through an opening as shown in Figure 6.1. Unlike fluid flow, friction between granular particles plays an essential role during the discharge. It has been found the stagnant zone exits when the granular particles in a flat-bottom bin flow through an opening (Nedderman, 1992), and the angle of this stagnant zone depends on the repose angle of the granular material.
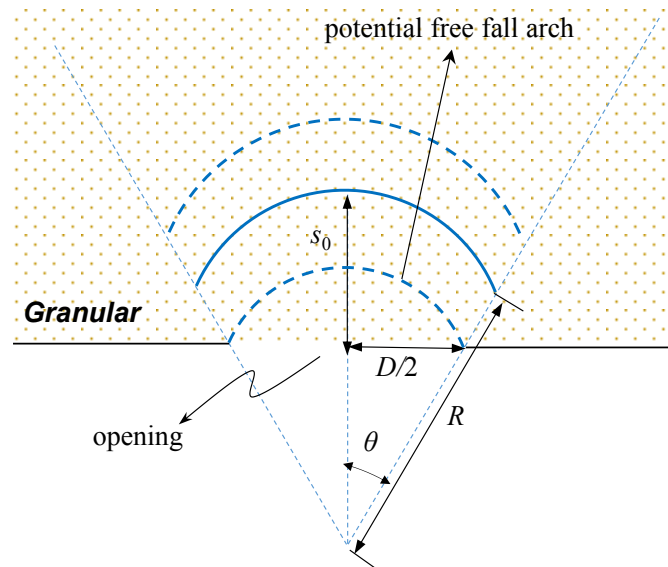
Figure 6.1 Schematic of a potential free-fall arch

The schematic of this analytical model for the free-fall arch is shown in Figure 6.2. In this analytical model, the granular particles are the same size and they flow through a two-dimensional opening. In addition, friction between particles follow the Coulomb's theory (Rao and Nott, 2008).

The arch is formed above the opening, while the location of the arch is unknown. The number of particles formed the arch is also unknown and the arch is assumed to be circular in shape (Brown and Richards, 1965; Hilton and Cleary, 2011). Half of the central angle of this arch is θ, while the angle between any two adjacent particles is equally $\Delta\theta$ as shown in Figure 6.2. Two specific particles will be analyzed in following derivations, which is the particle at the center of the arch (particle 1) and the particle at the end (particle n). In this analytical model, particle 1 is the center one at the arch if the total particle number in the arch is an odd number. Otherwise, particle 1 consists of the two particles at the center of the arch.
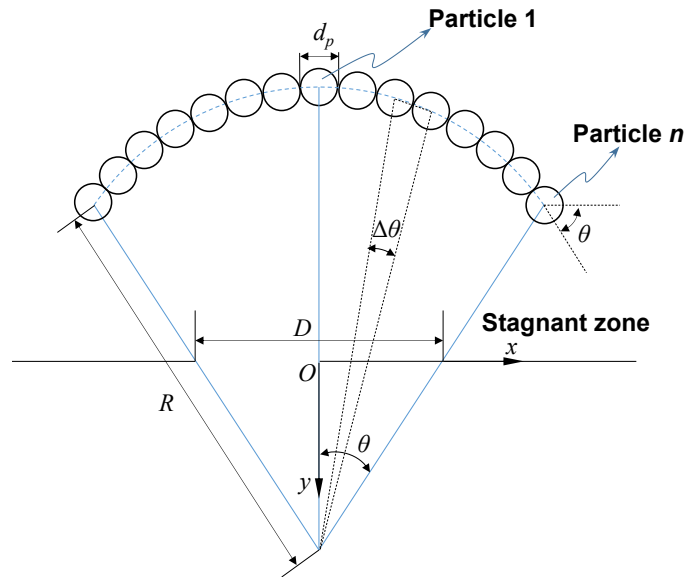
Figure 6.2 Schematic of the analytical model for the free-fall arch

Figure 6.3 shows the free-body diagram of particle n. Due to the discrete characteristic of the granular material, the slip surface between particles in the arch and the stagnant zone cannot be assumed to be a straight line. Therefore, the force on the particle n given by the particles in the stagnant zone is acted with an unknown angle α, which is not necessarily equal to θ. In other words,

the force on the free-fall arch by the slip surface is not necessarily perpendicular to the arch curve.

Applying the equations of equilibrium for the particle n:

$$\sum F_x = 0: \ N_1 \cos\theta - T_1 \sin\theta - N_2 \cos\alpha + T_2 \sin\alpha = 0 \tag{6.1}$$

$$\sum F_y = 0: \ -N_1 \sin\theta - T_1 \cos\theta - q + N_2 \sin\alpha + T_2 \cos\alpha = 0 \tag{6.2}$$
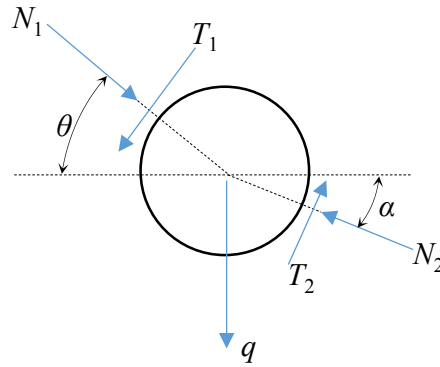
Figure 6.3 Free-body diagram of particle n

where, N_1 is the normal force by the adjacent particle n in arch; T_1 is the shear force due to the adjacent particle in arch; N_2 is the normal force by the particle in the stagnant zone; T_2 is the shear force by the particle in the stagnant zone; q is the sum of gravity of particle n and force applied by particles above the arch.

Figure 6.4 shows the free-body diagram of the free-fall arch as a structure. The force q is assumed to be equal for all the particles in the arch. Consider the force equilibrium of this arch structure:

$$\sum F_y = 0: \ 2\left(N_2 \sin\alpha + T_2 \cos\alpha\right) - qM = 0 \tag{6.3}$$

where, M is the number of particles formed the arch.

143
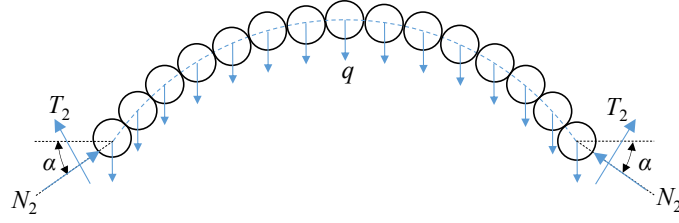
Figure 6.4 Free-body diagram of the free-fall arch

Substituting the Eq. (6.2) with Eq. (6.3):

$$\frac{qM}{2} - q - N_1 \sin\theta - T_1 \cos\theta = 0 \tag{6.4}$$

By introducing Coulomb's theory of friciton, the shear force between particles can be obtained from the normal force:

$$T_1 = N_1 \tan\varphi_p \tag{6.5}$$

$$T_2 = N_2 \tan\varphi_p \tag{6.6}$$

where, φ_p is the friction angle between granular particles.

Therefore, the normal force N_1 can be calculated from Eq. (6.4):

$$N_1 = \frac{qM - 2q}{2\left(\sin\theta + \tan\varphi_p \cos\theta\right)} \tag{6.7}$$

Similarly, the normal force N_2 can be calculated from Eq. (6.3):

$$N_2 = \frac{qM}{2\left(\sin\alpha + \tan\varphi_p \cos\alpha\right)} \tag{6.8}$$

Substituting N_2 in Eq. (6.1) with Eq. (6.8):

$$N_1\left(\cos\theta - \tan\varphi_p\sin\theta\right) + \frac{qM\left(\tan\varphi_p\sin\alpha - \cos\alpha\right)}{2\left(\sin\alpha + \tan\varphi_p\cos\alpha\right)} = 0 \tag{6.9}$$

Therefore, the normal force N_1 can be calculated from Eq. (6.9):

$$N_1 = -\frac{qM\left(\tan\varphi_p\sin\alpha - \cos\alpha\right)}{2\left(\sin\alpha + \tan\varphi_p\cos\alpha\right)\left(\cos\theta - \tan\varphi_p\sin\theta\right)} \tag{6.10}$$

Substituting N_1 obtained from Eq. (6.7) into Eq. (6.10), after simplifying and rearranging, it

gives:

$$\frac{(M-2)\left(\cos\theta - \tan\varphi_p\sin\theta\right)}{M\left(\sin\theta + \tan\varphi_p\cos\theta\right)} = \frac{\cos\alpha - \tan\varphi_p\sin\alpha}{\sin\alpha + \tan\varphi_p\cos\alpha} \tag{6.11}$$

From the geometric relationship in Figure 6.2:

$$R = \frac{d_p}{2\sin\left(\Delta\theta/2\right)} \tag{6.12}$$

The particle number M formed the free-fall arch can be determined based on the arch length

and particle size:

$$M = \frac{2\theta R}{d_p} = \frac{2\theta d_p}{2d_p\sin\left(\Delta\theta/2\right)} = \frac{\theta}{\sin\left(\Delta\theta/2\right)} \tag{6.13}$$

Figure 6.5 shows the free-body diagram of particle 1 which is located at the center of the

arch, and the equation of equilibrium is:

$$\sum F_y = 0: \ m\left(N\sin\Delta\theta + T\cos\Delta\theta\right) - q = 0 \tag{6.14}$$

where, m is determined based M. If M is an odd number, $m = 2$, otherwise, $m = 1$; N is the normal force acted on particle 1 by the adjacent particle in the arch; T is the shear force acted on particle 1 by the adjacent particle in the arch, which is assumed to follow Coulomb's theory:

$$T = N \tan \varphi_p \qquad\qquad (6.15)$$

(a)

(b)
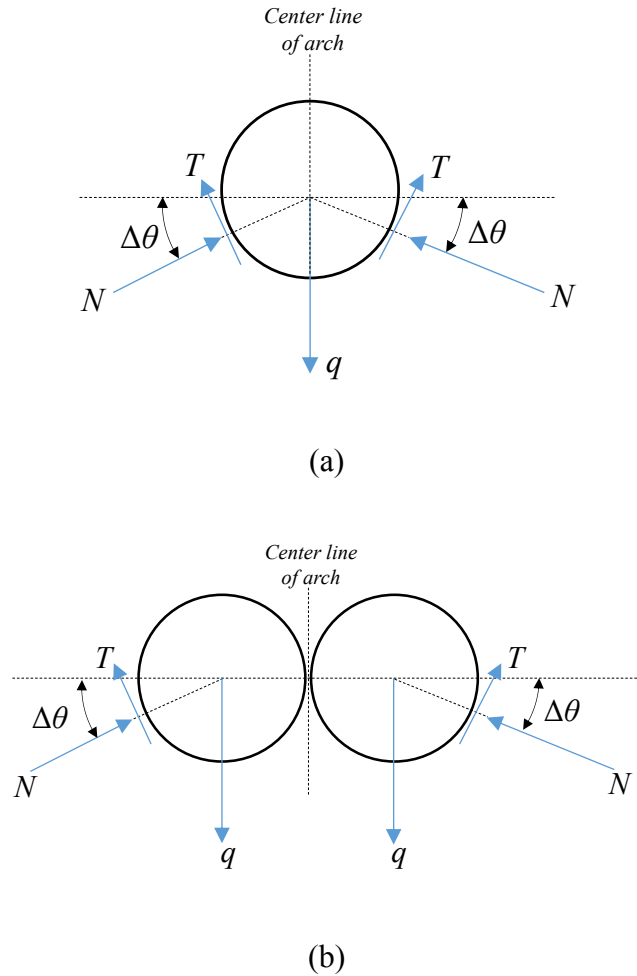
Figure 6.5 Free-body diagram of particle 1

(a) M is an odd number; (b) M is an even number

Figure 6.6 shows the free-body diagram of the half arch except particle 1. Applying the equations of equilibrium:

$$\sum F_x = 0: \ N_2 \cos\alpha - T_2 \sin\alpha - N\cos\Delta\theta + T\sin\Delta\theta = 0 \tag{6.16}$$
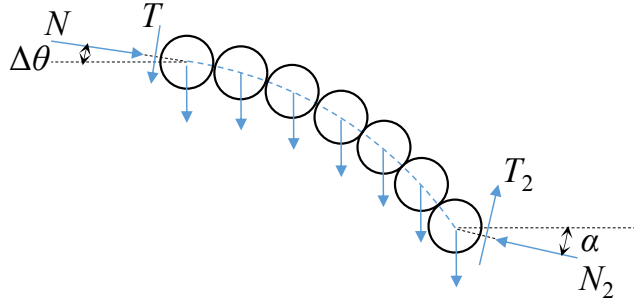
Figure 6.6 Free-body diagram of half free-fall arch

The normal force N_2 can be solved from equation (6.16):

$$N_2 = \frac{N\left(\cos\Delta\theta + \tan\varphi_p \sin\Delta\theta\right)}{\cos\alpha - \tan\varphi_p \sin\alpha} \tag{6.17}$$

After solving force N using Eq. (6.14), Eq. (6.17) can be simplified:

$$N_2 = \frac{q\left(\cos\Delta\theta + \tan\varphi_p \sin\Delta\theta\right)}{m\left(\cos\alpha - \tan\varphi_p \sin\alpha\right)\left(\sin\Delta\theta + \tan\varphi_p \cos\Delta\theta\right)} \tag{6.18}$$

Force N_2 can also be solved from Eq. (6.3), while Eq. (6.18) will be simplified after rearranging:

$$\frac{\cos\alpha - \tan\varphi_p \sin\alpha}{\sin\alpha + \tan\varphi_p \cos\alpha} = \frac{2\left(\cos\Delta\theta + \tan\varphi_p \sin\Delta\theta\right)}{Mm\left(\sin\Delta\theta + \tan\varphi_p \cos\Delta\theta\right)} \tag{6.19}$$

The left-hand side of Eq. (6.19) is the same as the right-hand side of Eq. (6.11). Therefore, it gives:

$$\frac{2\left(\cos\Delta\theta + \tan\varphi_p \sin\Delta\theta\right)}{m(M-2)\left(\sin\Delta\theta + \tan\varphi_p \cos\Delta\theta\right)} = \frac{\left(\cos\theta - \tan\varphi_p \sin\theta\right)}{\left(\sin\theta + \tan\varphi_p \cos\theta\right)} \tag{6.20}$$

The only unknown in Eq. (6.20) is $\Delta\theta$. Although an explicit expression for $\Delta\theta$ is difficult to be obtained, it can be solved numerically by an iterative method. If the opening size is modified as Beverloo's correlation, the modified opening size D_0 is: $D_0 = D - k_p d_p$, where k_p is taken as 1.5. Therefore, the distance s_0 from the apex of the arch to the opening can be determined by the geometric relationship:

$$s_0 = R - \frac{D_0}{2\tan\theta} \tag{6.21}$$

From this proposed analytical model of free-fall arch, it can be found that the size of free-fall arch is independent on the force q, which means that the granular height and stress state on the arch has no effect on the formation of free-fall arch. This statement is consistent with the classic theory of granular flow, which indicates that the granular flow rate through an opening is independent of the granular height.

6.2.2 Estimation of granular flow rate through an opening

Based on the assumption of free fall arch theory, granular particles will fall freely from the arch surface to the opening under gravity. The granular flow rate through the opening can be estimated if the particle velocity at the opening is determined. If the particle velocity at the free-fall arch is negligible, the particle velocity at the opening can be determined using this proposed free-fall arch model. The particle velocity at the opening is:

$$v = \sqrt{2gh} \tag{6.22}$$

where, h is the distance from the free fall arch surface to the opening, and can be determined as:

$$h = \sqrt{R^2 - x^2} - \frac{D_0}{2\tan\theta}, \quad x \in [0, D_0/2] \tag{6.23}$$

The volumetric flow rate through the opening can be estimated:

$$Q = 2(1-\varepsilon)\int_0^{D_0/2} v\mathrm{d}x = 2(1-\varepsilon)\int_0^{D_0/2} \sqrt{2g\left(\sqrt{R^2-x^2} - \frac{D_0}{2\tan\theta}\right)}\mathrm{d}x \qquad (6.24)$$

where, ε is the porosity of granular flow at the opening.

If $D_0 << R$, h can be simply estimated as a constant s_0, and the volumetric flow rate through opening can be approximately calculated as:

$$Q = 2(1-\varepsilon)\int_0^{D_0/2} v\mathrm{d}x = (1-\varepsilon)D_0\sqrt{2gs_0} \qquad (6.25)$$

6.3　Results and Discussion

The proposed analytical model has been verified by comparing with experimental results as listed in Table 6.1. The flow rate of glass beads through a slot was measured by Manmtani (2011), and the results using this proposed analytical method are consistent with the experimental measurements. We conducted the experiments using quartz sands. Sand with the diameter of 1.50 mm and 0.97 mm was discharged through a slot with a width of 0.08 m. It can be found the error between the analytical estimation and experimental measurements is within 10%, which shows the accuracy of this analytical method.

Table 6.1 Predicted granular volumetric flow rate comparing with the experimental results

	d_p (mm)	D (mm)	n	φ_p (°)	ρ_s (kg/m³)	Measured volumetric flow rate (m³/s/m)	Predicted volumetric flow rate (m³/s/m)	Error (%)
Glass Beads (Mamtani, 2011)	2.27	25	0.35	25.3	2580	6.22E-03	6.50E-03	4.43
	1.53	25	0.35	25.6	2500	7.28E-03	6.90E-03	5.26
	0.99	25	0.36	21.4	2450	8.22E-03	8.30E-03	0.95
	0.55	25	0.36	22.9	2490	8.57E-03	8.40E-03	1.96
Quartz Sand	1.50	9	0.40	36.0	2650	7.51E-04	7.94E-04	5.73
	0.97	9	0.40	36.0	2650	9.98E-04	9.25E-04	7.30

Although the estimation of granular flow rate shows the agreements with experiment results, the assumption of free-fall arch is difficult to be compared with the experimental results. In this proposed analytical method, the free-fall arch is assumed to be formed above the opening, while the particle velocity at the arch is assumed to be negligible. In the experiments, it is difficult to capture the free-fall arch. Although the PIV technique can be used to track the granular particle velocity, the free-fall arch is formed close to the opening. Therefore, it is difficult to measure the velocity in the experiments.

The discrete element method (DEM) is an effective approach to investigate the granular flow, which has been widely used to study the granular behavior (Hilton and Cleary, 2011). A numerical setup as shown in Figure 6.7 was used to simulate Mamtani's experiment with a particle diameter of 2.27 mm. The simulated volumetric flow rate of granular material agrees well with the experimental measurements as shown in Figure 6.8, which indicates the validity of this numerical simulation. As the discharge of granular particles in the simulation, the flow rate reaches a steady stage, which agrees well with the experimental results, and the flow rate starts to be decreased at approximately 4 seconds because not enough particles supply the granular flow. To investigate the

free-fall arch theory and verify the assumption in this analytical model, granular particles (A, B, C and D) at various locations were tracked as shown in Figure 6.7.
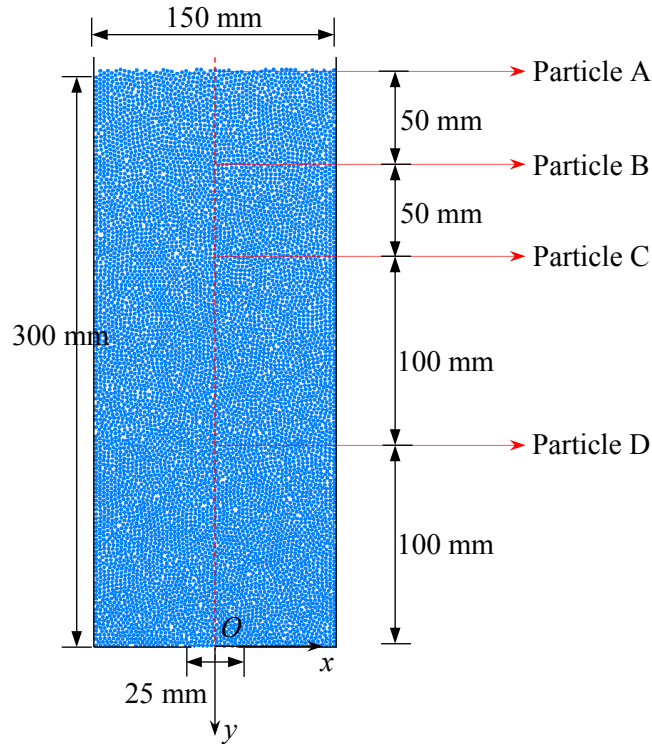
Figure 6.7 Setup of the numerical simulation
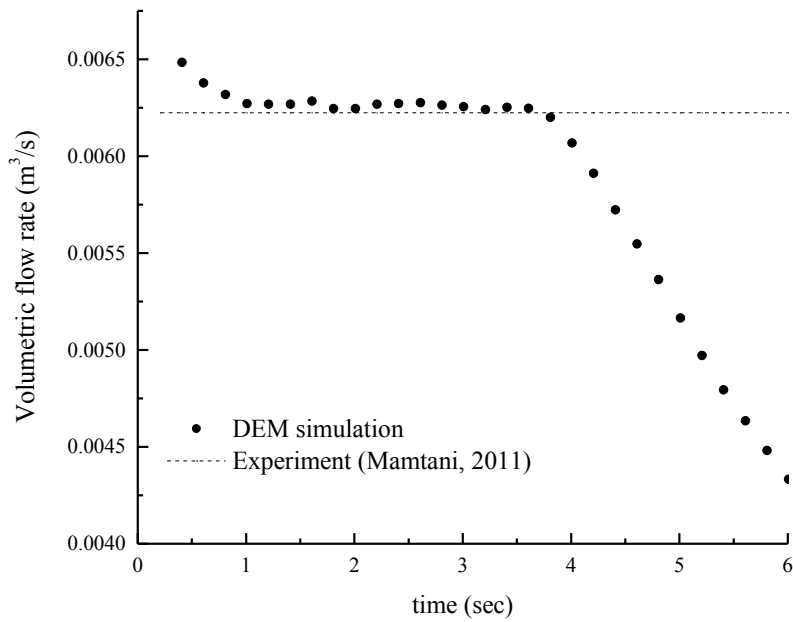
Figure 6.8 Granular volumetric flow rate from the numerical simulation

The particle velocities in the *y* direction at different time are shown in Figure 6.9. Particle A is initially located at the upper surface of the model. At the beginning of granular discharge, the velocity of particle A is significantly increased from 0 to about 0.15 m/s. After that, the particle motion reaches a quasi-steady state with a slight fluctuation of velocity due to the collision between particles. The velocity of particle A is tended to be increased with a small amount before 2.5 seconds as shown in Figure 6.9(a). At about 2.75 seconds, there is a significant decrease in velocity for particle A, while the particle velocity will be rapidly increased after that. This variation of particle velocity in Figure 6.9(a) can be used to verify the assumption of free-fall arch theory. As the particle moves adjacent to the opening, an arch is formed, at which the particle velocity is very small or even close to zero. In Figure 6.9, the change in velocity for particles B, C and D shows the similar trend as that of particle A, which also supports the free-fall arch theory. Because of different initial locations of these tracked particles, the duration from the initial location to the opening is different as shown in Figure 6.9.
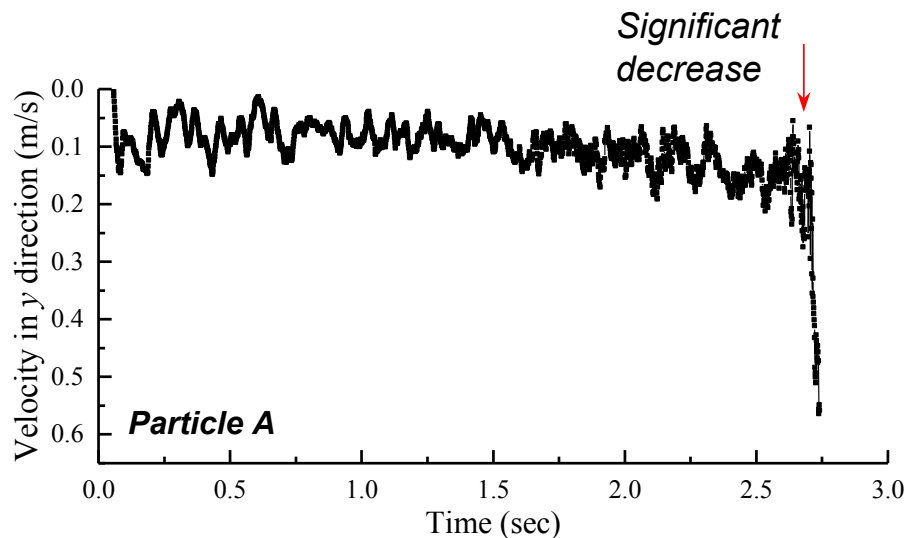
(a) Particle A
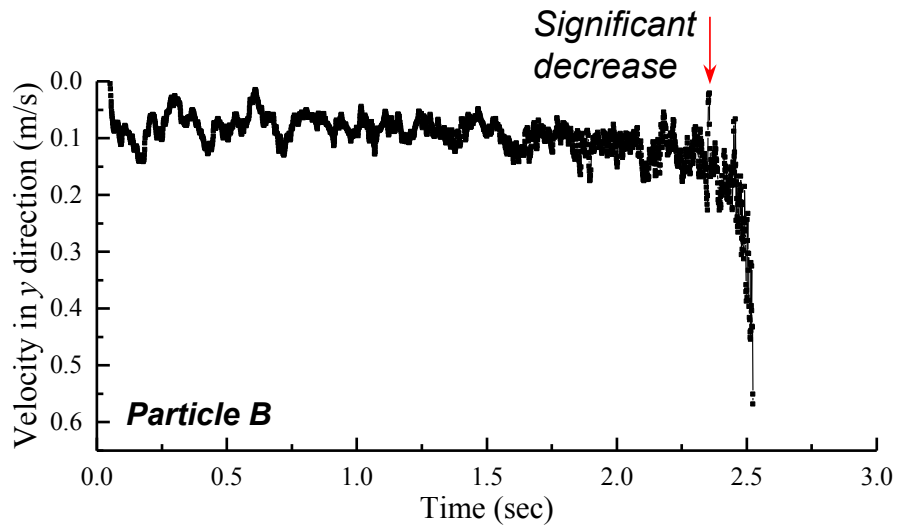
(b) Particle B
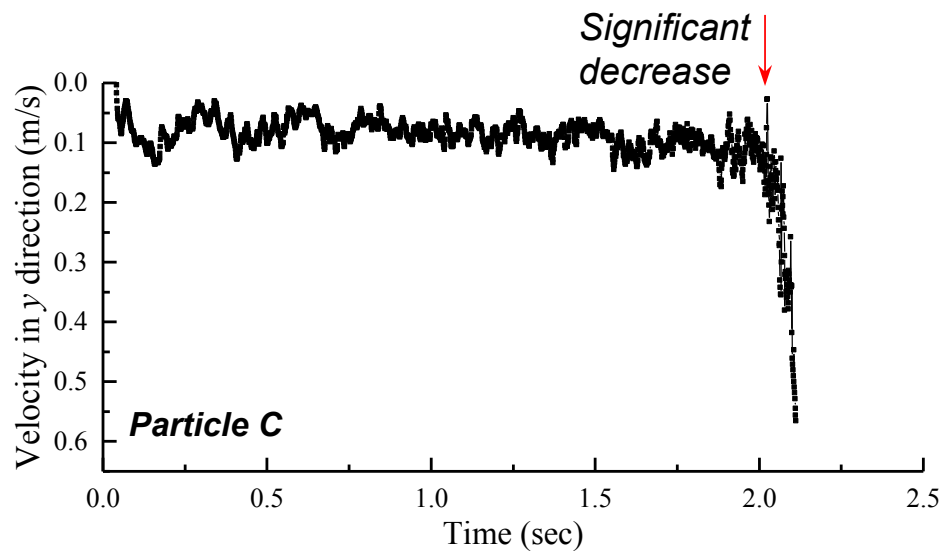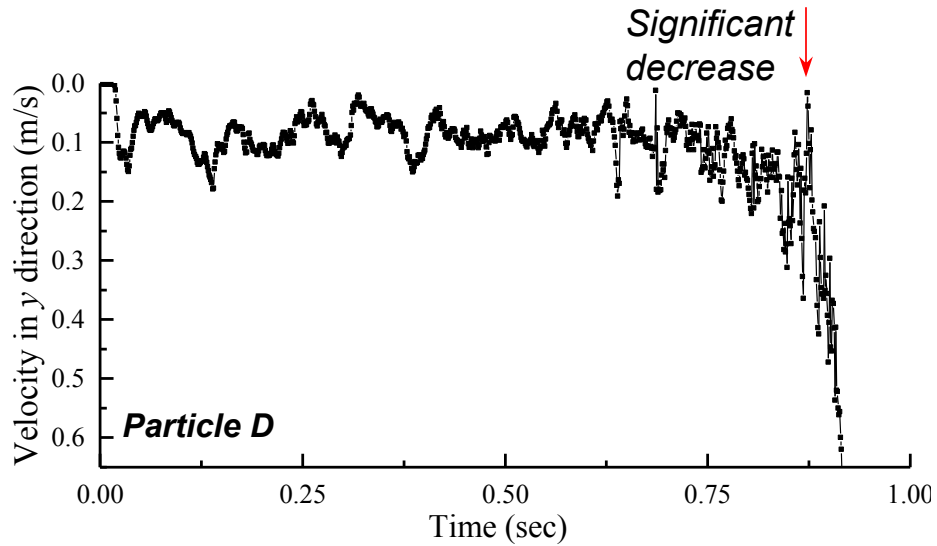
(c) Particle C

(d) Particle D

Figure 6.9 Change of different particle velocities with time: (a) Particle A; (b) Particle B; (c) Particle C; (d) Particle D;

The particle velocity at various locations are plotted in Figure 6.10(a). For all four particles being tracked, the velocity shows the fluctuation and slight increase if $y < -0.075$ m, while the velocity starts to be rapidly decreased as the free-fall arch is formed. As shown in Figure 6.10(a), the particle velocity is significantly decreased and then shows a rapid increase in the zone just above the opening (-0.075 m $< y < -0.0125$ m). The particle acceleration in the y direction supports the free-fall arch as well in Figure 6.10(b). If the particle is far away from the opening ($y < -0.075$ m), particle acceleration is small with a slight fluctuation, while it fluctuates significantly in the zone close to the opening ((-0.075 m $< y < -0.0125$ m). When the particle moves out of this zone ($y > -0.0125$ m), acceleration reaches gravitational acceleration ($g = -9.81$ m^2/s) as shown in Figure 6.10(b), which shows that the particle starts to fall freely. Because of the particle collisions, the acceleration cannot be exactly equal to gravitational acceleration.

The distance from the free-fall arch apex to the opening is determined to be 0.06 m using this proposed analytical model, which is consistent with the numerical simulation as shown in Figure 6.10(a). The size of the arch in numerical simulation is slightly smaller than the analytical prediction, which can be due to the particle collision in the discharge. In the analytical model, the particles are in the static state without the dynamic behavior. Although there is the difference between the numerical and analytical results of free-fall arch size, the particle acceleration in the free-fall zone is greater than the gravitational acceleration as shown in Figure 6.10(b) because of the particle collisions. Therefore, the difference in the granular flow rate estimation can be reduced leading to a reasonable prediction of flow rate as listed in Table 6.1.
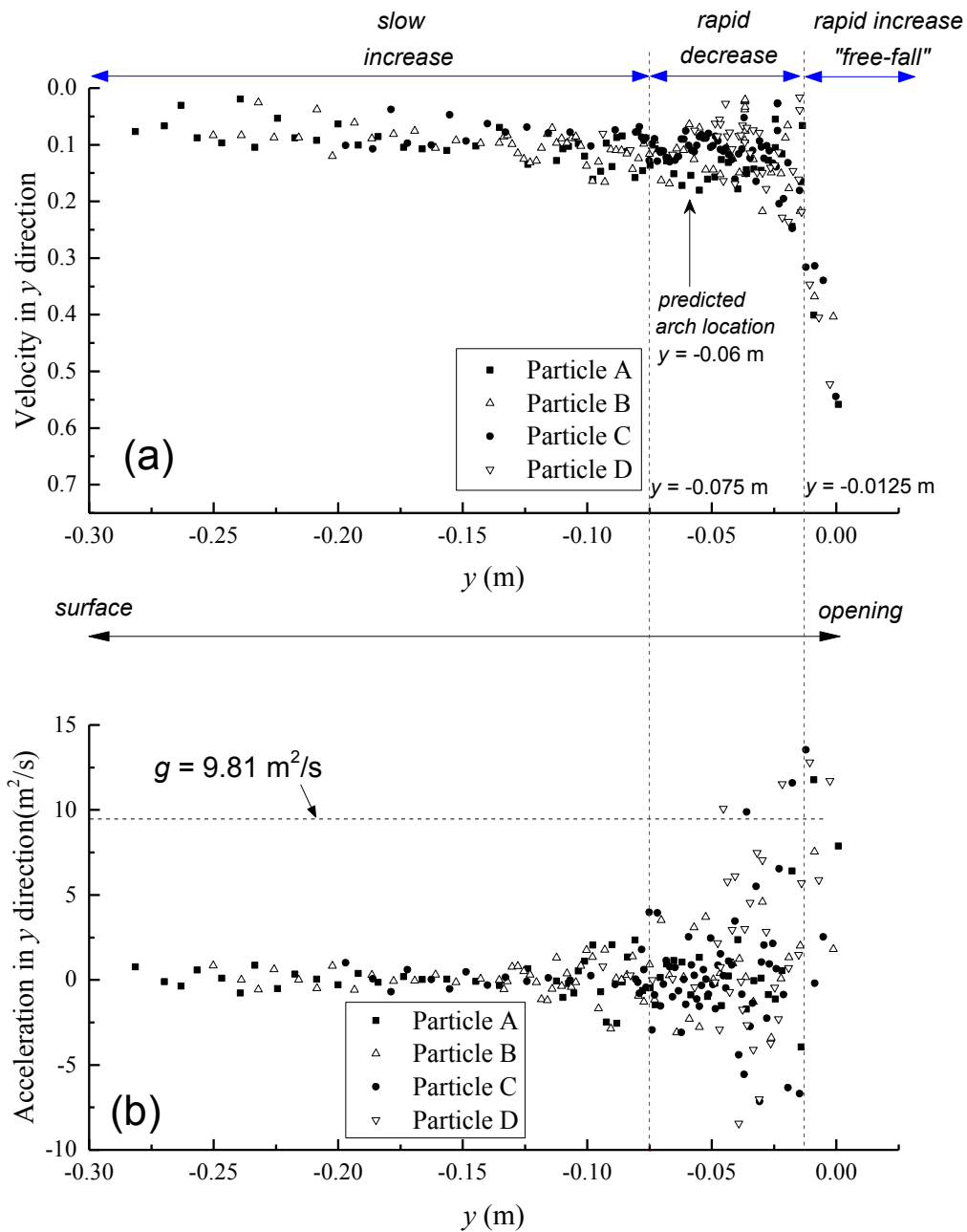
Figure 6.10 Particle velocity and acceleration in *y*-direction during the discharge

The variation of particle acceleration and velocity during the granular discharge shows the different stages of particle motion. Particles move towards the opening with a slow increase of velocity when they are far away from the opening. As particles approach to the opening, a free-

fall arch is formed, and the particle velocity suddenly decreased to a small value. After that, the particles will freely fall through the opening under gravity. Since the particle velocity at the free-fall arch is quite small and can be negligible, which is supported by the numerical simulation, the particle velocity through the opening is mostly dependent on the distance from the free-fall arch to the opening. In this proposed analytical model, this distance can be estimated, which is shown to be independent of the granular height above the arch while only related to the particle size, opening size, and granular friction.

Figure 6.11 shows the development of force chains between granular particles adjacent to the opening in numerical simulation. The forces between particles are indicated using the black curves, and the thickness of the curve shows the force magnitude. As the granular particles discharge through a two-dimensional opening, the force chain is created above the opening in the shape of an arch, whereas the force chain close to the opening is discontinuous, which indicates the particle collision and free-fall zone. In Figure 6.11(a), there are several arch-shaped force chains above the opening. The force decreases, and the arch becomes break-up as the particles flow out the opening, as shown in Figure 6.11(b). Comparing Figure 6.11(c) with 6.11(d), the arch is formed again as the particles move towards the opening. The distance between the continuous arch-shaped force chain to the opening is about 0.035 m, as shown in Figure 6.11(d), which is consistent with the measured free-fall arch zone in numerical simulation, as shown in Figure 6.10.
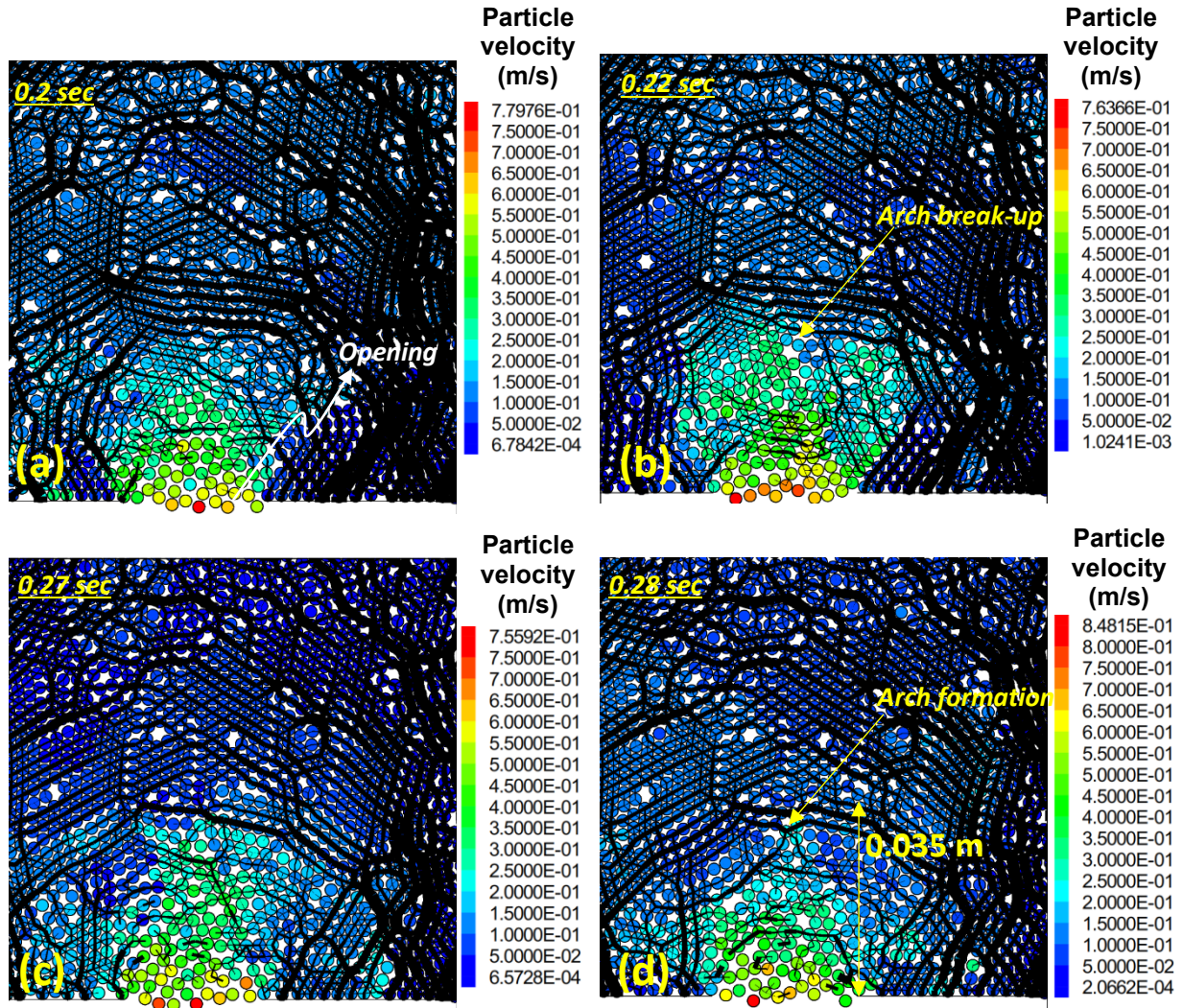
Figure 6.11 Force chain development in the granular flow through a two-dimensional opening (the black curve shows the force between particles, and the thickness indicates the force magnitude)

6.4   Summary and Conclusions

In this chapter, an analytical model is proposed to predict the free-fall arch as the granular particles flow through an opening for estimating the granular discharge rate. Experimental results and numerical simulation have been used to verify this analytical model. Based on these analytical studies, following conclusions can be obtained:

- As the granular particles discharge through an opening, the potential free-fall arch will be formed as the particles approach to the opening. The distance from the free-fall arch to the opening is independent of the granular height and the stress state above this arch, while it is only affected by the granular particle size, opening size, and granular friction.

- From the numerical simulation, the particle velocity at the free-fall arch is relatively small and can be negligible, while the particles below the arch will freely fall under the gravity. Therefore, the granular flow rate can be estimated using the analytical model of free-fall arch.

- The particle behaves under three stages from the granular surface to the opening. Above the free-fall arch, the granular particles move towards the opening with a small acceleration. When the particle moves close to the free-fall arch, the particle velocity suddenly decreased to a negligible value. Below the free-fall arch, the particle velocity will be significantly increased and freely fall through the opening under gravity.

List of Symbols

The following symbols are used in this chapter:

D	opening size, m
D_0	modified opening size, m
d_p	particle size, m
g	gravitational acceleration, m/s^2
k_p	coefficient in Beverloo's equation
h	distance from the free-fall arch to the opening, m
M	particle number in the free-fall arch
Q	granular flow rate through the opening, m^3/s
q	sum of the gravity and force applied by the particles above the free-fall arch, N
R	radius of the free-fall arch, m
s_0	distance between the free-fall arch apex and opening, m

v	particle velocity at the opening, m/s
α	Angle of the force acted on the boundary particle in the free-fall arch, °
$\Delta\theta$	Angle between any two particles in the free-fall arch, °
ε	porosity
θ	half of the central angle of the free-fall arch, °
ρ_s	particle density, kg/m^3
φ_p	friction angle between particles, °

Chapter 7 Analytical Model for the Granular and Water Flow through a Two-dimensional Opening[5]

7.1   Introduction

In Chapter 6, an analytical model was developed to predict the dry granular flow based on the free-fall arch theory. The water flow is an essential factor on the urban sinkhole formation. Therefore, a model is necessary to predict the sand flow rate considering the effect of water flow. In this chapter, an analytical model is developed in the light of free-fall arch theory, and the effect of water flow is taken into account using Stokes' law. This proposed analytical model is verified comparing with the experimental results, and numerical simulations using the coupled discrete element model are conducted to support this analytical model and analyze the granular flow through an opening considering the effect of water flow.

7.2   Analytical Model

7.2.1   Motion of the granular particle

The schematic of this analytical model for the granular flow through an opening considering the water flow is shown in Figure 7.1. The particles in the zone adjacent to the opening move freely based on the free-fall theory, and the driving force by the water flow will be taken into account in this study. In this analytical model, v_f is the water velocity in the granular particle free-fall stage, while vs is the granular particle velocity. In this derivation, the water velocity v_f is assumed to be

---

[5] This chapter is currently being prepared as a journal manuscript: Tang, Y., Chan, D. H. and Zhu, D. Z. (2017). "Analytical Model for Granular and Water Flow through a Two-dimensional Opening." *ASCE Journal of Engineering Mechanics*, to be submitted.

constant from the free-fall arch to the opening, which is reasonable considering the small scale of free-fall arch and water flow continuity.
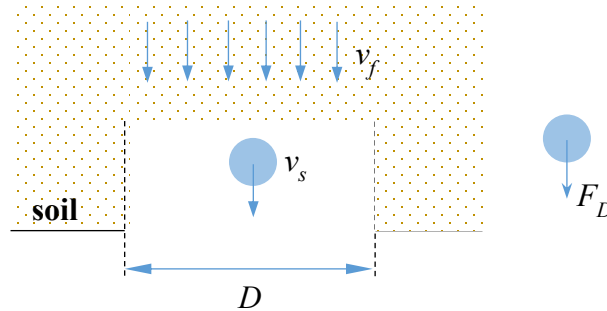
Figure 7.1 Schematic of granular particle motion considering the effect of water flow

The driving force on the granular particle due to relative velocity can be determined using Stokes' law:

$$F_D = 3\pi\mu d_p \left(v_f - v_s\right) \tag{7.1}$$

where, d_p is the granular particle diameter; μ is the dynamic viscosity of fluid; v_f is the fluid velocity; v_s is the granular particle velocity.

The free-body diagram of the granular particle is shown in Figure 7.1. If the gravity is neglected, the Newton's second law of an individual granular particle is:

$$F_D = m\frac{dv_s}{dt} \tag{7.2}$$

where, m is the mass of an individual granular particle, and can be determined as: $m = \pi d_p^3 \rho_s \Big/ 6$

Substituting the driving force from Eq. (7.1) into Eq. (7.2):

$$\frac{dv_s}{dt} + \frac{3\pi\mu d_p}{m}v_s = \frac{3\pi\mu d_p}{m}v_f \tag{7.3}$$

Eq. (7.3) is a 1st order ordinary differential equation in the term of v_s, which can be solved:

$$v_s = C_1 e^{-\frac{3\pi\mu d_p}{m}t} + e^{-\frac{3\pi\mu d_p}{m}t} \int \frac{3\pi\mu d_p}{m} v_f e^{\frac{3\pi\mu d_p}{m}t} dt$$

$$= C_1 e^{-\frac{3\pi\mu d_p}{m}t} + v_f$$

(7.4)

where, C_1 is a constant, and can be determined from the initial condition.

Initially, the particle is at the free-fall surface with a negligible velocity, which has been accepted by Hilton and Cleary (2011), and the numerical results in Chapter 6 also supports this assumption. Therefore, the initial condition is: @$t = 0$, $v_s = 0$. The constant C_1 in Eq. (7.4) can be determined: $C_1 = -v_f$. The granular velocity is:

$$v_s = -v_f e^{-\frac{3\pi\mu d_p}{m}t} + v_f$$

(7.5)

If the free-fall arch theory is introduced, the size of free-fall arch s_0 can be determined using the analytical model proposed in Chapter 6. If the time for the granular particle from the free-fall arch to the opening is t_0, we have:

$$s_0 = \int_0^{t_0} v_s dt = \int_0^{t_0} v_f \left(1 - e^{-\frac{3\pi\mu d_p}{m}t}\right) dt$$

(7.6)

After integration and simplification of Eq. (7.6), we have:

$$t_0 - \frac{e^{At_0}}{A} + \frac{1}{A} + B = 0$$

(7.7)

where, $A = -\frac{3\pi\mu d_p}{m}$, $B = -\frac{s_0}{v_f}$

Therefore, the time t_0 can be solved from Eq. (7.7):

$$t_0 = -B - W\left(-\frac{e^{-AB-1}}{A} - \frac{1}{A}\right) \tag{7.8}$$

where, W is the Lambert-W function. Although this Lambert-W function can be calculated using the mathematical software, it is difficult in practical application. If the Taylor approximation is introduced, an approximated function of the exponential function in Eq. (7.7) is:

$$e^{At_0} = 1 + At_0 + \frac{A^2}{2}t_0^2 \tag{7.9}$$

Therefore, Eq. (7.7) can be simplified:

$$t_0^2 - \frac{2B}{A} = 0 \tag{7.10}$$

Thus,

$$t_0 = \sqrt{2B\big/A} = \sqrt{\frac{2ms_0}{3\pi\mu d_p v_f}} \tag{7.11}$$

If the granular particle velocity at the opening is v_{s0}, the corresponding water flow velocity is v_{f0}. The relationship between v_{s0} and v_{f0} can be determined by plugging Eq. (7.11) into Eq. (7.5):

$$v_{s0} = v_{f0}\left(1 - e^{-\frac{3\pi\mu d_p}{m}\sqrt{\frac{2ms_0}{3\pi\mu d_p v_{f0}}}}\right) \tag{7.12}$$

7.2.2   Water flow velocity

An approximated analytical solution was proposed to estimate the water infiltration rate through the pipe defect by Guo et al. (2013b), and water velocity v_{f0} at the opening can be simply calculated as:

$$v_{f0} = \frac{2\pi k \left(h_s + h_w \right)}{nD \ln \dfrac{4\pi h_s}{D}}$$

(7.13)

where, h_s is the sand layer height; h_w is the water layer height; D is the opening width; k is the sand

permeability and can be estimated using the Kozeny-Carman equation:

$$k = \frac{\rho_f g d_p^2 n^3}{180 \mu \left(1 - n \right)^2}$$

(7.14)

7.2.3 Sand and water flow rate through the opening

After determining the water velocity from Eq. (7.14), the granular particle velocity at the

opening can be calculated using Eq. (7.12). After that, the water flow rate q_f and sand flow rate q_s

per unit width for the two-dimensional condition can be determined as:

$$q_f = v_{f_0} Dn$$

(7.15)

$$q_s = v_{s0} D \left(1 - n \right)$$

(7.16)

7.3   Results and Discussion

7.3.1   Verification with experimental results

This analytical model was verified in comparison with the experimental results in Chapter 3. The

experiments were conducted to simulate the submerged sand erosion through a two-dimensional

slot on the defective pipe. As shown in Figure 7.2(a), the sand and water flow rate were measured

for the fine sand with the diameter of 0.17 mm through a defect with the width of 3 mm. The

predicted sand flow rate agrees well with the experimental results. The medium sand with a

diameter of 0.97 mm was used in the experiments, and the opening width was 3 mm. The analytical

results for the medium sand are consistent with the measurement as shown in Figure 7.2(b). The analytical model was proposed using Stokes' law, which causes the exponential relationship between the sand and water flow rate. If the gravity is neglected, the sand particle motion is only induced by the water flow. At a small water velocity, the motion of a sand particle can be significantly triggered. At a larger water flow velocity, the effect of water flow on the granular particle motion is decreased since the driving force is proportional to the relative velocity between the water and granular particle. Therefore, the proposed exponential analytical relationship is reasonable.
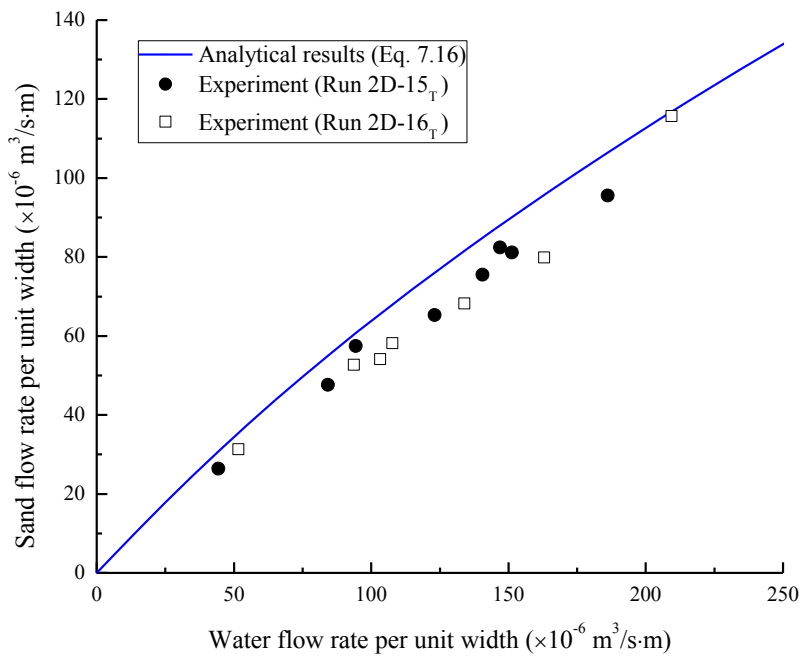
(a)
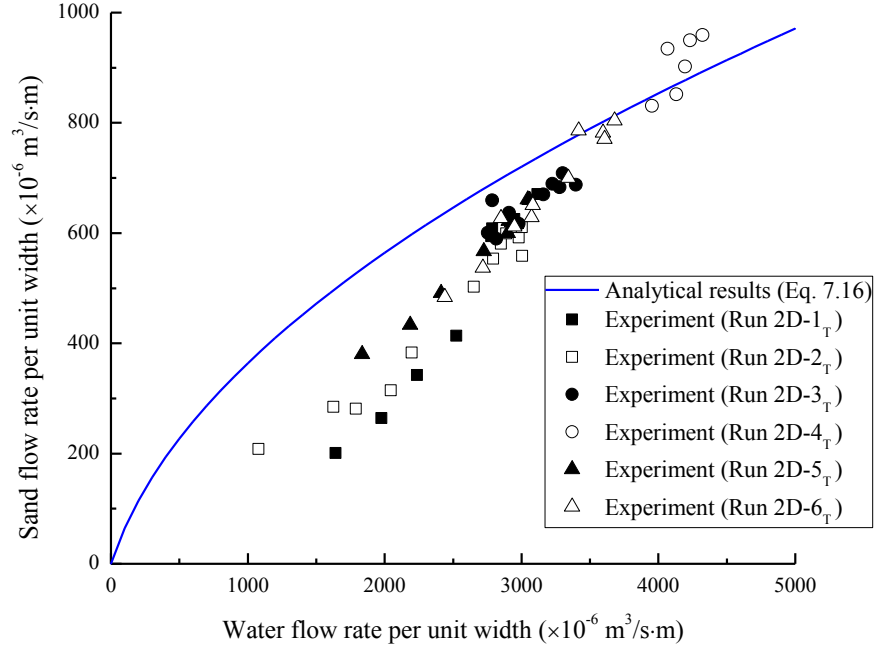
(b)

Figure 7.2 Predicted sand and water flow rate relationship in comparison with experimental
results: (a) $d_p = 0.17$ mm, $D = 3$ mm; (b) $d_p = 0.97$ mm, $D = 3$ mm

7.3.2 Numerical simulation using a coupled discrete element model

Numerical simulations were conducted to simulate the submerged sand erosion through the pipe

defect in a two-dimensional condition. A similar coupled discrete element model in Chapter 5 was

used, and Figure 7.3(a) shows the numerical mesh of the fluid domain. Because of the semi-circular

pipe, the governing equation in the polar coordinates was used:

$$\frac{1}{r}\left(k_r\,\frac{\partial\phi}{\partial r}\right)+\frac{\partial}{\partial r}\left(k_r\,\frac{\partial\phi}{\partial r}\right)+\frac{1}{r}\frac{\partial}{\partial\theta}\left(k_\theta\,\frac{1}{r}\frac{\partial\phi}{\partial\theta}\right)=n\beta_f\gamma\frac{\partial\phi}{\partial t} \tag{7.14}$$

where, k_r and k_θ are the coefficients of permeability in the radial and tangential directions; t

indicates time; ϕ is the total fluid head, which consists of the pressure head p/γ and elevation head

z, where γ is the unit weight of water; and β_f is the fluid compressibility, which is normally

considered as 4.4×10^{-10} Pa^{-1} when water flows through porous media (Freeze and Cherry, 1979).

Based on Darcy's law, the water velocity in the radial and tangential direction can be calculated:

$$\begin{cases} v_r = k_r \dfrac{\partial \phi}{\partial r} \\ v_\theta = k_\theta \dfrac{1}{r} \dfrac{\partial \phi}{\partial \theta} \end{cases}$$

(7.15)

For the coupling calculation, the water velocities in Cartesian coordinates are:

$$\begin{cases} v_x = v_r \cos\theta - v_\theta \sin\theta \\ v_z = v_r \cos\theta + v_\theta \cos\theta \end{cases}$$

(7.16)

In this simulation, the sand surface is the total water head boundary condition. If the bottom of the model is taken as the datum plane, the initial total water head at the sand surface is 0.45 m, while it will be updated after each coupling time step based on the mass conservation of water to simulate the decrease of the water level. Since water can freely flow through the defect, the pressure head at the defect is zero, which indicates that the total water head at defect is equal to the elevation head. From Eq. (7.14), the permeability is proportional to $e^3/(1+e)$, where e is the void ratio of soil. The initial sand porosity in the experiment is 0.4, and the permeability is calibrated to be 0.074 m/s to match the measured water flow rate. Thus, the change of permeability can be calculated based on the change of soil void ratio. The initial total water head distribution and water flow field are plotted in Figure 7.3(b).
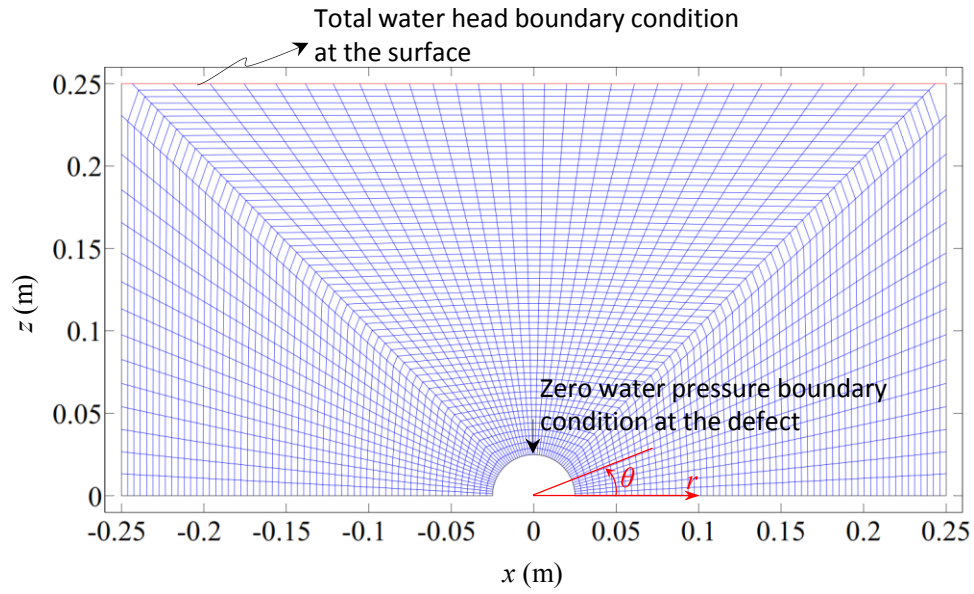
(a)
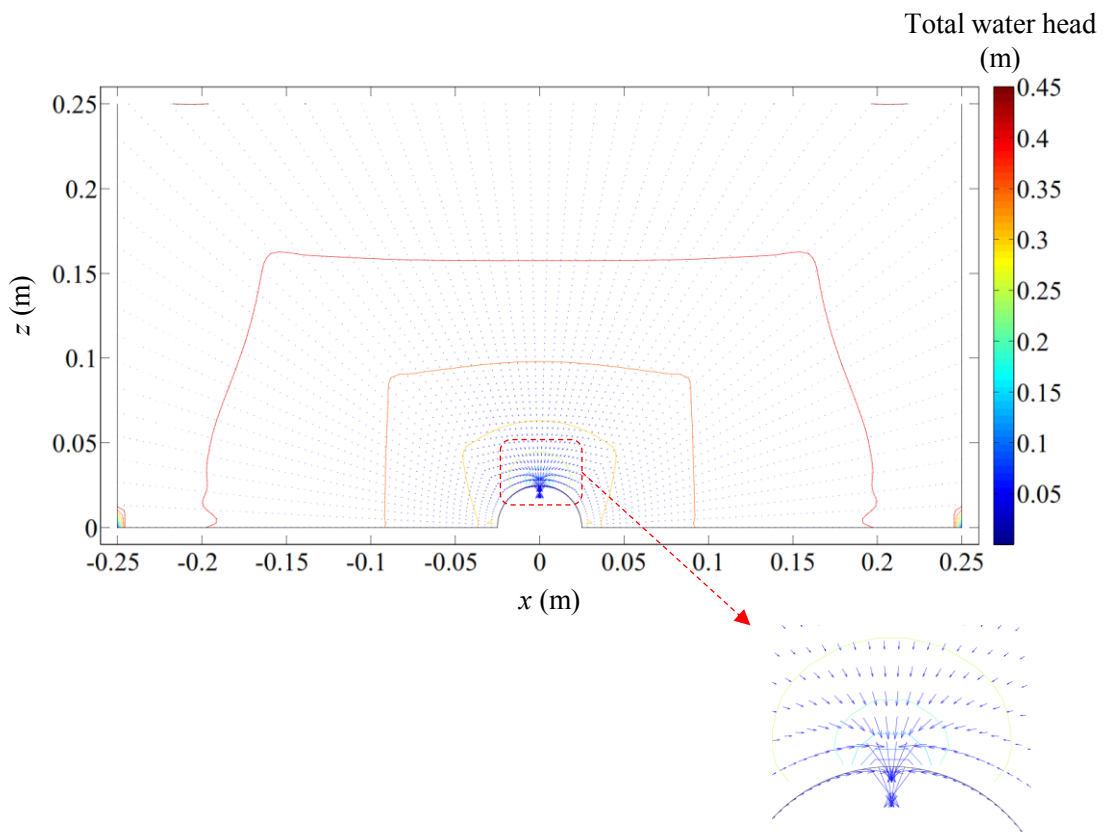
(b)

Figure 7.3 Numerical simulation of the fluid domain: (a) Numerical setup of the fluid domain;(b) Initial water head distribution and fluid flow field.

The numerical setup using discrete element method for the solid phase is shown in Figure 7.4. Although the experiment and proposed analytical model are under the two-dimensional condition, the behavior of granular particles will be affected if the granular particle is simulated as the disk with the two-dimensional assumption. Therefore, the granular particles are simulated in the three-dimensional condition using PFC^{3D}, while only the middle part of the whole experimental domain is simulated considering the computing cost. From the experimental visualization analysis in Chapter 3, this simplification is reasonable since the sand mobilized zone is mostly in the middle zone above the opening.
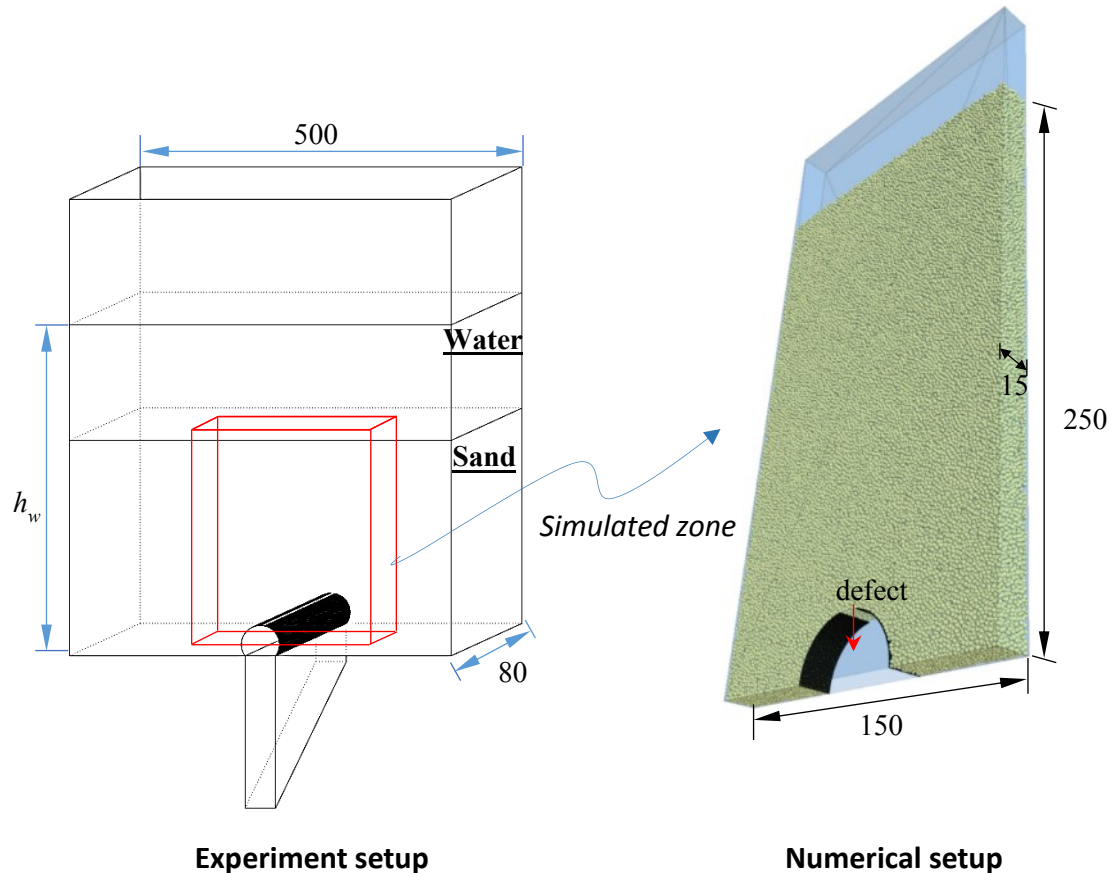
Figure 7.4 Numerical setup for the solid phase using DEM

In this numerical simulation, the width of numerical setup is 0.015 m, which is ten times greater than the mean particle size to avoid the particle jamming (Sheldon and Durian, 2010). The particle size distribution in this numerical simulation is shown in Figure 7.5, which is similar to the experiments, and 137,916 particles are generated in this numerical setup. The coupling effect between the solid and fluid phase is taken into account by calculating the buoyancy and drag force on the granular particles. The buoyancy is determined based on Eq. (5.4), and the drag force is calculated using Eq. (5.5). The implementation scheme in Figure 5.1 is used to consider the coupling effects. The simulation is started by the DEM simulation using PFC^{3D}, and and the particle information (particle positions, velocities, particle radii) will be imported into the fluid calculation by updating the permeability using the calculated porosity from DEM simulation. After that, the water flow simulation will be conducted to determine the water flow filed, and then the drag force on each DEM particle can be calculated and imported back into the DEM simulation. This coupling cycle will be again and again until reaching the required calculation steps.
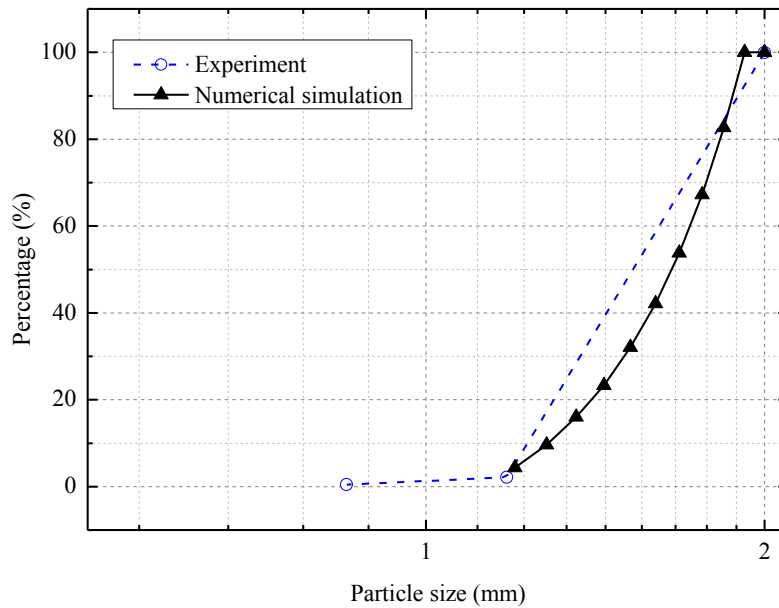
Figure 7.5 Particle size distribution in the DEM simulation

The parameters of the solid phase are listed in Table 7.1. Due to the enormous amount of particles, the model was generated layer by layer to avoid the unbalanced force. From Figure 7.6(a), the stress σ_z in the generated numerical model measured by the measurement sphere is consistent with the theoretical estimation. The stress σ_z theoretically can be determined as: $\sigma_z = \rho_s g (1-n)(h_s - z)$, where ρ_s is the sand particle density, n is the porosity, g is the gravitational acceleration, H is the total sand height, z is the coordinate in z-direction. For the calibration, the total water head at the sand surface is 0.45 m which is the same as the water head in experiment Run 2D-14$_\text{T}$. The predicted sand and water flow rate from this DEM simulation agrees well with the experimental measurements as shown in Figure 7.6(b). In this simulation, the water head at the sand surface boundary is updated based on the water mass conservation to simulate the decrease of water level. In Figure 7.6(c), the simulated water level variation is consistent with the experimental measurements.

Table 7.1 Parameters in the numerical simulation of the submerged sand erosion through a two-dimensional pipe defect

Soil phase	
Particle density (kg/m^3)	2600
Particle friction coefficient	0.50
Particle normal stiffness (N/m)	1.00×10^8
Particle shear stiffness (N/m)	1.00×10^8
Damping	0.10
Porosity of granular material	0.40
Fluid phase	
Density (kg/m^3)	1000
Viscosity (Pa·s)	0.001
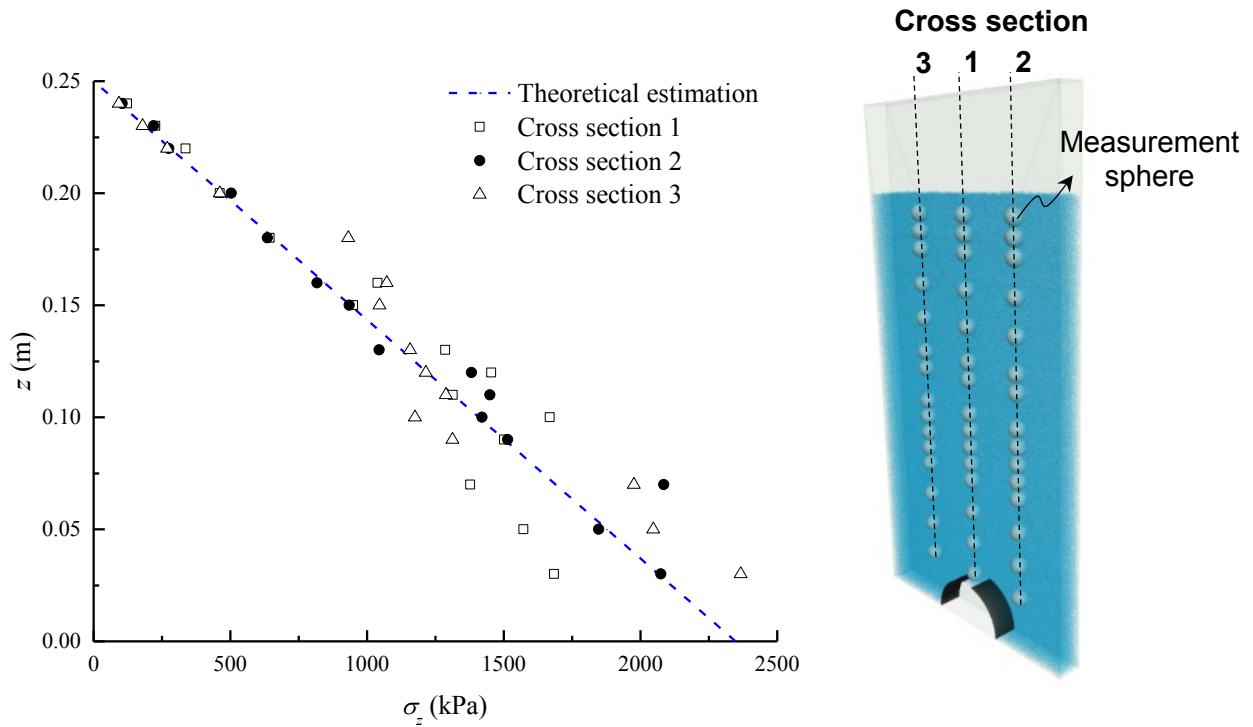
(a) Comparison of measured vertical stress in DEM model with theoretical estimation
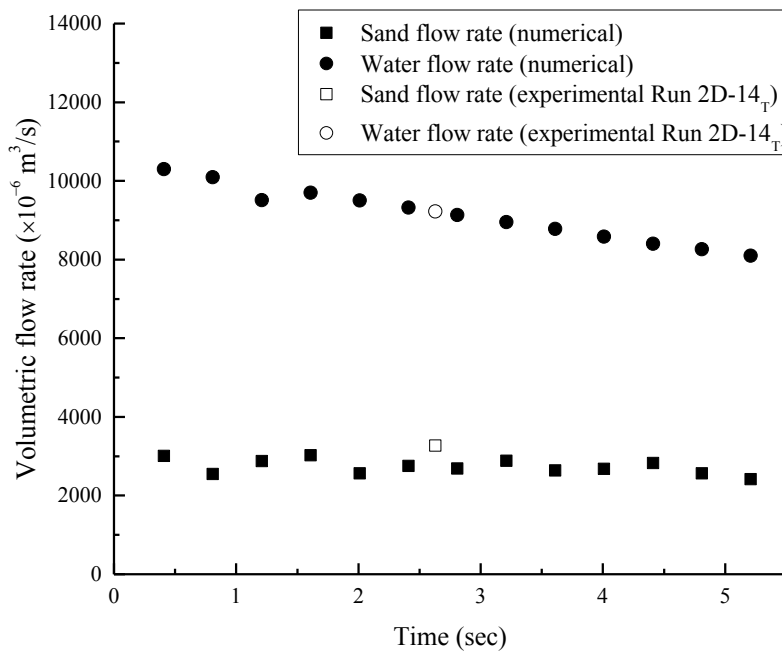
(b) Comparison of sand and water flow rate in numerical simulations with experiment results
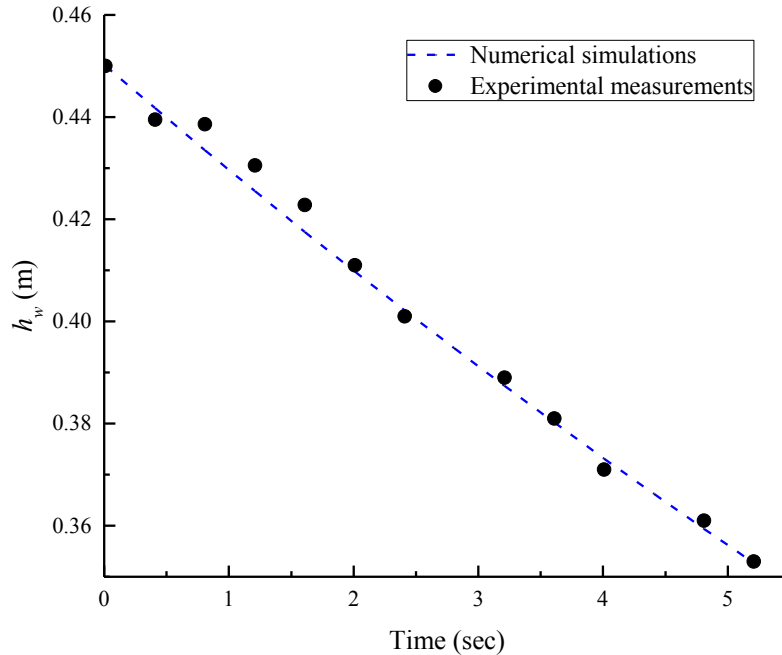
(c) Comparison of the water level in numerical simulations with experimental results

Figure 7.6 Numerical simulation of experiment Run 2D-14$_T$ using DEM

Figure 7.7 shows the sand particle mobilization through the center plane ($y = 0$) of this model. It can be found that the particle mobilization is similar to the experimental observation as shown in Figure 3.3. The mobilization of sand particle starts in a narrow zone just above the pipe defect, which can be found in Figure 3.3 from 0.2 sec to 0.5 sec. As the loss of sand particles, an erosion void starts to be formed from the sand surface at 1 sec. The erosion void will be expanded till reaching the pipe defect from 1.5 sec to 5 sec.
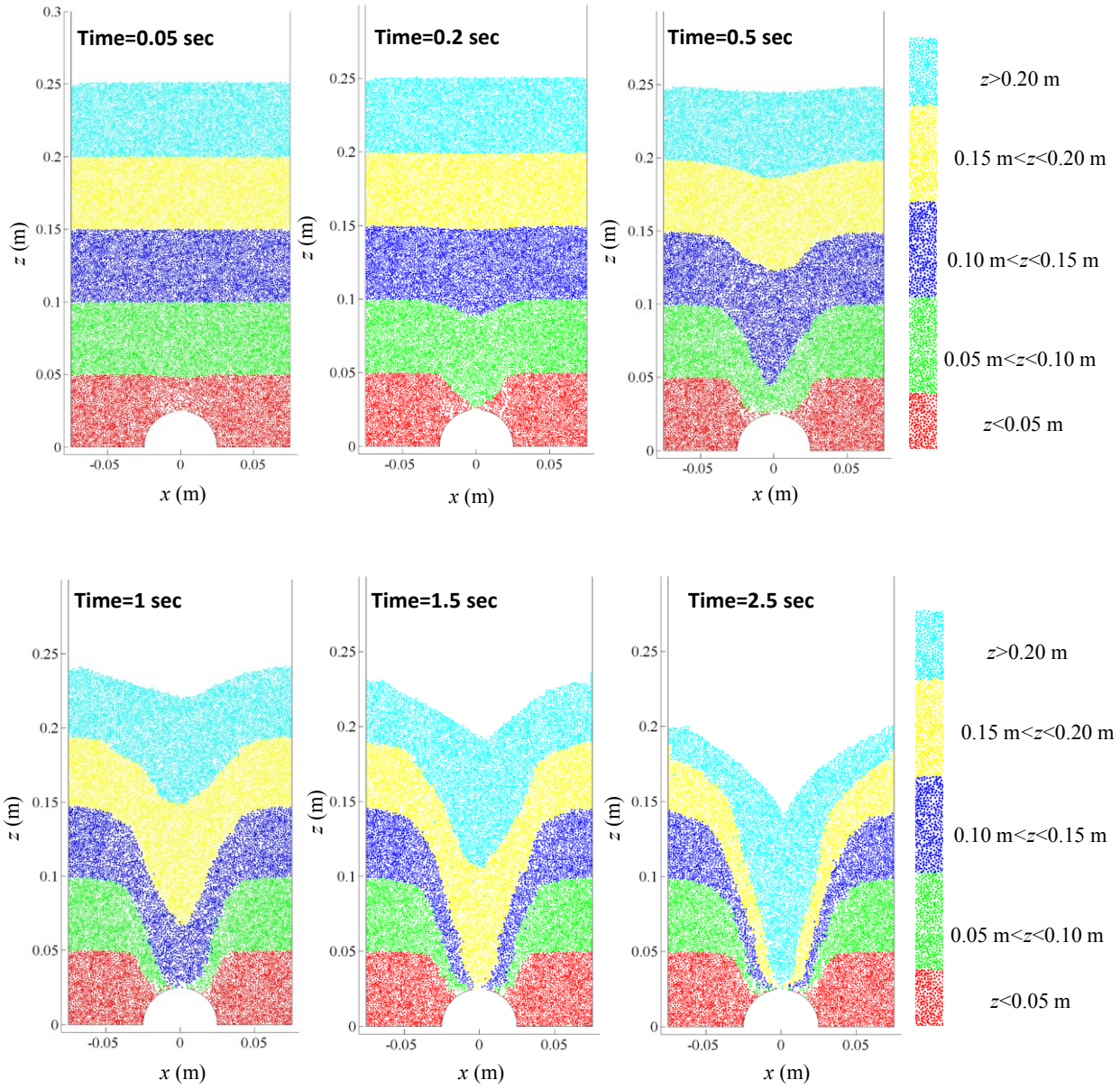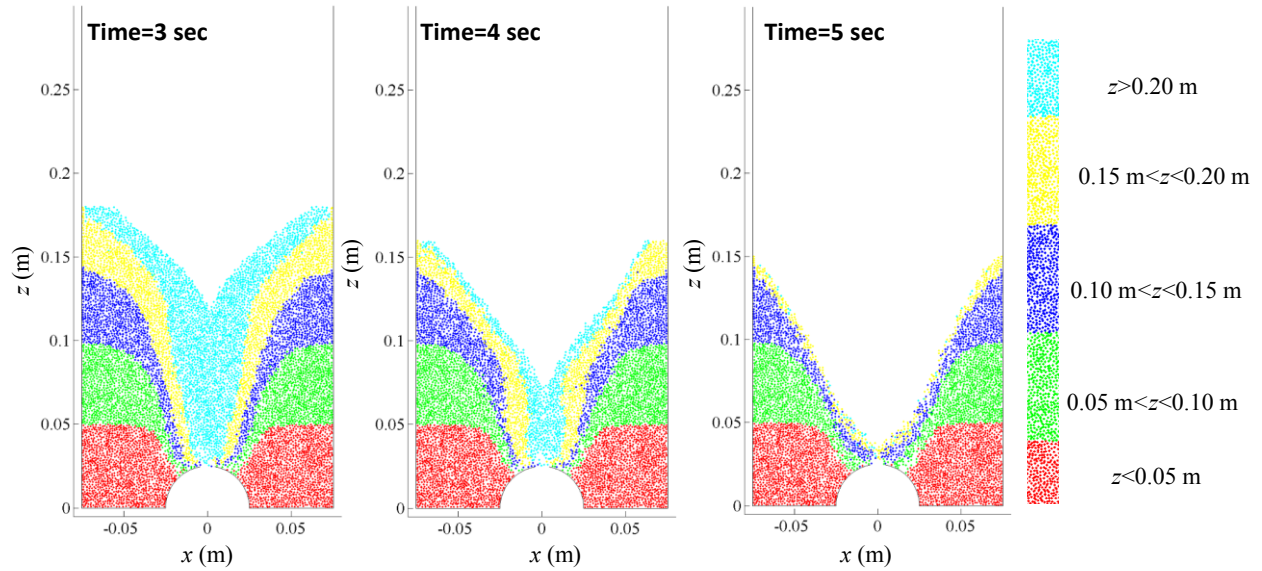
Figure 7.7 Observations of the sand erosion through the center plane using DEM at different time

It has been found that the water and sand flow rate shows steady relationship at the beginning erosion stage (Guo et al., 2013a). By changing the total water head at the sand surface boundary, the water flow rate through the defect changes, while the corresponding sand flow rate can be obtained from the numerical simulation. Two simulations with different initial h_w ($h_w = 0.675$ m and 0.32 m) were conducted. As shown in Figure 7.8, the relationship obtained from this proposed analytical model is consistent with the numerical and experimental results, which indicates the accuracy of this analytical model and also supports the validity of this numerical simulation.
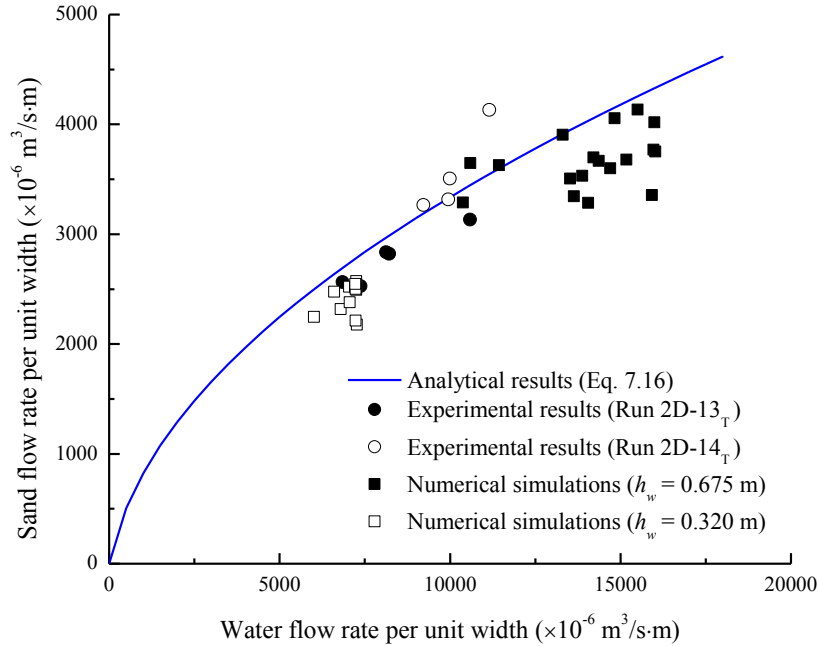
Figure 7.8 Numerical results comparing with the experimental results

The development of force chains between particles is shown in Figure 7.9. The black curves are the forces between the sand particles in this numerical simulation, while the thickness of curve shows the force magnitude between particles. It can be found that an arch with a continuous force chain is formed close to the pipe defect at Figure 7.9(a), while the force chain breaks up in Figure 7.9(b) indicating the break-up of the arch above the pipe defect. After that, a continuous force chain tends to be formed again in Figure 7.9(c), which is destructed in Figure 7.9(d) as the sand particle mobilization. Due to the formation and break-up of the arch, the sand flow rate keeps steady and is independent of the sand particle behavior above this arch boundary.
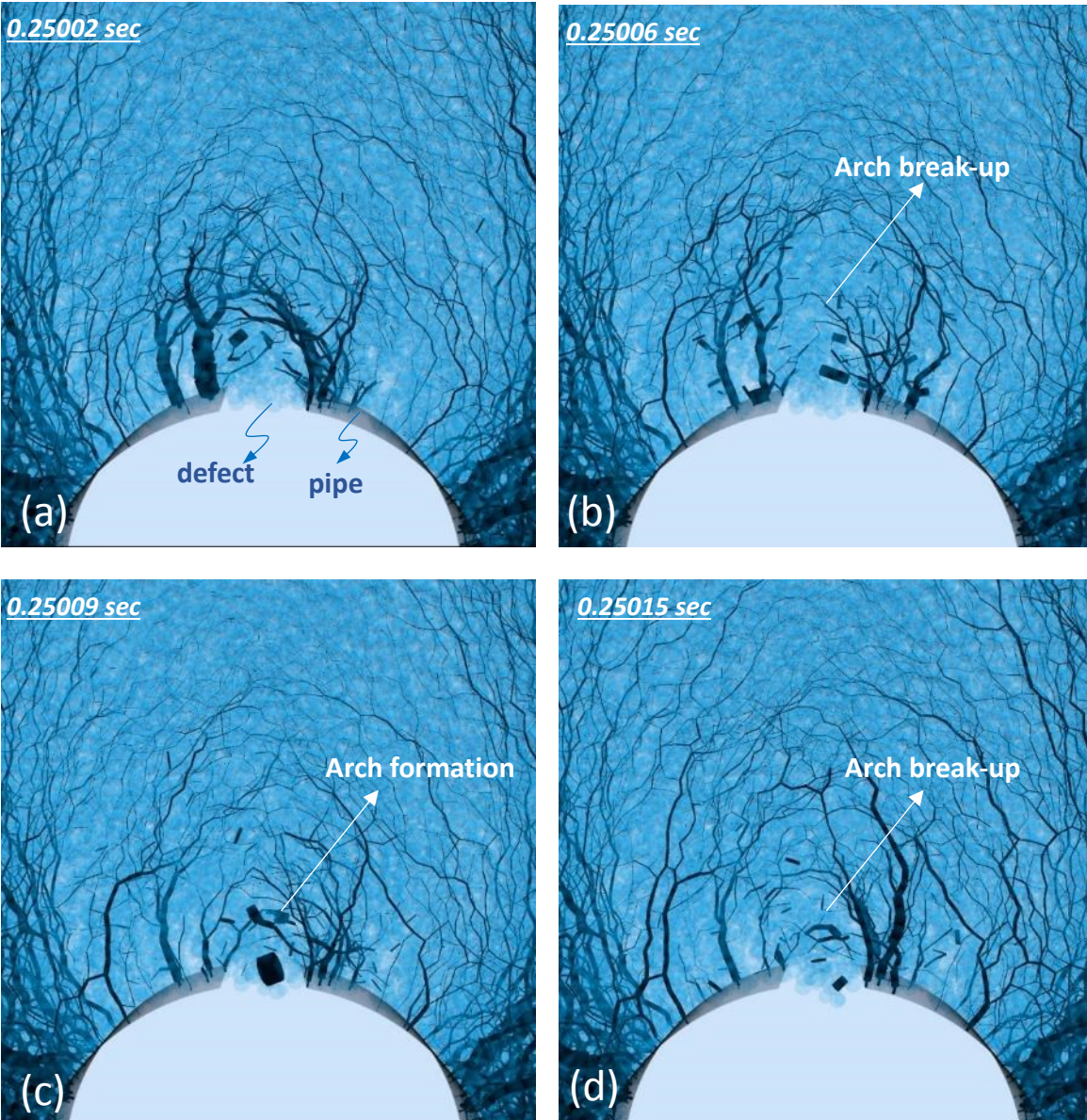
Figure 7.9 Force chain development in the sand erosion (the black curve shows the force between particles and thickness indicates the magnitude)

7.4   Summary and Conclusions

In this chapter, an analytical model was proposed to estimate the granular and water flow rate through an opening in the two-dimensional condition. From the Stokes' law, the granular particle motion is related to the water flow, which can be calculated using the previously developed model (Guo et al., 2013b). By introducing the free-fall arch theory, the granular flow rate through an

opening driven by the water flow can be calculated. The analytical results using this proposed model shows agreement with the experimental results. Numerical simulations using a coupled discrete element model also supports this analytical model, and the force chain analysis from the numerical results shows the reasonability of analytical model.

List of Symbols

The following symbols are used in this chapter:

D	opening size, m
d_p	particle size, m
e	void ratio
F_D	drag force on the granular particle, N
g	gravitational acceleration, m/s^2
h_s	height of the sand layer, m
h_w	height of the water layer, m
k	permeability, m/s
k_r	permeability in the radial direction, m/s
k_θ	permeability in the tangential direction, m/s
m	mass of an individual particle, kg
n	porosity
p	water pressure, Pa
q_f	water flow rate per unit width, m^3/s/m
q_s	sand flow rate per unit width, m^3/s/m
s_0	distance between the free-fall arch apex to the opening, m
t_0	time of particle moving from the free-fall arch to the opening
v_f	water velocity, m/s
v_{f0}	water velocity at the opening, m/s
v_s	sand particle velocity, m/s
v_{s0}	sand particle velocity at the opening, m/s

β_f	fluid compressibility, Pa^{-1}
γ	unit weight of water, kN/m^3
μ	fluid dynamic viscosity, Pa s
ρ_f	fluid density, kg/m^3
ρ_s	sand particle density, kg/m^3
σ_z	Stress in the vertical direction, Pa
ϕ	total water head, m

Chapter 8 Numerical Investigation of Sand-Bed Erosion by an Upward Water Jet[6]

8.1   Introduction

Another scenario of the urban sinkhole formation is due to the soil erosion by the water exfiltration through the pipe defect if there is a heavy rainfall, which can be simplified as the sand-bed erosion by an upward water jet. In this chapter, the computational fluid dynamics (CFD) technique combined with granular kinetic theory will be applied to investigate the sand-bed erosion behavior, and the commercial software (ANSYS Fluent 15.0) with the Eulerian approach will be used in this simulation. The numerical model is firstly verified by comparison with experiment results. The onset of sand-bed erosion is then explored to understand the mechanism of erosion. Furthermore, the effects of various factors on sand-bed erosion under a water jet is investigated through a numerical technique. Based on the mechanism revealed from the numerical simulations, a general analytical model is proposed to determine the critical water inlet velocity leading to the sand-bed erosion.

8.2   Numerical Model

The simulation of sand-bed erosion due to an upward water jet was conducted using CFD and granular kinetic theory using the commercial software ANSYS. The detailed theoretical basis of this numerical technique can be found in the software's manual (ANSYS, 2013) on the multiphase model, and the related models used in this study are listed in the Appendix C. Because this is a multiphase Eulerian model, the mass and momentum conservation laws for each phase were

---

[6] This chapter was accepted for publication in: Tang, Y., Chan, D. H. and Zhu, D. Z. (2017). "Numerical Investigation of Sand-Bed Erosion by an Upward Water Jet." *ASCE Journal of Engineering Mechanics*. DOI: 10.1061/(ASCE)EM.1943-7889.0001319

applied. The fluid turbulent property was taken into account using the standard k-ε model, which simulates the mean flow characteristics for the turbulent conditions satisfying the transport equations for turbulent kinetic energy k and turbulent dissipation ε. The granular temperature is defined as a measure of the specific kinetic energy of the velocity fluctuations or translational fluctuation energy resulting from the particle velocity fluctuations (Gidaspow et al., 1991). The granular bulk viscosity was calculated using the model by Lun et al. (1984), and the resistance of the emulsion to compression or expansion can be taken into consideration.

The model of the frictional viscosity proposed by Schaeffer (1987) was applied in this numerical framework. Kinetic viscosity was obtained using the model by Syamlal et al. (1993). Unlike the momentum conservation of fluid, momentum exchange occurred due to the collision of particles, and the collisional part of the shear viscosity was modeled using the equation by Gidaspow et al. (1991). The momentum transfer was taken into account as the interaction between the fluid and solid phase in this chapter. The momentum transfer was described by calculating the transfer forces between the two phases using the model of drag force by Gidaspow et al. (1991). This model combines the Ergun equation (1952) for the high-solid-fraction condition with Wen and Yu (1966) for the low-solid-fraction condition. The governing equations and constitutive models used in this chapter are briefly described in Appendix C.

8.2.1   Verification of the Two-dimensional Model

Two-dimension sand-bed erosion by injecting water through a bottom slot was studied by Alsaydalani and Clayton (2014) experimentally. Their 2D experimental results will be used to verify the numerical model. The schematic of the numerical model is shown in Figure 8.1. The dimension of this 2D numerical model is 600×300 mm ($L{\times}H$). The sand bed is set to be fully immersed in water of a height of 300 mm, and the water height was 100 mm above the sand layer.

The water inlet was located at the bottom of the model with a width denoted by din, and the water velocity at the orifice was initially set to be 3.22 m/s based on experimental observations. The water surface was defined as a zero-pressure outlet for the free water outflow. The parameters used in the numerical simulation are listed in Table 8.1, which are the same as those in the experiment conducted by Alsaydalani and Clayton (2014). The parameters in Table 8.1 with underlines are used in the base case for verification, while other values are used to investigate the effects of the factors.

The phase-coupled SIMPLE (Semi-Implicit Method for Pressure-Linked Equations) algorithm (Vasquez and Ivanov, 2000) as an extension of the SIMPLE algorithm to multiphase flows, which has been incorporated in ANSYS, was used to solve the model numerically. As listed in Table 1, the time step in this model was 0.0001 seconds, and 50 seconds was simulated in this condition. In the present numerical study, simulations were performed on a desktop with an Intel i7-4770 CPU and 24 GB of RAM.
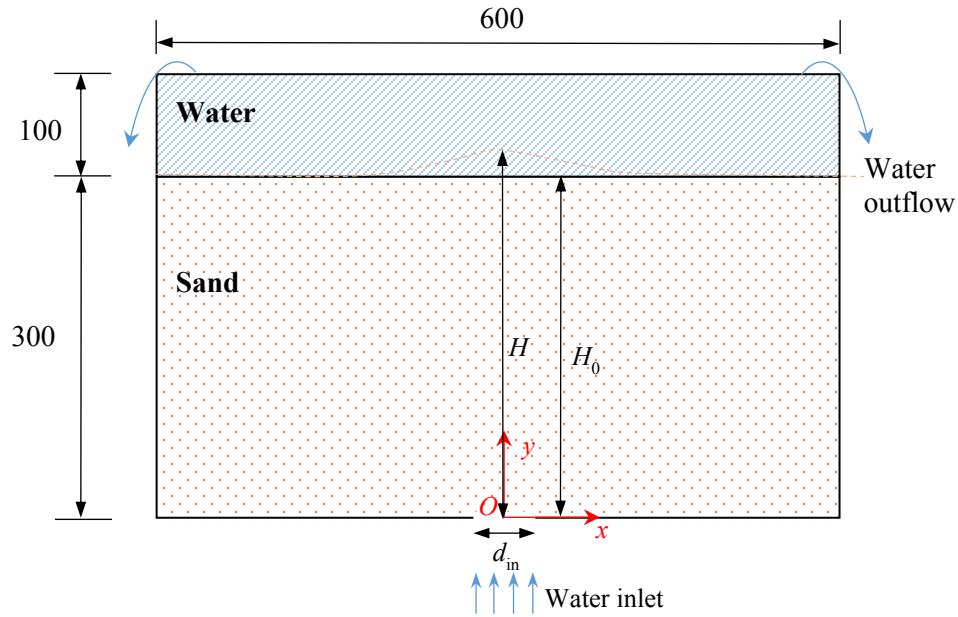
Figure 8.1 Schematic of simulation model (not to scale, unit: mm)

Table 8.1 Model parameters for 2D and 3D simulations

Description	Value in 2D Simulation (Alsaydalani and Clayton, 2014)	Value in 3D Simulation (He et al., 2017)
Granular density	2650 kg/m^3	2650 kg/m^3
Water density	1000 kg/m^3	1000 kg/m^3
Mean granular particle diameter	0.5, 0.9, 1.5 mm	0.25 mm
Internal friction angle of granular material	25º, 35º, 45º	35º
Initial porosity of granular	0.35	0.40
Inlet boundary condition	Velocity inlet	Velocity inlet
Outlet boundary condition	Zero pressure outlet	Zero pressure outlet
Orifice size d_{in}	0.33, 0.62, 0.92 mm	20 mm
Sand bed height	0.3, 0.4, 0.5 m	0.2, 0.25, 0.3, 0.35, 0.4 m
Convergence criteria	0.00001	0.00001
Time step	0.0001 sec	0.0001 sec

Note: the parameters with underlines were used in the base case, other values were used to investigate the corresponding effects.

Mesh sensitivity analysis was carried out first, and the water velocity and sand volume fraction through the center line of the model are plotted in Figure 8.2. Meshes with different sizes were used in the simulation, from a coarse mesh with 45,946 nodes to a fine mesh with 132,373 nodes. From the results in Figure 8.2, there are no significant differences with different meshes. Considering the computation cost and accuracy, the mesh with a total number of 60,678 nodes was adopted for this simulation.
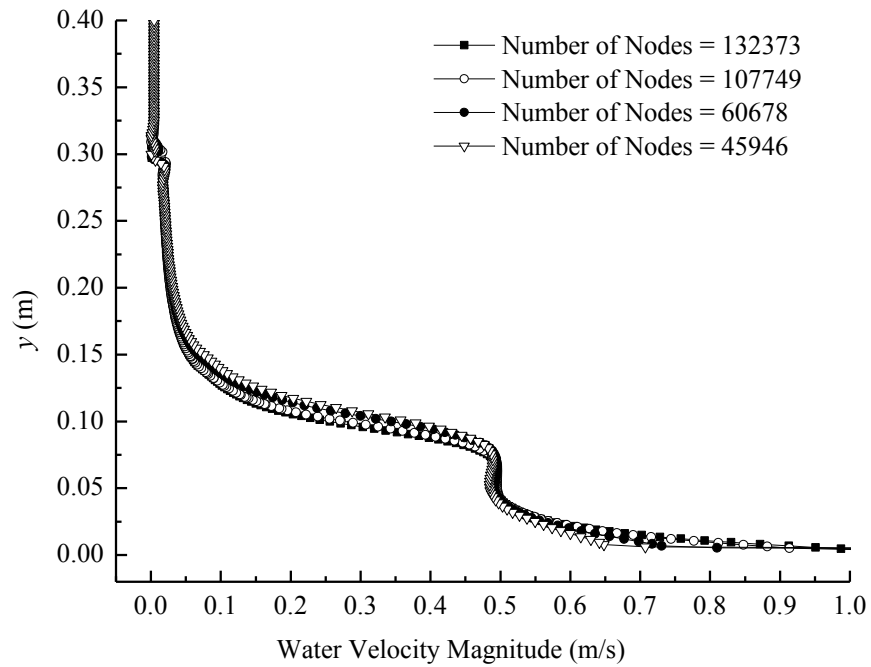
(a) Water velocity distribution at the centerline
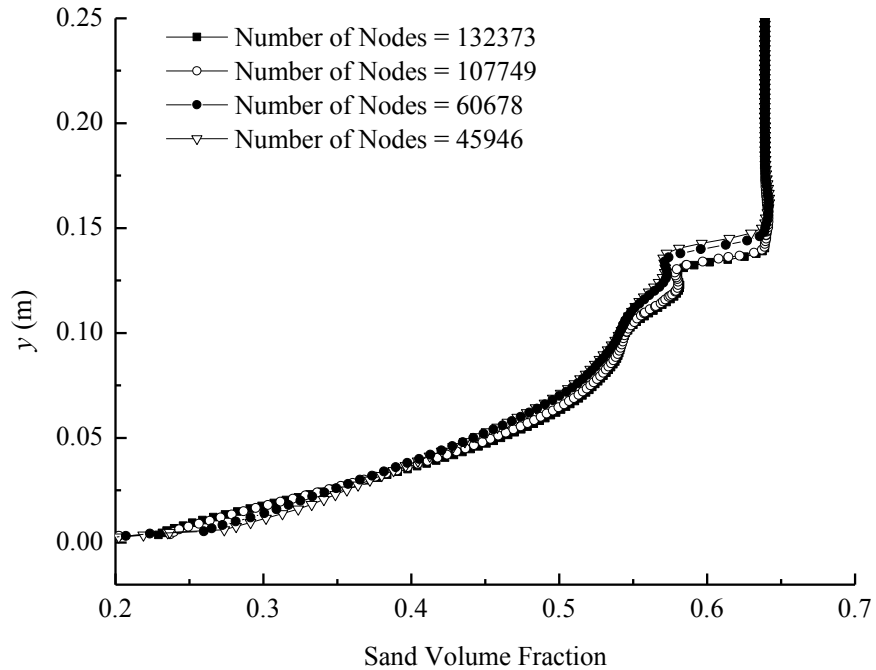
(b) Sand volume fraction at the centerline

Figure 8.2 Mesh sensitivity plots of water velocity and sand volume fraction at the centerline: (a) Water velocity distribution at the centerline; (b) Sand volume fraction at the centerline.

In Alsaydalni and Clayton (2013)'s experiment, the experiment inlet water velocity was increased slowly until fluidization of the sand bed, and the minimum velocity that can lead to sand-bed erosion is a critical value between the stable and unstable regimes. Fluidization is defined as the condition in which the top surface of the sand bed begins to heave due to the water jet. Normally this critical velocity is determined by monitoring the expansion ratio of the sand bed, which is the ratio between the sand-bed height H after injecting water and the initial height H_0 (Taghipour et al., 2005; Chen et al., 2011). The critical velocity is reached when the ratio starts to exceed 1, and the sand bed is significantly heaved. Therefore, the critical velocity is used to verify this numerical model.

The case with the inlet size of 0.62 mm was first simulated. From the experimental result (Alsaydalani and Clayton, 2014), the critical velocity was found to be 3.22 m/s. To find this critical

inlet velocity, the numerical simulation was conducted using the user-defined function (UDF) technique in *ANSYS*, which provides an approach to define a variable in Fluent by importing an individual UDF code. The boundary condition at the inlet was set to be the uniform velocity boundary condition, and the inlet velocity was defined as a variable changing with time. The inlet water velocity is slowly increased just as in the experiment. The boundary condition at the water layer surface was set to be the zero-pressure boundary condition. The other boundary conditions were simulated using the defaulted wall boundary settings. To evaluate the effect of increasing the rate of the velocity, three different functions of the inlet velocity were tested:

- Velocity function 1: $V_{in} = 0.15t$;

- Velocity function 2: $V_{in} = 0.1t$; and

- Velocity function 3: $V_{in} = 0.06t$,

where V_{in} is the inlet fluid velocity (m/s) and t is time (second).

From the simulation results using these three water-velocity functions, the expansion ratios of the sand bed increased as the inlet water velocity increased in Figure 8.3. Following the definition of Taghipour et al. (2005) and Chen et al. (2011), the critical velocity that can cause sand-bed erosion is determined from Figure 8.3 when the granular bed expansion ratio H/H_0 starts to exceed 1. The critical velocity was 3.18 m/s using the inlet velocity function #2 and #3 in UDF, which is approximately consistent with the experimental result of 3.22 m/s, whereas the critical velocity is about 3.48 m/s using the inlet velocity function #1. Sand-bed erosion will be delayed under a rapid increasing inlet water velocity, indicated by solid squares in Figure 8.3, whereas the sand bed can be eroded little by little as the gradual increase of the water velocity. From Figure 8.3, it is reasonable to adopt the water velocity function #2 in UDF, which will be used in this 2D numerical simulation.
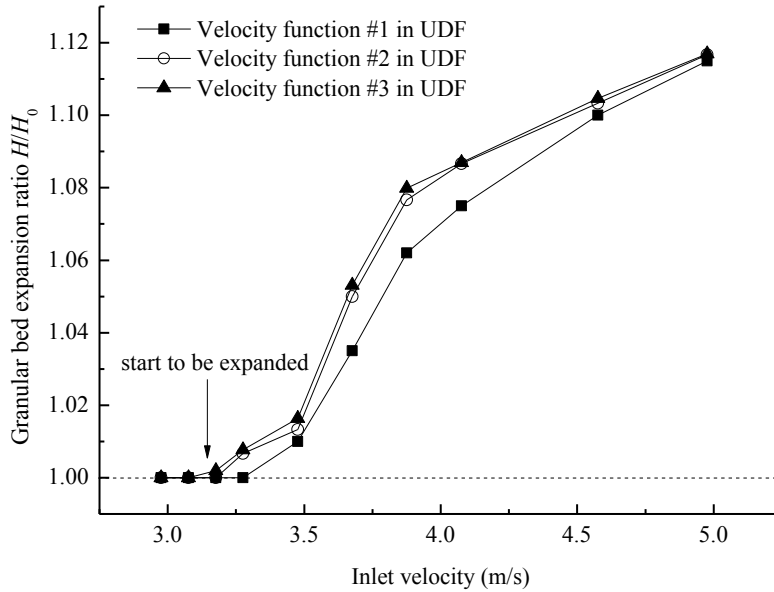
Figure 8.3 Variation of granular expansion ratio using different inlet velocity functions (d_{in} = 0.62mm)

Two more simulations with different orifice sizes are compared with the experimental results in Figure 8.4, and the deviations between the numerical and experimental results are within 5%, which validate the numerical model. As the orifice size increased, the critical velocity decreased. If the orifice size is large enough in the extreme condition, sand-bed erosion can be simplified as the fluidization of a sand column, and the inlet velocity will directly cause sand-column fluidization without the spreading of the water jet. Therefore, the velocity that can cause the sand bed erosion will be less than that with a smaller orifice.
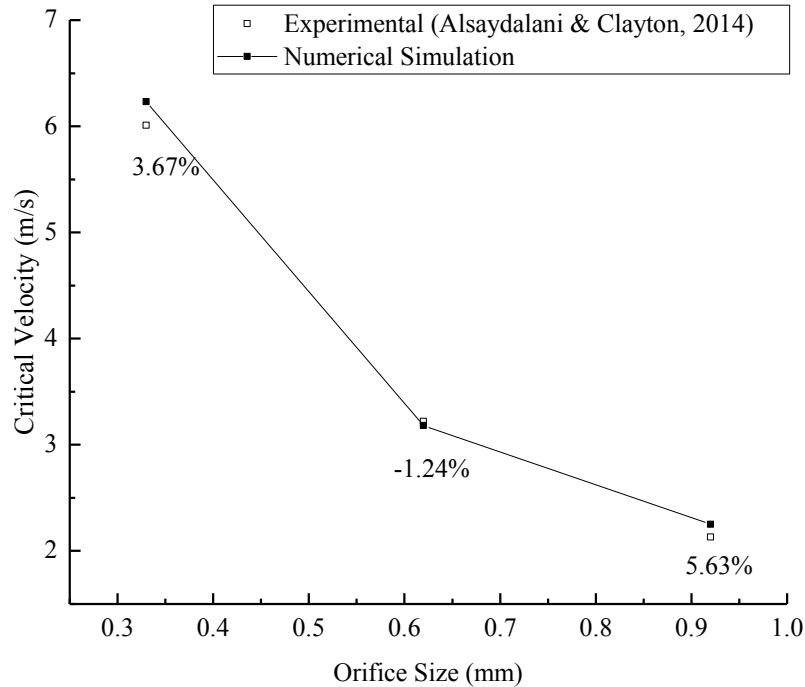
Figure 8.4 Comparison between the numerical and experimental results for the 2D model (the percentage shown here is the difference between experimental and numerical simulation results)

8.2.2 Verification of the Three-dimensional Model

He et al. (2017) carried out experimental studies on the initiation of sand-bed erosion by an upward water jet through an orifice. The dimensions of the experimental setup are shown in Figure 8.5(a), and the numerical setup is shown in Figure 8.5(b). To reduce the computational requirement, half of the experimental domain was simulated using symmetric boundary conditions. The dimensions of the numerical setup were 450×300×500 mm ($L \times W \times H$), with a sand layer of 300 mm in height under a 200-mm water layer. The water surface was set to be the zero-pressure outlet boundary condition. The water inlet at the bottom of the model was defined as the velocity boundary. The input parameters of this numerical simulation are listed in Table 8.1, and these parameters are the same as those in the experiment study (He et al., 2017).

189

Similarly, the water velocity at the orifice was defined as a function of time using UDF technique in *ANSYS*, and the velocity function in this three-dimensional (3D) verification is: $V_{in} = 0.03185t$ (m/s). The minimum velocity of the sand bed erosion can be determined by monitoring the expansion ratio of the sand bed as defined previously. The numerical results are plotted for comparison with the experimental and analytical results by He et al. (2017) in Figure 8.6. It was found that the numerical model can accurately calculate the minimum velocity for sand-bed erosion subjected to an upward water jet. The numerical results were closer to the analytical results, especially when the sand layer thickness is larger than 0.3 m, and the critical velocity is smaller than the experiment results. The deviation between the analytical and experimental results can be attributed to the boundary effects in the experiment (He et al., 2017).
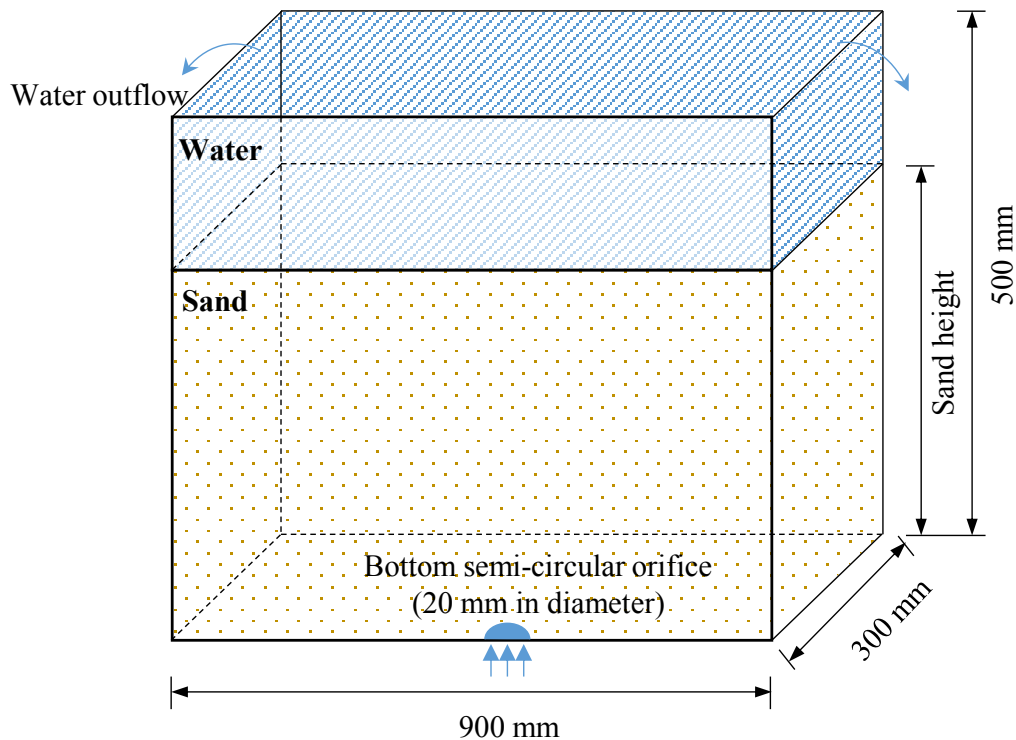
(a) Experiment model (He et al., 2017);
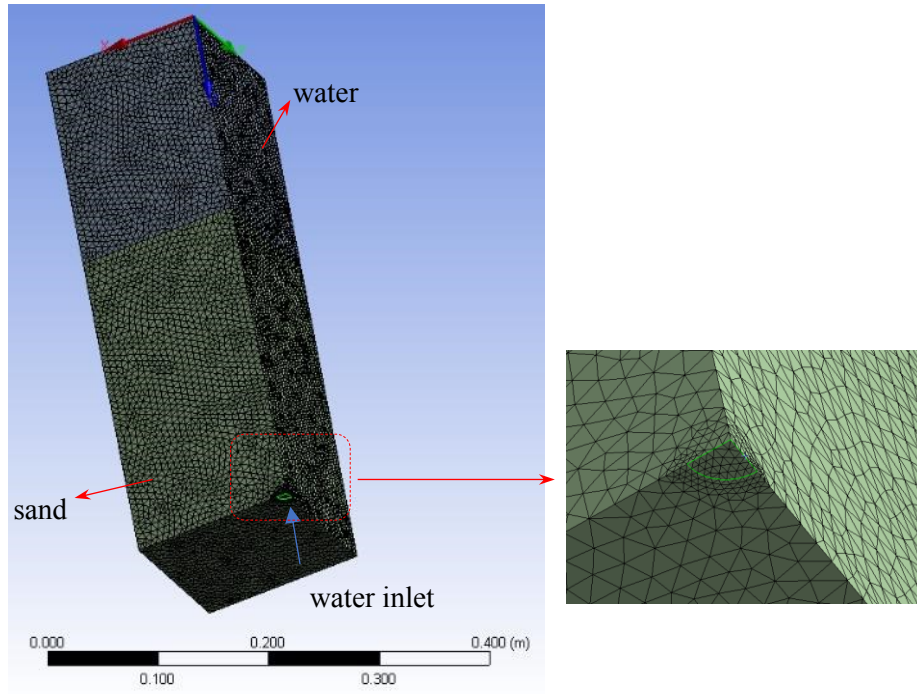
(b) Numerical setup

Figure 8.5 Schematic of the experiment model and numerical setup
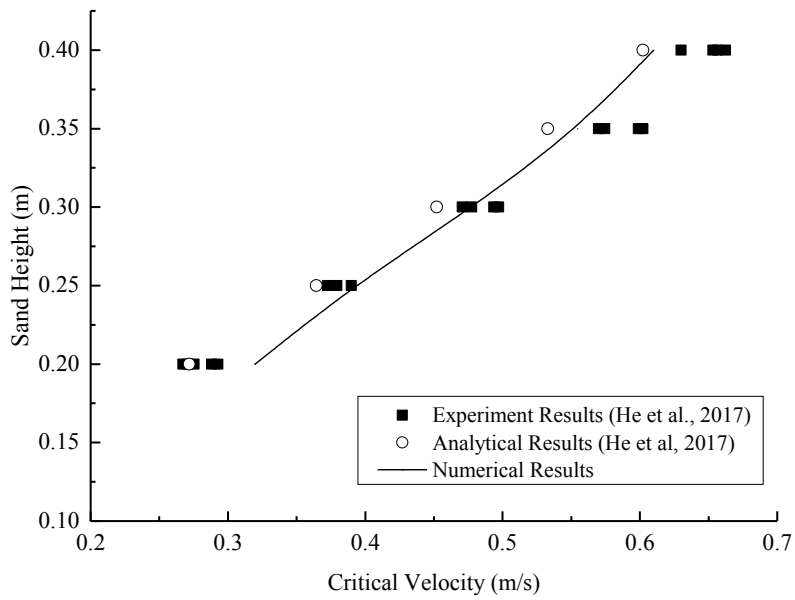
Figure 8.6 Comparison between the numerical and experimental results for the 3D model

8.3 Results and Discussions

From the preceding verification of this numerical model, the CFD technique combined with the kinetic theory of granular flow was shown to be an effective way to study sand-bed erosion by an upward water jet. Based on the 2D experimental conducted by Alsaydalani and Clayton (2014), the onset of sand-bed erosion and the effects of various factors on erosion will be simulated and analyzed next.

8.3.1 Onset of sand-bed erosion

The results of Alsaydalani and Clayton (2014) indicated that the critical velocity at the orifice is 3.22 m/s when the orifice size is 0.62 mm and the sand particle diameter is 0.9 mm. Numerical simulations with three different inlet velocities (2.90 m/s, 3.22 m/s and 3.54 m/s) were conducted to investigate the onset of sand-bed erosion, and the contour of the sand volume fraction is shown in Figure 8.7. The sand bed started to expand at an inlet velocity of 3.22 m/s, as shown in Figure 8.7. The sand bed heaved significantly when the inlet velocity reached 3.55 m/s. Based on mass balance, the sand bed will heave after the formation of a cavity, and the small cavity was formed without sand-bed heaving, which was attributable to the difference between the initial porosity 0.35 and minimum porosity 0.34 in the numerical settings. After the expansion of a small cavity, the sand bed heaved when the inlet velocity increased to 3.22 m/s.

In Figure 8.8, changes of porosity at the centerline of the model are plotted at the different times. Porosity is used to investigate the formation of the cavity due to water jetting through the orifice. As shown in Figure 8.8(a), there is a sudden turn of the curve at y equal to 0.3 m, which is the boundary between the sand surface and water. Although the porosity increased significantly at $y = 0.08$ m at 1.0 second, it rapidly returned to the initial value of 0.35 thereafter. The water jet

caused the formation of the small cavity around the orifice and compacted the sand above. The sand bed did not expand with time when the inlet velocity is 2.90 m/s. As the inlet velocity increased, as shown in Figures 8.8 (b) and (c), the top boundary of the sand is obviously heaving, which indicates sand-bed erosion has occurred, as shown in Figure 8.7. Additionally, unlike the vertical distribution of porosity in Figure 8.8(a) between $y = 0.1$ m and $y = 0.3$ m, the porosity distribution has a smooth transition at $y = 0.1$ m, as shown in Figures 8.8(b) and (c).
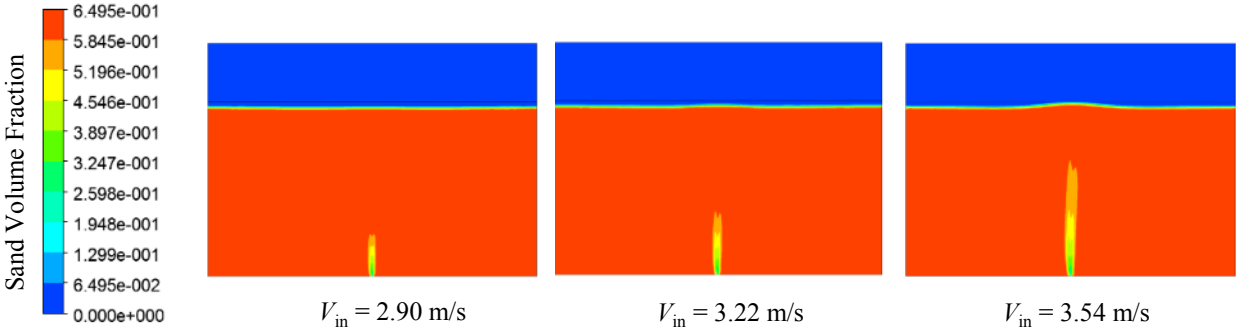
Figure 8.7 Contour of sand volume fraction at different inlet velocity (time = 10 second, $d_{in} = 0.62$ mm)
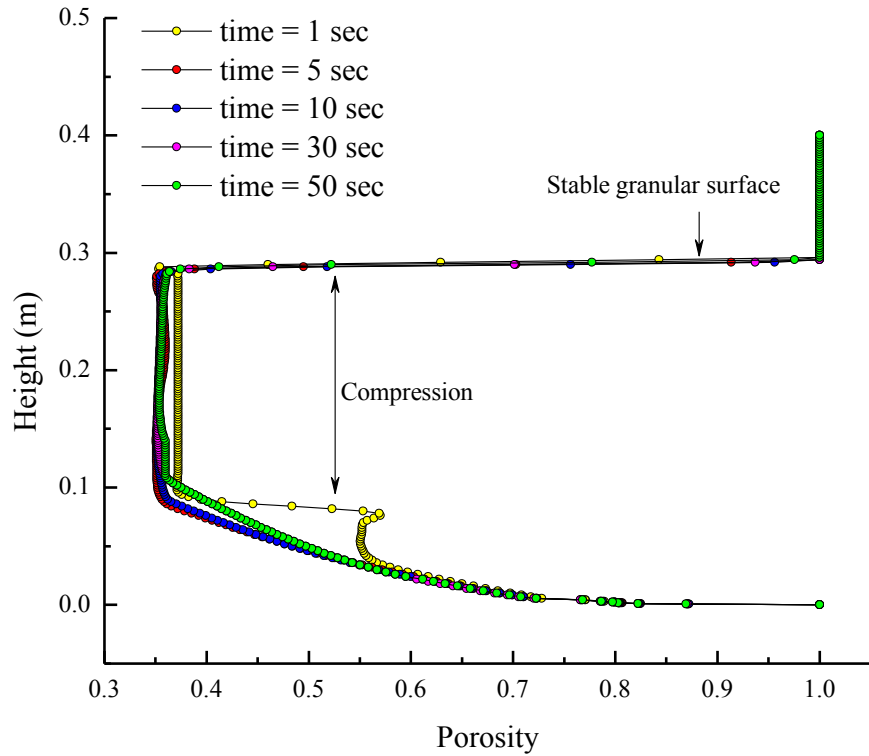
(a) Inlet water velocity = 2.90 m/s
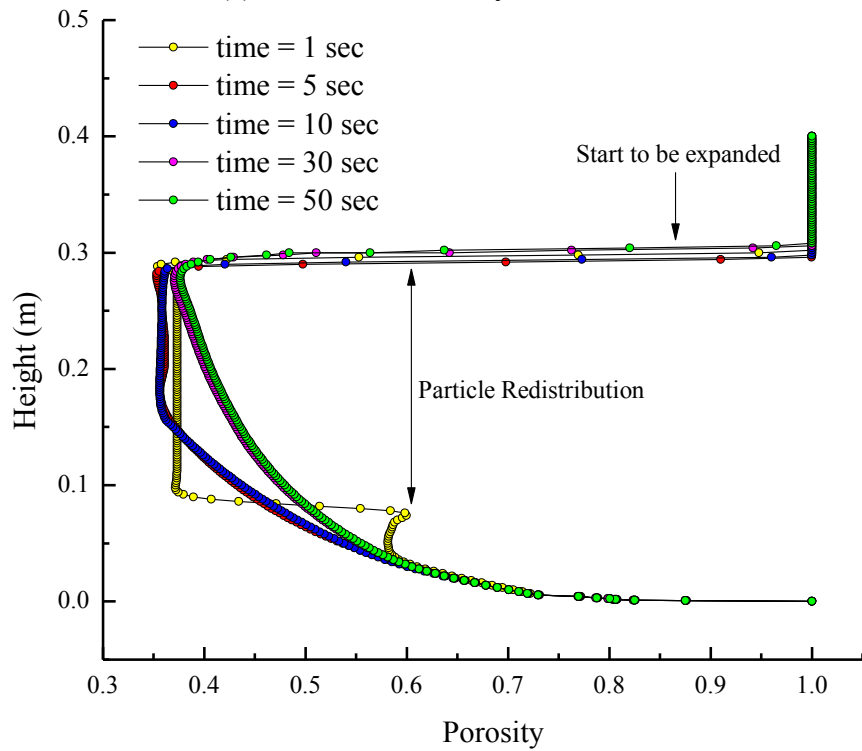
(b) Inlet water velocity = 3.22 m/s
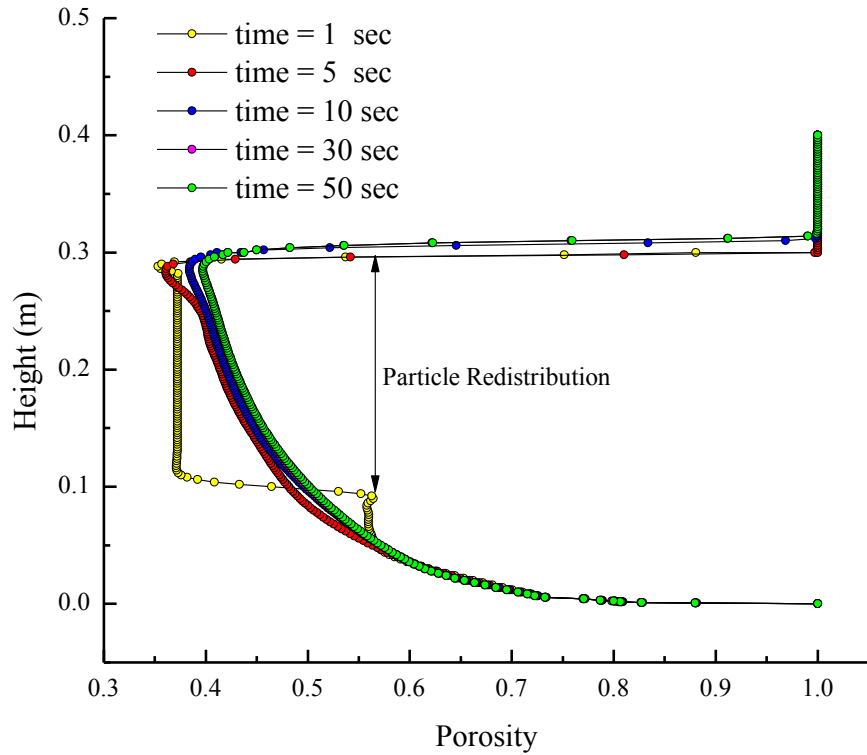
(c) Inlet water velocity = 3.54 m/s

Figure 8.8 Porosity distribution through centerline at different inlet velocities (d_{in} = 0.62 mm): (a) Inlet water velocity = 2.90 m/s; (b) Inlet water velocity = 3.22 m/s; (c) Inlet water velocity = 3.54 m/s.

This numerical simulation can effectively capture the response of a sand bed under an upward water jet. Figure 8.9 shows the contours of sand volume fraction at the different time when the inlet velocity was equal to 3.22 m/s. The contours of the sand velocities are plotted in Figure 8.10. It is shown that at time = 1.0 second the sand particles close to the orifice moved after the water was vertically injected into sand bed. From the contour in Figure 8.9 at 3.0 second, a narrow cavity was formed by the water jet, and the corresponding vortex can be seen in Figure 8.10. Based on the velocity contours and vectors, the formation of the void resulted in sand particles above the void moving upwards, which will compact the sand above. At the same time, the sand particles on the sides of the cavity are moving downwards to fill the void with a lower sand fraction.

This phenomenon was observed by Philippe and Badiane (2013) through experiments as well, where they described the movement of the grains as a turbulent convection roll, which shows a clockwise motion on the right of water jet and counter-clockwise on the other side. At 5.0 seconds, the erosional mechanism changes from a turbulent convection roll to heaving of the sand bed when the pressure reached a value that balanced the weight of the sand above, as shown in Figure 8.9. At 30 seconds, the void reached approximately one-half of the sand-bed height, which caused the significant heaving of the sand bed, which has been described as the formation of a chimney by others (e.g., Zoueshtiagh and Merlen, 2007). The chimney refers to a narrow region of upward flow of water and sand. As the upwards movement of the cavity continued, the sand in the chimney becomes entirely eroded and unstable.
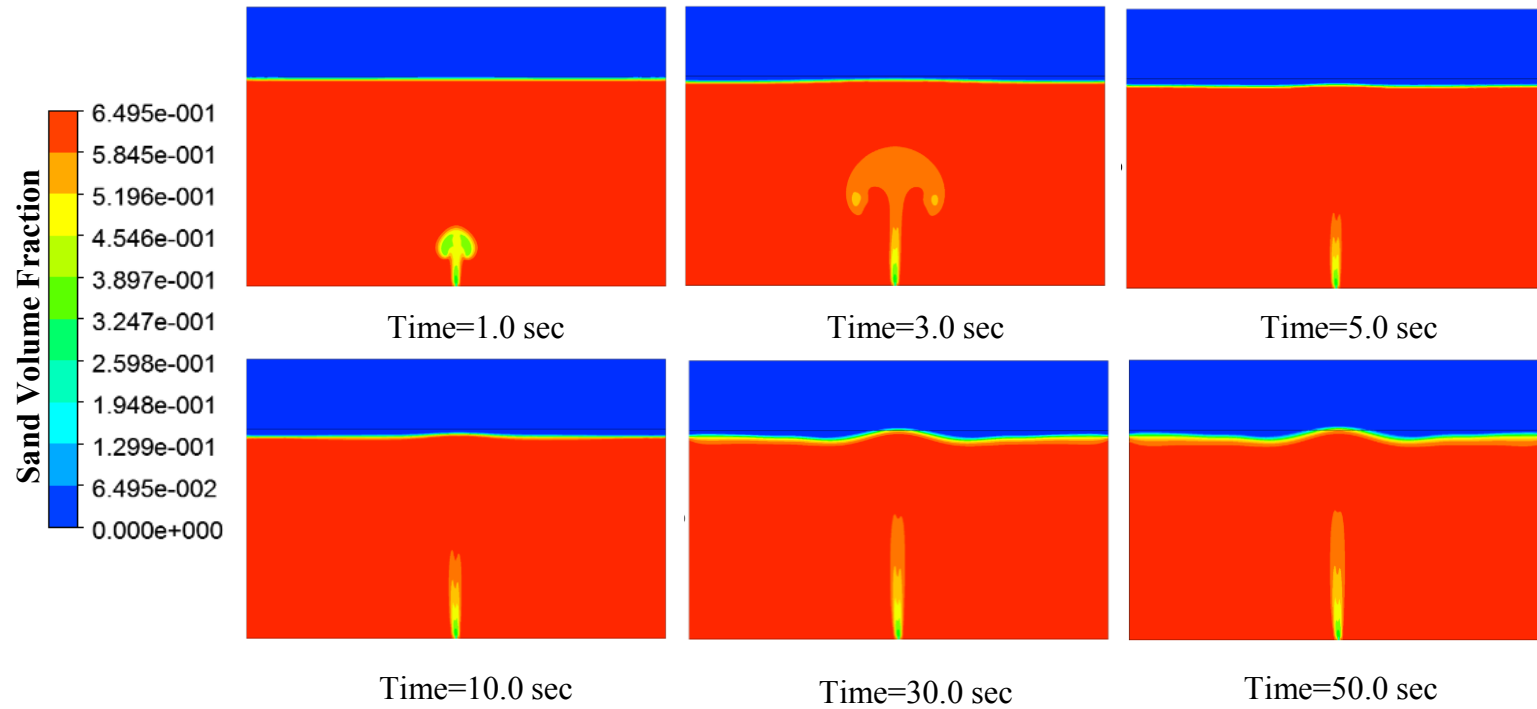
Figure 8.9 Contour of sand volume fraction at different time (V_{in} = 3.22m/s, d_{in} = 0.62 mm)
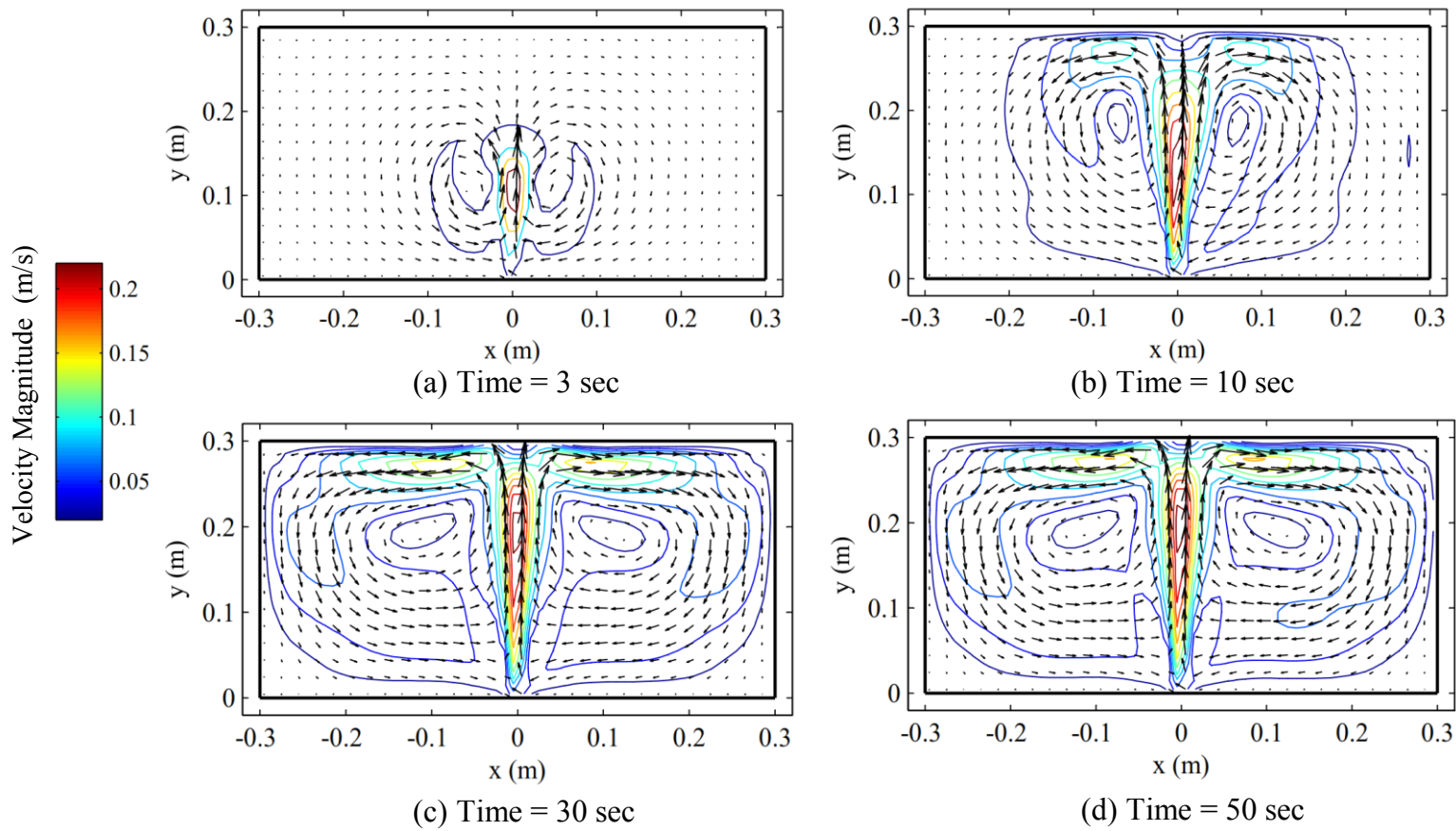
Figure 8.10 Contour and vectors of the sand velocity at different time (V_{in} = 3.22 m/s, d_{in} = 0.62 mm)

The water velocities at the centerline of the model are plotted in Figure 8.11(a) for various inlet water velocities. It can be seen the water velocities decreased with jet spreading, and there was a significant change when the inlet velocity increased between 2.90 and 3.22 m/s. The water-velocity distribution can be approximately divided into two stages when the inlet velocity is larger than 3.22 m/s. The first stage is roughly below the middle part ($y/d_{in} < 250$), during which the water flow behavior is similar to a pure water jet. The water velocity V/V_{in} is approximately proportional to $(y/d_{in})^{-1/2}$. After that, the change of water velocity showed a different pattern due to seepage into the sand bed. This phenomenon can also be observed in the contour of sand volume fraction (Figure 8.9), and the stability of the sand bed transformed the water jet into seepage flow. The water velocity decreased gradually without a sudden change of velocity at an inlet velocity of 2.58 m/s.
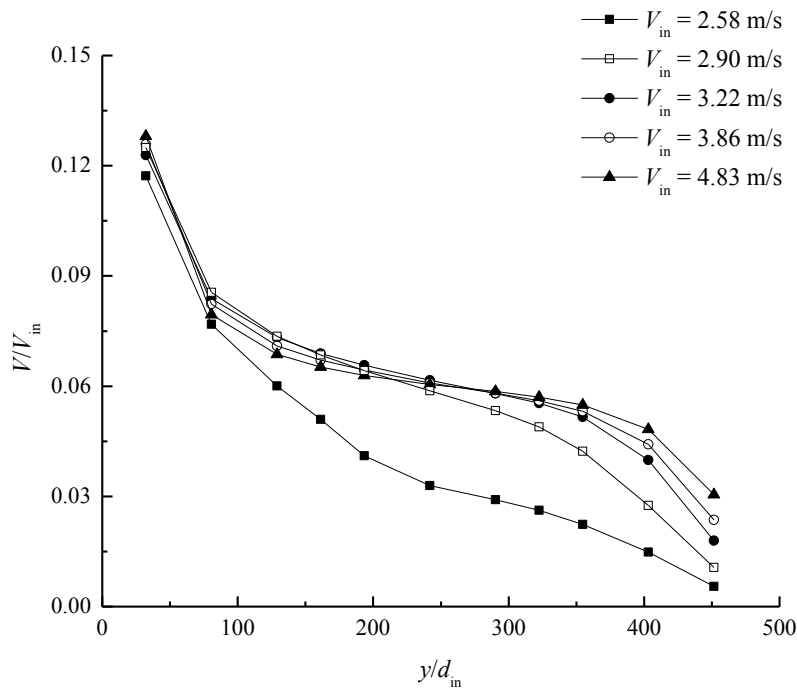
(a) Water velocity in y-direction for different inlet velocities
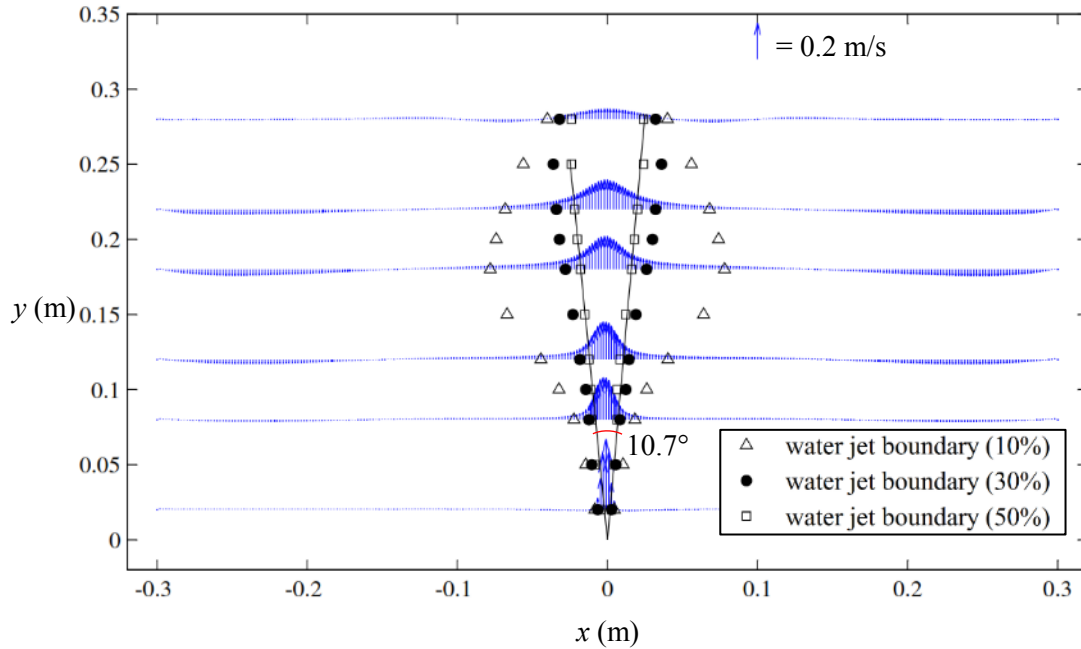
(b) Vertical water velocity distribution at various depths (blue vectors) and water jet boundaries denoted by percentage of the maximum water velocity

Figure 8.11 Characteristics of the water jet into the sand bed (V_{in} = 3.22 m/s, d_{in} = 0.62 mm, time = 30 sec)

To investigate the spreading of water flow into the sand bed, the locations where the jet velocity is equal to 10%, 30% or 50% of the maximum centerline water velocity at various elevations are shown in Figure 8.11(b). Based on the hydraulics of water jet, the spreading angle of the jet, defined as the angle corresponding to 50% of the centerline water velocity, is similar to that in pure water jets with a spreading angle of 10.7°. In contrast, the 30% velocity contour line shows a significant increase, and the form is even more dramatic for the 10% velocity contour. The water-velocity vectors at various elevations are also plotted in Figure 8.11(b). The water-velocity distribution suddenly becomes wider when y > 0.15 m because of the sand bed. Figure 8.11 shows two regimes of the water flow through the sand bed: water jet and the seepage flow.

8.3.2 Effects of particle size

Numerical simulations with three different particle sizes were conducted to investigate the effect of particle size on the erosion process. Figure 8.12(a) shows the change in sand-height expansion ratio as the inlet water velocity increased, and the minimum velocity inducing sand-bed erosion can be determined. The critical inlet velocity increased significantly as the particle size increased. Chen et al. (2011) stated that the driving force on sand bed decreases as the particle size increases, and this decrease of driving force makes the sand bed more difficult to erode. Alsaydalani and Clayton (2014) attributed the effect of the sand particle size on erosion to the changes in sand permeability. From the theoretical formula for calculating permeability, e.g., Kozeny-Carman equation (Lambe and Whitman, 1969), permeability is proportional to the square of the particle size. Pore-water pressure in the sand bed with higher permeability will be easily dissipated, which can strengthen the sand bed against erosion by water jet. In essence, the physical meaning of permeability is considered as the coefficient of the averaged driving force on the soil particle assembly due to the viscous friction at the fluid/solid interface. At this point, the driving force for the sand-bed erosion will be significantly reduced as the granular particle size increases.
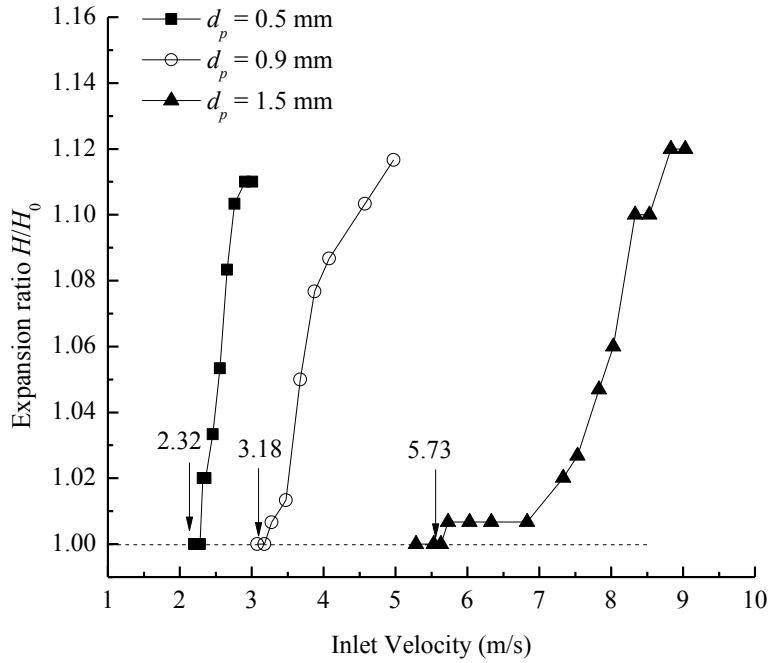
(a) Effect of the particle size on the sand-bed erosion
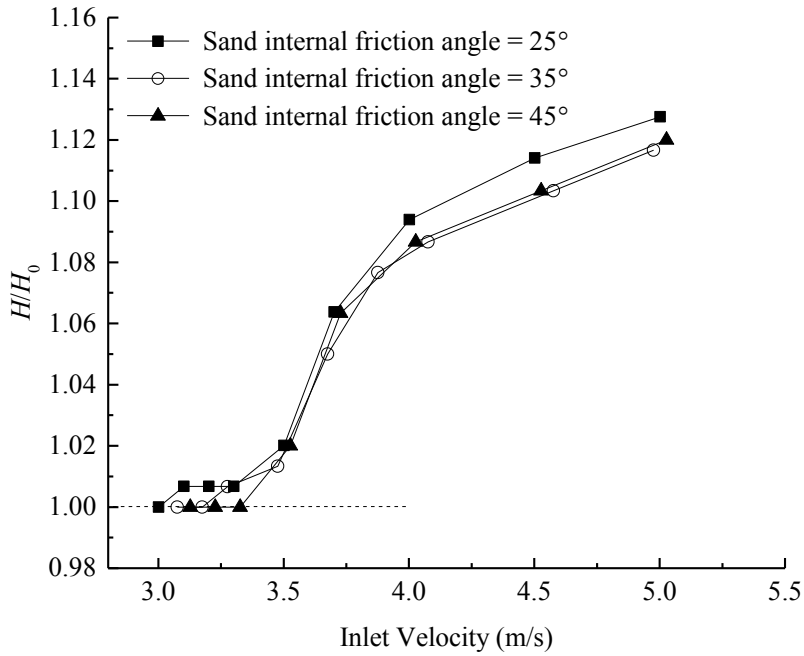
(b) Effect of the sand friction angle on the sand-bed erosion
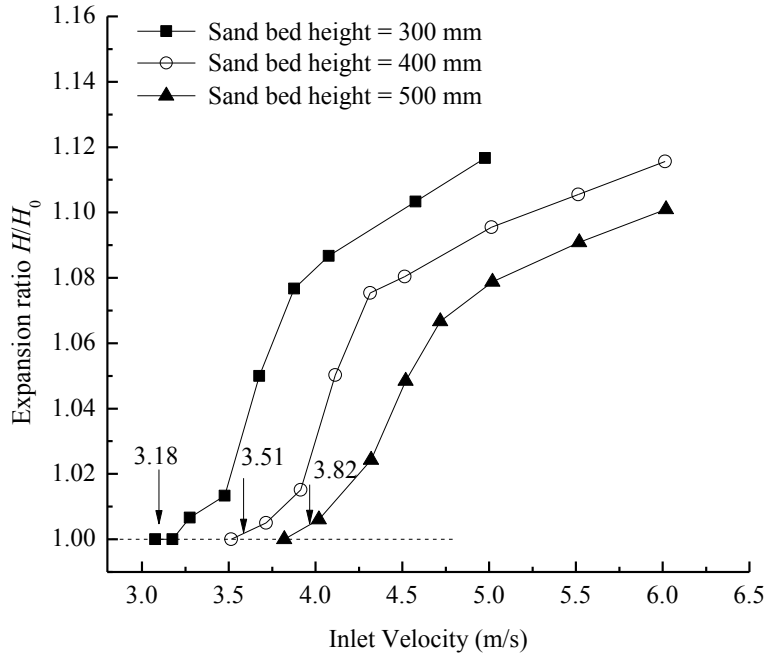
(c) Effect of the sand-bed height on the sand-bed erosion

Figure 8.12 Change of sand bed expansion ratio with the inlet water velocity under different conditions

Another interesting phenomenon is the heaving of the surface of the sand bed at the onset of erosion. Comparing Figures 8.13(a) with 8.13(b), the surface movement due to erosion shows a zigzag pattern if the particle diameter is 1.5 mm, whereas the surface movement is heaving smoothly if the particle size is 0.5 mm. Water can easily flow through the sand when the particle size is large, and sand-bed erosion is initiated at a higher inlet water velocity, as shown in Figure 8.12(a). This higher water velocity may cause local particle motion at the sand/water interface with fewer restrictions. On the other hand, it is more difficult to flow through the finer particles because of the lower permeability, and the sand bed will behave more like a continuum.

d_p = 1.5 mm

(b) d_p = 0.5 mm
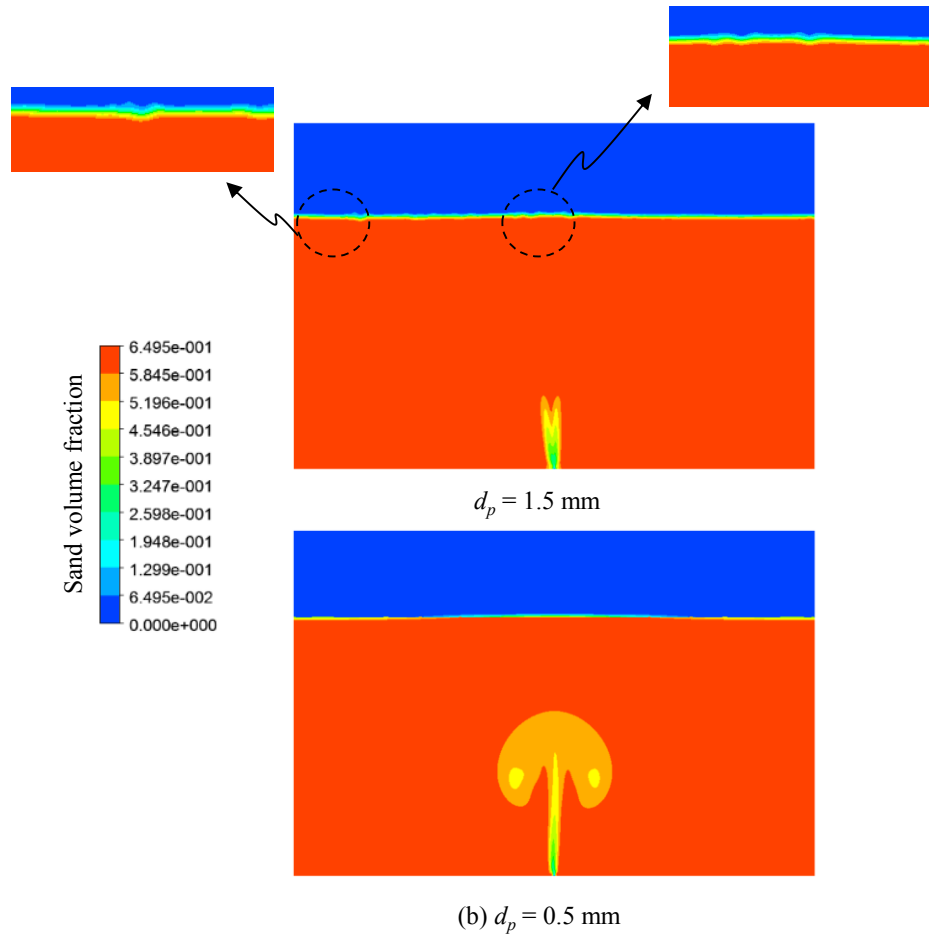
Figure 8.13 Contour of sand volume fraction at the onset of erosion (d_{in} = 0.62 mm)

8.3.3 Effects of internal friction angle

If the granular material has a high internal angle of friction, the stress caused by friction normally cannot be neglected. To investigate the effects of the sand angle of internal friction on sand-bed erosion, simulations using different friction angles have been conducted. The frictional viscosity proposed by Schaeffer (1987) was incorporated in this numerical model. Figure 8.12(b) plots changes in expansion ratio against the inlet water velocity with various friction angles. Although the resisting effect of the friction can be reflected from Figure 8.12(b), the effect of friction angle on the onset of sand-bed erosion is not significant. The critical velocity is only increased by 11%

when the friction angle increased from 25° to 45°, a typical range of friction angle for sand. Philippe and Badiane (2013) stated that the friction between granular particles could strengthen the mechanical resistance of the granular bed and stabilize the upper layer above the cavity. Although the effect of sand friction can be taken into account using the friction viscosity in the simulation, the granular material was taken as a fluid phase in the numerical study. Therefore, the corresponding effect of sand friction will be investigated in the following analytical model.

8.3.4 Effects of sand-bed height

The effect of the sand-bed height on erosion is explored here. The change of the expansion ratio H/H_0 with the inlet water velocity is plotted for various sand-bed heights in Figure 8.12(c). The sand-bed erosion required higher injection velocity as the height of the sand increased, which contradicts with other studies (Philippe and Badiane, 2013; Cui et al., 2014). The resisting forces of the mobilized sand body increased as the sand-bed height increased. Thus, the inlet water velocity needed to increase to erode the above sand bed. On the other hand, the thicker the sand layer, the higher the water jet has to propagate to reach the top of the sand layer, resulting in the erosion. The effect of the sand-bed height is less than the effect of particle size, which indicates that to reduce erosion risk, it will be more effective to change the particle size around the underground pipe.

8.3.5 Analytical model for sand-bed erosion

Based on the preceding analysis, the mechanism of sand-bed erosion can be simplified as shown in Figure 8.14. A simple analytical model can be developed by considering the driving and resisting forces on an elemental volume of sand. The mobilized zone of the sand bed can normally be simplified as a wedge in 2D (Alsaydalani and Clayton, 2014; Cui et al., 2014) or a cone in 3D

(He et al., 2017). The resisting forces come from the gravity of the wedge, and the interaction between the wedge and the surrounding sand. The driving force is provided by the vertical water jet, which is related to either the inlet velocity (Chen et al., 2011; He et al., 2017) or water pressure at the base of the wedge/cone (Alsaydalani and Clayton, 2014; Cui et al., 2014). In this chapter, the inlet water velocity is used to determine the critical inlet velocity resulting in the sand-bed erosion. The driving force can be simply calculated using Darcy's Law (He et al., 2017). Ergun's equation, which accounts for the nonlinear relationship between water velocity and pressure gradient, has also been used in other studies (Chen et al., 2011, Alsaydalani and Clayton, 2014; Cui et al., 2014) and will be incorporated in this analytical model. Using these simplifications and assumptions, a simplified analytical model can be developed.
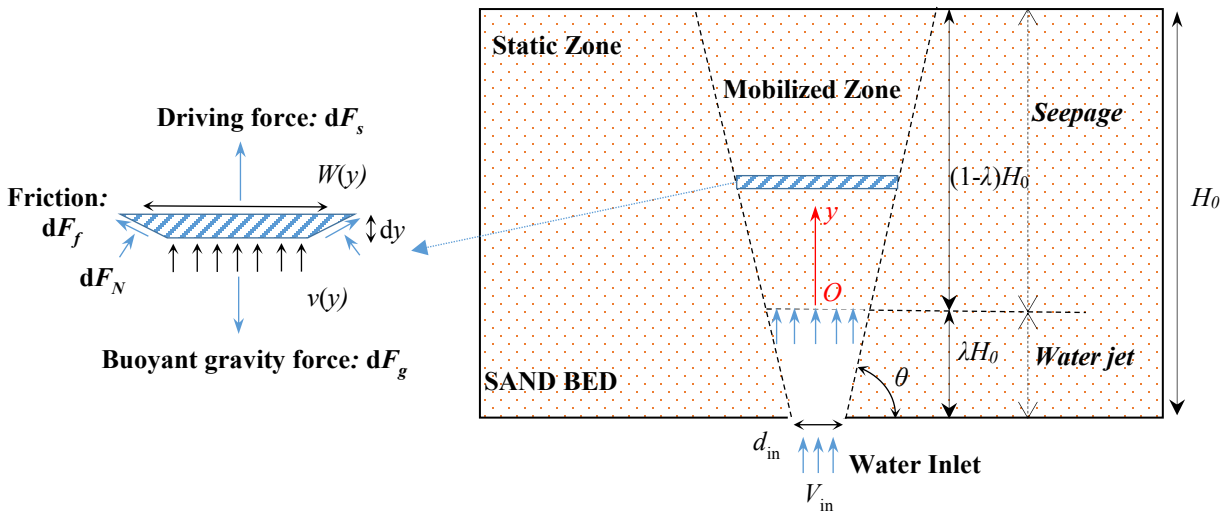
Figure 8.14 Schematics of the analytical model

The critical condition is defined when the upward driving forces are in equilibrium with the downward resisting forces. Considering the forces between the static and moving zones, the force balance equation can be written as:

$$F_s + F_y = F_g + F_f \tag{8.1}$$

where, F_s is the driving force caused by the water flow; F_y is the component in y-direction of the normal force at the interface between the mobilized and static zone; F_g is the gravitation force of the mobilized wedge; F_f is the friction between the mobilized and static zones. As shown in Figure 8.14, the driving forces in the sand bed resulting from water seepage can be calculated using Ergun's equation (1952) per unit length:

$$F_s = \int_0^{(1-\lambda)H_0} dF_s = \int_0^{(1-\lambda)H_0} \left\{ 150\mu_f \frac{1-n}{\left(\varphi_s d_p\right)^2 n} v(y) + 1.75 \frac{\rho_f}{\varphi_s d_p n} \left[v(y)\right]^2 \right\} \cdot W(y) \cdot 1 \cdot dy \qquad (8.2)$$

where φ_s is the sphericity of the sand particle; $v(y)$ is the water velocity distribution within the sand bed and the rest of the parameters are defined in the list of symbols in this chapter.

The buoyant weight of wedge per unit length is:

$$F_g = \int_0^{(1-\lambda)H_0} dF_g = \int_0^{(1-\lambda)H_0} \left(\rho_s - \rho_f\right) \cdot g \cdot (1-n) \cdot W(y) \cdot 1 \cdot dy \qquad (8.3)$$

where $W(y)$ is the width of the wedge.

Because of the frictional characteristic of the granular material, the friction between the sand particles provides the resistance against erosion. The normal force on the element per unit length between the mobilized and static zones can be calculated from:

$$dF_N = \frac{1}{2\sin\theta} \cdot \left(1 + K_0 + \cos 2\theta - K_0 \cos 2\theta\right) \left(\rho_s - \rho_f\right) \cdot g \cdot (1-n) \cdot y \cdot 1 \cdot dy \qquad (8.4)$$

where, K_0 is the coefficient of the static earth pressure under the confining condition, and can be estimated using Jacky's equation (Lambe and Whitman, 1969) for the granular material: $K_0 = 1 - \sin\varphi$, and φ is the internal friction angle of the sand.

Therefore, the frictional force can be determined based on the Coulomb's friction law:

$$F_f = \int_0^{(1-\lambda)H_0} \mathrm{d}F_f = \int_0^{(1-\lambda)H_0} 2\tan\varphi \mathrm{d}F_N \tag{8.5}$$

Meanwhile, the component in the y-direction of the normal force between the mobilized and static zones is notated as F_y:

$$F_y = \int_0^{(1-\lambda)H_0} \mathrm{d}F_y = \int_0^{(1-\lambda)H_0} 2\cos\theta \mathrm{d}F_N \tag{8.6}$$

The width $W(y)$ of each element can be determined from the geometry:

$$W(y) = d_{in} + 2y\cot\theta \tag{8.7}$$

The fluid velocity distribution can be simplified as a uniform flow in one direction, and then the velocity distribution is determined using the inlet velocity:

$$v(y) = \frac{V_{in}d_{in}}{d_{in} + 2y\cot\theta} \tag{8.8}$$

Combining Eqs. (8.2) – (8.6) with Eqs. (8.7) and (8.8), the force on the mobilized zone can be determined, and the critical velocity causing the sand bed erosion can be estimated from the force balance Eq. (8.1).

$$V_{in}(\lambda) = \frac{-B + \sqrt{B^2 - 4AC}}{2A} \tag{8.9}$$

where

$$A = \frac{1.75\rho_f^2 d_{in}(1-\lambda)H_0}{nd_p\left(d_{in} + 2H_0\cot\theta - 2\lambda H_0\cot\theta\right)},$$

$$B = \frac{75(1-n)d_{in}\mu}{n\left(\varphi_s d_p\right)^2\cot\theta}\ln\left(\frac{d_{in} + 2H_0\cot\theta - 2\lambda H_0\cot\theta}{d_{in}}\right),$$

$$C = \left(\rho_s - \rho_f\right) \cdot g \cdot (1-n) \cdot (1-\lambda) \cdot H_0 \cdot \left(d_{in} + H_0 \cot\theta + \lambda H_0 \cot\theta\right)$$
$$+ 0.5\left(1 + K_0 + \cos 2\theta - K_0 \cos 2\theta\right) \cdot \left(\rho_s - \rho_f\right) \cdot g \cdot (1-n) \cdot (1-\lambda)^2 \cdot H_0^{\,2} \cdot \left(\tan\varphi - \cot\theta\right)$$

From Eq. (8.9), the velocity leading to force equilibrium or the suspension of the sand bed can be determined depending on the function λ for various water-jet heights. For the case in this chapter (Figure 8.1), angle θ is equal to 64° (Alsaydalani and Clayton, 2014), and the same values as in Table 8.1 for 2D are used for the other parameters in this analytical model. As the water jet moves upward in the sand bed, the driving force generated by the water jet decreased with height, and the resistance on the sand-bed mobilization decreased as well. In this calculation case, the critical velocity occurs when the water jet at the orifice ($\lambda = 0$), where the critical velocity is minimum.

The critical velocity determined from this analytical model is plotted and compared with the experimental (Alsaydalani and Clayton, 2014) and numerical simulation results in Figure 8.15(a) with good agreement. The difference in particle shape might also result in the deviation between the analytical and numerical results. The particle sphericity in this analytical calculation is taken as 0.52, which is the same as the experiment measurements (Alsaydalani and Clayton, 2014). In the numerical simulation, the granular particle is assumed to be a perfect sphere, which may overestimate the particle size and lead to the overestimation of the critical velocity. With an increase in orifice size, the critical velocity decreased, as shown in Figure 8.15(a). If the orifice is large enough, the resistance force comes mainly from gravity and the effect of the spreading angle θ is small. The effect of sand internal friction angle on the critical velocity is plotted in Figure 8.15(b), which indicates the critical velocity decreased as the sand friction angle decreased. Although the results between analytical and numerical studies are close, the analytical model

appears to be more reasonable to account for the effect of sand friction based on the Coulomb friction criterion.

The critical Reynolds number Re_c at the orifice that will cause sand-bed erosion can be defined as:

$$\text{Re}_c = \frac{\rho_f V_c d_{in}}{\mu_f} \qquad (8.10)$$

where, V_c is the critical inlet water velocity that leads to sand-bed erosion, and μ_f is the dynamic viscosity of the fluid. The relationship between the critical Reynolds number and sand particle size can be plotted as shown in Figure 15(c), and the results from the experimental and numerical studies are also plotted in the same figure for comparison. As the height of the sand bed increased, higher Reynolds number were required to reach erosion. Moreover, a higher inlet velocity is required to initiate sand-bed erosion for the larger sand particles. The densimetric Froude number F_o compares the flow inertia to gravity and is commonly used in studying sand erosion (Rajaratnam, 1981):

$$F_o = \frac{V_c}{\sqrt{d_p g \frac{\left(\rho_s - \rho_f\right)}{\rho_f}}} \qquad (8.11)$$

By the definition of densimetric Froude number, the effect of sand particle size and density can be taken into account, and the densimetric Froude number from the numerical and experimental results are plotted in Figure 8.15(d) in comparison with analytical results. Simulations with different sand density ($\rho_s = 2200$ kg/m^3 and 1800 kg/m^3) were conducted, which were consistent with these analytical predictions. As sand density increased, the critical velocity increased because of the increase in resisting force on the sand mobilized zone. Also, the effect of

sand-bed height decreased as the orifice size increased. From the analysis of both Reynolds number and densimetric Froude number, this proposed analytical model is proven to be effective and able to predict the critical velocity considering the effects of various factors.
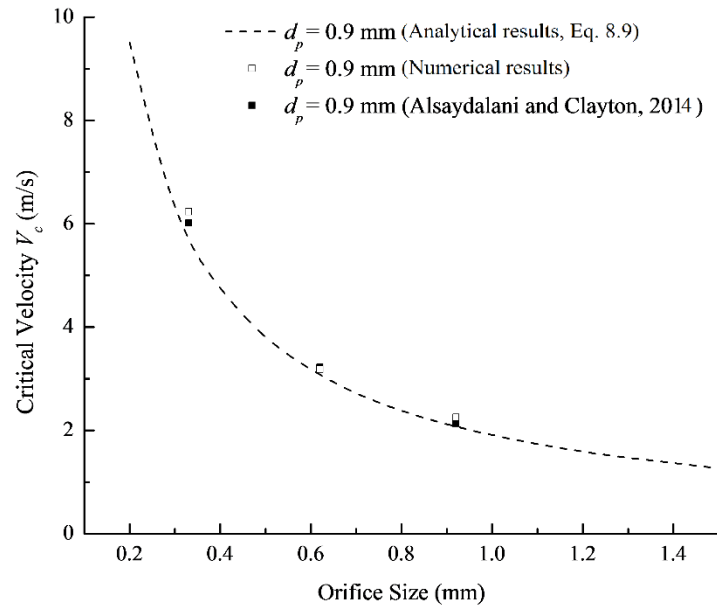
(a) Critical velocities at various orifice sizes
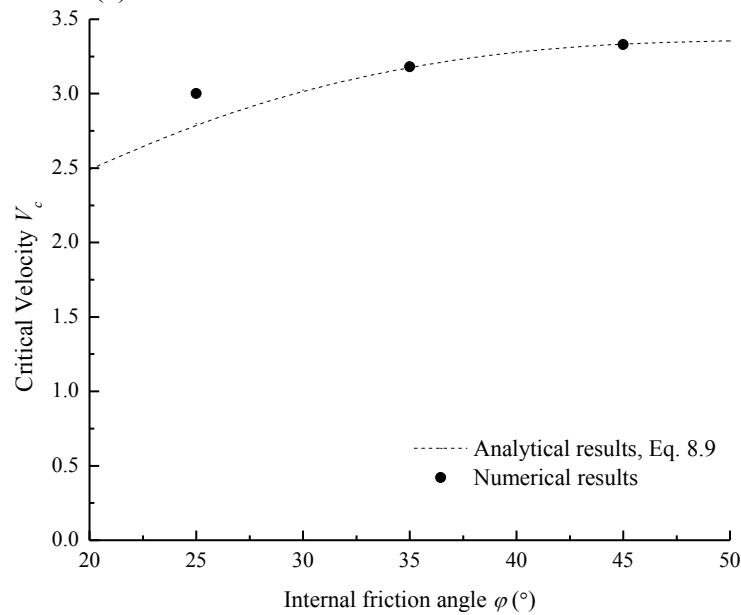
(b) Critical velocities at various internal friction angles ($d_p = 0.9$ mm, $d_{in} = 0.62$ mm)
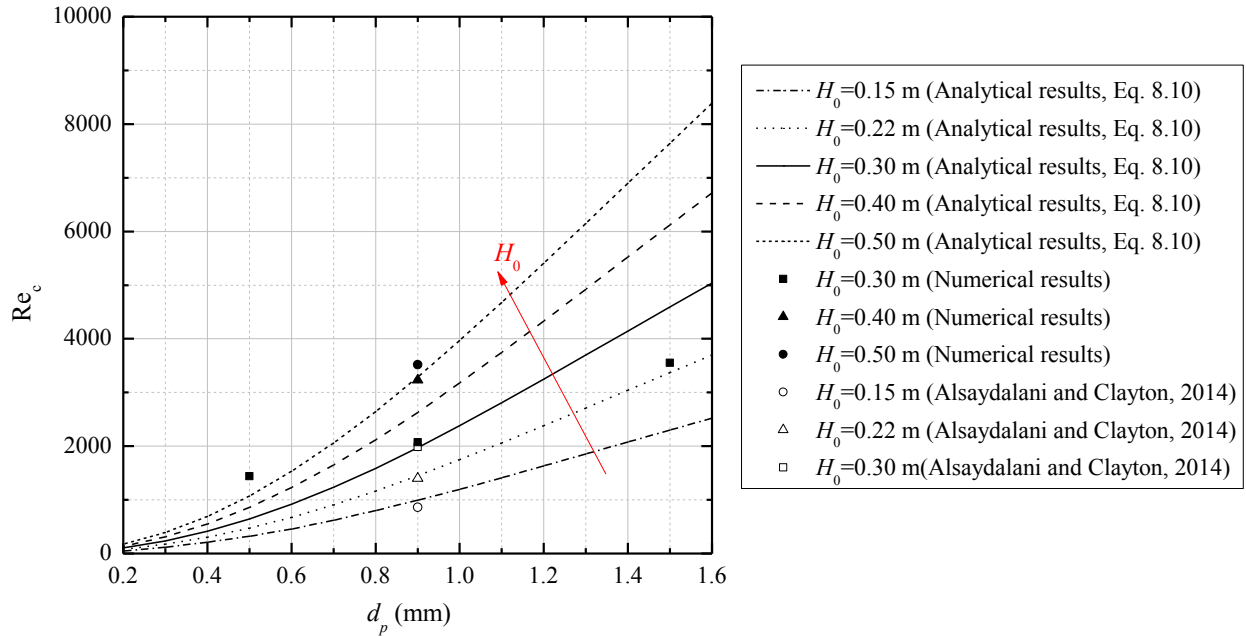
(c) Relationship between critical Reynolds number and sand particle size ($\varphi = 35°$)
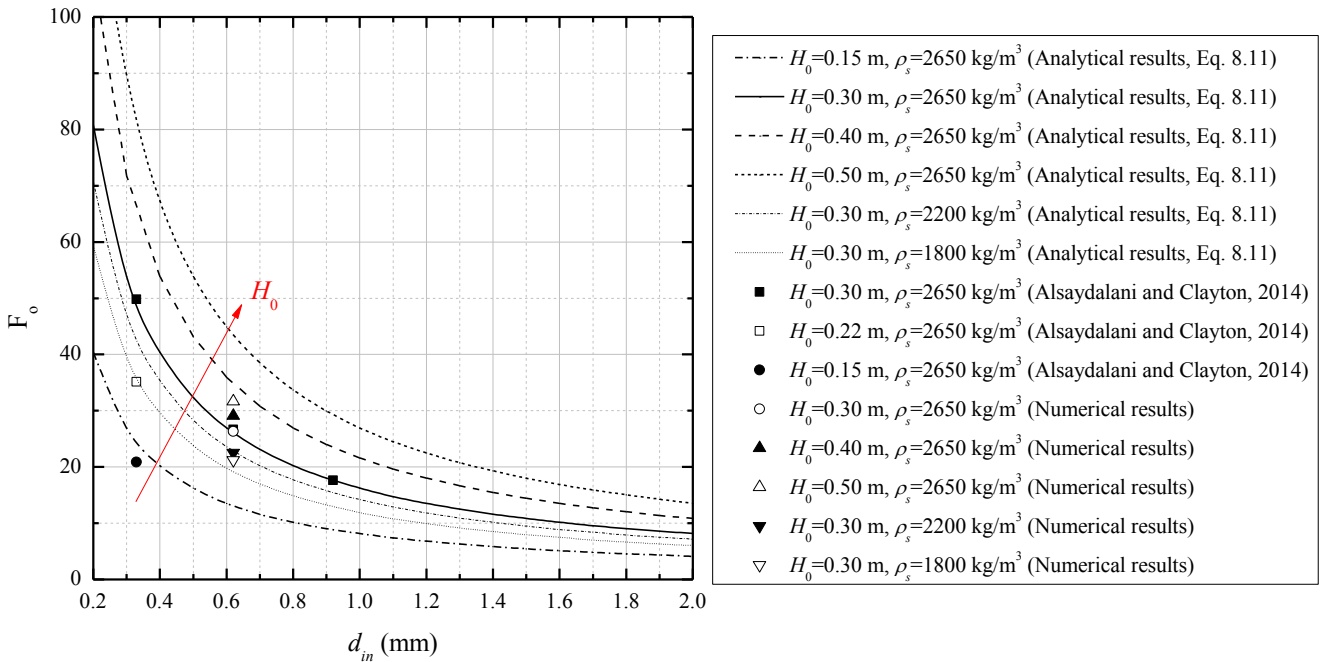
(d) Relationship between the densimetric Froude number and orifice size ($\varphi = 35°$)

Figure 8.15 Prediction of the critical velocity using the analytical model

8.4   Summary and Conclusions

From the numerical simulations of sand-bed erosion under an upward water jet, the following conclusions can be made:

- The CFD technique combined with the kinetic theory of granular flow provides an efficient and promising approach to investigate granular-material bed erosion under a water jet. This approach is verified by simulating both two-dimensional and three-dimensional experiments utilizing the user-defined function in *ANSYS*, which provides a realistic simulation of the real experimental condition by setting a time-dependent inlet water velocity;

- From the numerical simulation, the onset of the granular material erosion under a water jet can be simplified in two steps. The first step is the small-cavity formation around the water injection location. The second stage occurs as the inlet water velocity increased, while the cavity will expand towards the surface and a narrow chimney will be formed. In the first stage, the sand bed is not significantly expanded, and the initiation of the expansion is the transient point between the stable and erosion stages.

- The granular particle size is an important factor in sand-bed erosion, and the stability of the granular material can be effectively strengthened with increases in particle size. Therefore, granular material with larger particle sizes should be used to bury underground pipe. The critical velocity leading to sand-bed erosion decreased as the sand friction angle decreased. An increase of the sand-bed height means that a higher inlet water velocity is required to cause erosion; and

An analytical model has been developed based on force analysis considering the effect of the interaction between the mobilized and static zones in the sand bed. Ergun's equation is used to

calculate seepage forces. From the analytical model, the driving force provided by the water jet decreased with the upward movement of the water jet. The resisting force, which is due to the gravity of the sand bed and friction between mobilized and static zone, decreased with the upward movement of the water jet because the sand bed above the water jet becomes thinner. The critical condition is defined as the condition when the forces are in equilibrium and the minimum critical velocity for sand-bed instability. Therefore, the critical inlet water velocity leading to the sand-bed erosion can be determined from this proposed analytical model. By analyzing the Reynolds number and densimetric Froude number at the critical condition, this analytical model is proven to be effective.

List of Symbols

The following symbols are used in this chapter:

C_d	drag force coefficient
d_p	particle size in diameter, m
d_{in}	inlet size of the model, m
e_{ss}	restitution coefficient between particles
F_f	friction force acting on the sand bed, N
F_g	gravity of the mobilized sand bed, N
F_o	densimetric Froude number
F_s	driving force acting on the sand bed from the seepage, N
F_y	force acting on the mobilized sand bed in *y*-direction, N
g	gravitational acceleration, m/s^2
$g_{0,ss}$	radial distribution function between particles
H	sand bed height after injecting water
H_0	initial sand bed height
$\overline{\overline{I}}$	identity matrix
I_{2D}	the second invariant of the deviatoric stress tensor for solid phase

K_0	coefficient of the static earth pressure
K_{fs}	interphase exchange coefficient, kg m^2/s
$k_{\Theta s}$	diffusion coefficient for granular energy
n	porosity
p	pressure, Pa
p_s	granular pressure, Pa
Re_c	critical Reynolds number that can cause the sand bed erosion
R_{es}	particle Reynolds number
t	time, second
V_c	critical inlet fluid velocity that can cause the sand bed erosion, m/s
V_{in}	inlet fluid velocity, m/s
v_f	velocity of the fluid phase, m/s
v_s	velocity of the solid phase, m/s
α_f	volume fraction of fluid phase
α_s	volume fraction of solid phase
$\gamma_{\Theta s}$	the collisional dissipation of energy, m^2/s^2
Θ_s	granular temperature, m^2/s^2
θ	angle of the mobilized wedge in the sand bed, °
λ	water jet location on the sand bed
λ_s	The solid bulk viscosity, Pa·s
μ_f	fluid viscosity, Pa·s
μ_s	solid shear viscosity, Pa·s
$\mu_{s,col}$	solid collision viscosity, Pa·s
$\mu_{s,kin}$	solid kinetic viscosity, Pa·s
$\mu_{s,fr}$	solid frictional viscosity, Pa·s
ρ_f	fluid density, kg/m^3
ρ_s	solid density, kg/m^3
$\overline{\overline{\tau}}_f$	shear stress of fluid phase, Pa
$\overline{\overline{\tau}}_s$	shear stress of solid phase, Pa
φ	solid internal friction angle, °

φ_s sphericity of the sand particle

ϕ_{fs} the dissipation of granular energy caused by the fluctuating force, m^2/s^2

Chapter 9 General Conclusions and Recommendations for Future Research

9.1   General Conclusions

This thesis studied the mechanisms of soil erosion due to the defective sewer pipes. Soil adjacent to the pipe defect can be eroded as the water infiltrates through the pipe defect, which can lead to the soil loss and sinkhole formation. Experiments were conducted, and a coupled discrete element model was developed to simulate the erosion process. Based on the experimental and numerical results, analytical models were developed to predict the erosion. The water exfiltration through the pipe defect was simulated using the CFD technique, and an analytical model was proposed to evaluate the soil erosion as the water exfiltrates. Detailed conclusions can be found in each of the preceding chapters. More general conclusions are summarized as follows:

- In Chapter 2, based on the comprehensive literature review on the soil erosion due to the defective sewer pipes and other related studies, the mechanisms of erosion process and sinkhole formation were still not clear.

- In Chapter 3, based on the experimental studies of soil erosion through a two-dimensional slot on the pipe, the soil erosion initiates in a narrow mobilized zone just above the defect, and the erosion void is formed and expanded as the progressive soil loss. The sand flow rate through the pipe defect is found to be dependent on the defect size and sand particle size.

- In Chapter 4, based on the experimental study of the sand erosion through an orifice on the pipe with various locations, the sand flow rate during the erosion process is found to be dependent on the orifice size and sand particle size, while the defect position has little effect

on the sand flow rate. The erosion void is in the shape of a cone or truncated cone as the variation of the defect location on the pipe. The sand velocity distribution can be predicted using the proposed analytical model.

- In Chapter 5, it was found that the proposed coupling discrete element method can effectively simulate the sand/water flow through an orifice. From the numerical simulations, the sand permeability is the key factor controlling the fluid flow regime, which also influences the soil erosion process.

- In Chapter 6, from the numerical simulation using DEM, the assumption of free-fall arch is proved to be reasonable, and granular particle velocity is found to be negligible at the free-fall arch. The proposed analytical model is valid to predict the free-fall arch size and location in a two-dimensional condition, and the granular flow rate can be calculated based on this analytical model of free-fall arch.

- In Chapter 7, the proposed analytical model to estimate the sand and water flow rate through a two-dimensional opening is proved to be effective in comparison with the experimental and numerical results. From the numerical simulation, the free-fall arch theory is reasonable from the development of force chain between granular particles.

- In Chapter 8, based on the numerical simulation using CFD, the increase of sand particle size can significantly strength the sand bed against the erosion by the upward water jet, and the increase of sand bed height and friction angle can also increase the sand bed stability. From the proposed analytical model, the hydraulic Reynolds number and densimetric Froude number can be used to evaluate the sand bed critical state caused by the upward water jet.

9.2 Recommendations for Future Research

This thesis contributes to the knowledge of mechanisms of soil erosion due to the defective sewer pipe, which includes the soil erosion by water infiltration and exfiltration through the pipe defect. There are still many aspects left to continue research in these areas. The followings are recommended for future studies:

- The discrete element method used in this study on the soil erosion due to the defective sewer pipe is restricted by the scale of the simulation model, which can be improved in the future studies by introducing the combined numerical method using FEM and DEM. The eroded zone adjacent to the pipe defect shows the discrete behavior, which can be simulated using DEM, while the soil far away the erosion area can be simulated using FEM based on the continuum mechanics with higher computing efficiency.

- The mechanical analysis of the defective pipe behavior can be studied by taking the soil erosion process into account. In the erosion process, the stress distribution on the defective pipe is varied, which affects the mechanical behavior of pipe. If the hybrid FEM-DEM method can be developed and introduced, the pipe behavior can be simulated and studied.

- A three-dimensional free-fall arch theory should be developed to predict the free-fall arch formation when granular particles flow through an orifice. As the granular particles flow through an orifice, the free-fall arch will be formed as a 'dome' above the opening, while the size and location of this dome can be predicted using the force equilibrium. Therefore, the granular flow rate through an orifice can be predicted based on this analytical model, which will provide the theoretical basis for the analytical model of water/granular flow through an orifice.

- The Darcy fluid model will not be valid if water is flowing at higher Reynolds number, and another coupled discrete element model needs to be developed. This model can be used to simulate the soil erosion process by an upward water jet, and simulate the discrete behavior of the eroded soil.

- The risk analysis model can be developed to incorporate this study on the mechanisms of soil erosion by the defective sewer pipe. The risk of sinkhole accidents can be evaluated based on the soil property, pipe deterioration, and hydrogeology conditions, which can be applied to provide a risk map for the specific areas.

References

Adrian, R. J. (1991). "Particle-imaging techniques for experimental fluid mechanics." *Annual Review of Fluid Mechanics*, 23(1), 261-304.

Ahn, H., Başaranoğlu, Z., Yılmaz, M., Buğutekin, A., and Gül, M. Z. (2008). "Experimental investigation of granular flow through an orifice." *Powder Technology*, 186(1), 65-71.

Al-Din, N., and Gunn, D. J. (1984). "The flow of non-cohesive solids through orifices." *Chemical Engineering Science*, 39(1), 121-127.

Alsaydalani, M. O. A., and Clayton, C. R. I. (2014). "Internal fluidization in granular soils." *Journal of Geotechnical and Geoenvironmental Engineering*, 140(3).

Altenkirch, R. A., and Eichhorn, R. (1981). "Effect of fluid drag on low Reynolds number discharge of solids from a circular orifice." *AIChE Journal*, 27(4), 593-598.

Anderson, J. D. (1995). *Computational fluid dynamics: the basics with applications*, McGraw-Hill, New York.

Anderson, T. B., and Jackson, R. (1968). "Fluid mechanical description of fluidized beds. Stability of state of uniform fluidization." *Industrial & Engineering Chemistry Fundamentals*, 7(1), 12-21.

ANSYS Inc. (2013). "ANSYS FLUENT 15.0: Theory Guide." Canonsburg, PA.

Azimi, A. H., Zhu, D. Z., and Rajaratnam, N. (2012). "Computational investigation of vertical slurry jets in water." *International Journal of Multiphase Flow*, 47, 94-114.

Barletta, D., Donsì, G., Ferrari, G., and Poletto, M. (2003). "On the role and the origin of the gas pressure gradient in the discharge of fine solids from hoppers." *Chemical Engineering Science*, 58(23), 5269-5278.

Batchelor, G. K. (1967). *An introduction to fluid dynamics*, Cambridge University Press.

Bear, J. (1972). *Dynamics of fluids in porous media*, American Elsevier Pub. Co., New York.

Benyahia, S., Arastoopour, H., Knowlton, T. M., and Massah, H. (2000). "Simulation of particles and gas flow behavior in the riser section of a circulating fluidized bed using the kinetic theory approach for the particulate phase." *Powder Technology*, 112(1), 24-33.

Beverloo, W. A., Leniger, H. A., and Van de Velde, J. (1961). "The flow of granular solids through orifices." *Chemical Engineering Science*, 15(3), 260-269.

Bonilla, R. R. O. (2004). "Numerical simulations of undrained granular media." PhD, University of Waterloo.

Brown, R. L. (1961). "Minimum energy theorem for flow of dry granules through apertures." *Nature*, 191(4787), 458-461.

Brown, R. L., and Richards, J. (1965). "Kinematics of the flow of dry powders and bulk solids." *Rheologica Acta*, 4(3), 153-165.

Caquot, A. (1937). "Le rôle des matériaux inertes dans le béton." *mémoires de la Société des Ingénieurs Civils de France*, 90(5), 563-582.

Carman, P. C. (1956). *Flow of gases through porous media*, Butterworths Scientific Publications, London, England.

Cassa, A. M., van Zyl, J. E., and Laubscher, R. F. (2010). "A numerical investigation into the effect of pressure on holes and cracks in water supply pipes." *Urban Water Journal*, 7(2), 109-120.

Catalano, E., Chareyre, B., Cortis, A., and Barthélémy, E. (2011). "A pore-scale hydro-mechanical coupled model for geomaterials." *Particles 2011 II International Conference on Particle-Based Methods*, 798-809.

Chan, D. (1993). "Numerical simulation of wet granular flow." *The International Conference on Soft Soil Engineering,* Guangzhou, China, 68-73.

Chan, D., and Tipthavonnukul, S. (2008). "Numerical simulation of granular particles movement in fluid flow." *International Journal of Nonlinear Sciences and Numerical Simulation*, 9(3), 229-248.

Chang, M., and Huang, R.-C. (2015). "Observations of hydraulic fracturing in soils through field testing and numerical simulations." *Canadian Geotechnical Journal*, 53(2), 343-359.

Chareyre, B., Cortis, A., Catalano, E., and Barthélémy, E. (2012). "Pore-scale modeling of viscous flow and induced forces in dense sphere packings." *Transport in Porous Media*, 94(2), 595-615.

Chen, K., Stone, M. B., Barry, R., Lohr, M., McConville, W., Klein, K., Sheu, B. L., Morss, A. J., Scheidemantel, T., and Schiffer, P. (2006). "Flux through a hole from a shaken granular medium." *Physical Review E*, 74(1), 011306.

Chen, X.-Z., Shi, D.-P., Gao, X., and Luo, Z.-H. (2011). "A fundamental CFD study of the gas–solid flow field in fluidized bed polymerization reactors." *Powder Technology*, 205(1), 276-288.

Cheng, Y., and Zhu, J. X. J. (2005). "CFD Modelling and Simulation of Hydrodynamics in Liquid‑Solid Circulating Fluidized Beds." *The Canadian Journal of Chemical Engineering*, 83(2), 177-185.

Cook, B. K., Noble, D. R., and Williams, J. R. (2004). "A direct simulation method for particle-fluid systems." *Engineering Computations*, 21(2/3/4), 151-168.

Cooper, S., and Coronella, C. J. (2005). "CFD simulations of particle mixing in a binary fluidized bed." *Powder Technology*, 151(1), 27-36.

Cornelissen, J. T., Taghipour, F., Escudié, R., Ellis, N., and Grace, J. R. (2007). "CFD modelling of a liquid–solid fluidized bed." *Chemical Engineering Science*, 62(22), 6334-6348.

Crewdson, B. J., Ormond, A. L., and Nedderman, R. M. (1977). "Air-impeded discharge of fine particles from a hopper." *Powder Technology*, 16(2), 197-207.

Cui, X., Li, J., Chan, A., and Chapman, D. (2012). "A 2D DEM–LBM study on soil behaviour due to locally injected fluid." *Particuology*, 10(2), 242-252.

Cui, X., Li, J., Chan, A., and Chapman, D. (2014). "Coupled DEM–LBM simulation of internal fluidisation induced by a leaking pipe." *Powder Technology*, 254, 299-306.

Cui, X., Li, J., Chan, A., Chapman, D., Yu, A., Dong, K., Yang, R., and Luding, S. (2013). "A parametric study on the leakage-soil interaction due to a leaking pipe using the coupled DEM-LBM technique." *AIP Conference Proceedings*, AIP, 1035-1038.

Cui, Y., Chan, D., and Nouri, A. (2017). "Discontinuum modeling of solid deformation pore-water diffusion coupling." *International Journal of Geomechanics*, 04017033.

Cui, Y., Nouri, A., Chan, D., and Rahmati, E. (2016). "A new approach to DEM simulation of sand production." *Journal of Petroleum Science and Engineering*, 147, 56-67.

Cundall, P. A. (1971). "A computer model for simulating progressive large-scale movements in block rock mechanics." *Proceedings of the Symposium of International Society of Rock Mechanics*Nancy, France, No. II-8.

Cundall, P. A., and Strack, O. D. L. (1979). "A discrete numerical model for granular assemblies." *Géotechnique*, 29(1), 47-65.

Davidson, J. F., and Nedderman, R. M. (1973). "The hour-glass theory of hopper flow." *Trans. Inst. Chem. Eng*, 51, 29-35.

Davies, J. P., Clarke, B. A., Whiter, J. T., and Cunningham, R. J. (2001). "Factors influencing the structural deterioration and collapse of rigid sewer pipes." *Urban Water*, 3(1), 73-89.

de Jong, J. A. H., and Hoelen, Q. E. J. J. M. (1975). "Cocurrent gas and particle flow during pneumatic discharge from a bunker through an orifice." *Powder Technology*, 12(3), 201-208.

Desai, C. S., and Christian, J. T. (1977). *Numerical methods in geotechnical engineering*, McGraw-Hill, New York.

DeSilva, D., Burn, S., Tjandraatmadja, G., Moglia, M., Davis, P., Wolf, L., Held, I., Vollertsen, J., Williams, W., and Hafskjold, L. (2005). "Sustainable management of leakage from wastewater pipelines." *Water Science and Technology*, 52(12), 189-198.

Di Felice, R. (1994). "The voidage function for fluid-particle interaction systems." *International Journal of Multiphase Flow*, 20(1), 153-159.

Donsì, G., Ferrari, G., and Poletto, M. (1997). "Distribution of gas pressure inside a hopper discharging fine powders." *Chemical Engineering Science*, 52(23), 4291-4302.

Drescher, A. (1991). *Analytical methods in bin-load analysis*, Elsevier.

Drescher, A., Waters, A. J., and Rhoades, C. A. (1995a). "Arching in hoppers: I. Arching theories and bulk material flow properties." *Powder Technology*, 84(2), 165-176.

Drescher, A., Waters, A. J., and Rhoades, C. A. (1995b). "Arching in hoppers: II. Arching theories and critical outlet size." *Powder Technology*, 84(2), 177-183.

El Shamy, U., and Zeghal, M. (2005). "Coupled continuum-discrete model for saturated granular soils." *Journal of Engineering Mechanics*, 131(4), 413-426.

El Shamy, U., and Zeghal, M. (2007). "A micro-mechanical investigation of the dynamic response and liquefaction of saturated granular soils." *Soil Dynamics and Earthquake Engineering*, 27(8), 712-729.

El Tani, M. (2003). "Circular tunnel in a semi-infinite aquifer." *Tunnelling and Underground Space Technology*, 18(1), 49-55.

Ergun, S. (1952). "Fluid flow through packed columns." *Journal of Chemical Engineering Progress*, 48(2), 89-94.

Fathi-Moghadam, M., Emamgholizadeh, S., Bina, M., and Ghomeshi, M. (2010). "Physical modelling of pressure flushing for desilting of non-cohesive sediment." *Journal of Hydraulic Research*, 48(4), 509-514.

Feng, Y. T., Han, K., and Owen, D. R. J. (2007). "Coupled lattice Boltzmann method and discrete element modelling of particle transport in turbulent fluid flows: Computational issues." *International Journal for Numerical Methods in Engineering*, 72(9), 1111-1134.

Fenner, R. A. (1991). "Influence of sewer bedding arrangements on infiltration rates on soil migration." *Proceedings of ICE, Municipal Engineer (Institution of Civil Engineers)*, 8, 105-117.

Franklin, F. C., and Johanson, L. N. (1955). "Flow of granular material through a circular orifice." *Chemical Engineering Science*, 4(3), 119-129.

Freeze, R. A., and Cherry, J. A. (1979). *Groundwater*, Prentice-Hall, Englewood Cliffs, New Jersey.

Frisch, U., Hasslacher, B., and Pomeau, Y. (1986). "Lattice-gas automata for the Navier-Stokes equation." *Physical Review Letters*, 56(14), 1505.

Gidaspow, D. (1994). *Multiphase flow and fluidization: continuum and kinetic theory descriptions*, Academic Press.

Gidaspow, D., Bezburuah, R., and Ding, J. (1991). "Hydrodynamics of circulating fluidized beds: kinetic theory approach." Illinois Inst. of Tech., Chicago, IL (United States). Dept. of Chemical Engineering.

Gingold, R. A., and Monaghan, J. J. (1977). "Smoothed particle hydrodynamics: theory and application to non-spherical stars." *Monthly Notices of the Royal Astronomical Society*, 181(3), 375-389.

Goodarzi, M., Kwok, C. Y., and Tham, L. G. (2015). "A continuum‑discrete model using Darcy's law: formulation and verification." *International Journal for Numerical and Analytical Methods in Geomechanics*, 39(3), 327-342.

Guariguata, A., Pascall, M. A., Gilmer, M. W., Sum, A. K., Sloan, E. D., Koh, C. A., and Wu, D. T. (2012). "Jamming of particles in a two-dimensional fluid-driven flow." *Physical Review E*, 86(6), 061311.

Guo, S., Shao, Y., Zhang, T., Zhu, D. Z., and Zhang, Y. (2013a). "Physical modeling on sand erosion around defective sewer pipes under the influence of goundwater." *Journal of Hydraulic Engineering*, 139(12), 1247-1257.

Guo, S., Zhang, T., Zhang, Y., and Zhu, D. Z. (2013b). "An approximate solution for two-dimensional groundwater infiltration in sewer systems." *Water Science and Technology*, 67(2), 347-352.

Guo, S., and Zhu, D. Z. (2017). "Soil and groundwater erosion rates into a sewer pipe crack." *Journal of Hydraulic Engineering*, 06017008.

Hakuno, M., and Tarumi, Y. (1988). "A granular assembly simulation for the seismic liquefaction of sand." *Proceedings of the Japan Society of Civil Engineers*(398), 129-138.

Han, Y., and Cundall, P. A. (2013). "LBM–DEM modeling of fluid–solid interaction in porous media." *International Journal for Numerical and Analytical Methods in Geomechanics*, 37(10), 1391-1407.

He, Y., Zhu, D. Z., Zhang, T., Shao, Y., and Yu, T. (2017). "Experimental observations on the Initiation of sand-bed erosion by an upward water jet." *Journal of Hydraulic Engineering*, 06017007.

Hermosilla, R. G. (2012). "The Guatemala city sinkhole collapses." *Carbonates and Evaporites*, 27(2), 103-107.

Hilton, J. E., and Cleary, P. W. (2011). "Granular flow during hopper discharge." *Physical Review E*, 84(1), 011307.

Huang, Y. J., and Nydal, O. J. (2012). "Coupling of discrete-element method and smoothed particle hydrodynamics for liquid-solid flows." *Theoretical and Applied Mechanics Letters*, 2(1).

Hunt, M. L., Weathers, R. C., Lee, A. T., Brennen, C. E., and Wassgren, C. R. (1999). "Effects of horizontal vibration on hopper flows of granular materials." *Physics of Fluids*, 11(1), 68-75.

Indiketiya, S. H., Jegatheesan, P., and Rajeev, P. (2017). "Evaluation of defective sewer pipe induced internal erosion and associated ground deformation using laboratory model test." *Canadian Geotechnical Journal*.

Itasca Consulting Group (2008). "PFC3D version 4.0 manual." Minneapolis.

Janda, A., Zuriguel, I., Garcimartín, A., Pugnaloni, L. A., and Maza, D. (2008). "Jamming and critical outlet size in the discharge of a two-dimensional silo." *EPL (Europhysics Letters)*, 84(4), 44002.

Janda, A., Zuriguel, I., and Maza, D. (2012). "Flow rate of particles through apertures obtained from self-similar density and velocity profiles." *Physical Review Letters*, 108(24), 248001.

Janssen, H. A. (1895). "Versuche über getreidedruck in silozellen." *Zeitschr. d. Vereines deutscher Ingenieure*, 39(35), 1045-1049.

Jensen, R. P., and Preece, D. S. (2000). "Modeling sand production with Darcy-flow coupled with discrete elements." Sandia National Labs., Albuquerque, NM (US); Sandia National Labs., Livermore, CA (US).

Jeyisanker, K., and Gunaratne, M. (2009). "Analysis of water seepage in a pavement system using the particulate approach." *Computers and Geotechnics*, 36(4), 641-654.

Kafui, K. D., Thornton, C., and Adams, M. J. (2002). "Discrete particle-continuum fluid modelling of gas–solid fluidised beds." *Chemical Engineering Science*, 57(13), 2395-2410.

Kamel, S., and Meguid, M. A. (2013). "Investigating the effects of local contact loss on the earth pressure distribution on rigid pipes." *Geotechnical and Geological Engineering*, 31(1), 199-212.

Karpf, C., and Krebs, P. (2013). "Modelling of groundwater infiltration into sewer systems." *Urban Water Journal*, 10(4), 221-229.

Khanam, J., and Nanda, A. (2005). "Flow of granules through cylindrical hopper." *Powder Technology*, 150(1), 30-35.

Kim, J., Choi, C., Kang, J., Baek, W., and Chung, M. (2016). "Model test for the observation of cavity formation in sandy ground-with reference to ground water level and relative density." *Japanese Geotechnical Society Special Publication*, 4(4), 64-67.

Kozeny, J. (1927). *Über kapillare Leitung des Wassers im Boden:(Aufstieg, Versickerung und Anwendung auf die Bewässerung)*, Hölder-Pichler-Tempsky.

Lai, J.-S., and Shen, H. W. (1996). "Flushing sediment through reservoirs." *Journal of Hydraulic Research*, 34(2), 237-255.

Lambe, T. W., and Whitman, R. V. (1969). *Soil mechanics*, Wiley.

Lambert, A. (2001). "What do we know about pressure-leakage relationships in distribution systems ?" *IWA Conf. on Systems approach to leakage control and water distribution system management*, Citeseer, Brno, Czech Republic.

Lamptey, B. O. M., and Thorpe, R. B. (1991). "The discharge of solid-liquid mixtures from hoppers." *Chemical Engineering Science*, 46(9), 2197-2212.

Langford, M. T., Zhu, D. Z., and Leake, A. (2015). "Upstream hydraulics of a run-of-the river hydropower facility for fish entrainment risk assessment." *Journal of Hydraulic Engineering*, 05015006.

Le Pennec, T., Måløy, K. J., Hansen, A., Ammi, M., Bideau, D., and Wu, X.-l. (1996). "Ticking hour glasses: experimental analysis of intermittent flow." *Physical Review E*, 53(3), 2257.

Lettieri, P., Di Felice, R., Pacciani, R., and Owoyemi, O. (2006). "CFD modelling of liquid fluidized beds in slugging mode." *Powder Technology*, 167(2), 94-103.

Leung, C., and Meguid, M. A. (2011). "An experimental study of the effect of local contact loss on the earth pressure distribution on existing tunnel linings." *Tunnelling and Underground Space Technology*, 26(1), 139-145.

Li, J., Langston, P. A., Webb, C., and Dyakowski, T. (2004). "Flow of sphero-disc particles in rectangular hoppers—a DEM and experimental comparison in 3D." *Chemical Engineering Science*, 59(24), 5917-5929.

Li, L., and Holt, R. M. (2001). "Simulation of flow in sandstone with fluid coupled particle model." *DC Rocks 2001, The 38th US Symposium on Rock Mechanics (USRMS)*, American Rock Mechanics Association, Washington, D.C.

Li, L., and Holt, R. M. (2002). "Particle scale reservoir mechanics." *Oil & Gas Science and Technology*, 57(5), 525-538.

Li, X., Chu, X., and Sheng, D. C. (2007). "A saturated discrete particle model and characteristic-based SPH method in granular materials." *International Journal for Numerical Methods in Engineering*, 72(7), 858-882.

Liu, G., Rong, G., Peng, J., and Zhou, C. (2015). "Numerical simulation on undrained triaxial behavior of saturated soil by a fluid coupled-DEM model." *Engineering Geology*, 193, 256-266.

Liu, S. H. (2006). "Simulating a direct shear box test by DEM." *Canadian Geotechnical Journal*, 43(2), 155-168.

Liu, Y. (2014). "The theoretical calculation of the flow rate of granular matter from an inclined orifice." *Granular Matter*, 16(1), 133-139.

Lominé, F., Scholtès, L., Sibille, L., and Poullain, P. (2013). "Modeling of fluid–solid interaction in granular media with coupled lattice Boltzmann/discrete element methods: application to piping erosion." *International Journal for Numerical and Analytical Methods in Geomechanics*, 37(6), 577-596.

Lun, C. K. K., Savage, S. B., Jeffrey, D. J., and Chepurniy, N. (1984). "Kinetic theories for granular flow: inelastic particles in Couette flow and slightly inelastic particles in a general flow field." *Journal of Fluid Mechanics*, 140, 223-256.

Makar, J. M. (2000). "A preliminary analysis of failures in grey cast iron water pipes." *Engineering Failure Analysis*, 7(1), 43-53.

Mamtani, K. (2011). "Effect of Particle Shape on Hopper Discharge Rate." MSc, University of Florida.

Mankoc, C., Garcimartín, A., Zuriguel, I., Maza, D., and Pugnaloni, L. A. (2009). "Role of vibrations in the jamming and unjamming of grains discharging from a silo." *Physical Review E*, 80(1), 011309.

Mankoc, C., Janda, A., Arevalo, R., Pastor, J. M., Zuriguel, I., Garcimartín, A., and Maza, D. (2007). "The flow rate of granular materials through an orifice." *Granular Matter*, 9(6), 407-414.

Mitchell, J. K., and Soga, K. (2005). *Fundamentals of soil behavior*, John Wiley & Sons, New York.

Monaghan, J. J. (1994). "Simulating free surface flows with SPH." *Journal of Computational Physics*, 110(2), 399-406.

Moreea, S. B. M., and Nedderman, R. (1996). "Exact stress and velocity distributions in a cohesionless material discharging from a conical hopper." *Chemical Engineering Science*, 51(16), 3931-3942.

Morris, J. P., Fox, P. J., and Zhu, Y. (1997). "Modeling low Reynolds number incompressible flows using SPH." *Journal of Computational Physics*, 136(1), 214-226.

Morsi, S. A., and Alexander, A. J. (1972). "An investigation of particle trajectories in two-phase flow systems." *Journal of Fluid Mechanics*, 55(02), 193-208.

Mukunoki, T., Kumano, N., and Otani, J. (2012). "Image analysis of soil failure on defective underground pipe due to cyclic water supply and drainage using X-ray CT." *Frontiers of Structural and Civil Engineering*, 6(2), 85-100.

Mukunoki, T., Kumano, N., Otani, J., and Kuwano, R. (2009). "Visualization of three dimensional failure in sand due to water inflow and soil drainage from defective underground pipe using X-ray CT." *Soils and Foundations*, 49(6), 959-968.

Nedderman, R. M. (1992). *Statics and kinematics of granular materials*, Cambridge University Press.

Nedderman, R. M., and Laohakul, C. (1980). "The thickness of the shear zone of flowing granular materials." *Powder Technology*, 25(1), 91-100.

Nedderman, R. M., and Tüzün, U. (1979). "A kinematic model for the flow of granular materials." *Powder Technology*, 22(2), 243-253.

Nermoen, A., Raufaste, C., Daniel deVilliers, S., Jettestuen, E., Meakin, P., and Dysthe, D. K. (2010). "Morphological transitions in partially gas-fluidized granular mixtures." *Physical Review E*, 81(6), 061305.

Ng, T.-T. (2004). "Triaxial test simulations with discrete element method and hydrostatic boundaries." *Journal of Engineering Mechanics*, 130(10), 1188-1194.

O'Sullivan, C. (2011). *Particulate discrete element modelling: a geomechanics perspective*, Spon Press/Taylor & Francis, London.

Papazoglou, C. S., and Pyle, D. L. (1970). "Air-assisted flow from a bed of particles." *Powder Technology*, 4(1), 9-18.

Park, K.-H., Owatsiriwong, A., and Lee, J.-G. (2008). "Analytical solution for steady-state groundwater inflow into a drained circular tunnel in a semi-infinite aquifer: a revisit." *Tunnelling and Underground Space Technology*, 23(2), 206-209.

Philippe, P., and Badiane, M. (2013). "Localized fluidization in a granular medium." *Physical Review E*, 87(4), 042206.

Potapov, A. V., Hunt, M. L., and Campbell, C. S. (2001). "Liquid–solid flows using smoothed particle hydrodynamics and the discrete element method." *Powder Technology*, 116(2), 204-213.

Pournin, L., Ramaioli, M., Folly, P., and Liebling, T. M. (2007). "About the influence of friction and polydispersityon the jamming behavior of bead assemblies." *The European Physical Journal E*, 23(2), 229.

Powell, D. N., and Khan, A. A. (2012). "Scour upstream of a circular orifice under constant head." *Journal of Hydraulic Research*, 50(1), 28-34.

Powell, D. N., and Khan, A. A. (2014). "Flow field upstream of an orifice under fixed bed and equilibrium scour conditions." *Journal of Hydraulic Engineering*, 141(2), 04014076.

Preece, D. S., Jensen, R. P., Perkins, E. D., and Williams, J. R. (1999). "Sand production modeling using superquadric discrete elements and coupling of fluid flow and particle motion." *Rock Mechanics for Industry, Proc. 37th US Rock Mech. Symp.*, 161-167.

Rajaratnam, N. (1981). "Erosion by plane turbulent jets." *Journal of Hydraulic Research*, 19(4), 339-358.

Rao, K. K., and Nott, P. R. (2008). *An introduction to granular flow*, Cambridge University Press.

Resnick, W., Heled, Y., Klein, A., and Palm, E. (1966). "Effect of differential pressure on flow of granular solids through orifices." *Industrial & Engineering Chemistry Fundamentals*, 5(3), 392-396.

Rigord, P., Guarino, A., Vidal, V., and Géminard, J.-C. (2005). "Localized instability of a granular layer submitted to an ascending liquid flow." *Granular Matter*, 7(4), 191-197.

Ring, R. J., Buchanan, R. H., and Doig, I. D. (1973). "The discharge of granular material from hoppers submerged in water." *Powder Technology*, 8(3-4), 117-125.

Robinson, M., Ramaioli, M., and Luding, S. (2014). "Fluid–particle flow simulations using two-way-coupled mesoscale SPH–DEM and validation." *International Journal of Multiphase Flow*, 59, 121-134.

Rubio-Largo, S. M., Janda, A., Maza, D., Zuriguel, I., and Hidalgo, R. C. (2015). "Disentangling the free-fall arch paradox in silo discharge." *Physical Review Letters*, 114(23), 238002.

Sato, M., and Kuwano, R. (2013). "Effects of buried structures on the formation of underground cavity." *Proceedings on the 18th International Conference on Soil Mechanics and Geotechnical Engineering, Paris*, 1769-1772.

Sato, M., and Kuwano, R. (2015). "Influence of location of subsurface structures on development of underground cavities induced by internal erosion." *Soils and Foundations*, 55(4), 829-840.

Savage, S. B. (1965). "The mass flow of granular materials derived from coupled velocity-stress fields." *British Journal of Applied Physics*, 16(12), 1885.

Schaeffer, D. G. (1987). "Instability in the evolution equations describing incompressible granular flow." *Journal of Differential Equations*, 66(1), 19-50.

Shan, T., and Zhao, J. (2014). "A coupled CFD-DEM analysis of granular flow impacting on a water reservoir." *Acta Mechanica*, 225(8), 2449.

Sheldon, H. G., and Durian, D. J. (2010). "Granular discharge and clogging for tilted hoppers." *Granular Matter*, 12(6), 579-585.

Shimizu, Y. (2011). "Microscopic numerical model of fluid flow in granular material." *Géotechnique*, 61(10), 887-896.

Spasojevic, A. D., Mair, R. J., and Gumbel, J. E. (2007). "Centrifuge modelling of the effects of soil loading on flexible sewer liners." *Géotechnique*, 57(4), 331-341.

Ssozi, E. N., Reddy, B. D., and van Zyl, J. E. (2015). "Numerical Investigation of the Influence of Viscoelastic Deformation on the Pressure-Leakage Behavior of Plastic Pipes." *Journal of Hydraulic Engineering*, 04015057.

Suzuki, K., Bardet, J. P., Oda, M., Iwashita, K., Tsuji, Y., Tanaka, T., and Kawaguchi, T. (2007). "Simulation of upward seepage flow in a single column of spheres using discrete-element method with fluid-particle interaction." *Journal of Geotechnical and Geoenvironmental Engineering*, 133(1), 104-109.

Syamlal, M., Rogers, W., and O'Brien, T. J. (1993). "MFIX documentation: Theory guide." *Technical Note DOE/METC-95/1013 and NTIS/DE95000031*, National Energy Technology Laboratory, Department of Energy.

Taghipour, F., Ellis, N., and Wong, C. (2005). "Experimental and computational study of gas–solid fluidized bed hydrodynamics." *Chemical Engineering Science*, 60(24), 6857-6867.

Tan, Z., and Moore, I. D. (2007). "Effect of backfill erosion on moments in buried rigid pipes." *Transportation Research Board 86th Annual Meeting,* Washington, D.C.

Tao, H., Jin, B., Zhong, W., Wang, X., Ren, B., Zhang, Y., and Xiao, R. (2010). "Discrete element method modeling of non-spherical granular flow in rectangular hopper." *Chemical Engineering and Processing: Process Intensification*, 49(2), 151-158.

Taylor, D. W. (1948). *Fundamentals of soil mechanics*, Wiley, New York.

Taylor, Z. J., Gurka, R., Kopp, G. A., and Liberzon, A. (2010). "Long-duration time-resolved PIV to study unsteady aerodynamics." *Instrumentation and Measurement, IEEE Transactions on*, 59(12), 3262-3269.

Thallak, S., Rothenburg, L., and Dusseault, M. (1990). "Hydraulic fracture (parting) simulation in granular assemblies using the discrete element method." *AOSTRA Journal of Research*, 6, 141-153.

Thallak, S., Rothenburg, L., and Dusseault, M. (1991). "Simulation of multiple hydraulic fractures in a discrete element system." *The 32nd US Symposium on Rock Mechanics (USRMS)*, American Rock Mechanics Association, Norman, Oklahoma.

Tian, Y., Lin, P., Zhang, S., Wang, C. L., Wan, J. F., and Yang, L. (2015). "Study on free fall surfaces in three-dimensional hopper flows." *Advanced Powder Technology*, 26(4), 1191-1199.

To, K., Lai, P.-Y., and Pak, H. K. (2001). "Jamming of granular flow in a two-dimensional hopper." *Physical Review Letters*, 86(1), 71.

Tsuji, Y., Kawaguchi, T., and Tanaka, T. (1993). "Discrete particle simulation of two-dimensional fluidized bed." *Powder Technology*, 77(1), 79-87.

Tüzün, U., Houlsby, G. T., Nedderman, R. M., and Savage, S. B. (1982). "The flow of granular materials II: Velocity distributions in slow flow." *Chemical Engineering Science*, 37(12), 1691-1709.

Tüzün, U., and Nedderman, R. M. (1979). "Experimental evidence supporting kinematic modelling of the flow of granular media in the absence of air drag." *Powder Technology*, 24(2), 257-266.

van Zyl, J. E., Alsaydalani, M. O. A., Clayton, C. R. I., Bird, T., and Dennis, A. (2013). "Soil fluidisation outside leaks in water distribution pipes-preliminary observations." *Proceedings of the Institution of Civil Engineers*, 166(10), 546.

Vasquez, S. A., and Ivanov, V. A. (2000). "A phase coupled method for solving multiphase problems on unstructured meshes." *Proc., ASME Fluids Engineering Div. Summer Meeting,* New York, 743-748.

Wang, M., Feng, Y. T., and Wang, C. Y. (2016). "Coupled bonded particle and lattice Boltzmann method for modelling fluid–solid interaction." *International Journal for Numerical and Analytical Methods in Geomechanics*.

Wassgren, C. R., Hunt, M. L., Freese, P. J., Palamara, J., and Brennen, C. E. (2002). "Effects of vertical vibration on hopper flows of granular material." *Physics of Fluids*, 14(10), 3439-3448.

Wen, C. Y., and Yu, Y. H. (1966). "Mechanics of fluidization." *The Chemical Engineering Progress Symposium Series*, 162, 100-111.

White, D. J., Take, W. A., and Bolton, M. D. (2003). "Soil deformation measurement using particle image velocimetry (PIV) and photogrammetry." *Géotechnique*, 53(7), 619-632.

White, F. (2005). *Viscous fluid flow*, McGraw-Hill Education.

Widuliński, Ł., Kozicki, J., and Tejchman, J. (2009). "Numerical simulations of triaxial test with sand using DEM." *Archives of Hydro–Engineering and Environmental Mechanics*, 56(3-4), 149-172.

WRc (2001). *Sewerage rehabilitation manual*, Marlow, UK.

Wu, J., Chen, J., and Yang, Y. (2008). "A modified kinematic model for particle flow in moving beds." *Powder Technology*, 181(1), 74-82.

Yang, Y., Zhu, D. Z., Zhang, T., Liu, W., and Guo, S. (2016). "Improved model for contaminant intrusion induced by negative pressure events in water distribution systems." *Journal of Hydraulic Engineering*, 142(10), 06016012.

Zeghal, M., and El Shamy, U. (2004). "A continuum‐discrete hydromechanical analysis of granular deposit liquefaction." *International Journal for Numerical and Analytical Methods in Geomechanics*, 28(14), 1361-1383.

Zhu, H. P., Zhou, Z. Y., Yang, R. Y., and Yu, A. B. (2007). "Discrete particle simulation of particulate systems: theoretical developments." *Chemical Engineering Science*, 62(13), 3378-3396.

Zou, Y.-H., Chen, Q., Chen, X.-Q., and Cui, P. (2013). "Discrete numerical modeling of particle transport in granular filters." *Computers and Geotechnics*, 47, 48-56.

Zoueshtiagh, F., and Merlen, A. (2007). "Effect of a vertically flowing water jet underneath a granular bed." *Physical Review E*, 75(5), 056313.

Zuriguel, I., Garcimartín, A., Maza, D., Pugnaloni, L. A., and Pastor, J. M. (2005). "Jamming during the discharge of granular matter from a silo." *Physical Review E*, 71(5), 051303.

Zuriguel, I., Pugnaloni, L. A., Garcimartin, A., and Maza, D. (2003). "Jamming during the discharge of grains from a silo described as a percolating transition." *Physical Review E*, 68(3), 030301.

Appendix A: Sources of Urban Sinkholes in Table 2.1

1- Swanson, P. G., and Larson, T. W. (2000). "Sewer Tunnel Collapse: A Case History." *Forensic Engineering*.

2- Hermosilla, R. G. (2012). "The Guatemala city sinkhole collapses." *Carbonates and evaporites*, 27(2), 103-107.

3- CBC (2009). "Toronto sinkholes cause major disruption." <http://www.cbc.ca/news/canada/toronto/toronto-sinkholes-cause-major-disruption-1.828899>.

4- Than, K. (2010). "Guatemala Sinkhole Created by Humans, Not Nature." <http://news.nationalgeographic.com/news/2010/06/100603-science-guatemala-sinkhole-2010-humans-caused/>.

5- Shirk, J., and Stafford-Brown, K. (2012). "Pipe Collapse in an Amusement Park-Now What Do You Do?" *Pipelines 2012*.

6- Ben (2011). "Austin, Texas. February 1st, 2011.", <https://thesinkhole.org/2011/02/01/austin-texas-february-1st-2011/>.

7- Ben (2011). "Panama City, Florida. February 20th, 2011.", <https://thesinkhole.org/2011/02/20/panama-city-florida-february-20th-2011/>.

8- Ben (2011). "Middletown, Ohio. March 17th, 2011.", <https://thesinkhole.org/2011/03/17/middletown-ohio-march-17th-2011/>.

9- Ben (2011). "Manchester, Connecticut. March 18th, 2011.", <https://thesinkhole.org/2011/03/18/manchester-connecticut-march-18th-2011/>.

10- Ben (2011). "Gosford, New South Wales, Australia. March 21st, 2011.", <https://thesinkhole.org/2011/03/21/gosford-new-south-wales-australia-march-21st-2011/>.

11- CTV (2011). "Sinkhole on 22nd St. big enough to "swallow a car"." <http://saskatoon.ctvnews.ca/sinkhole-on-22nd-st-big-enough-to-quot-swallow-a-car-quot-1.631165>.

12- Hannagan, C. (2011). "Syracuse officials fear April storm created more sinkholes." <http://www.syracuse.com/news/index.ssf/2011/05/syracuse_officials_fear_april.html>.

13- Guttersohn, R. (2011). "Sinkhole appears suddenly on Belmont Ave.", <http://www.vindy.com/news/2011/may/17/sinkhole-appears-suddenly-on-belmont-ave/>.

14- Conte, M. (2011). "Sinkhole in Jersey City causes electric, gas and water service suspensions." <http://www.nj.com/hudson/index.ssf/2011/05/sink_hole_in_jersey_city_cause.html>.

15- Ben (2011). "Buffalo, New York. June 2nd, 2011.", <https://thesinkhole.org/2011/06/02/buffalo-new-york-june-2nd-2011/>.

16- Mangels, J. (2011). "Collapse of old sewer tunnel segment is culprit in Carnegie Avenue sinkhole." <http://blog.cleveland.com/metro/2011/06/collapse_of_old_sewer_tunnel_s.html>.

17- Strauch, J. A. (2012). "From Tiny Hole to Huge Problem Overnight-Emergency Culvert Pipe Repair." *Pipelines 2012*.

18- MCOT (2012). "Crater in downtown Bangkok road disrupts traffic, worries city officials." <http://www.pattayamail.com/thailandnews/crater-in-downtown-bangkok-road-disrupts-traffic-worries-city-officials-11865>.

19- Hurley, M. (2012). "Sinkhole swallows car, closes eastbound Highway 174." <http://www.ottawacitizen.com/Sinkhole+swallows+closes+eastbound+Highway/7189052/story.html>.

20- Xinmin (2012). "Sinkhole in Jinke Road, Shanghai." <http://hot.online.sh.cn/content/2012-09/24/content_5582795.htm>.

21- Tellez, R. (2013). "Two Weeks Later, West Pullman Sinkhole Bigger Than Ever." <http://chicago.cbslocal.com/2013/05/06/two-weeks-later-west-pullman-sinkhole-bigger-than-ever/>.

22- Harris, B. (2013). "Sinkhole delays Dryden traffic." <http://www.kenoraonline.com/index.php?option=com_content&task=view&id=5411&Itemid=160 > .

23- Tumilty , R. (2014). "Sinkhole opens up on 50th street in South Edmonton." <http://www.metronews.ca/news/edmonton/2014/05/25/sinkhole-opens-up-on-50th-street-in-south-edmonton.html>.

24- Melo, F. (2014). "St. Paul's East Side sinkhole opens up host of problems." <http://www.twincities.com/2014/05/19/st-pauls-east-side-sinkhole-opens-up-host-of-problems/>.

25- Sturgis, I. (2015). "Now that's a hazard! Historic golf course in Scotland begins repairs on massive sinkhole that nearly shut century-old club." <http://www.dailymail.co.uk/travel/travel_news/article-2961830/Now-s-hazard-Historic-golf-course-Scotland-begins-repairs-massive-sinkhole-nearly-shut-century-old-club.html>.

26- Ben (2015). "Oxford, Mississippi. April 29th 2015.", <https://thesinkhole.org/2015/04/29/oxford-mississippi-april-29th-2015/>.

27- Cain, B. (2015). "Solon sees about 100 sinkholes each year; most caused by sewer-related failures." <http://www.cleveland.com/solon/index.ssf/2015/11/solon_sees_about_100_sinkholes.html>.

28- Hoppa, K. (2016). "Sinkhole causes Herring Avenue closure." <http://www.wacotrib.com/news/traffic/sinkhole-causes-herring-avenue-closure/article_c6092054-d866-53d8-9a9f-1905e2606ceb.html>.

29- Sun, Y., Xu, J., Chen, K., Yu, W., and Sun, J. (2016). "Sinkhole, Hangzhou. April, 2016.", <http://zjnews.zjol.com.cn/system/2016/04/22/021120434.shtml>.

30- Martins, D. (2016). "Sinkhole: Officials hope Canada Day won't be impacted." <https://www.theweathernetwork.com/news/articles/watch-giant-sinkhole-in-downtown-ottawa/68718>.

31- Meng, Y. (2016). "Sinkhole, Beijing. July, 2016.", <http://epaper.ynet.com/html/2016-07/22/content_209707.htm?div=0>.

32- Cambridge (2016). "'It was all anyone talked about!' Sudden 'sinkhole' sparks alarm on Cambridge street." <http://www.cambridge-news.co.uk/8216-it-was-all-anyone-talked-about-8217-sudden-8216-sinkhole-8217-sparks-alarm-on-cambridge-street/story-29635777-detail/story.html>.

33- Sanchez, A., and Jones, J. (2016). "Crews work to repair sinkhole in downtown Paducah." <http://www.wpsdlocal6.com/story/32917277/crews-work-to-repair-sinkhole-in-downtown-paducah>.

34- Kinabalu, K. (2016). "Another sinkhole in Likas." <http://www.dailyexpress.com.my/news.cfm?NewsID=114013>.

35- McKirdy, E. (2016). "Giant sinkhole in Japan repaired in matter of days." <http://www.cnn.com/2016/11/15/asia/fukuoka-sinkhole-filled/>.

36- Shao, F. (2016). "Sinkhole, Shenzhen. Nov., 2016.", <http://news.163.com/16/1104/06/C50PGTN9000187VE.html>.

37- Press, A. (2017). "Officials: Drilled hole in pipe may have caused sinkhole." <http://www.dailymail.co.uk/wires/ap/article-4088896/Officials-Drilled-hole-pipe-caused-sinkhole.html>.

Appendix B: Implementation of the Coupled Discrete Element Model

From Eq. (5.1), the equation contains a second derivative of total water head, which can be solved using the finite difference method. Therefore, the governing equation can be rewritten in the following numerical scheme:

$$\phi^{t+\Delta t}_{i,j,k} = \phi^t_{i,j,k} + \frac{\Delta t}{n^t_{i,j,k}\beta_f\gamma}\overline{Q}_{i,j,k}$$

$$+ \frac{\Delta t}{n^t_{i,j,k}\beta_f\gamma}\left(\frac{k^t_{i+1,j,k} - k^t_{i-1,j,k}}{2\Delta x} \cdot \frac{\phi^t_{i+1,j,k} - \phi^t_{i-1,j,k}}{2\Delta x} + k^t_{i,j,k}\frac{\phi^t_{i+1,j,k} - 2\phi^t_{i,j,k} + \phi^t_{i-1,j,k}}{(\Delta x)^2}\right)$$

$$+ \frac{\Delta t}{n^t_{i,j,k}\beta_f\gamma}\left(\frac{k^t_{i,j+1,k} - k^t_{i,j-1,k}}{2\Delta y} \cdot \frac{\phi^t_{i,j+1,k} - \phi^t_{i,j-1,k}}{2\Delta y} + k^t_{i,j,k}\frac{\phi^t_{i,j+1,k} - 2\phi^t_{i,j,k} + \phi^t_{i,j-1,k}}{(\Delta y)^2}\right)$$

$$+ \frac{\Delta t}{n^t_{i,j,k}\beta_f\gamma}\left(\frac{k^t_{i,j,k+1} - k^t_{i,j,k-1}}{2\Delta z} \cdot \frac{\phi^t_{i,j,k+1} - \phi^t_{i,j,k-1}}{2\Delta z} + k^t_{i,j,k}\frac{\phi^t_{i,j,k+1} - 2\phi^t_{i,j,k} + \phi^t_{i,j,k-1}}{(\Delta z)^2}\right)$$

(B.1)

where k_x, k_y, and k_z are the coefficients of permeability in the x, y, and z directions, respectively; t indicates time; ϕ is the total fluid head, which consists of the pressure head p/γ and elevation head z, where γ is the unit weight of water; $\overline{Q}$ is the specified fluid flux; n is the porosity of the porous media; and β_f is the fluid compressibility, which is normally considered as 4.4×10^{-10} Pa^{-1} when water flows through porous media (Freeze and Cherry, 1979).

In Eq. (B.1), the time step is determined using the von Neumann stability method, which is commonly used to determine the time-step to ensure numerical stability in solving partial differential equations as follows (Anderson, 1995):

$$\Delta t = \min\left(\frac{n\beta_f\gamma(\Delta x)^2}{2k_x}, \frac{n\beta_f\gamma(\Delta y)^2}{2k_y}, \frac{n\beta_f\gamma(\Delta z)^2}{2k_z}\right)$$

(B.2)

Through this numerical scheme, the water head at each node during the transient flow process can be determined. Subsequently, the velocity at each node can be obtained directly from the hydraulic gradient and permeability based on Darcy's law.

A program has been developed that combines the DEM with the Darcy fluid model. The flow chart for the calculation procedure is shown in Figure B.1.
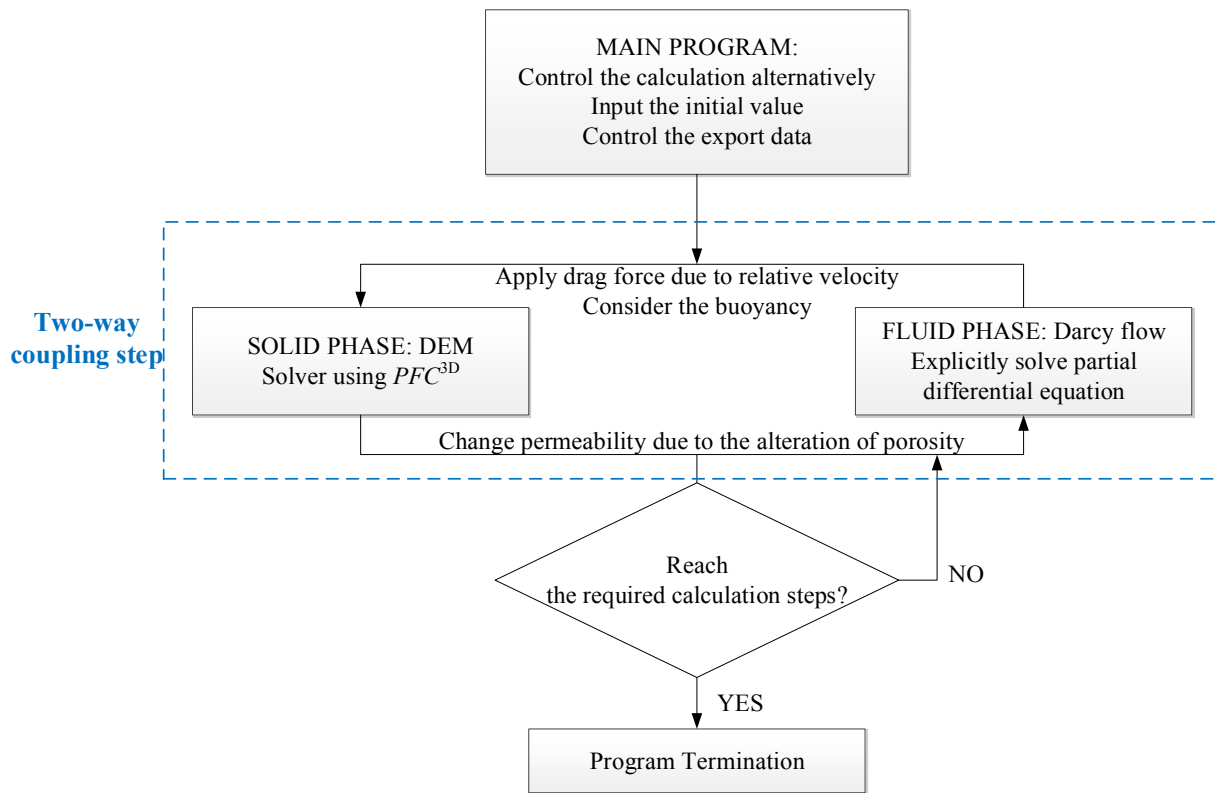

Figure B.1 Flowchart of the program implementation

Implementation is controlled by the main program, as shown in Figure B.1, which implements the DEM and the Darcy fluid model calculation cycle alternately, with the data file being saved and exported after one calculation cycle. By importing the initial information, the DEM will start initially by running PFC^{3D}, and the time step for this DEM simulation was determined by the default approach in PFC^{3D}. In this coupling model, the coupling time was 0.01

second, and fluid regime was assumed to be the same during this short period. After this DEM

calculation to 0.01 second, the particle information (e.g., particle coordinates, particle velocities,

and radii) will be exported to the fluid model program, and the time step in this fluid model was

determined by Eq. B.2. The local porosity at each fluid calculation node can be determined using

a measurement sphere from the particle information. The volume of DEM elements in this

measurement sphere is determined as V_{solid}, while the total volume of measurement sphere inside

this fluid domain is calculated as V_{total}. Therefore, the local porosity n can be calculated: $n = 1 - V_{\text{solid}}/V_{\text{total}}$. The corresponding forces by fluid on the DEM particles can be calculated. After

applying these forces onto the particles, the next DEM cycle will start again. This calculation loop

is implemented until the specified step number is reached, and then the program will be terminated.

Appendix C: Governing Equations in the CFD Simulation

The governing equations and constitutive models used in this chapter are briefly listed, which can be found in the theory guide manual of ANSYS on page 511 (ANSYS FLUENT 15.0: Theory Guide, 2013):

Mass conservation

$$\frac{\partial}{\partial t}\left(\alpha_i \rho_i\right)+\nabla \cdot\left(\alpha_i \rho_i \vec{v}_i\right)=0$$

$i = f$: the fluid phase

$i = s$: the solid phase

Momentum conservation

$$\frac{\partial}{\partial t}\left(\alpha_i \rho_i \vec{v}_i\right)+\nabla \cdot\left(\alpha_i \rho_i \vec{v}_i \vec{v}_i\right)=-\alpha_i \cdot \nabla p+\nabla \cdot \bar{\bar{\tau}}_i+\alpha_i \rho_i \vec{g}+K_{fs}\left(\vec{v}_f-\vec{v}_s\right)$$

Granular energy conservation

$$1.5\left[\frac{\partial}{\partial t}\left(\alpha_s \rho_s \Theta_s\right)+\nabla\left(\alpha_s \rho_s \Theta_s \vec{v}_s\right)\right]=\left(-p_s \bar{\bar{I}}+\bar{\bar{\tau}}_s\right): \nabla \vec{v}_s+\nabla\left(k_{\Theta s} \cdot \nabla \Theta_s\right)-\gamma_{\Theta s}+\phi_{fs}$$

$$k_{\Theta s}=\frac{15 d_p \rho_s \alpha_s \sqrt{\Theta_s \pi}}{4(41-33 \eta)}\left[1+\frac{12}{5} \eta^2(4 \eta-3) \alpha_s g_{0,ss}+\frac{16}{15 \pi}(41-33 \eta) \eta \alpha_s g_{0,ss}\right]$$

Syamlal et al. (1993)

where,

$$\eta=1+e_{ss}, \quad \gamma_{\Theta s}=\frac{12\left(1-e_{ss}^2\right) g_{0,ss}}{d_p \sqrt{\pi}} \rho_s \alpha_s^2 \Theta_s^{3/2}, \quad \phi_{fs}=-3 K_{fs} \Theta_s$$

Lun et al. (1984)

Granular pressure

$$p_s=\alpha_s \rho_s \Theta_s+2 \rho_s\left(1+e_{ss}\right) \alpha_s^2 g_{0,ss} \Theta_s$$

Lun et al. (1984)

Granular shear stress

$$\bar{\bar{\tau}}_s=\alpha_s \mu_s\left(\nabla \vec{v}_s+\nabla \vec{v}_s^T\right)+\alpha_s\left(\lambda_s-\frac{2}{3} \mu_s\right) \nabla \vec{v}_s \bar{\bar{I}}$$

Bulk viscosity

$$\lambda_s=\frac{4}{3} \alpha_s d_p \rho_s g_{0,ss}\left(1+e_{ss}\right)\left(\Theta_s / \pi\right)^{1/2}$$

Lun et al. (1984)

Solid shear viscosity

$$\mu_s=\mu_{s,col}+\mu_{s,kin}+\mu_{s,fr}$$

Solid collision viscosity

$$\mu_{s,\text{col}} = 0.8\alpha_s \rho_s d_p g_{0,ss} \left(1+e_{ss}\right)\left(\Theta_s / \pi\right)^{1/2}$$

Gidaspow et al. (1992)

Solid frictional viscosity

$$\mu_{s,\text{fr}} = \frac{p_s \sin\varphi}{2\sqrt{I_{2D}}}$$

Schaeffer (1987)

Kinetic viscosity

$$\mu_{s,\text{kin}} = \frac{\alpha_s d_p \rho_s \sqrt{\Theta_s \pi}}{6\left(3-e_{ss}\right)}\left[1+0.4\left(1+e_{ss}\right)\left(3e_{ss}-1\right)\alpha_s g_{0,ss}\right]$$

Syamlal et al. (1993)

Momentum exchange coefficient

$$K_{fs} = \begin{cases} \dfrac{3}{4}C_D \dfrac{\alpha_s \alpha_f \rho_f \left|\overrightarrow{v_s} - \overrightarrow{v_f}\right|}{d_p}\alpha_f^{-2.65}, & \text{for } \alpha_f > 0.8 \\[4mm] 150\dfrac{\alpha_s^{\,2}\mu_f}{\alpha_f d_p^{\,2}} + 1.75\dfrac{\alpha_s \rho_f \left|\overrightarrow{v_s} - \overrightarrow{v_f}\right|}{d_p}, & \text{for } \alpha_f \le 0.8 \end{cases}$$

Gidaspow et al. (1992)

where,

$$C_D = \frac{24}{\alpha_f Re_s}\left[1+0.15\left(\alpha_f Re_s\right)^{0.687}\right],\ Re_s = \frac{\rho_f d_p \left|\overrightarrow{v_s} - \overrightarrow{v_f}\right|}{\mu_f}$$